der Bundeswehr
Universität München

Volker Kempf

Pressure-robust discretizations for incompressible flow problems on anisotropic meshes

Vollständiger Abdruck der von der Fakultät für Bauingenieurwesen und Umweltwissenschaften der Universität der Bundeswehr München zur Erlangung des akademischen Grades eines

Doktors der Naturwissenschaften

genehmigten Dissertation.

Gutachter:
1. Univ.-Prof. Dr. rer. nat. Thomas Apel
2. Priv.-Doz. Dr. rer. nat. Alexander Linke
3. Univ.-Prof. Dr. rer. nat. Gunar Matthies

Die Dissertation wurde am 07. April 2022 bei der Universität der Bundeswehr München eingereicht und durch die Fakultät für Bauingenieurwesen und Umweltwissenschaften am 05. August 2022 angenommen. Die mündliche Prüfung fand am 22. August 2022 statt.

Acknowledgments

This document contains the results of my time as research associate at the Institute for Mathematics and Computer-Based Simulation of the Universität der Bundeswehr München since the summer of 2018. Since this dissertation marks the end of an important period in my professional life, I want to express my gratitude to the people that made it possible for me to get to this point.

First and foremost I thank my supervisor Univ.-Prof. Dr. rer. nat. Thomas Apel, who gave me the opportunity to pursue my ambition of earning a doctoral degree after my time as an officer in the Bundeswehr, and who always had patience, good ideas and advice when I encountered problems in my research. At the institute, Thomas provided an excellent environment for research by granting freedom to explore ideas and setting ambitious but achievable goals and realistic expectations for my work.

Also I am sincerely grateful to Priv.-Doz. Dr. rer. nat. Alexander Linke, who, together with Thomas, provided the idea for this thesis, mentored me during my brief stay at the Weierstrass Institute in Berlin in early 2019 and has agreed to serve as a reviewer even though he no longer is a full-time researcher. Furthermore I thank Univ.-Prof. Dr. rer. nat. Gunar Matthies for agreeing to review my dissertation.

Moreover I am thankful for the support of my colleagues at the institute. A special thanks in this regard goes to Christof Haubner, who has been a reliable coworker since I started here and has given me ideas for several issues related to the implementation aspects of my numerical examples.

Finally, I thank my girlfriend Songyuan for being by my side and supporting my academic aspiration, and my parents and siblings for their moral support.

Abstract

Recently there has been increased interest in a special class of discretizations for incompressible flows, which produce velocity approximations that are independent of how well the pressure can be approximated. For this reason such methods are called pressure-robust. While classical methods like the family of Taylor–Hood finite elements show a locking phenomenon induced by the viscosity parameter of the fluid, meaning that the error of the discrete velocity solution scales with the inverse of the viscosity, pressure-robust methods do not have this problem.

Moreover, incompressible flows tend to form layer structures, for example near walls, and exhibit singularities in the solution near re-entrant edges of the domain. These two effects cause additional difficulties for discretization approaches that can be addressed by anisotropic mesh grading, which uses highly stretched elements in boundary layer regions or near the re-entrant edges. A drawback with regard to anisotropic grading is that only few methods are shown to work for such meshes.

The aim of this thesis is to find a combined solution to both challenges, pressure-robustness and anisotropically graded meshes, in order to produce a framework for methods that can satisfy the demands of the two areas. To this effect we use the well known reconstruction approach, that alters classical discretizations in a way that makes them pressure-robust, and connect it with new results from anisotropic interpolation theory to show that a combined approach works.

The generated framework is applied to the modified Crouzeix–Raviart and Bernardi–Raugel methods, and the results are supported by a variety of numerical examples.

Zusammenfassung

In letzter Zeit hat das Interesse an einer speziellen Klasse von Diskretisierungsverfahren für inkompressible Strömungen zugenommen, die Geschwindigkeitsapproximationen liefern, welche unabhängig davon sind, wie gut der Druck angenähert werden kann. Solche Methoden werden aus diesem Grund druckrobust genannt. Während klassische Methoden wie die Familie der Taylor–Hood finiten Elemente ein durch den Viskositätsparameter des Fluids induziertes Locking-Phänomen aufweisen, d. h., dass der Fehler der diskreten Geschwindigkeitslösung mit dem Kehrwert der Viskosität skaliert, besteht dieses Problem bei druckrobusten Methoden nicht.

Außerdem neigen inkompressible Strömungen dazu, Schichtstrukturen zu bilden, z. B. in der Nähe von Wänden, und sie weisen Singularitäten in der Lösung in der Nähe von einspringenden Kanten des Gebiets auf. Diese beiden Effekte verursachen zusätzliche Schwierigkeiten für einen Diskretisierungsansatz, die jedoch durch anisotrope Netzverfeinerung angegangen werden können, wobei stark gedehnte Elemente in Grenzschichtregionen oder in der Nähe der einspringenden Kanten verwendet werden. Ein Schwachpunkt der anisotropen Netzverfeinerung ist, dass bisher nur für wenige Methoden gezeigt werden konnte, dass sie für solche Netze anwendbar sind.

Das Ziel dieser Arbeit ist es, eine kombinierte Lösung für beide Herausforderungen, Druckrobustheit und anisotrope Netze, zu finden, um einen Rahmen für Methoden zu schaffen, die den Anforderungen beider Bereiche gerecht werden können. Zu diesem Zweck verwenden wir den bekannten Rekonstruktionsansatz, der klassische Diskretisierungen so verändern kann, dass sie druckrobust werden, und verbinden ihn mit neuen Ergebnissen aus der anisotropen Interpolationstheorie, um zu zeigen, dass ein kombinierter Ansatz funktioniert.

Der entwickelte Rahmen wird auf die modifizierten Crouzeix–Raviart- und Bernardi–Raugel-Methoden angewandt, und die Ergebnisse werden durch numerische Beispiele untermauert.

Contents

1 Combining pressure-robustness and anisotropic elements **1**

2 Preliminaries and incompressible flows **7**
2.1 Fundamental notation and concepts 7
2.1.1 Classical and weighted function spaces 7
2.1.2 Helmholtz–Hodge projection 9
2.2 Incompressible flows 10
2.2.1 The Navier–Stokes equations 11
2.2.2 The Stokes equations 12
2.3 Pressure-robustness 15
2.3.1 An equivalence class of forces 15
2.3.2 Effect of missing pressure-robustness – an example 16
2.4 Anisotropic triangulations for flow problems 17
2.4.1 Notation for meshes and mesh regularity requirements 17
2.4.2 Boundary layers 21
2.4.3 Edge singularities 23

3 Pressure-robust discretization of the Stokes equations **25**
3.1 General notation for discrete setting 25
3.2 Exactly divergence-free methods 27
3.2.1 $\boldsymbol{H}^1_0(\Omega)$-conforming methods 27
3.2.2 $\boldsymbol{H}_0(\mathrm{div}, \Omega)$-conforming methods 29
3.3 Pressure-robustness by reconstruction 34
3.3.1 $\boldsymbol{H}^1_0(\Omega)$-smoothing 34
3.3.2 $\boldsymbol{H}_0(\mathrm{div}, \Omega)$-reconstruction 37

4 $\boldsymbol{H}(\mathrm{div}, \Omega)$-conforming interpolation on anisotropic triangulations **39**
4.1 Reference geometries 39
4.2 Brezzi–Douglas–Marini interpolation 41
4.2.1 Interpolation operators 41
4.2.2 Stability estimates 42

4.2.3 Interpolation error estimates 54
4.3 Raviart–Thomas interpolation 57
4.3.1 Interpolation operator 58
4.3.2 Interpolation error estimates 58
4.4 Alternative proof for lowest-order interpolation 59
4.5 Brezzi–Douglas–Marini interpolation on triangular prisms 63

5 A-priori error analysis of pressure-robust methods on anisotropic meshes 71
5.1 General error analysis 71
5.2 Modified Bernardi–Raugel method 77
5.3 Modified Crouzeix–Raviart method 81

6 Numerical examples 89
6.1 Boundary layer 89
6.2 Stagnation point flow 93
6.2.1 Stokes model 93
6.2.2 Stationary Navier–Stokes model 98
6.3 Edge singularity 100
6.3.1 Fixed exact solution 100
6.3.2 Fixed data function 103

7 Conclusion and outlook 105

References 107

List of Figures

2.1 Elementwise gradient norm $\|\nabla \boldsymbol{u}_h\|_{0,T}$ of discrete velocity solution for different methods and right hand sides. Note the logarithmic scaling on the color bar. 17
2.2 Triangles with decreasing regularity properties from left to right: Isotropic triangle, anisotropic triangle with maximum angle condition, anisotropic triangle without maximum angle condition. 19
2.3 Comparison of two anisotropic tetrahedra, with regular vertex property (left) and without regular vertex property (right). 19
2.4 Triangular prism subdivided into three tetrahedra. 20
2.5 Two example meshes of Shishkin-type for boundary layer phenomena. . 22
2.6 Visualization of domain for singular edge problems. Example triangulation of domain with anisotropic mesh grading. 23

3.1 Left: Barycentric refinement (orange) of a Shishkin-type mesh (black) with transition point $\tau = 0.1$ and $q = 0.5$. Right: Discrete inf-sup constant of the Scott–Vogelius pair on barycentrically refined Shishkin-type meshes. 28
3.2 Illustration of the geometric quantities in the modified penalty term. . . 30
3.3 Illustration of the three mesh families used in Example 3.2. The parameter to adjust the aspect ratio is highlighted. 32
3.4 Computed discrete inf-sup constants for the three mesh families from Example 3.2 plotted over the maximal aspect ratio in the mesh. 32
3.5 Comparison of the velocity gradient errors produced by the $\boldsymbol{H}_0(\mathrm{div}, \Omega)$-conforming discontinuous Galerkin methods using the standard and modified penalty terms. 33
3.6 Schematic of the mesh used in Example 3.4 and computational results. . 37

4.1 Reference tetrahedron $\widehat{T}$ with vertex numbering, transformed tetrahedron of reference family $\mathcal{R}_1$. 40
4.2 Reference tetrahedron $\overline{T}$ for family of tetrahedra without regular vertex property, transformed tetrahedron of reference family $\mathcal{R}_2$. 40
4.3 Family of triangles not satisfying a maximum angle condition for $h \to 0$. 53

4.4 Reference prism $\widehat{P}$ with vertex numbering, and a transformed prism of the reference family $\mathcal{R}_P$. 64

5.1 Comparison of Bernardi–Raugel facet bubble before and after reconstruction using Brezzi–Douglas–Marini interpolation. Color visualizes function magnitude $|\boldsymbol{t}_F(x,y)|$ resp. $\left|I_1^{\mathrm{BDM}}\boldsymbol{t}_F(x,y)\right|$. 81
5.2 Comparison of Crouzeix–Raviart basis function before and after reconstruction using Raviart–Thomas interpolation. Color visualizes function magnitude $|\boldsymbol{t}_{F,1}(x,y)|$ resp. $\left|I_0^{\mathrm{RT}}\boldsymbol{t}_{F,1}(x,y)\right|$. 87
5.3 Geometric setting for Remark 5.14 87

6.1 Magnitude of velocity solution for $\varepsilon = 10^{-2}$. The transition parameter τ is chosen so that the boundary layer is contained in the graded part of the mesh, see the dashed line in the figure. 90
6.2 Convergence plots for the boundary layer example for $\varepsilon \in \{10^{-4}, 10^{-5}\}$, $\nu = 10^{-3}$, with CR, CR-RT and CR-BDM methods. 91
6.3 Convergence plots for the boundary layer example for $\varepsilon \in \{10^{-4}, 10^{-5}\}$, $\nu = 10^{-4}$, with BR and BR-BDM methods. 92
6.4 Plot of the solution of (6.2) and its derivatives. 94
6.5 Visualization of the velocity (left) and pressure (right) solution $\boldsymbol{u}$ and p for $\nu = 0.01$, $a = 1$, $P_0 = 0$. Color indicates the magnitude of the velocity and the pressure value, respectively. Arrows show the flow direction and strength. The boundary layer width is indicated at $\delta = 0.24$. 94
6.6 Shishkin type mesh used in the calculations. Grading for $\nu = 10^{-4}$, resulting in an aspect ratio of $\sigma \approx 21.4$. 95
6.7 Convergence plots for the stagnation point example, $\nu = 10^{-4}$. 96
6.8 Squared elementwise gradient error $\|\nabla(\boldsymbol{u} - \boldsymbol{u}_h)\|_{0,T}^2$ of the velocity solution for the standard (left) and modified (right) method on uniform (top) and graded (bottom) meshes. 96
6.9 Helmholtz–Hodge decomposition of the data function $\boldsymbol{f} = -(\boldsymbol{u}\cdot\nabla)\boldsymbol{u}$ into divergence-free part $\mathbb{P}\boldsymbol{f}$ and irrotational part $\nabla\phi$. 97
6.10 Convergence plots for the stagnation point example, comparison of BR and BR-BDM methods, $\nu = 10^{-3}$. 97
6.11 Illustration of domain (6.3) for $\omega = \frac{3}{2}\pi$, velocity solution (left) and pressure solution at $z = 1$. 101
6.12 Convergence plots for the singular edge example for $\nu \in \{1, 10^{-2}\}$. . . . 102
6.13 Cellwise error $\|\nabla\boldsymbol{u} - \nabla\boldsymbol{u}_h\|_{1,T}^2$ aggregated on bottom mesh for quasi-uniform (left) and anisotropically graded (right) meshes. 103
6.14 Convergence plots for the singular edge example with fixed data on graded meshes for $\nu = 10^{-3}$. 104

List of Tables

5.1 References and results concerning the modified Crouzeix–Raviart method 83

6.1 Comparison of $\|\boldsymbol{u} - \boldsymbol{u}_h\|_{1,h}$ for parameters $\varepsilon = 10^{-4}$, $\nu \in \{10^{-3}, 10^{-5}\}$, computed with CR, CR-RT and CR-BDM methods on Shishkin-type meshes. 92

6.2 Iterations until convergence and convergence orders for gradient error of velocity, different viscosities on uniform and graded meshes. Comparison of CR and CR-RT methods. The entry *dnc* means the Picard-iteration did not converge to the required precision within 50 iterations. 99

6.3 Velocity gradient error $\|\boldsymbol{u} - \boldsymbol{u}_h\|_{1,h,rel}$ for numerical results corresponding to data from Table 6.2. 99

List of Symbols

$\{\!\{\boldsymbol{v}\}\!\}_F$, 25
$\langle F \rangle$, 30
$[\![\boldsymbol{v}]\!]_F$, 25
$\nabla_h \cdot$, 26
∇_h, 26
$|||\cdot|||_{e,\#}$, 30
$\|\cdot\|_{1,h}$, 26
$\|\cdot\|_{m,q,G}$, 8
$\|\cdot\|_{m,G}$, 8
$\|\cdot\|_{m,q;\beta,G}$, 9
$\|\cdot\|_{m;\beta,G}$, 9

β, 13
$\widetilde{\beta}$, 73
$\mathrm{BDM}_k(\mathcal{T}_h)$, 41
$\mathrm{BR}(\mathcal{T}_h)$, 77

$C^m(G)$, 7
$C_0^\infty(G)$, 8
$\mathrm{CR}(\mathcal{T}_h)$, 26

$\frac{\partial}{\partial \boldsymbol{l}}$, 9
$D^{\boldsymbol{\alpha}}$, 8
$D_{\boldsymbol{l}}^{\boldsymbol{\alpha}}$, 54
d, 17

E_h, 34
$\boldsymbol{e}_i$, 17

$\mathcal{F}(\mathcal{T}_h)$, 18
$\mathcal{F}^b(\mathcal{T}_h)$, 18
$\mathcal{F}^i(\mathcal{T}_h)$, 18

$\boldsymbol{H}(\mathrm{div}, \Omega)$, 9
$\boldsymbol{H}_0(\mathrm{div}, \Omega)$, 9
$H^m(G)$, 8
h_T, 17

I_h, 37
I_h^F, 72
I_k^{BDM}, 42
I_h^{BDM}, 82
$I_h^{\mathrm{BDM}'}$, 82
I_h^{BR}, 77
I_h^{CR}, 82
I_k^{RT}, 58
I_n, 18

$_iI_n$, 18

λ_i, 59
$L^q(G)$, 8
$\boldsymbol{L}^2_\sigma(\Omega)$, 10
$L^2_0(\Omega)$, 10
$\boldsymbol{l}_{T,i}$, 19

$MAC(\overline{\phi})$, 18

ν, 11
$\boldsymbol{N}_k(T)$, 42
$\boldsymbol{n}_{\partial\Omega}$, 9
$\boldsymbol{n}_{T,F}$, 18
$\boldsymbol{n}_F$, 18

$\mathbb{P}$, 10
$P_k(G)$, 9
$P_{m,n}(G)$, 64
$\mathcal{P}_{m,n}(G)$, 64
$P_k(\mathcal{T}_h)$, 18
$P_k^{\mathrm{nc}}(\mathcal{T}_h)$, 18
$\boldsymbol{p}_{T,i}$, 18

Q, 13
Q_h, 26
q, 21

$\mathcal{R}_1$, 40
$\mathcal{R}_2$, 40
$\mathcal{R}_P$, 67
$RVP(\overline{c})$, 19
$\mathrm{RT}_k(\mathcal{T}_h)$, 58

σ_T, 18

τ, 21
$\mathcal{T}_h$, 17

$\mathcal{V}(\mathcal{T}_h)$, 18
$\mathcal{V}^b(\mathcal{T}_h)$, 18
$\mathcal{V}^i(\mathcal{T}_h)$, 18
$V^{m,q}_\beta(G)$, 9

$W^{m,q}(G)$, 8
$W^{m,q}_0(G)$, 8
$W^{-m,q'}(G)$, 8

$\boldsymbol{X}$, 13
$\boldsymbol{X}_h$, 26
$\boldsymbol{X}^0$, 10
$\boldsymbol{X}^0_h$, 26
$\boldsymbol{x}_T$, 18
$\boldsymbol{x}_F$, 18

CHAPTER 1

Combining pressure-robustness and anisotropic elements

Most of the commonly used classical inf-sup stable finite element methods for incompressible flows, like, e.g., the Taylor–Hood finite element family, do not yield exactly divergence-free velocity solutions in the sense of $\boldsymbol{H}(\mathrm{div}, \Omega)$ in general settings. Instead, the divergence constraint is only satisfied approximately in order to obtain an inf-sup stable element pair. This phenomenon of discretizations is also called *poor mass conservation* and can lead to severe numerical inaccuracies in certain settings, see [Lin09].

For the Stokes equations

$$\begin{aligned} -\nu\Delta\boldsymbol{u} + \nabla p &= \boldsymbol{f} && \text{in } \Omega, \\ \nabla \cdot \boldsymbol{u} &= 0 && \text{in } \Omega, \end{aligned}$$

where ν is the viscosity of the fluid, such methods lead to error estimates of the type

$$\|\boldsymbol{u} - \boldsymbol{u}_h\|_1 \lesssim \inf_{\boldsymbol{v}_h \in \boldsymbol{X}_h} \|\boldsymbol{u} - \boldsymbol{v}_h\|_1 + \frac{1}{\nu} \inf_{q_h \in Q_h} \|p - q_h\|_0,$$

see, e.g., [Joh+17], where $\boldsymbol{X}_h$ and Q_h are the velocity and pressure approximation spaces. The second term in the bound shows that the quality of the velocity estimate depends on the pressure and the viscosity. For $\nu \to 0$ this term can deteriorate unboundedly, which characterizes a locking behavior in the sense of [BS92], and thus defeats the purpose of the estimate. Numerical examples show that this is not only of theoretical interest, but that the computed discrete solution is indeed affected, see, e.g., [AK21; AKLM21; BLMS15; LLMS17; Lin14].

In contrast, exactly divergence-free methods of polynomial order m, which can be $\boldsymbol{H}^1(\Omega)$-conforming methods like the Scott–Vogelius element, see [SV85], or $\boldsymbol{H}(\mathrm{div}, \Omega)$-conforming discontinuous Galerkin methods, see, e.g., [CKS07; LS18; LS16], using Raviart–Thomas or Brezzi–Douglas–Marini finite elements, see [BDM85; Néd80; Néd86; RT77],

yield velocity error estimates of the type

$$\|\boldsymbol{u} - \boldsymbol{u}_h\|_{1,h} \lesssim \inf_{\boldsymbol{v}_h \in \boldsymbol{X}_h} \|\boldsymbol{u} - \boldsymbol{v}_h\|_{1,h} + h^m |\boldsymbol{u}|_{m+1},$$

where the second term is a consistency error that is not present for the $\boldsymbol{H}^1(\Omega)$-conforming methods and converges with optimal order of h for the others. Clearly, this type of estimate is not prone to the locking effect described above. Methods for which such an error estimate can be obtained are called pressure-robust, as they yield a discrete velocity solution that is independent of the pressure approximation and the viscosity.

The exactly divergence-free methods we just touched on are inherently pressure-robust, but for classical inf-sup stable elements as the ones mentioned before pressure-robustness can also be attained by using the reconstruction approach that was established in [Lin14]. This approach applies a reconstruction operator I_h to the velocity test functions on the right hand side in the discretization of the Stokes problem, which alters the discrete weak formulation to: Find $(\boldsymbol{u}_h, p_h) \in \boldsymbol{X}_h \times Q_h$ for which

$$\begin{aligned} \nu(\nabla_h \boldsymbol{u}_h, \nabla_h \boldsymbol{v}_h) + (\nabla_h \cdot \boldsymbol{v}_h, p_h) &= (\boldsymbol{f}, I_h \boldsymbol{v}_h) && \forall \boldsymbol{v}_h \in \boldsymbol{X}_h, \\ (\nabla_h \cdot \boldsymbol{u}_h, q_h) &= 0 && \forall q_h \in Q_h, \end{aligned}$$

holds. With this modification, pressure-robustness is achieved at the cost of an additional consistency error that has to be bounded with the right order of h. The idea of this method is to think of the Helmholtz–Hodge decomposition of the data function, which can be written as $\boldsymbol{f} = \mathbb{P}\boldsymbol{f} + \nabla\phi$ with a divergence-free part $\mathbb{P}\boldsymbol{f}$ and an irrotational part $\nabla\phi$. Consider now the property of the continuous setting, where the part $(\nabla\phi, \boldsymbol{v})$ on the right hand side of the weak form of the problem vanishes for divergence-free test functions $\boldsymbol{v}$ due to the L^2-orthogonality of divergence-free and irrotational functions. The reconstruction approach aims to emulate this behavior by regaining the L^2-orthogonality of the irrotational part of the data and discretely divergence-free velocity test functions $\boldsymbol{v}_h$, which are suitably mapped by the reconstruction operator to exactly divergence-free functions. This approach has been used for various classical methods, e.g., the Crouzeix–Raviart, Bernardi–Raugel and Taylor–Hood finite element pairs, see [LLMS17; Lin14; LM16].

In addition to those aspects concerning pressure-robustness, incompressible flow models produce thin boundary layers near walls which could ideally be resolved with anisotropic elements, i.e., elements with large aspect ratio that are stretched in the direction parallel to the wall. Since the boundary layer is thinner for smaller values of the viscosity, it seems beneficial to combine anisotropic elements with pressure-robust methods, which do not exhibit viscosity locking. However, the known results for pressure-robust methods, except our recent contributions in [AK21; AKLM21] that form the basis of this thesis, assume shape-regularity of the used elements, which only allows isotropic triangulations, i.e., elements where the aspect ratio is bounded by a constant. This not only excludes the very common boundary layer adapted meshes, but also meshes that are anisotropically refined towards a re-entrant edge of the domain. The latter case is interesting, since the solution near such edges has reduced regularity and without an appropriate mesh refinement near the edge the convergence rates are reduced, see, e.g., [ANS01a; ANS01b].

In order to contribute to filling this gap in the theory, we combine results from anisotropic interpolation theory and pressure-robust discretizations for incompressible flows, which enables us to gain error estimates that are valid for the problem settings described in the previous paragraph. As such, we provide a theoretical foundation for the use of pressure-robust methods on anisotropic meshes, and extend the available research literature in this field.

For our results we mainly rely on the mentioned reconstruction approach from [Lin14], in combination with the Crouzeix–Raviart element in two- and three-dimensional settings and the Bernardi–Raugel element in certain two-dimensional domains and meshes. In general, the reconstruction approach allows the use of existing finite element implementations, that only need to be modified with the reconstruction operator. Implementing and optimizing newly developed, exactly divergence-free methods like those from, e.g., [GN14a; GN14b; LS16; Sch19], may be a more difficult task, to which the reconstruction approach may seem favorable.

Outline of the thesis

Chapter 2 starts with a recapitulation of some fundamentals on function spaces and the Helmholtz–Hodge projection. The fundamental mathematical model for incompressible flows, the Navier–Stokes system of partial differential equations, is introduced and the Stokes equations are presented as a simplified variant for which most of our analytical proofs are done. The need for pressure-robustness in discretizations for incompressible flows is then motivated and the chapter concludes with a description of the types of anisotropic meshes we are interested in.

Chapter 3 is dedicated to an overview of existing pressure-robust methods. Starting in Section 3.1 with the general description and notation for the discretizations, we present in Sections 3.2 and 3.3 several approaches to construct pressure-robust methods and investigate their suitability for anisotropic triangulations. From the different concepts for pressure-robust methods we concentrate in the following chapters on the reconstruction approach.

In Chapter 4 we derive interpolation error estimates for the Brezzi–Douglas–Marini interpolation operator and recall the analogous estimates for the Raviart–Thomas interpolation operator. Both operators can be used as reconstruction operators to build pressure-robust methods. Section 4.2 is based on our publication [AK20], but extends the results from Sobolev Hilbert spaces to the more general Sobolev Banach spaces, i.e., $p = 2$ is extended to $1 \leq p \leq \infty$. In addition, new anisotropic estimates for the Brezzi–Douglas–Marini interpolation on triangular prisms are proved.

Chapter 5 contains the a-priori error estimation of pressure-robust methods that use the reconstruction approach on anisotropic meshes. In Section 5.1 a generalized error analysis is presented, that uses a set of assumptions that represent the required properties of a discretization to yield the error estimates. After this, Sections 5.2 and 5.3 detail how the Bernardi–Raugel and Crouzeix–Raviart methods fit in this general error analysis.

A variety of numerical examples is showcased in Chapter 6. The performance of the

methods from Chapter 5 is compared to that of standard non-pressure-robust methods on anisotropic and quasi-uniform meshes in two- and three-dimensional settings.

Chapter 7 concludes the thesis with a brief summary, conclusions and ideas for future research projects that might extend the theory further.

Related publications

This thesis is founded on research that has already been partially published in research articles and conference proceedings contributions. The publications are listed below and their relevance for the thesis is noted.

Publication I

[AK20] T. Apel and V. Kempf. "Brezzi–Douglas–Marini interpolation of any order on anisotropic triangles and tetrahedra". *SIAM J. Numer. Anal.* 58.3 (2020), 1696–1718. DOI: 10.1137/19M1302910

Abstract: Recently, the $\boldsymbol{H}(\mathrm{div}, \Omega)$-conforming finite element families for second-order elliptic problems have come more into focus since, due to hybridization and subsequent advances in computational efficiency, their use is no longer mainly theoretical. Their property of yielding exactly divergence-free solutions for mixed problems makes them interesting for a variety of applications, including incompressible fluids. In this area, boundary and interior layers are present, which demand the use of anisotropic elements. While for the Raviart–Thomas interpolation of any order on anisotropic tetrahedra optimal error estimates are known, this contribution extends these results to the Brezzi–Douglas–Marini finite elements. Optimal interpolation error estimates are proved under two different regularity conditions on the elements, which both relax the standard minimal angle condition. Additionally, a numerical application on the Stokes equations is presented to illustrate the findings.

Relevance for thesis: The reconstruction approach to generate a pressure-robust method from classical inf-sup stable methods that was introduced in [Lin14] relies on $\boldsymbol{H}(\mathrm{div}, \Omega)$-conforming reconstruction operators. In this publication we showed the error estimates for the Brezzi–Douglas–Marini interpolation on anisotropic simplices that are necessary to extend the reconstruction approach to anisotropic meshes. The main results from the article are given in Chapter 4 and extended from the Hilbert-space setting to the general case of $\boldsymbol{W}^{m,p}(\Omega)$ spaces.

Publication II

[AKLM21] T. Apel, V. Kempf, A. Linke, and C. Merdon. "A nonconforming pressure-robust finite element method for the Stokes equations on anisotropic meshes". *IMA J. Numer. Anal.* 42.1 (2021), 392–416. DOI: 10.1093/imanum/draa097

Abstract: Most classical finite element schemes for the (Navier–)Stokes equations are neither pressure-robust, nor are they inf-sup stable on general anisotropic triangulations. A lack of pressure-robustness may lead to large velocity errors, whenever the Stokes momentum balance is dominated by a strong and complicated pressure gradient. It is a consequence of a method, which does not exactly satisfy the divergence constraint. However, inf-sup stable schemes can often be made pressure-robust just by a recent, modified discretization of the exterior force term, using $\boldsymbol{H}(\mathrm{div}, \Omega)$-conforming velocity reconstruction operators. This approach has so far only been analyzed on shape-regular triangulations. The novelty of the present contribution is that the reconstruction approach for the Crouzeix–Raviart method, which has a stable Fortin operator on arbitrary meshes, is combined with results on the interpolation error on anisotropic elements for reconstruction operators of Raviart–Thomas and Brezzi–Douglas–Marini type, generalizing the method to a large class of anisotropic triangulations. Numerical examples confirm the theoretical results in a two- and a three-dimensional test case.

Relevance for thesis: In this publication we showed that the consistency error for the reconstructed Crouzeix–Raviart method could be bounded with the necessary rate also on meshes with unbounded aspect ratio, as long as a maximum angle condition is satisfied. The proof is based on the results from [Lin14] and [AK20], and requires $\boldsymbol{H}^2(\Omega) \times H^1(\Omega)$ regularity of the Stokes solution $(\boldsymbol{u}, p)$. To our knowledge this is the first result of this type for a pressure-robust discretization for incompressible flows on anisotropic meshes in two and three dimensions. The results are included in Chapter 5 of this thesis.

Publication III

[AK21] T. Apel and V. Kempf. "Pressure-robust error estimate of optimal order for the Stokes equations: domains with re-entrant edges and anisotropic mesh grading". *Calcolo* 58.2 (2021), Art. No. 15. DOI: 10.1007/s10092-021-00402-z

Abstract: The velocity solution of the incompressible Stokes equations is not affected by changes of the right hand side data in form of gradient fields. Most mixed methods do not replicate this property in the discrete formulation due to a relaxation of the divergence constraint which means that they are not pressure-robust. A recent reconstruction approach for classical methods recovers this invariance property for the discrete solution, by mapping discretely divergence-free test functions to exactly divergence-free functions in the sense of $\boldsymbol{H}(\mathrm{div}, \Omega)$. Moreover, the Stokes solution has locally singular behavior in three-dimensional domains near concave edges, which degrades the convergence rates on quasi-uniform meshes and makes anisotropic mesh grading reasonable in order to regain optimal convergence characteristics. Finite element error estimates of optimal order on meshes of tensor-product type with appropriate anisotropic grading are shown for the pressure-robust modified Crouzeix–Raviart method using the reconstruction approach. Numerical examples support the theoretical results.

Relevance for thesis: This publication extends the results of [AKLM21] to situations where the domain contains a re-entrant edge and the regularity of the solution is thus reduced. With both publications we showed that the method can be used in the most relevant cases and produces reliable numerical results. The results from this publication are contained in Chapter 5.

Publication IV

[Kem21] V. Kempf. "Pressure-robustness for the Stokes equations on anisotropic meshes". *PAMM. Proc. Appl. Math. Mech.* (2021), e202100112. DOI: 10.1002/pamm.202100112

Abstract: Pressure-robustness has been widely studied since the conception of the notion and the introduction of the reconstruction approach for classical mixed methods in [Lin14]. Using discretizations capable of yielding velocity solutions that are independent of the pressure approximation has been recognized as essential, and a large number of recent articles attest to this fact, e.g., [AP21a; LMN20]. Apart from the pressure-robustness aspect, incompressible flows exhibit anisotropic phenomena in the solutions which can be dealt with by using anisotropic mesh grading. The recent publications [AK21; AKLM21] deal with the combination of both challenges. We briefly revisit the results from [AKLM21] and provide an insightful new numerical example.

Relevance for thesis: This short proceedings contribution features a numerical example dealing with a stagnation point flow. It illustrates the advantages of pressure-robust methods in combination with anisotropic meshes. We use and extend this example in Section 6.2.

CHAPTER 2

Preliminaries and incompressible flows

This chapter introduces the mathematical theory of incompressible flows and the associated concept of pressure-robustness which is described in detail in Section 2.3. Starting with notation and some necessary preliminary definitions and results in Section 2.1, the framework for our analysis is set in Section 2.2 with the introduction of the Navier–Stokes equations and one of its simplified variants, the Stokes equations, which will be used for most of the text as model problem. In Section 2.4 we motivate the need for anisotropic triangulations when investigating incompressible flows with finite element methods and introduce some classes of meshes with special gradings, which can be used for a large variety of problems.

2.1 Fundamental notation and concepts

In our estimates we may use the generic constant $C > 0$, which can change from line to line in the computations. If we want to make a dependence of the constant on a certain parameter or variable explicit, we write, e.g., $C(d)$. The expression $a \lesssim b$ means that there is a positive constant C, so that $a \leq Cb$, and $a \sim b$ means that there are positive constants C_1, C_2, so that $C_1 a \leq b \leq C_2 a$. Symbols in bold font indicate vectors, vector valued functions or function spaces of vector valued functions where each component has the stated regularity.

2.1.1 Classical and weighted function spaces

When dealing with partial differential equations, continuously differentiable functions are a prerequisite. We use the standard notation, see, e.g., [AF03, Paragraph 1.26], and denote by $C^m(G)$, $m \in \mathbb{N}_0$, the space of continuous functions f on an open set $G \subset \mathbb{R}^d$, $d \in \mathbb{N}$,

whose partial derivatives $D^{\boldsymbol{\alpha}} f$, $|\boldsymbol{\alpha}| \leq m$, are continuous. Here $\boldsymbol{\alpha} = (\alpha_1, \ldots, \alpha_d) \in \mathbb{N}_0^d$ is a multi-index with

$$|\boldsymbol{\alpha}| = \sum_{i=1}^{d} \alpha_i \qquad \text{and} \qquad D^{\boldsymbol{\alpha}} = \frac{\partial^{|\boldsymbol{\alpha}|}}{\partial x_1^{\alpha_1} \cdots \partial x_d^{\alpha_d}}.$$

Since continuous functions may be unbounded on an open domain, we also define the space $C^m(\overline{G})$, which consists of functions $f \in C^m(G)$ that have bounded and uniformly continuous derivatives $D^{\boldsymbol{\alpha}} f$, $0 \leq |\boldsymbol{\alpha}| \leq m$, see [AF03, Paragraph 1.28]. These spaces are Banach spaces with respect to the norm

$$\|f\|_{C^m(\overline{G})} = \max_{0 \leq |\boldsymbol{\alpha}| \leq m} \sup_{\boldsymbol{x} \in G} |D^{\boldsymbol{\alpha}} f(\boldsymbol{x})|.$$

Additionally we use the notation $L^q(G)$ for the usual Lebesgue spaces with $1 \leq q \leq \infty$.

With the notion of weak derivatives, see, e.g., [AF03, Paragraph 1.62], we can give a definition of the standard Sobolev spaces.

Definition 2.1. Let $G \subset \mathbb{R}^d$ be any domain. For all integers $m \geq 0$ the function spaces

$$W^{m,q}(G) = \{v \in L^q(G) : \|v\|_{m,q,G} < \infty\}, \qquad 1 \leq q \leq \infty,$$

are called *Sobolev spaces*, where the norms are defined by

$$\|\cdot\|_{m,q,G} = \left(\sum_{|\boldsymbol{\alpha}| \leq m} \|D^{\boldsymbol{\alpha}} v\|_{L^q(G)}^q \right)^{1/q}, \qquad 1 \leq q < \infty,$$
$$\|v\|_{m,\infty,G} = \max_{|\boldsymbol{\alpha}| \leq m} \|D^{\boldsymbol{\alpha}} v\|_{L^\infty(G)}.$$

Occasionally we may also use fractional order Sobolev spaces $W^{s,q}(\Omega)$, $s \geq 0$, which can be defined using an interpolation technique for Banach spaces, see [BS08, Section 14.1].

For the Hilbert space case $q = 2$ we simplify the notation of the norm to $\|\cdot\|_{m,2,G} = \|\cdot\|_{m,G}$, and when we consider the whole domain Ω of a problem we omit the symbol in the index and write $\|\cdot\|_{m,q,\Omega} = \|\cdot\|_{m,q}$ and $\|\cdot\|_{m,2,\Omega} = \|\cdot\|_m$. As usual, the Sobolev spaces for $q = 2$ are also denoted by $H^m(G)$.

With the space $C_0^\infty(G)$ of smooth functions with compact support we can define the spaces $W_0^{m,q}(G)$ as the closure of $C_0^\infty(G)$ in $W^{m,q}(G)$, see [AF03, p. 60]. In the special case of $m = 1$ and a bounded domain G, the space $W_0^{1,q}(G)$ contains the functions from $W^{1,q}(G)$ with vanishing trace in an $L^2(\partial G)$ sense, see [BS08, p. 40], where ∂G is the boundary of the domain G. The dual space of $W_0^{m,q}(G)$ is denoted by $W^{-m,q'}(G)$, where q' is the conjugate exponent of q, i.e., it holds

$$\frac{1}{q} + \frac{1}{q'} = 1.$$

For the case $q = 2$ we use the notation $W_0^{m,2}(G) = H_0^m(G)$ and $W^{-m,2}(G) = H^{-m}(G)$ as before.

In parts of the analysis we encounter singularities in the solution functions that are a result of re-entrant corners or edges, and certain types of weighted Sobolev spaces are useful for these cases.

Definition 2.2. Let $G \subset \mathbb{R}^d$, $d \in \{2, 3\}$, be a domain. Then the function spaces

$$V_\beta^{m,q}(G) = \{v \in \mathcal{D}'(G) : \|v\|_{m,q;\beta,G} < \infty\}, \qquad m \in \mathbb{N}_0,\ 1 < q < \infty,\ \beta \in \mathbb{R},$$

where $\mathcal{D}'(G)$ is the space of distributions, see [AF03, Paragraph 1.57], are called *weighted Sobolev spaces of Kondrat'ev type*. The norm is defined by

$$\|v\|_{m,q;\beta,G}^q = \sum_{|\boldsymbol{\alpha}| \le m} \left\| r^{\beta - m + |\boldsymbol{\alpha}|} D^{\boldsymbol{\alpha}} v \right\|_{0,q,G}^q,$$

where r is the radial coordinate in polar or cylindrical coordinates, measuring the distance to the origin or x_3-axis, respectively. If $q = 2$, we omit the parameter in the index of the norm and write $\|\cdot\|_{m;\beta,G}$. Note that the semicolon in the index is used to distinguish the notation from the norms of the standard Sobolev spaces.

In addition to the above introduced standard and weighted Sobolev spaces we often require the space

$$\boldsymbol{H}(\mathrm{div}, \Omega) = \{\boldsymbol{v} \in \boldsymbol{L}^2(\Omega) : \nabla \cdot \boldsymbol{v} \in L^2(\Omega)\}$$

and its subspace

$$\boldsymbol{H}_0(\mathrm{div}, \Omega) = \{\boldsymbol{v} \in \boldsymbol{H}(\mathrm{div}, \Omega) : \boldsymbol{v}|_{\partial\Omega} \cdot \boldsymbol{n}_{\partial\Omega} = 0\}$$

where $\boldsymbol{n}_{\partial\Omega}$ is the outward pointing unit normal vector on the boundary $\partial\Omega$ of the domain Ω. Due to the divergence constraint in the fluid equations these spaces are important in the treatment of flow problems.

For the finite element discretizations we require the spaces $P_k(G)$, which contain polynomials of maximal degree k on a domain G.

The symbol Ω will always denote a simply connected bounded domain in $\mathbb{R}^d$, $d \in \{2, 3\}$, that has a Lipschitz boundary, for a definition see [Sch98, p. 339]. For an arbitrary vector $\boldsymbol{l} \in \mathbb{R}^d$ we denote the directional derivative in direction $\boldsymbol{l}$ by $\frac{\partial}{\partial \boldsymbol{l}}$.

2.1.2 Helmholtz–Hodge projection

An important concept in the context of pressure-robustness is the orthogonal decomposition of vector fields into divergence-free and irrotational components. An extensive, application-oriented survey of this topic can be found in [BNPB13]. Most of the content of this subsection was similarly discussed in [AK21, Section 4] and [LMN20, Section 3].

Lemma 2.3. *Let $\boldsymbol{g} \in \boldsymbol{L}^2(\Omega)$. Then there is a unique decomposition $\boldsymbol{g} = \mathbb{P}\boldsymbol{g} + \nabla\phi$, where $\phi \in H^1(\Omega)/\mathbb{R}$ and*

$$\mathbb{P}\boldsymbol{g} \in \boldsymbol{L}^2_\sigma(\Omega) = \{\boldsymbol{v} \in \boldsymbol{L}^2(\Omega) : (\nabla q, \boldsymbol{v}) = 0 \quad \forall q \in H^1(\Omega)\}.$$

Here $H^1(\Omega)/\mathbb{R}$ is the quotient space of $H^1(\Omega)$ and $\mathbb{R}$, i.e., functions that differ only by a real constant are merged to an equivalence class.

Proof. For the proof see, e.g., Theorem I.3.6 in conjunction with Corollary I.3.4 in [GR86]. □

This decomposition is called *Helmholtz–Hodge decomposition*, and the operator $\mathbb{P} : \boldsymbol{L}^2(\Omega) \to \boldsymbol{L}^2_\sigma(\Omega)$ is the *Helmholtz–Hodge projector*. Since for all functions $\phi \in H^1(\Omega)$ the unique Helmholtz–Hodge decomposition of $\nabla\phi$ is given by $\nabla\phi = \boldsymbol{0} + \nabla\phi$, we immediately see that for the Helmholtz–Hodge projection of every gradient field it holds

$$\mathbb{P}(\nabla\phi) = \boldsymbol{0}. \tag{2.1}$$

By defining the restriction

$$\langle \mathbb{P}\boldsymbol{g}, \boldsymbol{v}\rangle = \langle \boldsymbol{g}, \boldsymbol{v}\rangle \qquad \forall \boldsymbol{v} \in \boldsymbol{X}^0 \tag{2.2}$$

of a functional $\boldsymbol{g} \in \boldsymbol{H}^{-1}(\Omega)$ to $\boldsymbol{X}^0 = \{v \in \boldsymbol{H}^1_0(\Omega) : (\nabla \cdot \boldsymbol{v}, q) = 0 \ \forall q \in L^2_0(\Omega)\}$, where $L^2_0(\Omega) = \{q \in L^2(\Omega) : \int_\Omega q \,\mathrm{d}\boldsymbol{x} = 0\}$, we can formally extend the projection operator $\mathbb{P}$ from $\boldsymbol{L}^2(\Omega)$ to $\boldsymbol{H}^{-1}(\Omega)$ with range in the dual space of $\boldsymbol{X}^0$, $(\boldsymbol{X}^0)'$. A detailed and technical introduction of this extension can be found in [Mon06, Section 2].

Assuming enough regularity, the Helmholtz–Hodge decomposition of a specific vector field $\boldsymbol{f}$ can in practice be found by solving the problem: Find $(\mathbb{P}\boldsymbol{f}, \phi) \in \boldsymbol{H}_0(\mathrm{div}, \Omega) \times H^1(\Omega)/\mathbb{R}$, so that

$$\mathbb{P}\boldsymbol{f} + \nabla\phi = \boldsymbol{f} \qquad \text{in } \Omega, \tag{2.3a}$$

$$\nabla \cdot \mathbb{P}\boldsymbol{f} = 0 \qquad \text{in } \Omega. \tag{2.3b}$$

2.2 Incompressible flows

After these fundamentals we now consider some facets of incompressible flows. The standard mathematical model to describe the velocity and pressure of fluid flows is the system of the Navier–Stokes equations, which in d spatial dimensions comprise d partial differential equations for the momentum balance and additionally the continuity equation which models the conservation of mass. We omit a detailed derivation of the partial differential equations from the physical principles, for that see, e.g., [Joh16, Chapter 2] or [CM90, Section 1.3], but discuss some aspects of the incompressibility constraint.

The continuity equation in the flow model is derived from the principle that the rate of change of mass over time inside every subdomain vanishes. After some mathematical manipulation of this premise, see, e.g., [Pan13, Section 5.1], we arrive at the form

$$\frac{\partial \rho}{\partial t} + \nabla \cdot (\rho \boldsymbol{u}) = 0, \tag{2.4}$$

where $\rho(\boldsymbol{x}, t)$ is the density of the fluid and $\boldsymbol{u}(\boldsymbol{x}, t)$ its velocity.

When considering incompressible flows, we assume that the continuity equation simplifies to $\nabla \cdot \boldsymbol{u} = 0$. This is a consequence of (2.4) when $\rho(\boldsymbol{x}, t) = \text{const}$, but that is only a special case. By using the material derivative $\frac{\mathrm{D}}{\mathrm{D}t} = \frac{\partial}{\partial t} + \boldsymbol{u} \cdot \nabla$ we can transform (2.4) to

$$\frac{1}{\rho} \frac{\mathrm{D}\rho}{\mathrm{D}t} = -\nabla \cdot \boldsymbol{u}$$

and see that the divergence-free condition also holds if $\frac{1}{\rho} \frac{\mathrm{D}\rho}{\mathrm{D}t} = 0$.

This means that incompressible flow may also occur in an incompressible fluid with variable density, see, e.g., the example in [CL14, Section 2.4.2], but also in certain cases of a compressible fluid at low Mach number, e.g., aerodynamics at velocities far below the speed of sound, where the compression of the fluid can be neglected.

2.2.1 The Navier–Stokes equations

The basic governing equations for incompressible flow problems in a domain $\Omega \subseteq \mathbb{R}^d$ are the Navier–Stokes equations

$$\partial_t \boldsymbol{u} - \nu \Delta \boldsymbol{u} + (\boldsymbol{u} \cdot \nabla)\boldsymbol{u} + \nabla p = \boldsymbol{f} \qquad \text{in } \Omega, \tag{2.5a}$$

$$\nabla \cdot \boldsymbol{u} = 0 \qquad \text{in } \Omega, \tag{2.5b}$$

$$\boldsymbol{u} = \boldsymbol{0} \qquad \text{on } \partial\Omega, \tag{2.5c}$$

where $\boldsymbol{u}$ and p are the velocity and pressure of the fluid, and ν is the kinematic viscosity of the fluid. Apart from (2.5c) several other types of boundary conditions are applied frequently, including the Dirichlet condition

$$\boldsymbol{u}(\boldsymbol{x}, t) = \boldsymbol{g}(\boldsymbol{x}, t) \qquad \text{on } \Gamma_D \subseteq \partial\Omega, \tag{2.6}$$

which can be used to prescribe an inflow or outflow on the boundary, the free-slip condition

$$\boldsymbol{u} \cdot \boldsymbol{n}_{\partial\Omega} = 0 \qquad \text{on } \Gamma_S \subseteq \partial\Omega, \tag{2.7a}$$

$$\boldsymbol{n}_{\partial\Omega}^T (\nu(\nabla \boldsymbol{u} + (\nabla \boldsymbol{u})^T) - p\,\mathrm{Id})\boldsymbol{t}_k = 0 \qquad \text{on } \Gamma_S \subseteq \partial\Omega,\ 1 \leq k \leq d-1, \tag{2.7b}$$

where $\boldsymbol{n}_{\partial\Omega}$, $\boldsymbol{t}_k$ are pairwise orthogonal, which describes a flow slipping along a non-penetrable wall without resistance, or the do-nothing condition

$$(\nu(\nabla \boldsymbol{u} + (\nabla \boldsymbol{u})^T) - p\,\mathrm{Id})\boldsymbol{n}_{\partial\Omega} = \boldsymbol{0} \qquad \text{on } \Gamma_N \subseteq \partial\Omega, \tag{2.8}$$

which is often used as an outflow condition and describes that the normal stress on the boundary Γ_N vanishes. A more detailed overview can be found in [Joh16, Section 2.4]. We however restrict ourselves, with the exception of some numerical examples in Chapter 6, to the homogeneous Dirichlet boundary condition (2.5c), which is also called *no-slip* condition.

As mentioned in [JKN18, Remark 2], the Navier–Stokes equations pose three major challenges when trying to solve them analytically or numerically:

- The coupling of velocity $\boldsymbol{u}$ and pressure p.
- The nonlinear convective term $(\boldsymbol{u} \cdot \nabla)\boldsymbol{u}$.
- The emerging turbulent structures if the convective term dominates the viscous term $-\nu\Delta\boldsymbol{u}$.

Due to these obstacles, the Navier–Stokes equations are still a very active research field for mathematicians and application-oriented scientists.

Since in the study of pressure-robustness we want to concentrate on the first aspect, the coupling of velocity and pressure, we use a simplified mathematical model in our analysis. A possible simplification would be the Oseen equations, which are stationary, i.e., $\partial_t \boldsymbol{u} = \boldsymbol{0}$, and where the nonlinear convective term is replaced by $(\boldsymbol{b} \cdot \nabla)\boldsymbol{u}$, with some divergence-free vector field $\boldsymbol{b}$. This effectively linearizes the differential equation and takes care of the second point in the above list. The Oseen equations arise when using certain discretization methods for the Navier–Stokes equations, see, e.g., [Joh16, Chapter 5].

Due to the convective term, dominating convection can still occur in the Oseen equations. To circumvent this difficulty, convection may be completely neglected, which leads to the Stokes equations that, from a practical point of view, model highly viscous fluids. From the three points in our list, the Stokes equations only exhibit the coupling of velocity and pressure, which makes them well suited for our theoretical analysis in the context of pressure-robustness. As we show in an example in Section 6.2, it is well justified looking at the Stokes equations instead of the full model when investigating pressure-robustness in incompressible flow discretizations, since the complexities that occur in the convective term for exact solutions of the Navier–Stokes equations can be brought to the Stokes equations in a complicated data function.

2.2.2 The Stokes equations

The Stokes equations emerge from the more general Navier–Stokes equations by only considering stationary flows, i.e., $\partial_t \boldsymbol{u} = \boldsymbol{0}$, and by additionally assuming that the convection term is dominated by the friction term and thus can be neglected, i.e., $(\boldsymbol{u} \cdot \nabla)\boldsymbol{u} = \boldsymbol{0}$. With these modeling assumptions we arrive at the Stokes equations

$$-\nu\Delta\boldsymbol{u} + \nabla p = \boldsymbol{f} \qquad \text{in } \Omega, \tag{2.9a}$$

$$\nabla \cdot \boldsymbol{u} = 0 \qquad \text{in } \Omega, \tag{2.9b}$$

$$\boldsymbol{u} = \boldsymbol{0} \qquad \text{on } \partial\Omega. \tag{2.9c}$$

Due to the linearity of the equation, the kinematic viscosity ν can be hidden from the momentum balance by multiplying with ν^{-1} and introducing a new pressure variable and right hand side which are scaled by ν^{-1}. However, since viscosity plays a major role in the context of pressure-robustness due to the viscosity locking described in the introduction, we explicitly retain this parameter in the equation.

The weak form of the Stokes equations is derived as usual, and after integration by

parts the problem takes the form: Find $(\boldsymbol{u}, p) \in \boldsymbol{X} \times Q = \boldsymbol{H}_0^1(\Omega) \times L_0^2(\Omega)$, so that

$$\nu a(\boldsymbol{u}, \boldsymbol{v}) + b(\boldsymbol{v}, p) = (\boldsymbol{f}, \boldsymbol{v}) \qquad \forall \boldsymbol{v} \in \boldsymbol{X}, \tag{2.10a}$$

$$b(\boldsymbol{u}, q) = 0 \qquad \forall q \in Q, \tag{2.10b}$$

where $L_0^2(\Omega) = \{q \in L^2(\Omega) : \int_\Omega q \,\mathrm{d}\boldsymbol{x} = 0\}$. The bilinear forms $a : \boldsymbol{X} \times \boldsymbol{X} \to \mathbb{R}$, $b : \boldsymbol{X} \times Q \to \mathbb{R}$ in this formulation are defined by

$$a(\boldsymbol{u}, \boldsymbol{v}) = \int_\Omega \nabla \boldsymbol{u} : \nabla \boldsymbol{v} \,\mathrm{d}\boldsymbol{x},$$

$$b(\boldsymbol{v}, q) = -\int_\Omega \nabla \cdot \boldsymbol{v} q \,\mathrm{d}\boldsymbol{x}.$$

From classical results, see, e.g., [GR86, Theorem I.5.1], we know that (2.10) has a unique solution.

Proposition 2.4. *Let $\Omega \subset \mathbb{R}^d$ be bounded, connected and open with Lipschitz-continuous boundary $\partial\Omega$ and let $\boldsymbol{f} \in \boldsymbol{H}^{-1}(\Omega)$. Then there is a unique pair of functions $(\boldsymbol{u}, p) \in \boldsymbol{X} \times Q$, so that* (2.10) *is satisfied.*

Even more general, existence and uniqueness of the solution is guaranteed for Dirichlet boundary data $\boldsymbol{g} \in \boldsymbol{H}^{1/2}(\partial\Omega)$. However, in our analysis we mostly do not require this general setting and restrict the assumptions to $\boldsymbol{f} \in \boldsymbol{L}^2(\Omega)$ and homogeneous boundary conditions.

One of the main properties required to prove Proposition 2.4 is the inf-sup stability condition, see, e.g., [Joh16, Theorem 3.46].

Lemma 2.5. *For the spaces $\boldsymbol{X}$ and Q there is a constant $\beta > 0$, so that*

$$\inf_{0 \neq q \in Q} \sup_{\boldsymbol{0} \neq \boldsymbol{v} \in \boldsymbol{X}} \frac{b(\boldsymbol{v}, q)}{\|\boldsymbol{v}\|_1 \|q_h\|_0} \geq \beta \tag{2.11}$$

holds.

Concerning the regularity of the Stokes solution there are several additional results, depending on the regularity of the data and the regularity of the domain. For right hand side data in $\boldsymbol{H}^{-1}(\Omega)$, the classical result for smooth domains, see [Cat61, p. 311], requires that the domain boundary is of class C^2, see [Sch98, p. 340] for a definition. This was improved upon in [GSS94], and we combine both results in the next proposition.

Proposition 2.6. *Let $\Omega \subset \mathbb{R}^d$ be open, bounded and connected with boundary of class C^{m+2} and let $\boldsymbol{f} \in \boldsymbol{W}^{m,q}(\Omega)$, with $m \geq -1$ and $q \in (1, \infty)$. Then for problem* (2.10) *there is a unique solution $\boldsymbol{u} \in \boldsymbol{W}^{m+2,q}(\Omega)$, $p \in W^{m+1,q}(\Omega)$ with $\int_\Omega p \,\mathrm{d}\boldsymbol{x} = 0$ and the estimate*

$$\nu \|\boldsymbol{u}\|_{m+2,q} + \|p\|_{m+1,q} \lesssim \|\boldsymbol{f}\|_{m,q}$$

is satisfied.

This proposition guarantees a higher regularity of the solution than Proposition 2.4 under the assumption of a certain regularity of the boundary of the domain. Additional results are available for the in finite element analysis important cases of polygonal and polyhedral domains. In [KO76] it was proved that the result from Proposition 2.6 holds in the Hilbert-space setting when the domain is a convex polygon and $m = 0$.

An extensive analysis of the solution regularity was conducted in [Dau89] for two- and three-dimensional domains. Additional results for prismatic domains with re-entrant edges are given in [ANS01a, Theorem 2.1] in the context of weighted Sobolev spaces.

Lemma 2.7. *Let $\Omega = G \times (0,1)$, where G is a polygon with exactly one re-entrant corner at the origin with interior angle $\omega \in (\pi, 2\pi)$. Additionally let $\boldsymbol{f} \in \boldsymbol{L}^2(\Omega)$ and let λ be the smallest positive solution of*

$$\sin(\lambda\omega) = -\lambda \sin(\omega). \tag{2.12}$$

Then the solution $(\boldsymbol{u}, p)$ of (2.10) satisfies for $\beta \in (1-\lambda, 1)$

$$\boldsymbol{u} \in \boldsymbol{V}^{2,2}_{\beta}(\Omega), \qquad p \in V^{1,2}_{\beta}(\Omega)$$
$$\frac{\partial \boldsymbol{u}}{\partial x_3} \in \boldsymbol{V}^{1,2}_{0}(\Omega), \qquad \frac{\partial p}{\partial x_3} \in L^2(\Omega),$$

and the estimate

$$\|\boldsymbol{u}\|_{2;\beta,\Omega} + \left\| \frac{\partial \boldsymbol{u}}{\partial x_3} \right\|_{1;0,\Omega} + \|p\|_{1;\beta,\Omega} + \left\| \frac{\partial p}{\partial x_3} \right\|_{0,\Omega} \lesssim \|\boldsymbol{f}\|_{0,\Omega}$$

holds.

Using the Helmholtz–Hodge projector from Section 2.1.2, we can derive a fundamental property that links the projections of the data function and the Laplacian of the Stokes velocity solution, see also [LMN20, Lemma 3.1].

Lemma 2.8. *Let $-\Delta : \boldsymbol{H}^1_0(\Omega) \to \boldsymbol{H}^{-1}(\Omega)$ be defined by*

$$\langle -\Delta \boldsymbol{v}, \boldsymbol{w} \rangle = (\nabla \boldsymbol{v}, \nabla \boldsymbol{w}) \qquad \forall \boldsymbol{w} \in \boldsymbol{H}^1_0(\Omega).$$

Then for the velocity solution $\boldsymbol{u}$ of (2.10) the equality

$$\mathbb{P}(-\Delta \boldsymbol{u}) = \nu^{-1} \mathbb{P} \boldsymbol{f}$$

and the estimate

$$\nu \|\mathbb{P}(-\Delta \boldsymbol{u})\|_0 = \|\mathbb{P}\boldsymbol{f}\|_0 \leq \|\boldsymbol{f}\|_0 \tag{2.13}$$

hold.

Proof. We have in general $\boldsymbol{f} = -\nu\Delta\boldsymbol{u} + \nabla p \in \boldsymbol{H}^{-1}(\Omega)$. Using the extension of the Helmholtz-Hodge projector, see (2.2), and its properties we get

$$\mathbb{P}\boldsymbol{f} = \mathbb{P}(-\nu\Delta\boldsymbol{u} + \nabla p) = \nu\mathbb{P}(-\Delta\boldsymbol{u}), \tag{2.14}$$

since $\mathbb{P}(\nabla p) = \boldsymbol{0}$. The estimate (2.13) follows immediately. □

A consequence of the preceding lemma is that even though in general $-\Delta\boldsymbol{u} \in \boldsymbol{H}^{-1}(\Omega)$, we see that for $\boldsymbol{f} \in \boldsymbol{L}^2(\Omega)$ it holds $\mathbb{P}(-\Delta\boldsymbol{u}) \in \boldsymbol{L}^2(\Omega)$, i.e., the divergence-free part of $-\Delta\boldsymbol{u}$ has a higher regularity.

2.3 Pressure-robustness

The concept of pressure-robust discretizations of incompressible flows is relatively new, see [Lin14], even though the underlying problem of classical discretizations, the inexact enforcement of the divergence constraint, known also as poor mass conservation, has been subject of research activity for substantially longer, see, e.g., [GJ05; GLB97; Lin09; OR04]. This relaxation of the divergence-free condition causes a coupling of the approximability of the discrete velocity with that of the discrete pressure. We briefly introduce the main ideas behind pressure-robustness based on [GLS19; Joh+17; Lin14; SLLL18].

2.3.1 An equivalence class of forces

The Stokes equations show a fundamental invariance property, meaning that the velocity solution is not affected by changes of the gradient part of the data function. This can be seen when looking at the formulation of the problem in the subspace of divergence-free functions: Find $\boldsymbol{u} \in \boldsymbol{X}^0 = \{\boldsymbol{v} \in \boldsymbol{X} : (\nabla \cdot \boldsymbol{v}, q) = 0 \ \forall q \in Q\}$ so that

$$\nu a(\boldsymbol{u}, \boldsymbol{v}) = (\boldsymbol{f}, \boldsymbol{v}) \qquad \forall \boldsymbol{v} \in \boldsymbol{X}^0. \tag{2.15}$$

This form of the Stokes problem is an equivalent problem to (2.10) for only the velocity field of (2.9), see [GR86, Remark 5.2]. In this setting, the pressure p is determined by the additional problem

$$b(\boldsymbol{v}, p) = (\boldsymbol{f}, \boldsymbol{v}) - \nu a(\boldsymbol{u}, \boldsymbol{v}) \qquad \forall \boldsymbol{v} \in \boldsymbol{X} \setminus \boldsymbol{X}^0,$$

which is well posed, assuming the inf-sup condition (2.11) holds, see also [BS08, Lemma 12.2.12]. Taking into account the Helmholtz–Hodge decomposition of the data function $\boldsymbol{f} = \mathbb{P}\boldsymbol{f} + \nabla\phi$, we get by using integration by parts

$$(\boldsymbol{f}, \boldsymbol{v}) = (\mathbb{P}\boldsymbol{f}, \boldsymbol{v}) + (\nabla\phi, \boldsymbol{v}) = (\mathbb{P}\boldsymbol{f}, \boldsymbol{v}) - (\phi, \nabla \cdot \boldsymbol{v}) + (\phi, \boldsymbol{v} \cdot \boldsymbol{n}_{\partial\Omega})_{L^2(\partial\Omega)}.$$

Since $\boldsymbol{v} \in \boldsymbol{X}^0$ the second and third term vanish and we are left with $(\mathbb{P}\boldsymbol{f}, \boldsymbol{v})$ on the right hand side of the variational formulation (2.15), i.e., the velocity solution $\boldsymbol{u} \in \boldsymbol{X}^0$ of (2.10) is determined by

$$\nu a(\boldsymbol{u}, \boldsymbol{v}) = (\mathbb{P}\boldsymbol{f}, \boldsymbol{v}) \qquad \forall \boldsymbol{v} \in \boldsymbol{X}^0. \tag{2.16}$$

Thus, two data functions $\boldsymbol{f}$ and $\boldsymbol{g}$ lead to the identical velocity solution of the Stokes equations, if they have the same Helmholtz–Hodge projection, i.e., $\mathbb{P}\boldsymbol{f} = \mathbb{P}\boldsymbol{g}$. This is the case if and only if they differ by a gradient field, which leads to the definition of an equivalence relation.

Definition 2.9. Two vector fields $\boldsymbol{f}, \boldsymbol{g} \in \boldsymbol{L}^2(\Omega)$ are called *velocity-equivalent*, if they differ only by a gradient field, i.e., there is a potential $\psi \in H^1(\Omega)$ so that $\boldsymbol{f} = \boldsymbol{g} + \nabla\psi$. If two functions $\boldsymbol{f}, \boldsymbol{g}$ are velocity-equivalent, we write $\boldsymbol{f} \cong \boldsymbol{g}$.

This property of the Stokes equations means that a change of the right hand side by a gradient field, i.e., $\boldsymbol{f} \to \boldsymbol{f} + \nabla\phi$, $\phi \in H^1(\Omega) \cap Q$, results only in a change of the pressure solution $(\boldsymbol{u}, p) \to (\boldsymbol{u}, p + \phi)$. As mentioned in [LMT16, Remark 2.1], this property also holds for any boundary condition that does not involve the pressure, e.g., general Dirichlet or free-slip conditions, see (2.6) and (2.7). For an explanation why the pressure must not be involved, suppose $(\boldsymbol{u}, p)$ is the solution of a problem with the do-nothing condition (2.8). Then inserting $(\boldsymbol{u}, p + \phi)$ into (2.8) gives

$$(\nu(\nabla\boldsymbol{u} + (\nabla\boldsymbol{u})^T) - (p + \phi)\,\mathrm{Id})\boldsymbol{n}_{\partial\Omega} = -\phi\boldsymbol{n}_{\partial\Omega},$$

which shows that the boundary condition is not satisfied for general functions $\phi \in H^1(\Omega) \cap Q$, which means that the mentioned property does not hold.

The basic idea of a pressure-robust discretization is that, as in the continuous case, the discrete velocity solution will not change if the right hand side data function is replaced by another velocity-equivalent function.

2.3.2 Effect of missing pressure-robustness – an example

In order to get an impression of the effect of using a pressure-robust method instead of a classical discretization like the Taylor–Hood element, we show an elementary example in advance of the detailed introduction in Chapter 3. A similar illustrative example was used in [GLS19, Section 2.5]. Consider a hydrostatic setting on the unit square $\Omega = (0, 1)^2$, i.e., the data function on the right hand side has the form $\boldsymbol{f} = \nabla\psi$ for some $\psi \in H^1(\Omega)$. This results in the solution functions $(\boldsymbol{0}, \psi)$ of problems (2.9) and (2.10).

We compare the classical Taylor–Hood $\boldsymbol{P}_k$–P_{k-1} element from [TH73], denoted by TH_k, with the pressure-robust modified Crouzeix–Raviart method from [Lin14], denoted by CR-RT, which is a lowest order method that we describe and investigate in more detail in Section 5.3. Figure 2.1 shows the elementwise gradient error of the discrete solution on an unstructured mesh for several orders of the Taylor–Hood element and the modified Crouzeix–Raviart method, each for different choices of ψ and the viscosity set to $\nu = 10^{-4}$.

Even though the velocity solution $\boldsymbol{u} = \boldsymbol{0}$ is contained in the discrete velocity space and it could be expected that all methods find the correct solution, this is not the case for all combinations. The discrete velocity solution of the Taylor–Hood element is severely degraded in settings where the pressure solution is not contained in the discrete pressure space. Even worse, when looking at the error estimates of the method, see, e.g., [Joh+17, Section 3], the best-approximation term for the pressure is scaled with the factor ν^{-1}, resulting in a viscosity induced locking effect.

On the other hand, the pressure-robust modified Crouzeix–Raviart method delivers the true velocity solution $\boldsymbol{u}_h = \boldsymbol{0}$ for all tested right hand sides, even though the pressure is only approximated by piecewise constants. Thus, this simple example already shows the potential of pressure-robust discretizations.

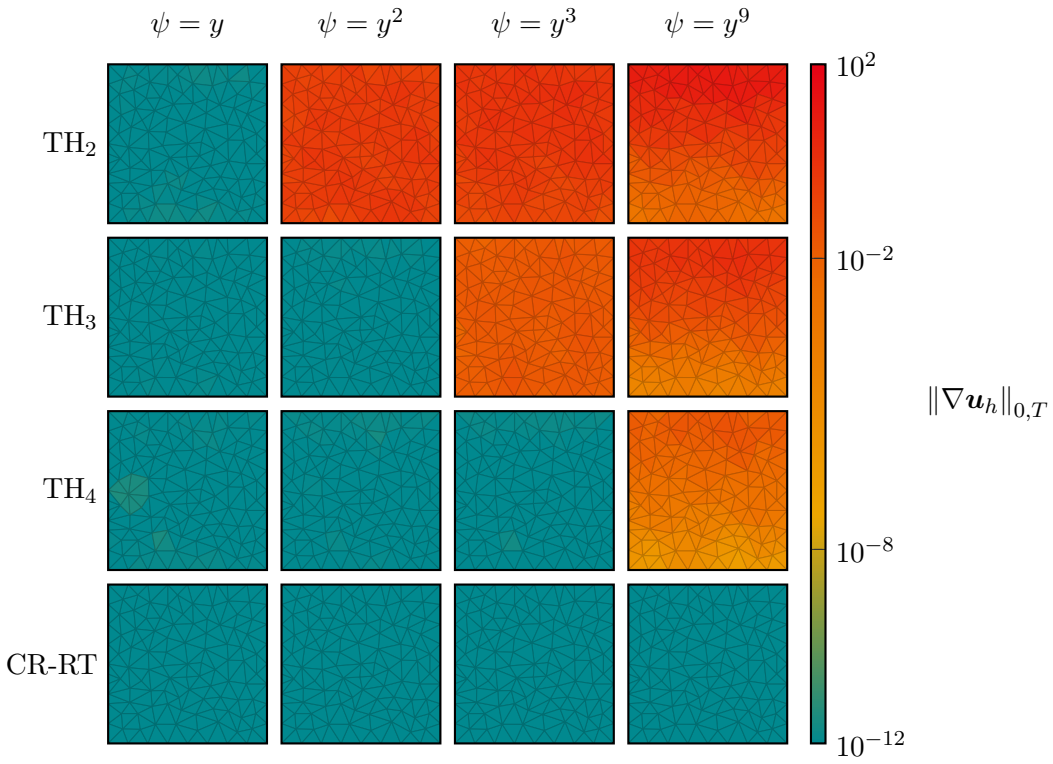

Figure 2.1: Elementwise gradient norm $\|\nabla \boldsymbol{u}_h\|_{0,T}$ of discrete velocity solution for different methods and right hand sides. Note the logarithmic scaling on the color bar.

2.4 Anisotropic triangulations for flow problems

We introduce some frequently used notation and concepts concerning meshes in general and specifically meshes using anisotropic, i.e., highly stretched elements. Additionally we detail the type of mesh gradings we use in the forthcoming analysis and numerical examples for boundary layers and edge singularities in flow problems.

2.4.1 Notation for meshes and mesh regularity requirements

We consider conforming, simplicial discretizations $\mathcal{T}_h$ of the domain $\Omega \subset \mathbb{R}^d$, with space dimension $d \in \{2, 3\}$. The Cartesian unit vectors are denoted by $\boldsymbol{e}_i$, $i \in \{1, \ldots, d\}$. For every element $T \in \mathcal{T}_h$, h_T is its diameter and the global mesh size parameter is defined as

$$h = \max_{T \in \mathcal{T}_h} h_T.$$

Since our focus is on anisotropic meshes, the aspect ratio

$$\sigma = \max_{T \in \mathcal{T}_h} \sigma_T$$

of a mesh is of interest, where

$$\sigma_T = \frac{h_T}{\rho_T}$$

is the aspect ratio of an element T, with ρ_T being the supremum of the diameters of all balls contained within T, see Figure 2.2 for an illustration.

The set of facets of a mesh is denoted by $\mathcal{F}(\mathcal{T}_h)$, the analog for an element by $\mathcal{F}(T)$. Interior facets of the mesh are collected in the set $\mathcal{F}^i(\mathcal{T}_h)$, boundary facets in $\mathcal{F}^b(\mathcal{T}_h) = \mathcal{F}(\mathcal{T}_h) \setminus \mathcal{F}^i(\mathcal{T}_h)$. Similarly, the set of vertices of a mesh, element $T \in \mathcal{T}_h$ and facet $F \in \mathcal{F}(\mathcal{T}_h)$ is denoted by $\mathcal{V}(\mathcal{T}_h)$, $\mathcal{V}(T)$ and $\mathcal{V}(F)$, respectively, and we also use the analogous notation for the subsets of interior vertices $\mathcal{V}^i(\mathcal{T}_h)$ and boundary vertices $\mathcal{V}^b(\mathcal{T}_h)$.

For $F \in \mathcal{F}(\mathcal{T}_h)$ and $T \in \mathcal{T}_h$, $\boldsymbol{x}_F$ and $\boldsymbol{x}_T$ denote the barycenter of the facet and element, respectively. The unit normal vectors on the facets are denoted by $\boldsymbol{n}_F$, are outward facing on boundary facets and have an arbitrary but fixed direction for interior facets. For an individual element, $\boldsymbol{n}_{T,F}$ is the unit normal vector on facet F with outward direction with respect to the element T.

When the numbering of facets and vertices of elements becomes important, we switch from the general notation of a facet with the symbol F to a more specific description, where we use the index sets $I_n = \{1, \dots, n\}$, $n \in \mathbb{N}$, and the reduced index sets ${}_iI_n = I_n \setminus \{i\}$. The vertices of an element $T \in \mathcal{T}_h$ are identified by their position vectors $\boldsymbol{p}_{T,i} \in \mathbb{R}^d$, $i \in I_{d+1}$, and the facet $e_{T,i} = \operatorname{conv}\{\boldsymbol{p}_{T,j} : j \in {}_iI_{d+1}\}$, $i \in I_{d+1}$, lies opposite to the vertex $\boldsymbol{p}_{T,i}$. When only one element is important we usually omit the index T.

Using the triangulation $\mathcal{T}_h$ of a domain Ω, we define the spaces

$$\begin{aligned} P_k(\mathcal{T}_h) &= \{\boldsymbol{v} : \boldsymbol{v}|_T \in P_k(T) \quad \forall T \in \mathcal{T}_h\} \cap C(\Omega), \\ P_k^{\mathrm{nc}}(\mathcal{T}_h) &= \{\boldsymbol{v} : \boldsymbol{v}|_T \in P_k(T) \quad \forall T \in \mathcal{T}_h\}, \end{aligned}$$

of continuous and discontinuous piecewise polynomials of order k, respectively.

Having introduced the basic notation for meshes, we now turn to the general notion of mesh regularity. Not imposing an upper bound on the aspect ratio σ can lead to degenerated elements with strongly stretched geometries and potentially very small or very large angles between facets and for three-dimensional settings also within facets. Such large angles can lead to unwanted behavior of finite element discretizations and interpolation errors, as the discussion in [AEHK21] and our Example 4.12 shows.

The solution to this problem is using meshes which satisfy a maximum angle condition. This requirement has a long history in finite element analysis, since it was first introduced for triangles in [Syn57, p. 211f] and later generalized for three-dimensional settings in [Kří92]. Figure 2.2 illustrates the different regularities in the case of triangles.

Definition 2.10. An element $T \in \mathcal{T}_h$ satisfies the *maximum angle condition*, if there is a constant $\overline{\phi} < \pi$, so that for the maximum angle ϕ_T between facets, and for $d = 3$ also within facets, $\phi_T \leq \overline{\phi}$ holds. We use the notation $MAC(\overline{\phi})$ for the maximum angle condition with constant $\overline{\phi}$.

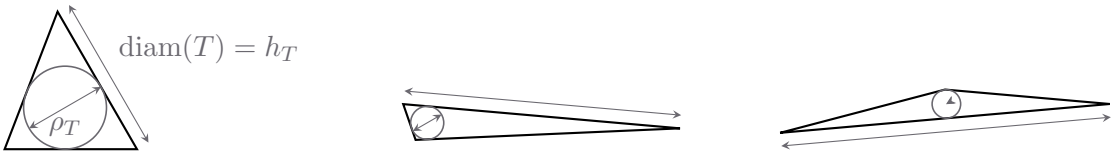

Figure 2.2: Triangles with decreasing regularity properties from left to right: Isotropic triangle, anisotropic triangle with maximum angle condition, anisotropic triangle without maximum angle condition.

Figure 2.3: Comparison of two anisotropic tetrahedra, with regular vertex property (left) and without regular vertex property (right).

The maximum angle condition is broadly used where the aspect ratio may be unbounded, but a certain regularity is required, see, e.g., [AADL11; AD99; Ape99; DL08].

For three-dimensional simplices there is another regularity assumption in use, the regular vertex property, that defines a proper subclass of the elements satisfying the maximum angle condition. For $d = 2$ it is equivalent to the maximum angle condition, see [AD99, Section 5, p. 29].

Definition 2.11. An element T satisfies the *regular vertex property*, if for one of its vertices $\boldsymbol{p}_{T,k}$ it holds

$$|\det N_{T,k}| \geq \bar{c} > 0, \quad \bar{c} \in \mathbb{R}_+, \tag{2.17}$$

where $N_{T,k} \in \mathbb{R}^{d\times d}$ consists of the column vectors

$$\boldsymbol{l}_{T,j}^k = \frac{\boldsymbol{p}_{T,j} - \boldsymbol{p}_{T,k}}{\left\|\boldsymbol{p}_{T,j} - \boldsymbol{p}_{T,k}\right\|_2}, \quad j \in {}_kI_{d+1}.$$

The vertex $\boldsymbol{p}_{T,k}$ is then called *regular vertex* of T. When using this property for an individual element in the remainder of the text, we assume that the vertices are numbered so that $\boldsymbol{p}_{T,d+1}$ is the regular vertex. This simplifies the notation of the vectors to $\boldsymbol{l}_{T,i} = \boldsymbol{l}_{T,i}^{d+1}$, $i \in I_d$. We write $RVP(\bar{c})$ for the regular vertex property with constant $\bar{c}$.

To make this definition more tangible we describe it in a more geometric sense, see also Figure 2.3: the vectors $\boldsymbol{l}_{T,i}$ are the unit vectors along the edges of the element outgoing from the regular vertex, and condition (2.17) means that these vectors need to be uniformly linearly independent, i.e., form a stable coordinate system for the element in order for $RVP(\bar{c})$ to hold.

When using anisotropic elements, it is important to precisely define size parameters for the contrasting scales. When the regular vertex property is satisfied, we can use the lengths of the edges associated with the vectors $\boldsymbol{l}_i$ as element size parameters h_i, $i \in I_d$.

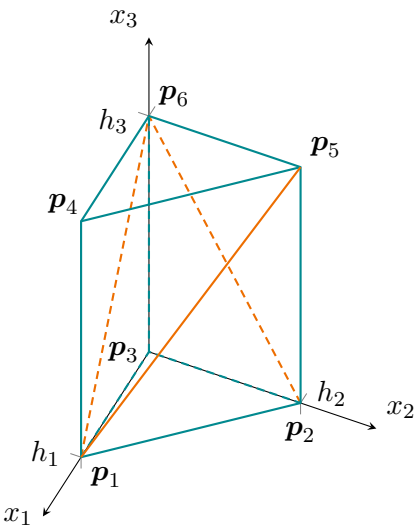

Figure 2.4: Triangular prism subdivided into three tetrahedra.

In addition to the regularity condition they satisfy, tetrahedra can have different types of anisotropy, which may determine whether a complete mesh for a domain can be built using only such elements. To illustrate this point, consider a triangular prism, as shown in Figure 2.4, that is subdivided into the three tetrahedra $\boldsymbol{p}_1\boldsymbol{p}_2\boldsymbol{p}_3\boldsymbol{p}_6$, $\boldsymbol{p}_1\boldsymbol{p}_4\boldsymbol{p}_5\boldsymbol{p}_6$ and $\boldsymbol{p}_1\boldsymbol{p}_2\boldsymbol{p}_5\boldsymbol{p}_6$. Independent of the prism's anisotropy, the first tetrahedron clearly satisfies the regular vertex property, with regular vertex $\boldsymbol{p}_3$.

Consider the situation $h_3 \gg h_1, h_2$, which can occur, e.g., when a mesh is anisotropically graded towards an edge, as in [Ape99; AK20; ANS01a]. Then the second tetrahedron has a regular vertex, e.g., $\boldsymbol{p}_6$. The remaining third tetrahedron however, which has two vertices each on the top and bottom surfaces of the prism, does not have a regular vertex. This means that such a mesh can not satisfy the regular vertex property globally.

On the other hand consider a flat prism, i.e., $h_1 \sim h_2 \gg h_3$, which may be used when grading a mesh to fit to a boundary layer. Then the second tetrahedron has the regular vertex $\boldsymbol{p}_4$ and for the third tetrahedron, which now has a flat shape, we may choose $\boldsymbol{p}_2$ or $\boldsymbol{p}_5$ as regular vertex.

Remark 2.12. We often use the terms *mesh refinement* and *mesh grading*, and to make the meaning clear, we define them properly here.

With (local) *mesh refinement* we mean a (local) change in element sizes of the mesh, introduced mainly by subdividing existing elements, but it can also be a result of creating a new mesh from scratch with a different mesh size parameter. Typically a mesh refinement that globally halves the mesh size parameter leads to an increase in the number of elements by a factor of 2^d, where d is the spatial dimension.

The term *mesh grading* on the other hand is used when we keep the number of elements constant, but move the vertices of the mesh so that locally a change in the element sizes manifests.

2.4.2 Boundary layers

A common characteristic of incompressible flows is that boundary layers are formed, for example near walls where no-slip boundary conditions are prescribed. Starting with the article [Pra05], this phenomenon hast been widely studied, see, e.g., [SG06].

In general, boundary layers exhibit a large directional derivative normal to the boundary, while the directional derivative parallel to the boundary is comparatively small. Since large gradients typically mean larger local errors of the discrete solution, smaller element sizes in the area of the boundary layer are necessary to counter the behavior of the solution. This could be achieved using local refinement with isotropic elements, but this wastes computational resources, since smaller element sizes are needed only in the direction with the large directional derivative. Thus we want to use anisotropic meshes, where stretched elements with small element size parameters in the right direction are used, which mostly means perpendicular to the wall. What we can typically expect from these types of meshes is a reduction of the error, e.g., in the energy and L^2-norms.

In the numerical examples in Chapter 6 that exhibit boundary layer structures we use meshes of *Shishkin-type*. The main idea is to generate a piecewise uniform mesh, where the element size in the boundary layer is fitted to the solution, see [Lin10, Section 2.1.2]. The process of constructing such a mesh can be best described for a one-dimensional domain, and the extension to two- or three-dimensional meshes is straightforward. Starting with the interval $[0, 1]$, we choose a transition point parameter $\tau \in (0, 1)$ and a mesh parameter $q \in (0, 1)$, which describe the width of the graded part of the mesh and the fraction of the total elements used therein, respectively. We assume $\tau \leq q$ since otherwise the smaller elements would be located in the area that is supposed to be outside of the boundary layer.

For a given number $N \geq 2$ of mesh elements, the grid vertices x^i, $i \in \{0, \dots, N\}$, are defined by

$$x^i = \begin{cases} i\frac{\tau}{qN}, & 0 \leq i \leq qN, \\ \tau + (i - qN)\frac{1-\tau}{(1-q)N}, & qN < i \leq N. \end{cases}$$

This interval mesh can then be extended into the second or third dimensions with, e.g., a uniform mesh size to yield a tensor product mesh of quadrilateral or hexahedral elements. By dividing the quadrilateral elements along a diagonal we get a simplicial triangulation that has $n = 2N^2$ elements and a maximal aspect ratio of

$$\sigma = \frac{\sqrt{q^2 + \tau^2}}{q + \tau - \sqrt{q^2 + \tau^2}}. \tag{2.18}$$

To get a three-dimensional mesh, either the quadrilateral mesh can be extended and subsequently the resulting hexahedral mesh can be subdivided into tetrahedra, see, e.g., [AD03], or the quadrilateral mesh in two dimensions can first be subdivided as described, so that the extension into the third dimension results in prismatic elements with triangular base. To get a simplicial mesh in this case, the prisms can be partitioned into tetrahedra as seen in Figure 2.4.

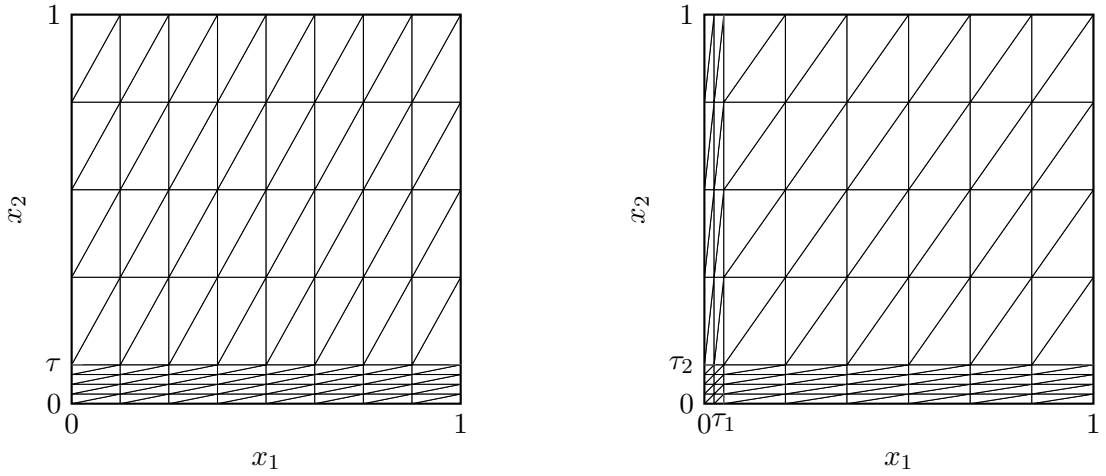

Figure 2.5: Two example meshes of Shishkin-type for boundary layer phenomena.

The left hand side of Figure 2.5 shows an example mesh of this type with parameter choices $\tau = 0.1$ and $q = 0.5$ for the x_2-direction and a uniform mesh size for the x_1-direction. The right hand side of the figure shows a mesh that has been graded for layers on two sides of the boundary, with parameters $\tau_1 = 0.05$, $q_1 = 0.25$ in the x_1-direction and the same parameters as in the first mesh for the x_2-direction. A comparison of the two meshes shows that if more than one direction contains a Shishkin-type grading, (2.18) sets a lower bound on the actual aspect ratio.

The transition point can be chosen so that the mesh is optimally adapted to the layer. For the original mesh type introduced by Shishkin for singularly perturbed problems, the transition point is set to $\tau = \min\{q, D \ln N\}$, where $D \in \mathbb{R}_+$ is a problem specific constant, see [Lin10, Section 2.1.2]. However, we will mostly not include a dependency on the mesh density in our choice of the transition point, and thus we proceed to call our meshes Shishkin-*type*.

Mostly motivated by the study of singularly perturbed problems, e.g., reaction-diffusion problems with a small parameter in front of the diffusion term, a large variety of layer-adapted meshes has been investigated, e.g., Bakhvalov meshes [Bak69], Bakhvalov-Shishkin meshes [Lin99; Lin00] and several variants [Vul83; Vul01]. An extensive overview of these meshes is given in [Lin10]. Since our focus lies on the interplay of pressure-robustness and anisotropic meshes, we choose to use a simple type of layer-adapted mesh, as described above. The Shishkin-type mesh may not be perfectly adapted to incompressible flow boundary layers, but it can sufficiently show the effects of anisotropically graded meshes without getting lost in the details of mesh adaption.

The use of these layer-adapted meshes in general does not improve the asymptotic convergence characteristics of a discretization method but does improve the dependence of the constant in the error estimates on the perturbation parameter, which in our case is the viscosity ν. Still, the gain in accuracy can be significant, as shown in the discussion in [Ape99, Section 5.2] and in our examples in Chapter 6.

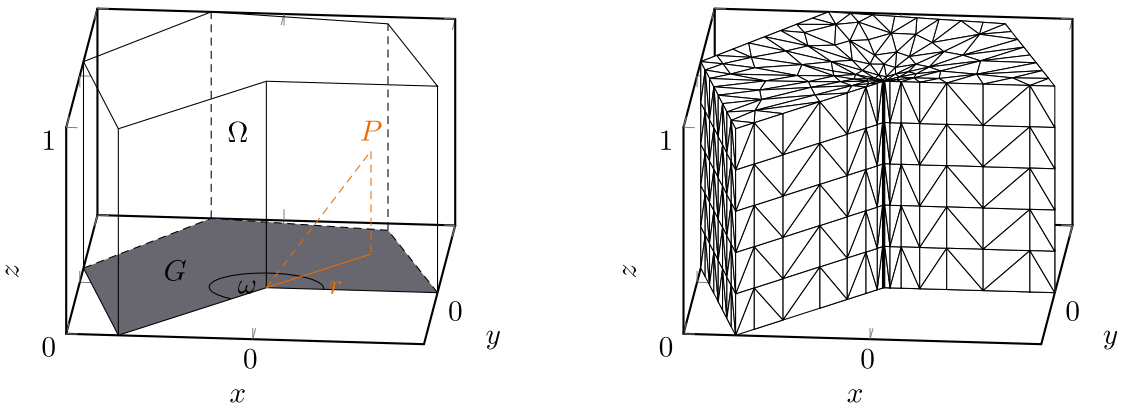

Figure 2.6: Visualization of domain for singular edge problems. Example triangulation of domain with anisotropic mesh grading.

2.4.3 Edge singularities

Similar to the boundary layer phenomenon, large gradients in form of singularities are introduced in the solution of elliptic boundary value problems by non-convexities in the domain, see, e.g., [Gri11]. After a suitable generalization of the definition of ellipticity in the sense of [ADN64], the Stokes equations can be seen as elliptical, see [Hac17, p. 313], so these types of singularities also occur here and were investigated in, e.g., [Dau89; KO76]. Local mesh refinement has been proven to ameliorate the detrimental effects of these singularities when working with the finite element method, see, e.g., [Ape99; AK21; ANS01a]. Our interest in anisotropic elements leads us to consider mainly non-convex edges, since there anisotropic grading towards the edge makes sense.

In this subsection we introduce an approach to generate meshes which are anisotropically graded towards a re-entrant edge, by first building a quasi-uniform mesh and then moving the vertices towards the singular edge in a specific grading process. The technique was introduced in [AD92], is well established, see, e.g., [Ape99; AK21; ANS01a; FNP01], and yields tensor-product-type meshes that satisfy the maximum angle condition.

A hierarchical mesh refinement procedure that results in similarly graded meshes exists, see [AS02], however the prismatic macro-elements that arise in the above mesh generation process are required for the anisotropic analysis later on. In [Li18; LN18] another kind of mesh refinement procedure was introduced that also generates a mesh which has an analogous grading towards re-entrant edges. However those meshes do not satisfy the maximum angle condition, which we require for our error estimates.

In the following paragraphs we consider prismatic domains $\Omega = G \times (0,1)$, with a polygonal base G that has one non-convex corner at the origin with interior angle $\omega \in (\pi, 2\pi)$, as illustrated in Figure 2.6.

Suppose $\mathcal{D}_h$ is a shape regular, conforming triangulation of the base area G, with mesh size parameter $h = \max_{D\in\mathcal{D}_h} h_D$, with $h_D = \operatorname{diam}(D)$. Given a grading parameter $\mu \in (0,1]$, the vertices of this mesh are moved towards the non-convex corner so that

after the grading every element satisfies the condition

$$h_D \sim \begin{cases} h^{1/\mu}, & \text{if } r_D = 0, \\ h r_D^{1-\mu}, & \text{if } 0 < r_D < R, \\ h, & \text{else,} \end{cases}$$

where $r_D = \inf\{\operatorname{dist}(\boldsymbol{x}, \mathbf{0}) : \boldsymbol{x} \in D\}$ is the distance of an element $D \in \mathcal{D}_h$ to the concave corner and $R > 0$ is the radius of the refinement zone. Since edge singularities are a local phenomenon, it is possible to choose R quite small, given that the overall mesh size parameter h is small so that enough graded elements are in the mesh. The local nature of the singularities is also the reason why for analytical purposes it is sufficient to concentrate on the setting as it is described here.

After the two-dimensional mesh is graded, it is extended in the z-direction with uniform mesh size $h_3 \sim h$, resulting in a mesh of prismatic elements with triangular bases. Subdividing the prisms into three tetrahedra each, see Figure 2.4, yields the desired simplicial mesh $\mathcal{T}_h$. For an element $T \in \mathcal{T}_h$ let r_T be the distance of the element to the z-axis, and $h_{1,T}$, $h_{2,T}$, $h_{3,T}$ the lengths of the projections on the x-, y-, z-axis, respectively, then it holds

$$h_{3,T} \sim h, \qquad h_{1,T} \sim h_{2,T} \sim \begin{cases} h^{1/\mu}, & \text{if } r_T = 0, \\ h r_T^{1-\mu}, & \text{if } 0 < r_T < R, \\ h, & \text{else,} \end{cases}$$

and the number of elements in the mesh satisfies $N \sim h^{-3}$.

In contrast to the anisotropic mesh grading for boundary layers that was introduced in the previous section, this type of mesh grading is employed to recover the optimal convergence rate of a method, that is reduced due to the low regularity of the solution in non-convex domains when using quasi-uniform meshes. Note also that when constructing meshes in this way with a fixed grading parameter μ, the anisotropy increases when the mesh size parameter is decreased, which is also in contrast to the layer meshes, where the anisotropy depends only on the mesh parameter q and the chosen transition point τ.

CHAPTER 3

Pressure-robust discretization of the Stokes equations

The ideas behind pressure-robustness were already introduced in Section 2.3, and now we get into the possible discretization approaches that result in pressure-robust methods. While there are techniques like grad-div-stabilization, see, e.g., [Joh+17, Section 5.1], that decrease the impact of missing pressure-robustness of certain discretizations, we concentrate on truly pressure-robust methods. In Section 3.1 we introduce the discrete formulation for the Stokes equations and essential notation. The following Sections 3.2 and 3.3 contain a brief description of exactly divergence-free methods, i.e., methods that yield weakly divergence-free velocity solutions by design and are thereby pressure-robust, and the reconstruction method for classical element pairs first introduced in [Lin14].

3.1 General notation for discrete setting

In order to use non-conforming discretizations we introduce some tools from the framework of discontinuous Galerkin methods, where we mostly follow [DE12, Section 1]. For a function $\boldsymbol{v}$ the *jump* over an interior facet F, belonging to the two elements T_F^1 and T_F^2, is defined pointwise by

$$[\![\boldsymbol{v}]\!]_F(\boldsymbol{x}) = \boldsymbol{v}|_{T_F^1}(\boldsymbol{x}) - \boldsymbol{v}|_{T_F^2}(\boldsymbol{x}), \qquad \boldsymbol{x} \in F,$$

while the *average* on that facet is defined by

$$\{\!\{\boldsymbol{v}\}\!\}_F(\boldsymbol{x}) = \frac{1}{2}\left(\boldsymbol{v}|_{T_F^1}(\boldsymbol{x}) + \boldsymbol{v}|_{T_F^2}(\boldsymbol{x})\right), \qquad \boldsymbol{x} \in F.$$

To fix the sign of the jump we say that the adjacent elements of facet F are denoted so that the arbitrary but fixed direction of the normal vector $\boldsymbol{n}_F$ points from T_F^1 to T_F^2. On

boundary facets we set $[\![\boldsymbol{v}]\!]_F(\boldsymbol{x}) = \{\!\{\boldsymbol{v}\}\!\}_F(\boldsymbol{x}) = \boldsymbol{v}|_T(\boldsymbol{x})$. Where it is unambiguous we usually omit the index on the jump and average notation. To accommodate discrete function spaces for which $\boldsymbol{X}_h \nsubseteq \boldsymbol{X}$, we need the broken gradient $\nabla_h : \boldsymbol{X} \oplus \boldsymbol{X}_h \to L^2(\Omega)^{d\times d}$ and broken divergence $\nabla_h\cdot : \boldsymbol{X} \oplus \boldsymbol{X}_h \to L^2(\Omega)$ operators, that use the elementwise definitions

$$(\nabla_h \boldsymbol{v}_h)|_T = \nabla(\boldsymbol{v}_h|_T),$$
$$(\nabla_h \cdot \boldsymbol{v}_h)|_T = \nabla \cdot (\boldsymbol{v}_h|_T),$$

for all elements $T \in \mathcal{T}_h$. Note that on $\boldsymbol{X}$ the broken variants coincide with the standard gradient and divergence operators, see, e.g., [DE12, Lemma 1.22], so that for conforming methods where $\boldsymbol{X} \oplus \boldsymbol{X}_h = \boldsymbol{X}$ we can still use the broken notation. These definitions of the two operators assume that functions from $\boldsymbol{X}_h$ have enough regularity at least elementwise, which is satisfied for piecewise polynomials.

This leads us to our general formulation for the discrete Stokes problem: Find $(\boldsymbol{u}_h, p_h) \in \boldsymbol{X}_h \times Q_h$, where not necessarily $\boldsymbol{X}_h \subset \boldsymbol{X}$, so that

$$\nu a_h(\boldsymbol{u}_h, \boldsymbol{v}_h) + b_h(\boldsymbol{v}_h, p_h) = l_h(\boldsymbol{v}_h) \qquad \forall \boldsymbol{v}_h \in \boldsymbol{X}_h, \tag{3.1a}$$
$$b_h(\boldsymbol{u}_h, q_h) = 0 \qquad \forall q_h \in Q_h. \tag{3.1b}$$

There are several ways to define the bilinear and linear forms a_h, b_h and l_h depending on the method that is used.

Introducing the space $\boldsymbol{X}_h^0 = \{\boldsymbol{v}_h \in \boldsymbol{X}_h : b_h(\boldsymbol{v}_h, q_h) = 0 \ \forall q_h \in Q_h\}$, we can write, analogously to the continuous setting, a Poisson-like problem for the velocity: Find $\boldsymbol{u}_h \in \boldsymbol{X}_h^0$ so that

$$\nu a_h(\boldsymbol{u}_h, \boldsymbol{v}_h) = l_h(\boldsymbol{v}_h) \qquad \forall \boldsymbol{v}_h \in \boldsymbol{X}_h^0. \tag{3.2}$$

To give a specific example of a possible discretization, we introduce the classical Crouzeix–Raviart method from [CR73]. As velocity approximation space $\boldsymbol{X}_h$ this method uses piecewise linear functions that are continuous at the barycenters of the element interfaces,

$$\mathrm{CR}(\mathcal{T}_h) = \{\boldsymbol{v}_h \in \boldsymbol{L}^2(\Omega) : \boldsymbol{v}_h|_T \in \boldsymbol{P}_1(T) \ \forall T \in \mathcal{T}_h, [\![\boldsymbol{v}_h]\!](\boldsymbol{x}_F) = \boldsymbol{0} \ \forall F \in \mathcal{F}(\mathcal{T}_h)\}, \tag{3.3}$$

which, since $\mathrm{CR}(\mathcal{T}_h) \nsubseteq \boldsymbol{X}$, means that this is a non-conforming method. The pressure is approximated using piecewise constants, i.e.,

$$Q_h = \{q_h \in Q : q_h|_T \in P_0(T) \ \forall T \in \mathcal{T}_h\}. \tag{3.4}$$

Concerning the bilinear forms, only a small adjustment compared to the continuous variants is necessary. Due to the non-conformity, the broken gradient and divergence are needed which leads to the definitions

$$a_h(\boldsymbol{u}_h, \boldsymbol{v}_h) = (\nabla_h \boldsymbol{u}_h, \nabla_h \boldsymbol{v}_h), \qquad b_h(\boldsymbol{v}_h, q) = -(\nabla_h \cdot \boldsymbol{v}_h, q), \qquad l_h(\boldsymbol{v}_h) = (\boldsymbol{f}, \boldsymbol{v}_h).$$

With this bilinear form a_h we associate the mesh-dependent norm

$$\|\boldsymbol{v}_h\|_{1,h} = \|\nabla_h \boldsymbol{v}_h\|_0$$

for functions $\boldsymbol{v}_h \in \boldsymbol{X} \oplus \boldsymbol{X}_h$. The Crouzeix–Raviart method is used at various instances throughout the thesis, which is why it is introduced at this point. Other discretizations are made explicit when needed.

3.2 Exactly divergence-free methods

Many methods exist that are naturally pressure-robust and this is a very active field of research, as indicated by many recent publications, e.g., [AP21a; AP21b; KR19; MYZ21; RW18; RW20]. We give a brief overview of such finite element methods without going into too much detail and discuss their use for anisotropic triangulations. There are also approaches using the framework of isogeometric analysis to achieve exactly divergence-free approximations, see, e.g., [BFS11; EH13a; EH13b], but we will not consider those.

3.2.1 $\boldsymbol{H}_0^1(\Omega)$-conforming methods

We start with a brief section on exactly divergence-free conforming methods, where $\boldsymbol{X}_h \subset \boldsymbol{X}$. Such methods are characterized by the property $\nabla \cdot \boldsymbol{X}_h \subseteq Q_h$, i.e., the divergence of every possible discrete velocity field is contained in the pressure space, see [Joh+17, Section 4], which leads to pressure-independent velocity errors. The term exactly divergence-free comes from the fact that since $\nabla \cdot \boldsymbol{v}_h \in Q_h$ it holds

$$\boldsymbol{X}_h^0 = \{\boldsymbol{v}_h \in \boldsymbol{X}_h : (\nabla \cdot \boldsymbol{v}_h, q_h) = 0 \quad \forall q_h \in Q_h\} \subseteq \{\boldsymbol{v}_h \in \boldsymbol{X}_h : \|\nabla \cdot \boldsymbol{v}_h\|_0 = 0\} \subset \boldsymbol{X}^0,$$

which means that discretely divergence-free functions are exactly divergence-free.

The first method of this type is the Scott–Vogelius finite element pair that was investigated in [SV85] for two-dimensional settings. Here the velocity is approximated in $\boldsymbol{P}_k(\mathcal{T}_h)$ and the pressure in $P_{k-1}^{\mathrm{nc}}(\mathcal{T}_h)$. While this pair has the desired property $\nabla \cdot \boldsymbol{P}_k(\mathcal{T}_h) \subseteq P_{k-1}^{\mathrm{nc}}(\mathcal{T}_h)$ to be exactly divergence-free, showing inf-sup stability is a bit more involved. Depending on the order k and the dimension d, various mesh properties need to be satisfied to achieve inf-sup stability. For the low-order case with $k = 2$ and $d = 2$, which was investigated in [Qin94, Chapter 4], it was proved that on barycentrically refined meshes the inf-sup condition holds. Such meshes are constructed by dividing each triangle of a regular mesh into three new triangles by using the barycenter of the original element as an additional vertex, see Figure 3.1. Recently this pair was investigated concerning the dependence of the inf-sup constant on the aspect ratio of the involved meshes, see [KNS21]. According to [KNS21, Theorem 3.12], with a maximum angle condition and some additional general assumptions on the mesh, the inf-sup constant of the low-order Scott–Vogelius pair depends linearly on the inverse of the aspect ratio.

Example 3.1. We show that the inf-sup constant of the $\boldsymbol{P}_2(\mathcal{T}_h)$–$P_1^{\mathrm{nc}}(\mathcal{T}_h)$ Scott–Vogelius pair is not robust with respect to an increasing aspect ratio in the mesh. For this test we choose a series of $2(4 \times 4)$ Shishkin type meshes with a barycentric subdivision as the one pictured in Figure 3.1. By letting $\tau \to 0$, we get an increasing aspect ratio σ in the meshes.

Computing the discrete inf-sup constant

$$\widetilde{\beta} = \inf_{q_h \in Q_h} \sup_{\boldsymbol{v}_h \in \boldsymbol{X}_h} \frac{(\nabla_h \cdot \boldsymbol{v}_h, q_h)}{\|q_h\|_0 \|\boldsymbol{v}_h\|_1},$$

we observe the expected linear dependence on σ^{-1} as shown in Figure 3.1.

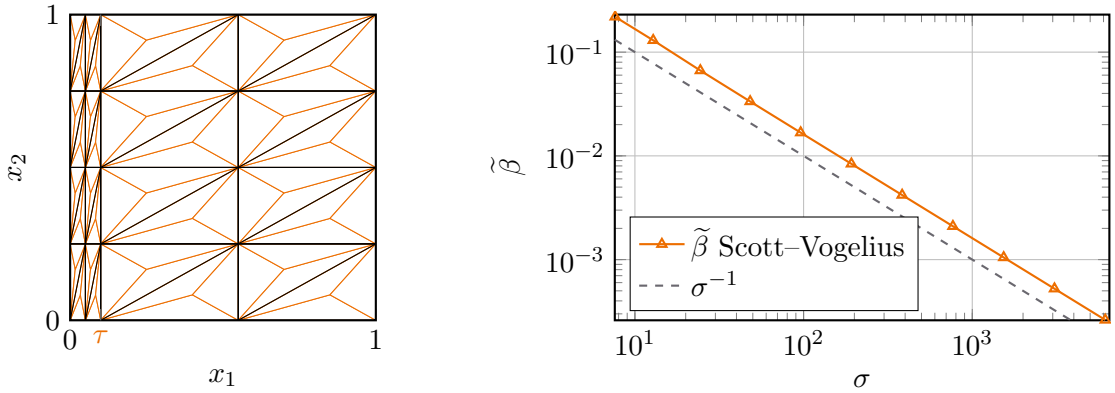

Figure 3.1: Left: Barycentric refinement (orange) of a Shishkin-type mesh (black) with transition point $\tau = 0.1$ and $q = 0.5$. Right: Discrete inf-sup constant of the Scott–Vogelius pair on barycentrically refined Shishkin-type meshes.

The Scott–Vogelius method has been extended to three dimensions, see [Zha05; Zha11], and several additional results concerning the required mesh properties have been produced for different polynomial orders, see [Sco18, p. 146] for an overview. Another approach to achieve an exactly divergence-free method uses complicated finite element spaces using rational bubble functions, see [GN14a; GN14b]. An important concept in the context of constructing new conforming divergence-free methods is the exact sequence property of de-Rham complexes, see, e.g., [Joh+17, Section 4.3], which we explain using the description from [AP21a, Section 1].

For $\Omega \subset \mathbb{R}^2$, the sequence

$$\mathbb{R} \xrightarrow{\subset} H^2(\Omega) \xrightarrow{\nabla\times} \boldsymbol{H}^1(\Omega) \xrightarrow{\nabla\cdot} L^2(\Omega) \longrightarrow 0,$$

where $\nabla\times$ is the two-dimensional curl operator, i.e., $\nabla \times v = (\partial_y v, -\partial_x v)^T$, has the exact sequence property, meaning that the kernel of one of the operators above the arrows is the range of the preceding operator. For the spaces $\boldsymbol{H}^1_0(\Omega)$ and $L^2_0(\Omega)$ that occur in the weak formulation of the Stokes equations, there is also a sequence,

$$0 \xrightarrow{\subset} H^2_0(\Omega) \xrightarrow{\nabla\times} \boldsymbol{H}^1_0(\Omega) \xrightarrow{\nabla\cdot} L^2_0(\Omega) \longrightarrow 0,$$

which has the exactness property as above. This means that for every velocity $\boldsymbol{u} \in \boldsymbol{H}^1_0(\Omega)$ we get $q = \nabla \cdot \boldsymbol{u} \in L^2_0(\Omega)$, which by testing the divergence constraint of the Stokes equations with this q further implies $\|\nabla \cdot \boldsymbol{u}\|^2_0 = 0$, i.e., $\nabla \cdot \boldsymbol{u} = 0$ almost everywhere. By choosing finite element spaces $\Sigma_h \subset H^2_0(\Omega)$, $\boldsymbol{X}_h \subset \boldsymbol{H}^1_0(\Omega)$ and $Q_h \subset L^2_0(\Omega)$ which also form a sequence

$$0 \xrightarrow{\subset} \Sigma_h \xrightarrow{\nabla\times} \boldsymbol{X}_h(\Omega) \xrightarrow{\nabla\cdot} Q_h(\Omega) \longrightarrow 0,$$

with the exactness property, the discrete velocity solution would be automatically exactly divergence-free. The before mentioned low-order Scott–Vogelius element on a barycentrically refined mesh satisfies this discrete exact sequence properties in combination with

the cubic Hsieh–Clough–Tocher element as the space Σ_h, see [Joh+17, Section 4.3]. In [AP21a; AP21b], a new family of arbitrary order approximation spaces is constructed using this principle, with a modified version of the TUBA finite element spaces, see [AFS68; MS75], used for the space Σ_h.

3.2.2 $\boldsymbol{H}_0(\mathrm{div}, \Omega)$-conforming methods

Apart from the conforming methods mentioned in the previous subsection where $\boldsymbol{X}_h \subset \boldsymbol{X}$, there is a lot of current research concerning pressure-robust methods that build on discontinuous Galerkin discretizations. Especially methods using hybridization, see [BF91], have become popular in this area, see, e.g., [KR19; LR20; RW17; RW18; RW20; Sch19; SLLL18], since this technique can mitigate the higher computational cost introduced by more nonzero matrix entries when high order methods are used, see the study in the appendix of [SLLL18].

We present in particular the $\boldsymbol{H}_0(\mathrm{div}, \Omega)$-conforming discontinuous Galerkin method that was investigated in, e.g., [LS18; SL18]. The approximation spaces in this case are chosen as

$$\begin{aligned}\boldsymbol{X}_h &= \{\boldsymbol{v}_h \in \boldsymbol{H}_0(\mathrm{div}, \Omega) : \boldsymbol{v}_h|_T \in \boldsymbol{P}_{\leq k}(T)\ \forall T \in \mathcal{T}_h\},\\ Q_h &= \{q_h \in Q : q_h|_T \in P_{k-1}(T)\ \forall T \in \mathcal{T}_h\},\end{aligned}$$

where $k \geq 1$ and $\boldsymbol{P}_{\leq k}(T)$ is a space containing possibly a subset of the vector valued polynomials with maximal degree k on the element T. This space is not defined more precisely, since a variety of concrete spaces can be used in applications. A possible choice for $\boldsymbol{P}_{\leq k}(T)$ is the full $\boldsymbol{P}_k(T)$ space, which corresponds to the well known Brezzi–Douglas–Marini element, see [BDM85; Néd86]. Another possibility is the Raviart–Thomas space of the appropriate order, see [Néd80; RT77].

The diffusion term is discretized by the standard symmetric interior penalty formulation, see, e.g., [DE12, Section 6.1.2.1], which takes the form

$$\begin{aligned}a_h(\boldsymbol{u}_h, \boldsymbol{v}_h) = &\int_\Omega \nabla_h \boldsymbol{u}_h : \nabla_h \boldsymbol{v}_h \,\mathrm{d}\boldsymbol{x} + \eta \sum_{F \in \mathcal{F}(\mathcal{T}_h)} h_F^{-1} \int_F [\![\boldsymbol{u}_h]\!] \cdot [\![\boldsymbol{v}_h]\!] \,\mathrm{d}\boldsymbol{s}\\ &- \sum_{F \in \mathcal{F}(\mathcal{T}_h)} \int_F \{\!\{\nabla_h \boldsymbol{u}_h\}\!\} \boldsymbol{n}_F \cdot [\![\boldsymbol{v}_h]\!] \,\mathrm{d}\boldsymbol{s} - \sum_{F \in \mathcal{F}(\mathcal{T}_h)} \int_F \{\!\{\nabla_h \boldsymbol{v}_h\}\!\} \boldsymbol{n}_F \cdot [\![\boldsymbol{u}_h]\!] \,\mathrm{d}\boldsymbol{s},\end{aligned}$$

where $\eta > 0$ is a penalty parameter that must be chosen large enough so that the bilinear form is coercive, see [DE12, Lemma 4.12]. We define the parameter h_F as the diameter of the facet F, but different choices are possible, see [DE12, Remark 4.6].

The bilinear form for the pressure-velocity coupling is the same as for the Crouzeix–Raviart method

$$b_h(\boldsymbol{v}_h, q_h) = -(\nabla_h \cdot \boldsymbol{v}_h, q_h).$$

Using this discretization, a pressure-robust error estimate can be proved, see, e.g., [Sch19, Theorem 5.4],

$$|||\boldsymbol{u} - \boldsymbol{u}_h|||_{e,\#} \lesssim \inf_{\boldsymbol{v}_h \in \boldsymbol{X}_h^0} |||\boldsymbol{u} - \boldsymbol{v}_h|||_{e,\#},$$

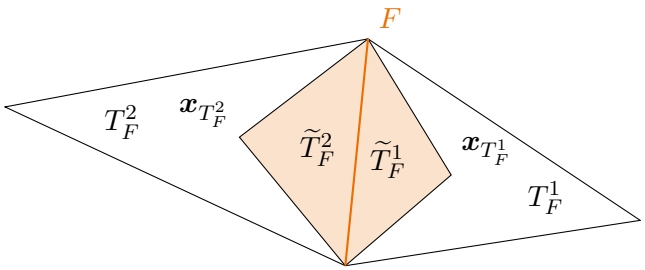

Figure 3.2: Illustration of the geometric quantities in the modified penalty term.

where the norm for $\boldsymbol{v} \in \boldsymbol{X}_h \oplus \boldsymbol{X}$ is defined by

$$|||\boldsymbol{v}|||_{e,\#}^2 = \|\nabla_h \boldsymbol{v}\|_0^2 + \sum_{F \in \mathcal{F}(\mathcal{T}_h)} h_F^{-1} \|[\![\boldsymbol{v}]\!]\|_{0,F}^2 + \sum_{T \in \mathcal{T}_h} h_T \|(\nabla_h \boldsymbol{v}) \boldsymbol{n}_{\partial T}\|_{0,\partial T}^2.$$

With the aim of using anisotropic triangulations in mind, we demonstrated in the numerical example in Section 5 of our publication [AK20] that the method seems to work adequately when combined with meshes that have a large aspect ratio. However, for the form a_h to be coercive, the penalty parameter η has to be chosen sufficiently large. Unfortunately this parameter shows a clear dependence not only on the polynomial degree that is used for the spaces $\boldsymbol{X}_h$ and Q_h, see [DE12, Lemma 4.12, Remark 1.48], but also on the aspect ratio of the mesh, see [LS16, Remark 3].

In the example in our article [AK20] we incorporated a factor $\log(\sigma)$ in the penalty parameter, which worked for the meshes used in the computations. In fact tracing the coercivity constants of the bilinear form, see [DE12, Lemma 4.12, Lemma 1.46], it seems that for a robust implementation a linear scaling of the penalty parameter with the aspect ratio would be necessary. Logarithmic and linear scaling employ the strategy of simply using a large enough penalty parameter, however, in practice a large penalty parameter has been linked to bad conditioning of the linear system, see [SL13].

In [KT21] a modified penalty term is introduced for the scalar version of a_h, where the factor h_F^{-1} for every facet $F \in \mathcal{F}(\mathcal{T}_h)$ is replaced by a better parameter. Let T_F^1, $T_F^2, T_F \in \mathcal{T}_h$ so that $F = \partial T_F^1 \cap \partial T_F^2$ if $F \in \mathcal{F}^i(\mathcal{T}_h)$ and $F = \partial T_F \cap \partial\Omega$ if $F \in \mathcal{F}^b(\mathcal{T}_h)$, then the new parameter is defined by

$$\langle F \rangle = \begin{cases} \frac{|F|}{|\widetilde{T}_F^1|} + \frac{|F|}{|\widetilde{T}_F^2|}, & \text{if } F \in \mathcal{F}^i(\mathcal{T}_h), \\ \frac{|F|}{|\widetilde{T}_F|}, & \text{if } F \subset \partial\Omega, \end{cases}$$

where $\widetilde{T}_F^i$, $i \in \{1,2\}$ and $\widetilde{T}_F$ are the simplices that arise from taking the convex hull of the facet F and the barycenters $\boldsymbol{x}_{T_F^i}, \boldsymbol{x}_{T_F}$ of the elements $T_F^i, T_F \in \mathcal{T}_h$, as shown in Figure 3.2 for two dimensions. Computing $\langle F \rangle$ is not expensive, as $|\widetilde{T}_F^i| = |T_F^i|(d+1)^{-1}$, where $d \in \{2,3\}$ is the spatial dimension.

The purpose of this modification is to make the penalty parameter η independent of the aspect ratio of the mesh. Let $h_F^i = \inf_{\boldsymbol{x} \in F} \operatorname{dist}(\boldsymbol{x}, \boldsymbol{x}_{T_F^i})$ be the distances of the facet

F to the barycenters of the adjacent elements. For the large facets of a stretched element, where $h_F \sim h$, this means $h_F^i \sim \frac{h}{\sigma}$, and the new combined parameter

$$\eta\langle F\rangle \sim \frac{|F|}{\left|\widetilde{T}_F^1\right|} + \frac{|F|}{\left|\widetilde{T}_F^2\right|} \sim \frac{1}{h_F^1} + \frac{1}{h_F^2} \sim \frac{\sigma}{h}$$

acts similarly to the standard penalty term with an included linear scaling on the aspect ratio

$$\eta(\sigma) h_F^{-1} \sim \frac{\sigma}{h_F} \sim \frac{\sigma}{h}.$$

In the case of a small facet, where $h_F \sim \frac{h}{\sigma}$ and $h_F^i \sim h$, the new parameter gives

$$\eta\langle F\rangle \sim \frac{1}{h},$$

however the standard parameter becomes

$$\eta(\sigma) h_F^{-1} \sim \frac{\sigma}{h_F} \sim \frac{\sigma^2}{h}.$$

This shows that the geometric parameter $\langle F\rangle$ is adapted to both cases and enforces a scaling with the aspect ratio only where necessary, while the standard term is unfavorable for the second case.

Adapting this approach to the vector valued version of the symmetric interior penalty formulation for the Stokes equations, we get the bilinear form

$$\begin{aligned} a_h(\boldsymbol{u}_h, \boldsymbol{v}_h) = &\int_\Omega \nabla_h \boldsymbol{u}_h : \nabla_h \boldsymbol{v}_h \,\mathrm{d}\boldsymbol{x} + \eta \sum_{F\in\mathcal{F}(\mathcal{T}_h)} \langle F\rangle \int_F [\![\boldsymbol{u}_h]\!] \cdot [\![\boldsymbol{v}_h]\!] \,\mathrm{d}\boldsymbol{s} \\ &- \sum_{F\in\mathcal{F}(\mathcal{T}_h)} \int_F \{\!\{\nabla_h \boldsymbol{u}_h\}\!\} \boldsymbol{n}_F \cdot [\![\boldsymbol{v}_h]\!] \,\mathrm{d}\boldsymbol{s} - \sum_{F\in\mathcal{F}(\mathcal{T}_h)} \int_F \{\!\{\nabla_h \boldsymbol{v}_h\}\!\} \boldsymbol{n}_F \cdot [\![\boldsymbol{u}_h]\!] \,\mathrm{d}\boldsymbol{s}. \end{aligned}$$

The analysis of this method still needs to be done, and we show in the following numerical experiments that it seems promising to investigate further.

Example 3.2. We compute the discrete inf-sup constant of the lowest-order Brezzi–Douglas–Marini element pair on the unit square for a variety of two-dimensional mesh families with anisotropic elements to see whether the discretization is stable on such triangulations with respect to increasing aspect ratios.

The first mesh family consists of Shishkin-type meshes, see Section 2.4.2, with the fixed number $2(10 \times 2)$ of mesh elements, $q = 0.5$ and a transition point τ so that for $\tau \to 0$ the aspect ratio increases, see the illustration on the left hand side of Figure 3.3.

The second mesh family partitions the unit square in $2(N \times 2)$ elements, so that for $N \to \infty$ we get an increasing aspect ratio, see the center illustration in Figure 3.3.

Lastly the third type of mesh is again a Shishkin-type mesh, also with $2(N \times 2)$ elements and for the x_1-direction a fixed transition point $\tau = 0.5$ and $q = \frac{N-1}{N}$, which results in meshes as pictured on the right hand side of Figure 3.3.

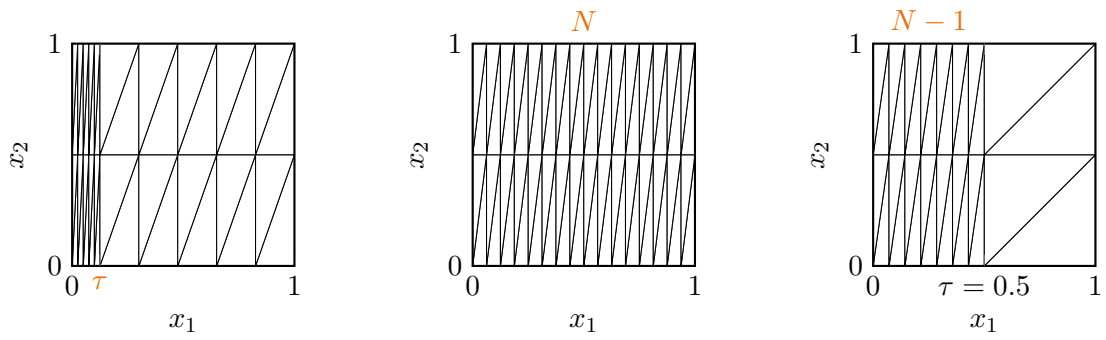

Figure 3.3: Illustration of the three mesh families used in Example 3.2. The parameter to adjust the aspect ratio is highlighted.

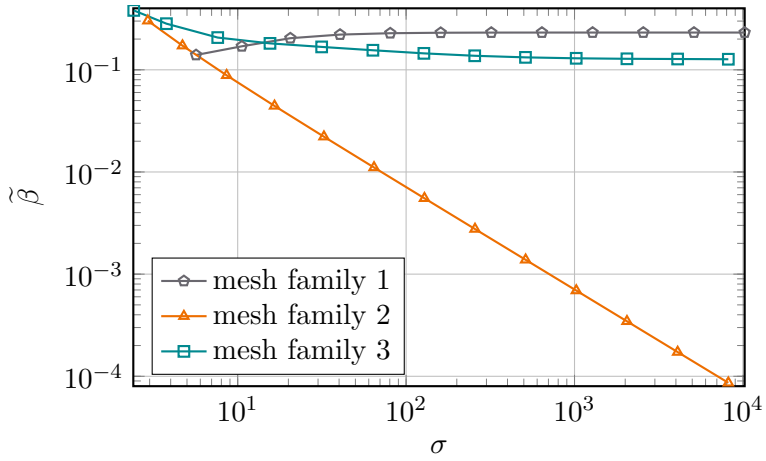

Figure 3.4: Computed discrete inf-sup constants for the three mesh families from Example 3.2 plotted over the maximal aspect ratio in the mesh.

The discrete inf-sup constant

$$\widetilde{\beta} = \inf_{q_h \in Q_h} \sup_{\boldsymbol{v}_h \in \boldsymbol{X}_h} \frac{(\nabla_h \cdot \boldsymbol{v_h}, q_h)}{\|q_h\|_0 \|\boldsymbol{v}_h\|_{1_h}},$$

with the norm $\|\cdot\|_{1_h}$ defined by

$$\|\boldsymbol{v}_h\|_{1_h}^2 = \sum_{T \in \mathcal{T}_h} \|\nabla \boldsymbol{v}_h\|_{0,T}^2 + \sum_{F \in \mathcal{F}(\mathcal{T}_h)} \langle F \rangle \|[\![\boldsymbol{v}_h]\!]\|_{0,F}^2,$$

can be computed as the square root of the smallest positive eigenvalue of certain eigenvalue problems, as described in [Mal81].

The results are shown in Figure 3.4 in dependence of the aspect ratio σ of the triangulation.

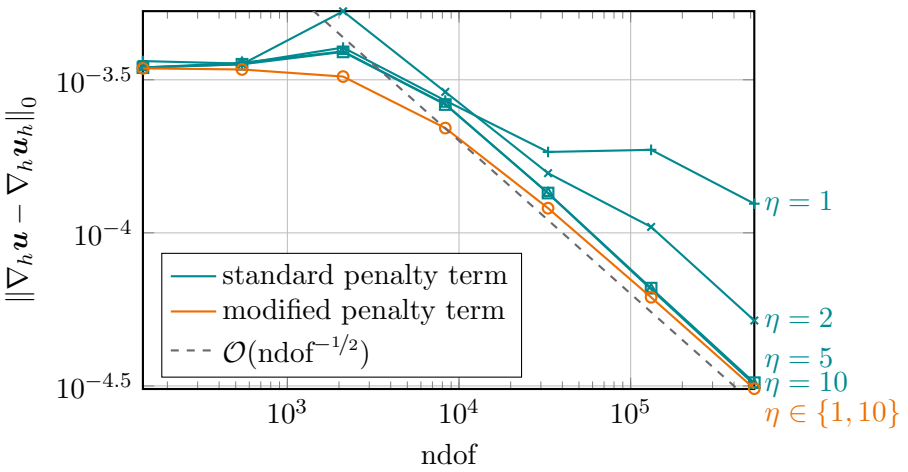

Figure 3.5: Comparison of the velocity gradient errors produced by the $\boldsymbol{H}_0(\mathrm{div}, \Omega)$-conforming discontinuous Galerkin methods using the standard and modified penalty terms.

For the second mesh family the inf-sup constant clearly tends to zero for increasing aspect ratio, which makes these types of mesh unsuitable for computations. Mesh families 1 and 3 on the other hand show a stable positive lower bound for the inf-sup constant even for very large aspect ratios.

Example 3.3. We investigate the example from [AK20, Section 5], where the standard symmetric interior penalty formulation is used, see, e.g., [CKS07; LS18], and compare the results to the method using the new formulation for the penalty term from [KT21]. The example uses a manufactured solution for the Stokes equations on the domain $\Omega = (0,1)^2$ given by

$$\boldsymbol{u}(\boldsymbol{x}) = \left(\frac{\partial \xi}{\partial x_2}, -\frac{\partial \xi}{\partial x_1} \right), \qquad p(\boldsymbol{x}) = \exp\left(-\frac{x_1}{\varepsilon}\right) - C(\varepsilon),$$

with stream function $\xi(\boldsymbol{x}) = x_1^2(1-x_1)^2 x_2^2(1-x_2)^2 \exp\left(-\frac{x_1}{\varepsilon}\right)$. The parameter $\varepsilon > 0$ introduces for small values an exponential boundary layer in the velocity and pressure solutions near $x_1 = 0$. To see the performance on anisotropic triangulations we again use Shishkin-type meshes, with parameters $\tau = 3\varepsilon|\log \varepsilon|$ and $q = 0.5$, which fit into the mesh families with stable inf-sup constant seen in the previous example.

We use the lowest-order Brezzi–Douglas–Marini element, as described in [BBF13, Section 2.3.1]. The parameters are set to $\varepsilon = 10^{-4}$ and $\nu = 10^{-4}$. This choice of ε leads to extremely anisotropic meshes with an aspect ratio of $\sigma \approx 417$, cf. (2.18).

In Figure 3.5 the velocity gradient errors $\|\nabla_h \boldsymbol{u} - \nabla_h \boldsymbol{u}_h\|_0$ for the two methods are shown for different choices of the penalty parameter η. It is immediately clear that the choices $\eta \in \{1, 2\}$ for the standard method are not suitable for this example, but the values $\eta \in \{5, 10\}$ yield usable results. The method using the modified penalty term on

the other hand yields the same good results for the parameter choices $\eta \in \{1, 10\}$, and thus shows a robustness with regard to the aspect ratio in the triangulation.

3.3 Pressure-robustness by reconstruction

In addition to the discretizations from Section 3.2 which are naturally pressure-robust, a separate approach can be taken to construct pressure-robust methods from classical inf-sup stable element pairs by using a reconstruction operator on the test functions. With this design, the L^2-orthogonality of discretely divergence-free test functions and arbitrary gradient fields is restored, and the method can once again see the velocity-equivalence of functions on the right hand side of the Stokes equations. The approach has been proved and tested for the Crouzeix–Raviart element, see [Lin14; VZ19], general elements with discontinuous pressures, see [LMT16], and the Taylor–Hood element, see [LLMS17].

Two different approaches can be taken when constructing appropriate reconstruction operators: the first maps the test functions into $\boldsymbol{H}^1_0(\Omega)$, the second into $\boldsymbol{H}_0(\mathrm{div}, \Omega)$. For our goal of using anisotropic triangulations we will see that the first one is not easily realizable. Both approaches are introduced in the next subsections.

Besides the methods from this and the previous sections, there are some other approaches for pressure-robust methods, e.g., using the virtual element method, see [FM20], and weak Galerkin methods, see [MYZ21]. However, we do not discuss those approaches in more detail.

3.3.1 $\boldsymbol{H}^1_0(\Omega)$-smoothing

We concentrate in this subsection on the method from [VZ19], where a stable *smoothing operator* for the Crouzeix–Raviart method is constructed, that maps discrete velocity test functions on the right hand side into $\boldsymbol{H}^1_0(\Omega)$ and discretely divergence-free functions to exactly divergence-free functions. This results in a discretization that is quasi-optimal in the sense that a velocity error estimate of the form

$$\|\boldsymbol{u} - \boldsymbol{u}_h\|_{1,h} \leq C \inf_{\boldsymbol{v}_h \in \boldsymbol{X}_h} \|\boldsymbol{u} - \boldsymbol{v}_h\|_{1,h}$$

can be shown. Building on the findings in this reference, [KZ20] uses a similar approach to get quasi-optimal results for a larger class of discretizations, and [KVZ21] further improves on this.

We assume that the Crouzeix–Raviart element is used in the discretization, so we set $\boldsymbol{X}_h = \mathrm{CR}(\mathcal{T}_h)$. The only non-standard part of the discretization in this approach is a modified definition of the linear form $l_h(\boldsymbol{v}_h)$ from (3.1a), i.e.,

$$l_h(\boldsymbol{v}_h) = (\boldsymbol{f}, E_h \boldsymbol{v}_h),$$

with the smoothing operator $E_h : \boldsymbol{X}_h \to \boldsymbol{H}^1_0(\Omega)$. When this operator satisfies the

properties

$$\int_F E_h \boldsymbol{v}_h \,\mathrm{d}\boldsymbol{s} = \int_F \boldsymbol{v}_h \,\mathrm{d}\boldsymbol{s} \qquad \forall F \in \mathcal{F}(\mathcal{T}_h), \tag{3.5a}$$

$$\int_T E_h \boldsymbol{v}_h \,\mathrm{d}\boldsymbol{x} = \int_T \boldsymbol{v}_h \,\mathrm{d}\boldsymbol{x} \qquad \forall T \in \mathcal{T}_h, \tag{3.5b}$$

$$\|\nabla_h (E_h \boldsymbol{v}_h)\|_0 \leq C_{\mathrm{stab}} \|\nabla_h \boldsymbol{v}_h\|_0, \tag{3.5c}$$

for any $\boldsymbol{v}_h \in \boldsymbol{X}_h$, which implies $a_h(\boldsymbol{w}_h, E_h \boldsymbol{v}_h) = a_h(\boldsymbol{w}_h, \boldsymbol{v}_h)$ for all $\boldsymbol{w}_h, \boldsymbol{v}_h \in \boldsymbol{X}_h^0$, it is possible to show quasi-optimality, i.e., the estimate

$$\|\boldsymbol{u} - \boldsymbol{u}_h\|_{1,h} \leq C_{\mathrm{qopt}} \inf_{\boldsymbol{v}_h \in \mathrm{CR}(\mathcal{T}_h)} \|\boldsymbol{u} - \boldsymbol{v}_h\|_{1,h},$$

where C_{qopt} is the operator norm of E_h, see [VZ19, Theorem 4.2]. The discretization is thus pressure-robust. The challenging part is to find an operator that satisfies these properties.

The construction of the smoothing operator in [VZ19, Section 4] consists of three steps which, assuming a Crouzeix–Raviart function $\boldsymbol{v}_h$ is to be mapped, are:

Simplified averaging: In the first step, for every interior vertex $\boldsymbol{p}$ of the triangulation one of its adjacent elements $T_{\boldsymbol{p}}$ is chosen and fixed, and the linear nodal basis function $\varphi_{\boldsymbol{p}}$ for this vertex is multiplied with the value of $\boldsymbol{v}_h$ on that element, i.e., the operator is defined by

$$A\boldsymbol{v}_h = \sum_{\boldsymbol{p} \in \mathcal{V}^i(\mathcal{T}_h)} \varphi_{\boldsymbol{p}} \boldsymbol{v}_h|_{T_{\boldsymbol{p}}}(\boldsymbol{p}).$$

With this definition $A\boldsymbol{v}_h$ vanishes on the boundary. This first part ensures that the mapping is into $\boldsymbol{H}_0^1(\Omega)$ and the next steps do not disturb this property.

Facet bubbles: The next step defines facet bubble functions t_F for every interior facet $F \in \mathcal{F}^i(\mathcal{T}_h)$ by

$$t_F = \frac{(2d-1)!}{(d-1)!|F|} \prod_{\boldsymbol{p} \in \mathcal{V}(F)} \varphi_{\boldsymbol{p}}$$

and uses them to set

$$B\boldsymbol{v}_h = \sum_{F \in \mathcal{F}^i(\mathcal{T}_h)} t_F \int_F \boldsymbol{v}_h \,\mathrm{d}\boldsymbol{s}.$$

This step is used to set the facet moments of the mapped function so that (3.5a) is satisfied.

Scott–Vogelius sub-problems: The final step is more involved and we omit the details for brevity. It consists of solving local small Stokes sub-problems on a barycentric refinement of each element T with homogeneous Dirichlet boundary conditions and non-homogeneous divergence constraint $r \in Q$ using Scott–Vogelius finite elements, see Section 3.2.1. The results are operators C_T with mapping $r \mapsto \boldsymbol{u}_T$, where $\boldsymbol{u}_T$ is the velocity solution of the sub-problem. This construction can be used to correct the divergence of the mapped function to the desired value.

With these operators, the smoothing operator is defined by

$$E_h \boldsymbol{v}_h = A\boldsymbol{v}_h + B(\boldsymbol{v}_h - A\boldsymbol{v}_h) - \sum_{T\in\mathcal{T}_h} C_T(\nabla\cdot(A\boldsymbol{v}_h + B(\boldsymbol{v}_h - A\boldsymbol{v}_h)) - \nabla_h\cdot\boldsymbol{v}_h).$$

By [VZ19] it is $\boldsymbol{H}^1(\Omega)$ stable on shape regular triangulations, i.e., property (3.5c) holds, and by the intricate definition of B and C_T it also satisfies the other two properties (3.5a), (3.5b).

However, as mentioned in [VZ19, Remark 4.5], the $\boldsymbol{H}^1(\Omega)$ stability constant depends on the shape of the elements in $\mathcal{T}_h$, which makes it unsuitable for the types of anisotropically graded meshes we intend to use. To demonstrate this dependence we use an illustrative example.

Example 3.4. We compute the stability constant C_{stab} of estimate (3.5c) for a special setting to see that there are cases where a dependence on the aspect ratio σ can be observed. Instead of the complete smoothing operator E_h, we use only the combined simplified averaging and facet bubble function operator, i.e., we compute

$$C_{\text{stab}} = \frac{\|\nabla_h(A\boldsymbol{v}_h + B(\boldsymbol{v}_h - A\boldsymbol{v}_h))\|_0}{\|\nabla_h\boldsymbol{v}_h\|_0}$$

for a Crouzeix–Raviart function $\boldsymbol{v}_h$. This is enough to make our argument, since the stability of E_h hinges on the stability of this part of the operator, as mentioned in [VZ19, p. 1088].

The example mesh consists of eight triangular elements with nine vertices, as pictured in Figure 3.6, where we can adjust the aspect ratio of the elements with the parameter h. Since just the vertex $\boldsymbol{p}_h = (0.5, h)^T$ is in the interior of the domain, only this vertex has to be considered for the simplified averaging.

As function $\boldsymbol{v}_h$ we choose for both components the scalar Crouzeix–Raviart basis function associated with the edge e_h. This function is constant and equal to one on the edge e_h, decreases linearly to a value of -1 at the opposite vertices of the adjacent triangles and vanishes on all other elements. We choose the element $T_{\boldsymbol{p}_h}$ as indicated in Figure 3.6 for the averaging process at vertex $\boldsymbol{p}_h$, so that we get $A\boldsymbol{v}_h = (\varphi_{\boldsymbol{p}_h}, \varphi_{\boldsymbol{p}_h})^T$, where $\varphi_{\boldsymbol{p}_h}$ is the nodal linear basis function associated with $\boldsymbol{p}_h$. As a consequence, bubble functions must be computed for all edges that end in $\boldsymbol{p}_h$.

After implementing this procedure we get the results shown in Figure 3.6 in dependence of h. For $h < 1$, that means when the edge e_h is the small edge of the adjacent elements, the stability constant C_{stab} shows a clear dependence on the aspect ratio. However for large values of h, when the edge e_h is a long edge of the anisotropic triangles, the constant seems to be independent of the aspect ratio.

As seen in the example, this construction of a smoothing operator is not suitable for anisotropic triangulations and it is an open problem to find a stable operator for this purpose.

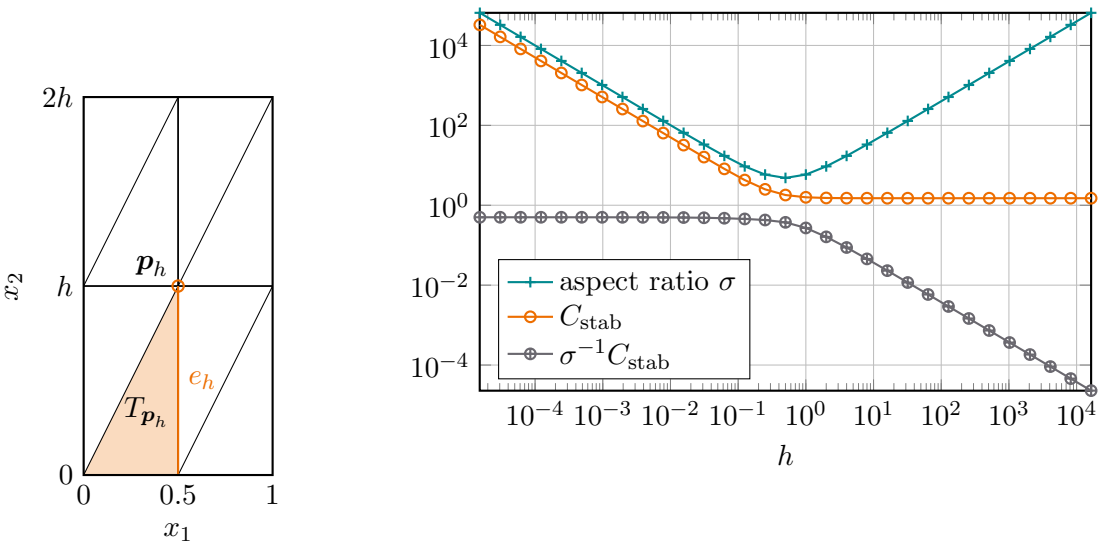

Figure 3.6: Schematic of the mesh used in Example 3.4 and computational results.

3.3.2 $\boldsymbol{H}_0(\mathrm{div}, \Omega)$-reconstruction

The idea to use an operator on the test functions in the linear form of the discretization was first introduced in [Lin14], and subsequently this operator was named *reconstruction operator*. It has slightly different properties than the smoothing operator from the previous subsection. The main distinction is that the reconstruction operator I_h maps into the space $\boldsymbol{H}_0(\mathrm{div}, \Omega)$ instead of $\boldsymbol{H}_0^1(\Omega)$, while analogous properties to (3.5) hold.

The main idea of this approach is to repair the $L^2(\Omega)$-orthogonality of the irrotational part of the data function and the discretely divergence-free test functions by using the modified linear form

$$l_h(\boldsymbol{v}_h) = (\boldsymbol{f}, I_h \boldsymbol{v}_h) \tag{3.6}$$

with the reconstruction operator I_h, so that on the right hand side of (3.2) the identity

$$(\boldsymbol{f}, I_h \boldsymbol{v}_h) = (\mathbb{P}\boldsymbol{f}, I_h \boldsymbol{v}_h) \qquad \forall \boldsymbol{v}_h \in \boldsymbol{X}_h^0$$

holds, where I_h maps discretely divergence-free test functions to exactly divergence-free functions.

The first use of this type of non-standard discretization in [Lin14] was for the Crouzeix–Raviart method, and since then the approach has been extended to a large variety of classical finite element methods, see [Joh+17; LLMS17; LMT16], but we will concentrate mainly on the Crouzeix–Raviart element as base for the reconstruction since it proves exceptionally well suited for anisotropic meshes.

The right choice of reconstruction operator is of special importance when using anisotropic triangulations since, as already demonstrated in Example 3.4, the stability constant C_{stab} in (3.5c) needs to be independent of the aspect ratio. Two possible choices

of reconstruction operators for mixed methods with discontinuous pressure approximation, which includes the Crouzeix–Raviart method, are the Raviart–Thomas and Brezzi–Douglas–Marini interpolation operators, see [LMT16].

In contrast to the smoothing approach where, since $E_h \boldsymbol{v}_h \in \boldsymbol{H}_0^1(\Omega)$, it is possible to extend the discretization approach to problems with data $\boldsymbol{f} \in \boldsymbol{H}^{-1}(\Omega)$ by using the duality pairing $l_h(\boldsymbol{v}_h) = \langle \boldsymbol{f}, E_h \boldsymbol{v}_h \rangle$, this is not possible with the reconstruction operator due to the lower regularity of $I_h \boldsymbol{v}_h \in \boldsymbol{H}_0(\mathrm{div}, \Omega) \not\subset \boldsymbol{H}_0^1(\Omega)$. On the other hand this lower regularity of the reconstruction operator's codomain allows for more flexibility when choosing the operator.

Since this reconstruction approach is the main method used in this thesis, we conclude this subsection after this brief introduction and use the next chapters for a detailed analysis. In Chapter 4 two families of possible reconstruction operators on anisotropic meshes, the Raviart–Thomas and Brezzi–Douglas–Marini interpolation operators, are introduced and interpolation error estimates for anisotropic elements are derived. In Chapter 5 we further investigate the reconstruction approach and present discretizations for use with anisotropic triangulations.

CHAPTER 4

$\boldsymbol{H}(\mathrm{div}, \Omega)$-conforming interpolation on anisotropic triangulations

In this chapter we introduce two $\boldsymbol{H}(\mathrm{div}, \Omega)$-conforming interpolation operators and prove anisotropic interpolation error estimates. For the Brezzi–Douglas–Marini interpolation, we showed these results in [AK20] for the Hilbert space setting. Although mainly following the reference, we generalize the analysis in terms of L^p-norms for the more general Banach-space setting in Section 4.2. Section 4.3 is concerned with the interpolation error of the Raviart–Thomas interpolation. The results from this section are adapted from [AADL11], which was also the basis for the results in [AK20]. Section 4.5 contains new anisotropic error estimates for the Brezzi–Douglas–Marini interpolation on triangular prisms. In advance, Section 4.1 introduces the setting and some notation. Throughout this chapter the symbol p does not denote the pressure variable as in the other chapters, but the parameter of the Lebesgue and Sobolev spaces, which throughout the chapter is assumed to take the values $1 \leq p \leq \infty$, where not stated otherwise.

4.1 Reference geometries

Before we get into the specifics of the two types of interpolation, we introduce the reference geometries needed for the analysis. Regarding mesh regularity, for the nodal Lagrange interpolation mainly the maximum angle condition, see Definition 2.10, matters, but for the Brezzi–Douglas–Marini and Raviart–Thomas interpolations a better estimate is possible when the assumption that the element satisfies the regular vertex property, see Definition 2.11, is used. Thus two types of reference elements are required, and the analysis will be separated into a case with regular vertex property, and a case with no regular vertex property but with the maximum angle condition.

In the course of deriving the interpolation error estimates we use two affine mappings, the first from a reference element to a reference family of elements, and the second from

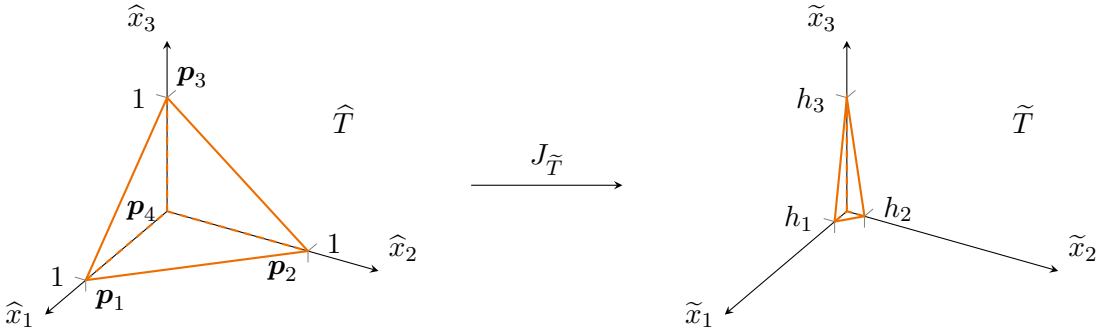

Figure 4.1: Reference tetrahedron $\widehat{T}$ with vertex numbering, transformed tetrahedron of reference family $\mathcal{R}_1$.

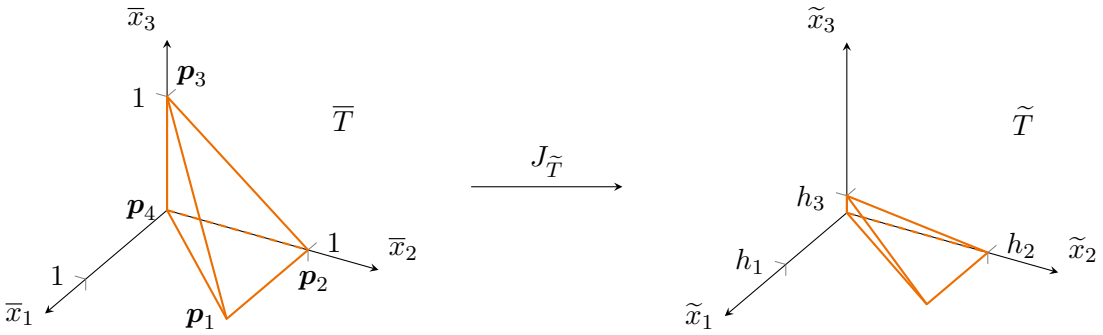

Figure 4.2: Reference tetrahedron $\overline{T}$ for family of tetrahedra without regular vertex property, transformed tetrahedron of reference family $\mathcal{R}_2$.

the reference family to the actual element, e.g., in a mesh. Figures 4.1 and 4.2 show on the left hand side the reference tetrahedra $\widehat{T}$ and $\overline{T}$, which we use for the regular vertex property case and the maximum angle condition without regular vertex property case, respectively. On the right hand side of the figures two representatives from the reference families $\mathcal{R}_1$ and $\mathcal{R}_2$ with vertices at $\mathbf{0}$, $h_1\boldsymbol{e}_1$, $h_2\boldsymbol{e}_2$, $h_3\boldsymbol{e}_3$ and $\mathbf{0}$, $h_1\boldsymbol{e}_1 + h_2\boldsymbol{e}_2$, $h_2\boldsymbol{e}_2$, $h_3\boldsymbol{e}_3$ are visualized, where $h_i \in \mathbb{R}_+$, $i \in I_d$, are arbitrary element size parameters.

By using a reasonable affine transformation E, any tetrahedron satisfying $RVP(\overline{c})$ or $MAC(\overline{\phi})$ can be produced from elements of the two reference families of elements.

Lemma 4.1. *Let an element T satisfy $MAC(\overline{\phi})$. Then there is an element $\widetilde{T} \in \mathcal{R}_1 \cup \mathcal{R}_2$ so that an affine transformation $E(\widetilde{\boldsymbol{x}}) = J_T\widetilde{\boldsymbol{x}} + \boldsymbol{x}_0$ with $\|J_T\|_\infty, \left\|J_T^{-1}\right\|_\infty \leq C(\overline{\phi})$ that maps $\widetilde{T}$ to T exists, where the constant $C(\overline{\phi})$ depends only on $\overline{\phi}$.*

Now let T satisfy $RVP(\overline{c})$. Then there is an element $\widetilde{T} \in \mathcal{R}_1$ so that an affine transformation mapping, like before, $\widetilde{T}$ to T with $\|J_T\|_\infty, \left\|J_T^{-1}\right\|_\infty \leq C(\overline{c})$ exists, where $C(\overline{c})$ depends only on $\overline{c}$. If the edges of T incident to the regular vertex have lengths h_i, $i \in I_d$, then it is possible to take $\widetilde{T} \in \mathcal{R}_1$ with vertices at $h_i\boldsymbol{e}_i$ and $\mathbf{0}$.

Proof. For the proof see [AADL11, Theorems 2.2 and 2.3]. □

This justifies the intended strategy of first mapping the reference element $\widehat{T}$ or $\overline{T}$ to an element $\widetilde{T}$ of one of the reference families and then using another affine mapping to the actual element T. This strategy permits us to utilize the simple structure of the transformation from reference element to reference family in our proofs.

The use of the diacritical marks hat, bar and tilde indicates the type of element on which an operator, function or coordinate is defined, corresponding to the introduction above.

4.2 Brezzi–Douglas–Marini interpolation

While [AK20] is written to accommodate the two- as well as the three-dimensional case, we will mostly concentrate on tetrahedra. Note that the interpolation error results are still valid for triangles, even when not explicitly mentioned. Concerning anisotropic quadrilateral elements some additional progress has been made in [Fra21] and triangular prisms are discussed in Section 4.5.

4.2.1 Interpolation operators

The Brezzi–Douglas–Marini element was first introduced in [BDM85] in two dimensions and later generalized to three-dimensional settings in [Néd86]. The Brezzi–Douglas–Marini space of order $k \in \mathbb{N}$ on an element is the full $\boldsymbol{P}_k(T)$ space. On a mesh the degrees of freedom result in functions with continuous normal components at the element interfaces, which makes the global function space a subspace of $\boldsymbol{H}(\operatorname{div}, \Omega)$.

Definition 4.2. The space defined by

$$\operatorname{BDM}_k(\mathcal{T}_h) = \{\boldsymbol{v} \in \boldsymbol{H}(\operatorname{div}, \Omega) : \boldsymbol{v}|_T \in P_k(T)\ \forall T \in \mathcal{T}_h\}$$

is called *Brezzi–Douglas–Marini function space of order k* on the mesh $\mathcal{T}_h$.

In this section we are mainly concerned with the local interpolation errors, while the global function space is needed later.

The original defining functionals for the local space and interpolation operator from [BDM85], see also [BF91, Section III.3.3], are given by

$$\int_{e_i} (I_k^{\mathrm{BDM}} \boldsymbol{v}) \cdot \boldsymbol{n}_{T,e_i} z \,\mathrm{d}\boldsymbol{s} = \int_{e_i} \boldsymbol{v} \cdot \boldsymbol{n}_{T,e_i} z \,\mathrm{d}\boldsymbol{s} \qquad \forall z \in P_k(e_i), \quad i \in I_{d+1}, \tag{4.1a}$$

$$\int_T (I_k^{\mathrm{BDM}} \boldsymbol{v}) \cdot \nabla z \,\mathrm{d}\boldsymbol{x} = \int_T \boldsymbol{v} \cdot \nabla z \,\mathrm{d}\boldsymbol{x} \qquad \forall z \in P_{k-1}(T), \tag{4.1b}$$

$$\int_T (I_k^{\mathrm{BDM}} \boldsymbol{v}) \cdot \boldsymbol{z} \,\mathrm{d}\boldsymbol{x} = \int_T \boldsymbol{v} \cdot \boldsymbol{z} \,\mathrm{d}\boldsymbol{x} \qquad \forall \boldsymbol{z} \in \boldsymbol{G}_k(T), \tag{4.1c}$$

where we use the piecewise polynomial function space

$$\boldsymbol{G}_k(T) = \{\boldsymbol{z} \in \boldsymbol{P}_k(T) : \nabla \cdot \boldsymbol{z} = 0,\ \boldsymbol{z} \cdot \boldsymbol{n}|_{\partial T} = 0\}.$$

This definition however turns out to be unsuitable for our proof, as we show below in Remark 4.4. Instead we use the degrees of freedom from [Néd86], see also [BBF13, Section 2.5.1], which define the interpolation operator by

$$\int_{e_i} (I_k^{\mathrm{BDM}}\boldsymbol{v})\cdot\boldsymbol{n}_{T,e_i} z \,\mathrm{d}\boldsymbol{s} = \int_{e_i} \boldsymbol{v}\cdot\boldsymbol{n}_{T,e_i} z \,\mathrm{d}\boldsymbol{s} \qquad \forall z\in P_k(e_i),\quad i\in I_{d+1}, \tag{4.2a}$$

$$\int_{T} (I_k^{\mathrm{BDM}}\boldsymbol{v})\cdot\boldsymbol{z} \,\mathrm{d}\boldsymbol{x} = \int_{T} \boldsymbol{v}\cdot\boldsymbol{z} \,\mathrm{d}\boldsymbol{x} \qquad \forall \boldsymbol{z}\in \boldsymbol{N}_{k-1}(T) \text{ if } k\geq 2, \tag{4.2b}$$

where

$$\begin{aligned} \boldsymbol{N}_{k-1}(T) &= \boldsymbol{P}_{k-2}(T)\oplus \boldsymbol{S}_{k-1}(T), \\ \boldsymbol{S}_{k-1}(T) &= \{\boldsymbol{p}\in \boldsymbol{P}_{k-1}(T) : \boldsymbol{p}(\boldsymbol{x})\cdot\boldsymbol{x} = 0 \ \forall \boldsymbol{x}\in T\}. \end{aligned} \tag{4.3}$$

Both types of degrees of freedom result in globally $\boldsymbol{H}(\mathrm{div},\Omega)$-conforming finite element spaces.

4.2.2 Stability estimates

For the first stability estimate on the reference element $\widehat{T}$, we need the following technical lemma, see [AK20, Lemma 3.1].

Lemma 4.3. *Let $\widehat{T}$ be the reference element from Figure 4.1, $\widehat{f_j}\in L^p(e_j)$, $j\in I_d$, $1\leq p\leq\infty$, and*

$$\widehat{\boldsymbol{u}}(\widehat{\boldsymbol{x}}) = \begin{pmatrix} \widehat{f}_1(\widehat{x}_2,\widehat{x}_3)\\ 0\\ 0\end{pmatrix}, \qquad \widehat{\boldsymbol{v}}(\widehat{\boldsymbol{x}}) = \begin{pmatrix} 0\\ \widehat{f}_2(\widehat{x}_1,\widehat{x}_3)\\ 0\end{pmatrix}, \qquad \widehat{\boldsymbol{w}}(\widehat{\boldsymbol{x}}) = \begin{pmatrix} 0\\ 0\\ \widehat{f}_3(\widehat{x}_1,\widehat{x}_2)\end{pmatrix}.$$

Then there are functions $\widehat{q}_j\in P_k(e_j)$, $j\in I_d$, so that

$$\widehat{I}_k^{\mathrm{BDM}}\widehat{\boldsymbol{u}} = \begin{pmatrix} \widehat{q}_1(\widehat{x}_2,\widehat{x}_3)\\ 0\\ 0\end{pmatrix}, \quad \widehat{I}_k^{\mathrm{BDM}}\widehat{\boldsymbol{v}} = \begin{pmatrix} 0\\ \widehat{q}_2(\widehat{x}_1,\widehat{x}_3)\\ 0\end{pmatrix}, \quad \widehat{I}_k^{\mathrm{BDM}}\widehat{\boldsymbol{w}} = \begin{pmatrix} 0\\ 0\\ \widehat{q}_3(\widehat{x}_1,\widehat{x}_2)\end{pmatrix}.$$

Proof. We can show the claim by proving that the functions $\widehat{q}_j$ are uniquely defined by the interpolation relations (4.2). We detail the proof for $j=1$, the cases $j=2,3$ then follow analogously.

On the reference element $\widehat{T}$, see Figure 4.1, the normal vectors in the facets e_i, $i\in I_{d+1}$ are given by

$$\boldsymbol{n}_{\widehat{T},e_1} = \begin{pmatrix}-1\\0\\0\end{pmatrix}, \qquad \boldsymbol{n}_{\widehat{T},e_2} = \begin{pmatrix}0\\-1\\0\end{pmatrix}, \qquad \boldsymbol{n}_{\widehat{T},e_3} = \begin{pmatrix}0\\0\\-1\end{pmatrix}, \qquad \boldsymbol{n}_{\widehat{T},e_4} = \frac{1}{\sqrt{3}}\begin{pmatrix}1\\1\\1\end{pmatrix}.$$

With this, relation (4.2a) for $i=1$ reduces to

$$\int_{e_1} \widehat{f}_1 z \,\mathrm{d}\boldsymbol{s} = \int_{e_1} \widehat{q}_1 z \,\mathrm{d}\boldsymbol{s} \qquad \forall z\in P_k(e_1), \tag{4.4}$$

which defines $\widehat{q}_1$ uniquely. So for the rest of the proof, we need to show that the remaining relations are compatible with this result.

From (4.2a) for $i = 2, 3$ we get trivial equations immediately, while for $i = 4$ we calculate

$$\begin{aligned}\int_{e_4} (\widehat{\boldsymbol{u}} - \widehat{I}_k^{\mathrm{BDM}}\widehat{\boldsymbol{u}}) \cdot \boldsymbol{n}_{\widehat{T},e_4} z \,\mathrm{d}\boldsymbol{s} &= \int_0^1 \int_0^{1-\widehat{x}_2} (\widehat{f}_1(\widehat{x}_2,\widehat{x}_3) - \widehat{q}_1(\widehat{x}_2,\widehat{x}_3)) \\ &\qquad\qquad z(1-\widehat{x}_2-\widehat{x}_3,\widehat{x}_2,\widehat{x}_3)\,\mathrm{d}\widehat{x}_3\mathrm{d}\widehat{x}_2 \\ &= \int_{e_1} (\widehat{f}_1(\widehat{x}_2,\widehat{x}_3) - \widehat{q}_1(\widehat{x}_2,\widehat{x}_3)) z(1-\widehat{x}_2-\widehat{x}_3,\widehat{x}_2,\widehat{x}_3)\,\mathrm{d}\widehat{x}_3\mathrm{d}\widehat{x}_2 \\ &= 0,\end{aligned}$$

since $z(1-\widehat{x}_2-\widehat{x}_3,\widehat{x}_2,\widehat{x}_3)$ is a polynomial of degree k in the variables $\widehat{x}_2$, $\widehat{x}_3$ and we have (4.4).

For $k \geq 2$, take an arbitrary $\boldsymbol{z} = (z_1, z_2, z_3)^T \in \boldsymbol{N}_{k-1}(\widehat{T}) \subset \boldsymbol{P}_{k-1}(\widehat{T})$, and let $Z \in P_k(\widehat{T})$ be so that $\frac{\partial Z}{\partial \widehat{x}_1} = z_1$. Then, since $\widehat{f}_1$ and $\widehat{q}_1$ do not depend on $\widehat{x}_1$, we get

$$\begin{aligned}\int_{\widehat{T}} \widehat{\boldsymbol{u}} \cdot \boldsymbol{z} \,\mathrm{d}\boldsymbol{x} &= \int_{\widehat{T}} \widehat{f}_1 z_1 \,\mathrm{d}\boldsymbol{x} = \int_{\widehat{T}} \widehat{f}_1 \frac{\partial Z}{\partial \widehat{x}_1} \,\mathrm{d}\boldsymbol{x} = \int_{\partial\widehat{T}} \widehat{f}_1 Z n_1 \,\mathrm{d}\boldsymbol{s} - \int_{\widehat{T}} \frac{\partial \widehat{f}_1}{\partial \widehat{x}_1} Z \,\mathrm{d}\boldsymbol{x} \\ &= \int_{\partial\widehat{T}} \widehat{q}_1 Z n_1 \,\mathrm{d}\boldsymbol{s} = \int_{\widehat{T}} \widehat{q}_1 \frac{\partial Z}{\partial \widehat{x}_1} \,\mathrm{d}\boldsymbol{x} = \int_{\widehat{T}} \widehat{q}_1 z_1 \,\mathrm{d}\boldsymbol{x},\end{aligned}$$

where we used the outward normal vector $\boldsymbol{n}_T = (n_1, n_2, n_3)^T$ and integration by parts. This shows the compatibility of (4.2b) and concludes the proof. □

Remark 4.4. We now get back briefly to the already mentioned difference in the definitions of the degrees of freedom in (4.1) and (4.2). While we showed Lemma 4.3 using the latter, the lemma does not hold for the original definition of the interpolation operator. The difference only appears for $k \geq 2$ when the interior degrees of freedom become relevant, since the facet degrees of freedom are the same.

Consider $k = 2$ and a function $\widehat{\boldsymbol{v}} = (0, \widehat{x}_1^3)^T$ on the reference triangle with vertices $\boldsymbol{p}_1 = (1,0)^T$, $\boldsymbol{p}_2 = (0,1)^T$ and $\boldsymbol{p}_3 = (0,0)^T$. Then by using the interpolation defined by (4.2) we get the function

$$\widehat{I}_2^{\mathrm{BDM}}\widehat{\boldsymbol{v}} = \begin{pmatrix} 0 \\ \frac{1}{20} - \frac{3}{5}\widehat{x}_1 + \frac{3}{2}\widehat{x}_1^2 \end{pmatrix},$$

which, as expected, shows the property from Lemma 4.3. Now using (4.1) to calculate the interpolant, we get

$$\widehat{I}_2^{\mathrm{BDM}^*}\widehat{\boldsymbol{v}} = \begin{pmatrix} \frac{3}{140}\widehat{x}_1(1-\widehat{x}_1-2\widehat{x}_2) \\ \frac{1}{20} - \frac{3}{5}\widehat{x}_1 + \frac{3}{2}\widehat{x}_1^2 - \frac{3}{140}\widehat{x}_2(1-2\widehat{x}_1-\widehat{x}_2) \end{pmatrix}.$$

Clearly, this second interpolant does not possess the quality from the lemma.

For the second reference element $\overline{T}$, which later leads to the results for elements without regular vertex property, we get an analogous lemma, see also [AK20, Lemma 3.6].

Lemma 4.5. *Let $\overline{T}$ be the reference element from Figure 4.2, e_i, $i \in I_{d+1}$ its facets, and let $\overline{f}_1 \in L^p(e_1)$, $\overline{f}_2 \in L^p(\overline{e}_2)$, $\overline{f}_3 \in L^p(e_3)$, $1 \leq p \leq \infty$, where $\overline{e}_2$ is the projection of e_2 onto the plane $\overline{x}_2 = 0$. Then for*

$$\overline{\boldsymbol{u}}(\overline{\boldsymbol{x}}) = \begin{pmatrix} \overline{f}_1(\overline{x}_2, \overline{x}_3) \\ 0 \\ 0 \end{pmatrix}, \qquad \overline{\boldsymbol{v}}(\overline{\boldsymbol{x}}) = \begin{pmatrix} 0 \\ \overline{f}_2(\overline{x}_1, \overline{x}_3) \\ 0 \end{pmatrix}, \qquad \overline{\boldsymbol{w}}(\overline{\boldsymbol{x}}) = \begin{pmatrix} 0 \\ 0 \\ \overline{f}_3(\overline{x}_1, \overline{x}_2) \end{pmatrix},$$

there are functions $\overline{q}_1 \in P_k(e_1)$, $\overline{q}_2 \in P_k(\overline{e}_2)$, $\overline{q}_3 \in P_k(e_3)$, so that

$$\overline{I}_k^{\mathrm{BDM}} \overline{\boldsymbol{u}} = \begin{pmatrix} \overline{q}_1(\overline{x}_2, \overline{x}_3) \\ 0 \\ 0 \end{pmatrix}, \quad \overline{I}_k^{\mathrm{BDM}} \overline{\boldsymbol{v}} = \begin{pmatrix} 0 \\ \overline{q}_2(\overline{x}_1, \overline{x}_3) \\ 0 \end{pmatrix}, \quad \overline{I}_k^{\mathrm{BDM}} \overline{\boldsymbol{w}} = \begin{pmatrix} 0 \\ 0 \\ \overline{q}_3(\overline{x}_1, \overline{x}_2) \end{pmatrix}.$$

Proof. The proof is analogous to the proof of Lemma 4.3, only that we now need to take a closer look at the interpolation relation for facet e_2 instead of e_4.

The normal vectors for $\overline{T}$ are

$$\boldsymbol{n}_{\overline{T},e_1} = \begin{pmatrix} -1 \\ 0 \\ 0 \end{pmatrix}, \quad \boldsymbol{n}_{\overline{T},e_2} = \frac{1}{\sqrt{2}} \begin{pmatrix} 1 \\ -1 \\ 0 \end{pmatrix}, \quad \boldsymbol{n}_{\overline{T},e_3} = \begin{pmatrix} 0 \\ 0 \\ -1 \end{pmatrix}, \quad \boldsymbol{n}_{\overline{T},e_4} = \frac{1}{\sqrt{2}} \begin{pmatrix} 0 \\ 1 \\ 1 \end{pmatrix},$$

which again yields for $i = 1$ of (4.2a)

$$\int_{e_1} \overline{f}_1 z \,\mathrm{d}\boldsymbol{s} = \int_{e_1} \overline{q}_1 z \,\mathrm{d}\boldsymbol{s} \qquad \forall z \in P_k(e_1).$$

This defines $\overline{q}_1$ uniquely and we can use it in the calculation for $i = 2$:

$$\begin{aligned} \int_{e_2} (\overline{\boldsymbol{u}} - \overline{I}_k^{\mathrm{BDM}} \overline{\boldsymbol{u}}) \cdot \boldsymbol{n}_{\overline{T},e_2} z \,\mathrm{d}\boldsymbol{s} &= \frac{1}{\sqrt{2}} \int_{e_2} (\overline{f}_1 - \overline{q}_1) z \,\mathrm{d}\boldsymbol{s} \\ &= \int_0^1 \int_0^{1-\overline{x}_2} (\overline{f}_1(\overline{x}_2, \overline{x}_3) - \overline{q}_1(\overline{x}_2, \overline{x}_3)) z(\overline{x}_2, \overline{x}_2, \overline{x}_3) \,\mathrm{d}\overline{x}_3 \,\mathrm{d}\overline{x}_2 \\ &= \int_{e_1} (\overline{f}_2(\overline{x}_2, \overline{x}_3) - \overline{q}_1(\overline{x}_2, \overline{x}_3)) z(\overline{x}_2, \overline{x}_2, \overline{x}_3) \,\mathrm{d}\overline{x}_3 \,\mathrm{d}\overline{x}_2 = 0. \end{aligned}$$

For $i = 3, 4$ in (4.2a) we get trivial equalities. The interior degrees of freedom are treated completely analogous to the proof of Lemma 4.3. □

Using the two preceding lemmas we can prove the stability estimates on the reference elements, where we get a better estimate on $\widehat{T}$ compared to the estimate on $\overline{T}$. The lemmas are analogous to [AK20, Lemmas 3.3, 3.7].

Lemma 4.6. *Let $\widehat{\boldsymbol{u}} \in \boldsymbol{W}^{1,p}(\widehat{T})$, $1 \le p \le \infty$. Then the estimates*

$$\left\|(\widehat{I}_k^{\mathrm{BDM}}\widehat{\boldsymbol{u}})_i\right\|_{0,p,\widehat{T}} \lesssim \|\widehat{u}_i\|_{1,p,\widehat{T}} + \left\|\widehat{\operatorname{div}}\,\widehat{\boldsymbol{u}}\right\|_{0,p,\widehat{T}}, \qquad i \in I_d, \tag{4.5}$$

hold.

Proof. Since the proof is analogous for all values of i, we only show the result for $i = 1$. Let

$$\widehat{\boldsymbol{u}}_* = \begin{pmatrix} 0 \\ \widehat{u}_2(\widehat{x}_1, 0, \widehat{x}_3) \\ \widehat{u}_3(\widehat{x}_1, \widehat{x}_2, 0) \end{pmatrix}, \qquad \widehat{\boldsymbol{v}} = \widehat{\boldsymbol{u}} - \widehat{\boldsymbol{u}}_* = \begin{pmatrix} \widehat{u}_1 \\ \widehat{u}_2 - \widehat{u}_2(\widehat{x}_1, 0, \widehat{x}_3) \\ \widehat{u}_3 - \widehat{u}_3(\widehat{x}_1, \widehat{x}_2, 0) \end{pmatrix}.$$

From Lemma 4.3 we know that $(\widehat{I}_k^{\mathrm{BDM}}\widehat{\boldsymbol{v}})_1 = (\widehat{I}_k^{\mathrm{BDM}}\widehat{\boldsymbol{u}})_1$, and $\widehat{\operatorname{div}}\,\widehat{\boldsymbol{v}} = \widehat{\operatorname{div}}\,\widehat{\boldsymbol{u}} - \widehat{\operatorname{div}}\,\widehat{\boldsymbol{u}}_* = \widehat{\operatorname{div}}\,\widehat{\boldsymbol{u}}$. We construct two new functions

$$\widehat{\boldsymbol{v}}_* = \begin{pmatrix} 0 \\ \widehat{x}_2\widehat{q}_2 \\ \widehat{x}_3\widehat{q}_3 \end{pmatrix}, \qquad \widehat{\boldsymbol{w}} = \widehat{\boldsymbol{v}} - \widehat{\boldsymbol{v}}_* = \begin{pmatrix} \widehat{v}_1 \\ \widehat{v}_2 - \widehat{x}_2\widehat{q}_2 \\ \widehat{v}_3 - \widehat{x}_3\widehat{q}_3 \end{pmatrix},$$

where we take $\widehat{q}_j \in P_{k-1}(\widehat{T})$, $j = 2, 3$, so that

$$\int_{\widehat{T}} \widehat{w}_j z \,\mathrm{d}\boldsymbol{x} = \int_{\widehat{T}} (\widehat{v}_j - \widehat{x}_j\widehat{q}_j) z \,\mathrm{d}\boldsymbol{x} = 0 \qquad \forall z \in P_{k-1}(\widehat{T}). \tag{4.6}$$

This means that the functions $\widehat{q}_j$ are well defined as the projections of $\frac{\widehat{v}_j}{\widehat{x}_j}$, $\widehat{v}_j \in L^p(\widehat{T})$, into $P_{k-1}(\widehat{T})$ with respect to the weighted scalar product $(q, z) = \int_{\widehat{T}} \widehat{x}_j q z \,\mathrm{d}\boldsymbol{x}$.

Since $\widehat{I}_k^{\mathrm{BDM}}$ preserves polynomials of degree k, it holds $\widehat{I}_k^{\mathrm{BDM}}\widehat{\boldsymbol{v}}_* = \widehat{\boldsymbol{v}}_*$, from which follows $(\widehat{I}_k^{\mathrm{BDM}}\widehat{\boldsymbol{w}})_1 = (\widehat{I}_k^{\mathrm{BDM}}\widehat{\boldsymbol{v}})_1 = (\widehat{I}_k^{\mathrm{BDM}}\widehat{\boldsymbol{u}})_1$. The interpolated function $\widehat{I}_k^{\mathrm{BDM}}\widehat{\boldsymbol{w}} = \widehat{\boldsymbol{t}} = (\widehat{t}_1, \widehat{t}_2, \widehat{t}_3)^T$, due to (4.2), is thus defined by the relations

$$\begin{aligned}
\int_{e_1} \widehat{t}_1 z \,\mathrm{d}\boldsymbol{s} &= \int_{e_1} \widehat{w}_1 z \,\mathrm{d}\boldsymbol{s} = \int_{e_1} \widehat{u}_1 z \,\mathrm{d}\boldsymbol{s} && \forall z \in P_k(e_1), \\
\int_{e_2} \widehat{t}_2 z \,\mathrm{d}\boldsymbol{s} &= \int_{e_2} \widehat{w}_2 z \,\mathrm{d}\boldsymbol{s} = \int_{e_2} (\widehat{v}_2 - \widehat{x}_2\widehat{q}_2) z \,\mathrm{d}\boldsymbol{s} = 0 && \forall z \in P_k(e_2), \\
\int_{e_3} \widehat{t}_3 z \,\mathrm{d}\boldsymbol{s} &= \int_{e_3} \widehat{w}_3 z \,\mathrm{d}\boldsymbol{s} = \int_{e_3} (\widehat{v}_3 - \widehat{x}_3\widehat{q}_3) z \,\mathrm{d}\boldsymbol{s} = 0 && \forall z \in P_k(e_3), \\
\int_{e_4} (\widehat{\boldsymbol{t}} \cdot \boldsymbol{n}_{\widehat{T},e_4}) z \,\mathrm{d}\boldsymbol{s} &= \int_{e_4} (\widehat{\boldsymbol{w}} \cdot \boldsymbol{n}_{\widehat{T},e_4}) z \,\mathrm{d}\boldsymbol{s} \\
&= \int_{\widehat{T}} (\widehat{\operatorname{div}}\,\widehat{\boldsymbol{w}}) z \,\mathrm{d}\boldsymbol{x} + \int_{\widehat{T}} \widehat{\boldsymbol{w}} \cdot \nabla z \,\mathrm{d}\boldsymbol{x} \\
&\quad - \sum_{i=1}^{3} \int_{e_i} (\widehat{\boldsymbol{w}} \cdot \boldsymbol{n}_{\widehat{T},e_i}) z \,\mathrm{d}\boldsymbol{s}
\end{aligned}$$

$$= \int_{\widehat{T}} (\widehat{\mathrm{div}}\,\widehat{\boldsymbol{w}}) z \,\mathrm{d}\boldsymbol{x} + \int_{\widehat{T}} \widehat{w}_1 \frac{\partial z}{\partial \widehat{x}_1} \,\mathrm{d}\boldsymbol{x} - \int_{e_1} \widehat{w}_1 z \,\mathrm{d}\boldsymbol{s} \qquad \forall z \in P_k(e_4),$$

$$\int_{\widehat{T}} \widehat{\boldsymbol{t}} \cdot \boldsymbol{z} \,\mathrm{d}\boldsymbol{x} = \int_{\widehat{T}} \widehat{\boldsymbol{w}} \cdot \boldsymbol{z} \,\mathrm{d}\boldsymbol{x} \qquad \forall \boldsymbol{z} \in \boldsymbol{N}_{k-1}(\widehat{T}).$$

The last relation can be split up into individual conditions by using the definition $\boldsymbol{N}_{k-1}(\widehat{T}) = \boldsymbol{P}_{k-2}(\widehat{T}) \oplus \boldsymbol{S}_{k-1}(\widehat{T})$, which yields

$$\int_{\widehat{T}} \widehat{t}_1 z \,\mathrm{d}\boldsymbol{x} = \int_{\widehat{T}} \widehat{w}_1 z \,\mathrm{d}\boldsymbol{x} \qquad \forall z \in P_{k-2}(\widehat{T}),$$

$$\int_{\widehat{T}} \widehat{t}_2 z \,\mathrm{d}\boldsymbol{x} = \int_{\widehat{T}} \widehat{w}_2 z \,\mathrm{d}\boldsymbol{x} = 0 \qquad \forall z \in P_{k-2}(\widehat{T}),$$

$$\int_{\widehat{T}} \widehat{t}_3 z \,\mathrm{d}\boldsymbol{x} = \int_{\widehat{T}} \widehat{w}_3 z \,\mathrm{d}\boldsymbol{x} = 0 \qquad \forall z \in P_{k-2}(\widehat{T}),$$

$$\int_{\widehat{T}} \widehat{\boldsymbol{t}} \cdot \boldsymbol{z} \,\mathrm{d}\boldsymbol{x} = \int_{\widehat{T}} \widehat{\boldsymbol{w}} \cdot \boldsymbol{z} \,\mathrm{d}\boldsymbol{x} = \int_{\widehat{T}} (\widehat{w}_1 z_1 + \widehat{w}_2 z_2 + \widehat{w}_3 z_3) \,\mathrm{d}\boldsymbol{x} = \int_{\widehat{T}} \widehat{w_1} z_1 \,\mathrm{d}\boldsymbol{x} \quad \forall \boldsymbol{z} \in \boldsymbol{S}_{k-1}(\widehat{T}),$$

where in the calculations (4.6) was used. So the terms

$$\int_{e_1} \widehat{w}_1 z \,\mathrm{d}\boldsymbol{s} = \int_{e_1} \widehat{u}_1 z \,\mathrm{d}\boldsymbol{s}, \tag{4.7a}$$

$$\int_{\widehat{T}} \widehat{w}_1 z \,\mathrm{d}\boldsymbol{x} = \int_{\widehat{T}} \widehat{u}_1 z \,\mathrm{d}\boldsymbol{x}, \tag{4.7b}$$

$$\int_{\widehat{T}} (\widehat{\mathrm{div}}\,\widehat{\boldsymbol{w}}) z \,\mathrm{d}\boldsymbol{x} = \int_{\widehat{T}} \widehat{\mathrm{div}}\,(\widehat{\boldsymbol{u}} - \widehat{\boldsymbol{v}}_*) z \,\mathrm{d}\boldsymbol{x} \tag{4.7c}$$

define the interpolant which, by definition, can be written as

$$(I_k^{\mathrm{BDM}} \widehat{\boldsymbol{u}})_1 = \widehat{t}_1 = \sum_{i=1}^{n} \alpha_i (\phi_i)_1,$$

where α_i are the interpolation functionals evaluated with the interpolated function, and ϕ_i are the basis functions of the Brezzi–Douglas–Marini space, see, e.g., [BS08, Section 3.3]. To estimate the norm of the interpolant we write

$$\left\| (\widehat{I}_k^{\mathrm{BDM}} \widehat{\boldsymbol{u}})_1 \right\|_{0,p,\widehat{T}} = \left\| \widehat{t}_1 \right\|_{0,p,\widehat{T}} = \left\| \sum_i \alpha_i (\phi_i)_1 \right\|_{0,p,\widehat{T}} \leq \sum_i |\alpha_i| \|(\phi_i)_1\|_{0,p,\widehat{T}} \leq \sum_i |\alpha_i|,$$

since the norms of the basis functions on the reference element are bounded by 1. From all these functionals only those from (4.7) are relevant for the interpolation. Let z_1 be the dual basis function to $(\phi_1)_1$, then we can estimate $\alpha_1 = \int_{e_1} \widehat{u}_1 z_1 \,\mathrm{d}\boldsymbol{s}$ by

$$|\alpha_1| = \left| \int_{e_1} \widehat{u}_1 z_1 \,\mathrm{d}\boldsymbol{s} \right| \leq \|\widehat{u}_1\|_{0,p,e_1} \|z_1\|_{0,q,e_1} \lesssim \|\widehat{u}_1\|_{0,p,e_1},$$

since also the norms of the dual basis functions on the reference element are bounded by a constant. Analogous estimates for the remaining α_i terms and using a trace theorem yields

$$\begin{aligned}\left\|(\widehat{I}_k^{\mathrm{BDM}}\widehat{\boldsymbol{u}})_1\right\|_{0,p,\widehat{T}} = \|\widehat{t}_1\|_{0,p,\widehat{T}} &\lesssim \|\widehat{u}_1\|_{0,p,e_1} + \|\widehat{u}_1\|_{0,p,\widehat{T}} + \left\|\widehat{\operatorname{div}}\,\widehat{\boldsymbol{u}}\right\|_{0,p,\widehat{T}} + \left\|\widehat{\operatorname{div}}\,\widehat{\boldsymbol{v}}_*\right\|_{0,p,\widehat{T}} \\ &\leq \|\widehat{u}_1\|_{1,p,\widehat{T}} + \left\|\widehat{\operatorname{div}}\,\widehat{\boldsymbol{u}}\right\|_{0,p,\widehat{T}} + \left\|\widehat{\operatorname{div}}\,\widehat{\boldsymbol{v}}_*\right\|_{0,p,\widehat{T}}. \end{aligned} \tag{4.8}$$

Estimating $\left\|\widehat{\operatorname{div}}\,\widehat{\boldsymbol{v}}_*\right\|_{0,p,\widehat{T}}$ is the last step of the proof. We choose $\widehat{\boldsymbol{v}}_0 = (0, \widehat{v}_2, \widehat{v}_3)^T$, and again using (4.6) we get, since for $z \in P_k(\widehat{T})$ it holds $\nabla z \in \boldsymbol{P}_{k-1}(\widehat{T})$,

$$\begin{aligned} 0 &= \int_{\widehat{T}} (\widehat{\boldsymbol{v}}_0 - \widehat{\boldsymbol{v}}_*) \cdot \nabla z \,\mathrm{d}\boldsymbol{x} = \int_{\partial\widehat{T}} (\widehat{\boldsymbol{v}}_0 - \widehat{\boldsymbol{v}}_*) \cdot \boldsymbol{n}_{\widehat{T}} z \,\mathrm{d}\boldsymbol{s} - \int_{\widehat{T}} \widehat{\operatorname{div}}\,(\widehat{\boldsymbol{v}}_0 - \widehat{\boldsymbol{v}}_*) z \,\mathrm{d}\boldsymbol{x} \\ &= \int_{e_4} (\widehat{\boldsymbol{v}}_0 - \widehat{\boldsymbol{v}}_*) \cdot \boldsymbol{n}_{\widehat{T},e_4} z \,\mathrm{d}\boldsymbol{s} - \int_{\widehat{T}} \widehat{\operatorname{div}}\,(\widehat{\boldsymbol{v}}_0 - \widehat{\boldsymbol{v}}_*) z \,\mathrm{d}\boldsymbol{x}. \end{aligned}$$

Setting $z = (1 - \widehat{x}_1 - \widehat{x}_2 - \widehat{x}_3) z_*$, $z_* \in P_{k-1}(\widehat{T})$, we further get

$$\int_{\widehat{T}} (1-\widehat{x}_1-\widehat{x}_2-\widehat{x}_3)(\widehat{\operatorname{div}}\,\widehat{\boldsymbol{v}}_*) z_* \,\mathrm{d}\boldsymbol{x} = \int_{\widehat{T}} (1-\widehat{x}_1-\widehat{x}_2-\widehat{x}_3)(\widehat{\operatorname{div}}\,\widehat{\boldsymbol{v}}_0) z_* \,\mathrm{d}\boldsymbol{x} \qquad \forall z_* \in P_{k-1}(\widehat{T}),$$

since $z = 0$ on e_4. Choosing $z_* = \widehat{\operatorname{div}}\,\widehat{\boldsymbol{v}}_*$, using the equivalence of norms on finite-dimensional spaces and the Hölder inequality we get

$$\begin{aligned} \left\|\widehat{\operatorname{div}}\,\widehat{\boldsymbol{v}}_*\right\|_{0,p,\widehat{T}}^2 &\lesssim \left\|\widehat{\operatorname{div}}\,\widehat{\boldsymbol{v}}_*\right\|_{0,2,\widehat{T}}^2 \lesssim \int_{\widehat{T}} (1 - \widehat{x}_1 - \widehat{x}_2 - \widehat{x}_3)(\widehat{\operatorname{div}}\,\widehat{\boldsymbol{v}}_*)^2 \\ &\lesssim \left\|\widehat{\operatorname{div}}\,\widehat{\boldsymbol{v}}_*\right\|_{0,q,\widehat{T}} \left\|\widehat{\operatorname{div}}\,\widehat{\boldsymbol{v}}_0\right\|_{0,p,\widehat{T}} \lesssim \left\|\widehat{\operatorname{div}}\,\widehat{\boldsymbol{v}}_*\right\|_{0,p,\widehat{T}} \left\|\widehat{\operatorname{div}}\,\widehat{\boldsymbol{v}}_0\right\|_{0,p,\widehat{T}} \\ &\lesssim \left\|\widehat{\operatorname{div}}\,\widehat{\boldsymbol{v}}_*\right\|_{0,p,\widehat{T}} \left(\left\|\widehat{\operatorname{div}}\,\widehat{\boldsymbol{v}}\right\|_{0,p,\widehat{T}} + \left\|\frac{\partial \widehat{v}_1}{\partial \widehat{x}_1}\right\|_{0,p,\widehat{T}} \right) \\ &= \left\|\widehat{\operatorname{div}}\,\widehat{\boldsymbol{v}}_*\right\|_{0,p,\widehat{T}} \left(\left\|\widehat{\operatorname{div}}\,\widehat{\boldsymbol{u}}\right\|_{0,p,\widehat{T}} + \left\|\frac{\partial \widehat{u}_1}{\partial \widehat{x}_1}\right\|_{0,p,\widehat{T}} \right). \end{aligned}$$

Dividing by $\left\|\widehat{\operatorname{div}}\,\widehat{\boldsymbol{v}}_*\right\|_{0,p,\widehat{T}}$ and combining this estimate with (4.8) yields the desired result. □

For the second reference element we get a similar but slightly worse estimate, since the sum of the norms of the derivatives appears on the right hand side, instead of the norm of the divergence.

Lemma 4.7. *Let $\overline{\boldsymbol{u}} \in \boldsymbol{W}^{1,p}(\overline{T})$, $1 \leq p \leq \infty$. Then the estimates*

$$\left\|(\overline{I}_k^{\mathrm{BDM}}\overline{\boldsymbol{u}})_i\right\|_{0,p,\widehat{T}} \lesssim \|\overline{u}_i\|_{1,p,\overline{T}} + \sum_{j \in_i I_d} \left\|\frac{\partial \overline{u}_j}{\partial \overline{x}_j}\right\|_{0,p,\overline{T}} \tag{4.9}$$

Proof. It is possible to show the same results as in the previous lemma for $i = 1, 3$ using the same proof, which can clearly be bounded by the right hand side of (4.9) using the triangle inequality.

The second component of the interpolant however does not satisfy the stronger estimate, so we need to alter the proof in order to arrive at (4.9). Consider the functions

$$\overline{\boldsymbol{u}}_* = \begin{pmatrix} \overline{u}_1(0,\overline{x}_2,\overline{x}_3) \\ 0 \\ \overline{u}_3(\overline{x}_1,\overline{x}_2,0) \end{pmatrix}, \qquad \overline{\boldsymbol{v}} = \overline{\boldsymbol{u}} - \overline{\boldsymbol{u}}_* = \begin{pmatrix} \overline{u}_1 - \overline{u}_1(0,\overline{x}_2,\overline{x}_3) \\ \overline{u}_2 \\ \overline{u}_3 - \overline{u}_3(\overline{x}_1,\overline{x}_2,0) \end{pmatrix},$$

then we have $\overline{\operatorname{div}}\,\overline{\boldsymbol{v}} = \overline{\operatorname{div}}\,\overline{\boldsymbol{u}}$ and by Lemma 4.5 $(\overline{I}_k^{\mathrm{BDM}}\overline{\boldsymbol{v}})_2 = (\overline{I}_k^{\mathrm{BDM}}\overline{\boldsymbol{u}})_2$. We introduce another two functions

$$\overline{\boldsymbol{v}}_* = \begin{pmatrix} \overline{x}_1\overline{q}_1 \\ 0 \\ \overline{x}_3\overline{q}_3 \end{pmatrix}, \qquad \overline{\boldsymbol{w}} = \overline{\boldsymbol{v}} - \overline{\boldsymbol{v}}_* = \begin{pmatrix} \overline{v}_1 - \overline{x}_1\overline{q}_1 \\ \overline{v}_2 \\ \overline{v}_3 - \overline{x}_3\overline{q}_3 \end{pmatrix},$$

where the polynomials $\overline{q}_j \in P_{k-1}(\overline{T})$, $j = 1, 3$, are defined by

$$\int_{\overline{T}} \overline{w}_j z \,\mathrm{d}\boldsymbol{x} = \int_{\overline{T}} (\overline{v}_j - \overline{x}_j\overline{q}_j)\,\mathrm{d}\boldsymbol{x} \qquad \forall z \in P_{k-1}(\overline{T}). \tag{4.10}$$

As for the polynomial $\overline{\boldsymbol{v}}_* \in \boldsymbol{P}_k(\overline{T})$ the equality $\overline{I}_k^{\mathrm{BDM}}\overline{\boldsymbol{v}}_* = \overline{\boldsymbol{v}}_*$ holds, we get $(\overline{I}_k^{\mathrm{BDM}}\overline{\boldsymbol{w}})_2 = (\overline{I}_k^{\mathrm{BDM}}\overline{\boldsymbol{v}})_2 = (\overline{I}_k^{\mathrm{BDM}}\overline{\boldsymbol{u}})_2$. From (4.2) by using (4.10) we get the defining relations for $\overline{I}_k^{\mathrm{BDM}}\overline{\boldsymbol{w}} = \overline{\boldsymbol{t}} = (\overline{t}_1, \overline{t}_2, \overline{t}_3)^T$:

$$\begin{aligned}
\int_{e_1} \overline{t}_1 z \,\mathrm{d}\boldsymbol{s} &= \int_{e_1} \overline{w}_1 z \,\mathrm{d}\boldsymbol{s} = 0 && \forall z \in P_k(e_1), \\
\int_{e_2} (\overline{t}_1 - \overline{t}_2) z \,\mathrm{d}\boldsymbol{s} &= \int_{e_2} (\overline{w}_1 - \overline{w}_2) z \,\mathrm{d}\boldsymbol{s} \\
&= \sqrt{2}\left(\int_{\overline{T}} \overline{w}_2 \frac{\partial z}{\partial \overline{x}_2} \,\mathrm{d}\boldsymbol{x} + \int_{\overline{T}} \overline{\operatorname{div}}\,(\overline{w}_1, \overline{w}_2, 0) \,\mathrm{d}\boldsymbol{x} \right) \\
&\quad - \int_{e_4} \overline{w}_2 z \,\mathrm{d}\boldsymbol{s} && \forall z \in P_k(e_2), \\
\int_{e_3} \overline{t}_3 z \,\mathrm{d}\boldsymbol{s} &= \int_{e_4} \overline{w}_3 z \,\mathrm{d}\boldsymbol{s} = 0 && \forall z \in P_k(e_3), \\
\int_{e_4} (\overline{t}_2 + \overline{t}_3) z \,\mathrm{d}\boldsymbol{s} &= \int_{e_1} (\overline{w}_2 + \overline{w}_3) z \,\mathrm{d}\boldsymbol{s} \\
&= \sqrt{2}\left(\int_{\overline{T}} \overline{w}_2 \frac{\partial z}{\partial \overline{x}_2} \,\mathrm{d}\boldsymbol{x} + \int_{\overline{T}} \overline{\operatorname{div}}\,(0, \overline{w}_2, \overline{w}_3) \,\mathrm{d}\boldsymbol{x} \right) \\
&\quad - \int_{e_2} \overline{w}_2 z \,\mathrm{d}\boldsymbol{s} && \forall z \in P_k(e_4),
\end{aligned}$$

and

$$\begin{aligned}
\int_{\overline{T}} \overline{t}_1 z \,\mathrm{d}\boldsymbol{x} &= \int_{\widehat{T}} \overline{w}_1 z \,\mathrm{d}\boldsymbol{x} = 0 && \forall z \in P_{k-2}(\overline{T}),\\
\int_{\overline{T}} \overline{t}_2 z \,\mathrm{d}\boldsymbol{x} &= \int_{\overline{T}} \overline{w}_2 z \,\mathrm{d}\boldsymbol{x} && \forall z \in P_{k-2}(\overline{T}),\\
\int_{\overline{T}} \overline{t}_3 z \,\mathrm{d}\boldsymbol{x} &= \int_{\overline{T}} \overline{w}_3 z \,\mathrm{d}\boldsymbol{x} && \forall z \in P_{k-2}(\overline{T}),\\
\int_{\overline{T}} \overline{\boldsymbol{t}} \cdot \boldsymbol{z} \,\mathrm{d}\boldsymbol{x} &= \int_{\overline{T}} \overline{\boldsymbol{w}} \cdot \boldsymbol{z} \,\mathrm{d}\boldsymbol{x} = \int_{\overline{T}} (\overline{w}_1 z_1 + \overline{w}_2 z_2 + \overline{w}_3 z_3) \,\mathrm{d}\boldsymbol{x} = \int_{\overline{T}} \overline{w}_2 z \,\mathrm{d}\boldsymbol{x} && \forall \boldsymbol{z} \in \boldsymbol{S}_{k-1}(\overline{T}).
\end{aligned}$$

Similar to the proof of Lemma 4.6 and using the definition of $\overline{\boldsymbol{w}}$ we can now estimate

$$\begin{aligned}
\left\| (\overline{I}_k^{\mathrm{BDM}} \overline{\boldsymbol{u}})_2 \right\|_{0,p,\overline{T}} &= \left\| \overline{t}_2 \right\|_{0,p,\overline{T}} \\
&\lesssim \left\| \overline{w}_2 \right\|_{1,p,\overline{T}} + \left\| \overline{\operatorname{div}} \,(0, \overline{w}_2, \overline{w}_3) \right\|_{0,p,\overline{T}} + \left\| \overline{\operatorname{div}} \,(\overline{w}_1, \overline{w}_2, 0) \right\|_{0,p,\overline{T}} \\
&\lesssim \left\| \overline{u}_2 \right\|_{1,p,\overline{T}} + \sum_{j \in {}_2 I_d} \left[\left\| \frac{\partial \overline{u}_j}{\partial \overline{x}_j} \right\|_{0,p,\overline{T}} + \left\| \frac{\partial (\overline{x}_j \overline{q}_j)}{\partial \overline{x}_j} \right\|_{0,p,\overline{T}} \right]. \qquad (4.11)
\end{aligned}$$

Estimating the second terms in the sum is the last step. Note that for $z \in P_k(\overline{T})$ we get

$$0 = \int_{\overline{T}} \overline{w}_3 \frac{\partial z}{\partial \overline{x}_3} \,\mathrm{d}\boldsymbol{x} = -\int_{\overline{T}} \frac{\partial \overline{w}_3}{\partial \overline{x}_3} z \,\mathrm{d}\boldsymbol{x} + \int_{\partial \overline{T}} \overline{w}_3 n_3 z \,\mathrm{d}\boldsymbol{s}.$$

By setting $z = (1 - \overline{x}_2 - \overline{x}_3) z_*$, $z_* \in P_{k-1}(\overline{T})$, the boundary term vanishes and using the definition of $\overline{w}_3$ we get

$$\int_{\overline{T}} \frac{\partial (\overline{x}_3 \overline{q}_3)}{\partial \overline{x}_3} z_* \,\mathrm{d}\boldsymbol{x} = \int_{\overline{T}} \frac{\partial \overline{u}_3}{\partial \overline{x}_3} z_* \,\mathrm{d}\boldsymbol{x},$$

from which analogous reasoning as in the proof of Lemma 4.6 yields

$$\left\| \frac{\partial (\overline{x}_3 \overline{q}_3)}{\partial \overline{x}_3} \right\|_{0,p,\overline{T}} \lesssim \left\| \frac{\partial \overline{u}_3}{\partial \overline{x}_3} \right\|_{0,p,\overline{T}}.$$

By the same steps we get

$$\left\| \frac{\partial (\overline{x}_1 \overline{q}_1)}{\partial \overline{x}_1} \right\|_{0,p,\overline{T}} \lesssim \left\| \frac{\partial \overline{u}_1}{\partial \overline{x}_1} \right\|_{0,p,\overline{T}}.$$

Combining the last two estimates with (4.11) yields the statement of the lemma. □

The next step is now to transfer the stability estimates to the reference families of elements. To do this, we need the transformations

$$\widetilde{\boldsymbol{x}} = J_{\widetilde{T}} \widehat{\boldsymbol{x}}, \qquad\qquad \widetilde{\boldsymbol{x}} = J_{\widetilde{T}} \overline{\boldsymbol{x}},$$

of the reference elements $\widehat{T}$ and $\overline{T}$ to elements of the reference families $\mathcal{R}_1$ and $\mathcal{R}_2$, respectively. The matrix is identical for both transformations and given by

$$J_{\widetilde{T}} = \begin{pmatrix} h_1 & & 0 \\ & \ddots & \\ 0 & & h_d \end{pmatrix} \in \mathbb{R}^{d\times d},$$

with h_i, $i \in I_d$, being the element size parameters of the element $\widetilde{T}$ which can be seen in Figures 4.1 and 4.2. In order to preserve the normal traces of functions under the transformations, we use the contravariant Piola transform, which means a function $\widehat{\boldsymbol{v}} \in \boldsymbol{L}^p(\widehat{T})$ gets transformed to $\widetilde{\boldsymbol{v}} \in \boldsymbol{L}^p(\widetilde{T})$ by

$$\widetilde{\boldsymbol{v}}(\widetilde{\boldsymbol{x}}) = \frac{1}{\det J_{\widetilde{T}}} J_{\widetilde{T}} \widehat{\boldsymbol{v}}(\widehat{\boldsymbol{x}}) = \begin{pmatrix} {}_1h^{-1} & & 0 \\ & \ddots & \\ 0 & & {}_dh^{-1} \end{pmatrix} \widehat{\boldsymbol{v}}(\widehat{\boldsymbol{x}}),$$

where ${}_ih = \Pi_{j\in {}_iI_d} h_j$. The definition is analogous in the case of a function $\overline{\boldsymbol{v}} \in \boldsymbol{L}^p(\overline{T})$. Using this transformation we can transfer the stability estimates from the reference elements to the reference families, see also [AK20, Lemmas 3.4, 3.8].

Lemma 4.8. *Let $\widetilde{T} = J_{\widetilde{T}}\widehat{T} + \boldsymbol{x}_0$ and $\widetilde{\boldsymbol{v}} \in \boldsymbol{W}^{1,p}(\widetilde{T})$, $1 \le p \le \infty$. Then on the transformed element $\widetilde{T}$ the estimate*

$$\left\| \widetilde{I}_k^{\mathrm{BDM}} \widetilde{\boldsymbol{v}} \right\|_{0,p,\widetilde{T}} \lesssim \sum_{|\boldsymbol{\alpha}|\le 1} h^{\boldsymbol{\alpha}} \|D^{\boldsymbol{\alpha}} \widetilde{\boldsymbol{v}}\|_{0,p,\widetilde{T}} + h_{\widetilde{T}} \left\| \widetilde{\mathrm{div}}\, \widetilde{\boldsymbol{v}} \right\|_{0,p,\widetilde{T}} \tag{4.12}$$

holds, where $h_{\widetilde{T}} = \max\{h_i : i \in I_d\}$.

Proof. The proof follows along the lines of the proof of [AADL11, Proposition 3.4]. Direct calculations yield

$$\begin{aligned} \|\widetilde{\boldsymbol{w}}\|_{0,p,\widetilde{T}} = \left(\int_{\widetilde{T}} \sum_{i\in I_d} |\widetilde{w}_i|^p \,\mathrm{d}\boldsymbol{x} \right)^{1/p} &\le (\det J_{\widetilde{T}})^{1/p} \sum_{i\in I_d} {}_ih^{-1} \left(\int_{\widehat{T}} |\widehat{w}_i|^p \,\mathrm{d}\boldsymbol{x} \right)^{1/p} \\ &= (\det J_{\widetilde{T}})^{1/p} \sum_{i\in I_d} {}_ih^{-1} \|\widehat{w}_i\|_{0,p,\widehat{T}}, \end{aligned} \tag{4.13}$$

and

$$(\det J_{\widetilde{T}})^{1/p} \|\widehat{v}_i\|_{1,p,\widehat{T}} = {}_ih \sum_{|\boldsymbol{\alpha}|\le 1} h^{\boldsymbol{\alpha}} \|D^{\boldsymbol{\alpha}} \widetilde{v}_i\|_{0,p,\widetilde{T}} \tag{4.14}$$

for $i \in I_d$. Applying (4.13) to $\widetilde{I}_k^{\mathrm{BDM}}\widetilde{\boldsymbol{v}}$ and using Lemma 4.6 and (4.14) we arrive at

$$\begin{aligned}
\left\|\widetilde{I}_k^{\mathrm{BDM}}\widetilde{\boldsymbol{v}}\right\|_{0,p,\widetilde{T}} &\leq (\det J_{\widetilde{T}})^{1/p} \sum_{i\in I_d} {}_ih^{-1} \left\|(\widehat{I}_k^{\mathrm{BDM}}\widehat{v})_i\right\|_{0,p,\widehat{T}} \\
&\lesssim (\det J_{\widetilde{T}})^{1/p} \sum_{i\in I_d} {}_ih^{-1} \left(\|\widehat{v}_i\|_{1,p,\widehat{T}} + \left\|\widehat{\operatorname{div}}\,\widehat{\boldsymbol{v}}\right\|_{0,p,\widehat{T}}\right) \\
&\lesssim \sum_{i\in I_d} {}_ih^{-1} \left({}_ih \sum_{|\boldsymbol{\alpha}|\leq 1} h^{\boldsymbol{\alpha}} \|D^{\boldsymbol{\alpha}}\widetilde{v}_i\|_{0,p,\widetilde{T}} + \det J_{\widetilde{T}} \left\|\widetilde{\operatorname{div}}\,\widetilde{\boldsymbol{v}}\right\|_{0,p,\widetilde{T}}\right) \\
&\lesssim \sum_{|\boldsymbol{\alpha}|\leq 1} h^{\boldsymbol{\alpha}} \|D^{\boldsymbol{\alpha}}\widetilde{\boldsymbol{v}}\|_{0,p,\widetilde{T}} + h_{\widetilde{T}} \left\|\widetilde{\operatorname{div}}\,\widetilde{\boldsymbol{v}}\right\|_{0,p,\widetilde{T}}.
\end{aligned}$$

□

Lemma 4.9. *Let $\widetilde{T} = J_{\widetilde{T}}\overline{T} + \boldsymbol{x}_0$ and $\widetilde{\boldsymbol{v}} \in \boldsymbol{W}^{1,p}(\widetilde{T})$, $1 \leq p \leq \infty$. Then on the transformed element $\widetilde{T}$ the estimate*

$$\left\|\widetilde{I}_k^{\mathrm{BDM}}\widetilde{\boldsymbol{v}}\right\|_{0,p,\widetilde{T}} \lesssim \sum_{|\boldsymbol{\alpha}|\leq 1} h^{\boldsymbol{\alpha}} \|D^{\boldsymbol{\alpha}}\widetilde{\boldsymbol{v}}\|_{0,p,\widetilde{T}} + \sum_{i\in I_d} h_i \left(\sum_{j\in {}_iI_d} \left\|\frac{\partial \widetilde{v}_j}{\partial \widetilde{x}_j}\right\|_{0,p,\widetilde{T}}\right) \lesssim \|\widetilde{\boldsymbol{v}}\|_{0,p,\widetilde{T}} + h_{\widetilde{T}}|\widetilde{\boldsymbol{v}}|_{1,p,\widetilde{T}}$$

holds.

Proof. The proof is entirely analogous to the proof of Lemma 4.8, but Lemma 4.7 is used instead of Lemma 4.6. □

Looking at the estimates componentwise, we see that estimates of type (4.5) and (4.12) could be obtained for the first and third component on the reference element $\overline{T}$. However for a complete better estimate all components would need to be estimated like this, and the proof fails for the second component, thus in general only Lemma 4.9 holds.

After these preparatory results on the separate reference geometries, we can finally transfer the stability results to general elements satisfying the regular vertex property and maximum angle condition, see [AK20, Theorem 3.5, 3.10].

Theorem 4.10. *Let an element T satisfy the regular vertex property RVP($\overline{c}$), let $\boldsymbol{p}_{d+1}$ be the regular vertex and let $\boldsymbol{l}_i$, h_i, $i \in I_d$ be the corresponding vectors and element size parameters from Definition 2.11. Then for $\boldsymbol{v} \in \boldsymbol{W}^{1,p}(T)$, $1 \leq p \leq \infty$, the estimate*

$$\left\|I_k^{\mathrm{BDM}}\boldsymbol{v}\right\|_{0,p,T} \lesssim \|\boldsymbol{v}\|_{0,p,T} + \sum_{j\in I_d} h_j \left\|\frac{\partial \boldsymbol{v}}{\partial \boldsymbol{l}_j}\right\|_{0,p,T} + h_T \|\operatorname{div}\boldsymbol{v}\|_{0,p,T} \tag{4.15}$$

is satisfied and the constant only depends on $\overline{c}$.

Proof. The proof follows [AADL11, Proof of Theorem 3.1]. Assume that the regular vertex $\boldsymbol{p}_{d+1}$ is located at the origin, so the transformation from the element $\widetilde{T} \in \mathcal{R}_1$ to the general element T is $\boldsymbol{x} = J_T\widetilde{\boldsymbol{x}}$ and $J_T\boldsymbol{e}_j = \boldsymbol{l}_j$, $j \in I_d$. The existence of the transformation matrix and $\|J_T\|_\infty, \left\|J_T^{-1}\right\|_\infty \leq C(\overline{c})$ is given due to Lemma 4.1.

For a function $\widetilde{\boldsymbol{v}} \in \boldsymbol{W}^{1,p}(\widetilde{T})$ let

$$\boldsymbol{v}(\boldsymbol{x}) = \frac{1}{\det J_T} J_T \widetilde{\boldsymbol{v}}(\widetilde{\boldsymbol{x}})$$

be its Piola transform. Then using Lemma 4.8 yields

$$\left\|I_k^{\mathrm{BDM}}\boldsymbol{v}\right\|_{0,p,T}^p \lesssim \frac{\|J_T\|_\infty^p}{(\det J_T)^{p-1}} \left(\|\widetilde{\boldsymbol{v}}\|_{0,p,\widetilde{T}}^p + \sum_{j\in I_d} h_j^p \left\| \frac{\partial \widetilde{\boldsymbol{v}}}{\partial \widetilde{x}_j} \right\|_{0,p,\widetilde{T}}^p + h_{\widetilde{T}}^p \left\| \widetilde{\mathrm{div}}\, \widetilde{\boldsymbol{v}} \right\|_{0,p,\widetilde{T}}^p \right).$$

Combining this with

$$\frac{\partial \widetilde{\boldsymbol{v}}}{\partial \widetilde{x}_j} = (\det J_T) J_T^{-1} \frac{\partial \boldsymbol{v}}{\partial \boldsymbol{l}_j}, \qquad \widetilde{\mathrm{div}}\, \widetilde{\boldsymbol{v}} = (\det J_T)\mathrm{div}\, \boldsymbol{v}, \qquad h_{\widetilde{T}} \le \left\|J_T^{-1}\right\|_\infty h_T,$$

we arrive at the estimate

$$\left\|I_k^{\mathrm{BDM}}\boldsymbol{v}\right\|_{0,p,T}^p \lesssim \|J_T\|_\infty^p \left\|J_T^{-1}\right\|_\infty^p \left(\|\boldsymbol{v}\|_{0,p,T}^p + \sum_{j\in I_d} h_j^p \left\| \frac{\partial \boldsymbol{v}}{\partial \boldsymbol{l}_j} \right\|_{0,p,T}^p + h_T^p \|\mathrm{div}\, \boldsymbol{v}\|_{0,p,T}^2 \right). \quad \square$$

When no regular vertex property holds, we accordingly get a weaker estimate.

Theorem 4.11. *Let an element T satisfy the maximum angle condition $MAC(\overline{\phi})$. Then for $\boldsymbol{v} \in \boldsymbol{W}^{1,p}(T)$, $1 \le p \le \infty$, the estimate*

$$\left\|I_k^{\mathrm{BDM}}\boldsymbol{v}\right\|_{0,p,T} \lesssim \|\boldsymbol{v}\|_{0,p,T} + h_T \sum_{j\in I_d} \left\| \frac{\partial \boldsymbol{v}}{\partial x_j} \right\|_{0,p,T} \tag{4.16}$$

is satisfied and the constant only depends on $\overline{\phi}$.

Proof. The proof is analogous to the proofs of [AADL11, Theorem 4.1] and [AK20, Theorem 3.10]. Let $\widetilde{T}$ be an element so that $\widetilde{T}$ is mapped to T by the affine transformation $\widetilde{\boldsymbol{x}} \mapsto J_T\widetilde{\boldsymbol{x}} + \boldsymbol{x}_0$, where $\|J_T\|_\infty, \left\|J_T^{-1}\right\|_\infty \le C(\overline{\phi})$. We can assume that $\widetilde{T} \in \mathcal{R}_2$, because the case $\widetilde{T} \in \mathcal{R}_1$ is covered in Theorem 4.10 as the element T would then satisfy the regular vertex property. In addition we set $\boldsymbol{x}_0 = \boldsymbol{0}$ to simplify notation.

The definition of the Piola transforms

$$\boldsymbol{v}(\boldsymbol{x}) = \frac{1}{\det J_T} J_T \widetilde{\boldsymbol{v}}(\widetilde{\boldsymbol{x}}), \qquad I_k^{\mathrm{BDM}}\boldsymbol{v}(\boldsymbol{x}) = \frac{1}{\det J_T} J_T \widetilde{I}_k^{\mathrm{BDM}}\widetilde{\boldsymbol{v}}(\widetilde{\boldsymbol{x}}),$$

combined with Lemma 4.9 and a change in variables gives

$$\begin{aligned} \left\|I_k^{\mathrm{BDM}}\boldsymbol{v}\right\|_{0,p,T} &\lesssim \frac{\|J_T\|_\infty}{(\det J_T)^{(p-1)/p}} \left\|\widetilde{I}_k^{\mathrm{BDM}}\widetilde{\boldsymbol{v}}\right\|_{0,p,\widetilde{T}} \\ &\lesssim \|J_T\|_\infty \left\|J_T^{-1}\right\|_\infty \left(\|\boldsymbol{v}\|_{0,p,T} + h_T \sum_{i,j\in I_d} \left\| \frac{\partial v_i}{\partial x_j} \right\|_{0,p,T} \right). \end{aligned} \quad \square$$

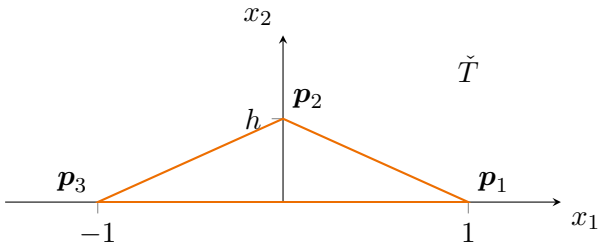

Figure 4.3: Family of triangles not satisfying a maximum angle condition for $h \to 0$.

When comparing Theorems 4.10 and 4.11, it is clear that (4.15) is a stronger estimate and implies (4.16). Another difference is the use of directional derivatives in the stronger estimate, and standard partial derivatives in the second estimate. There are different ways to properly use the anisotropy in elements to get to a finely tuned estimate. One is the shown use of element specific coordinate systems and directional derivatives, like in [AADL11; AK20], another would be using a coordinate system that is independent of the individual element and setting a condition relating the element size parameters to the position of the element in this coordinate system, see [Ape99]. For both cases care has to be taken when defining the element size parameters, and in general they are not the same for the two approaches.

To complete this subsection, we show by an example that the estimate from Theorem 4.11 requires the maximum angle condition.

Example 4.12. Consider the case $p = 2$ and the triangle $\check{T}$ from Figure 4.3. For $h \to 0$, the triangle does not satisfy a maximum angle condition with any constant $\overline{\phi}$ uniformly, as the angle at $\boldsymbol{p}_2$ gets arbitrarily close to π.

Choose the function $\boldsymbol{v} \in \boldsymbol{L}^2(\check{T})$ as $\boldsymbol{v}(\boldsymbol{x}) = (0, x_1^2)^T$. The lowest-order Brezzi–Douglas–Marini interpolant of $\boldsymbol{v}$ on $\check{T}$ can then be computed as

$$I_1^{\mathrm{BDM}}\boldsymbol{v}(\boldsymbol{x}) = \begin{pmatrix} \frac{1}{2h}x_1 \\ -\frac{1}{2h}x_2 + \frac{1}{3} \end{pmatrix},$$

from which we can directly compute

$$\begin{aligned} \left\|I_1^{\mathrm{BDM}}\boldsymbol{v}\right\|_{0,\check{T}} &= \sqrt{\frac{1}{24h} + \frac{h}{24}} &&\xrightarrow[h\to 0]{} \quad \infty, \\ \|v_2\|_{0,\check{T}} &= \sqrt{\frac{h}{15}} &&\xrightarrow[h\to 0]{} \quad 0, \\ \left\|\frac{\partial v_2}{\partial x_1}\right\|_{0,\check{T}} &= \sqrt{\frac{2h}{3}} &&\xrightarrow[h\to 0]{} \quad 0. \end{aligned}$$

This observation shows that stability estimate (4.16), which for this example can be written as

$$\left\|I_1^{\mathrm{BDM}}\boldsymbol{v}\right\|_{0,\check{T}} \lesssim \|\boldsymbol{v}\|_{0,\check{T}} + \sum_{i,j\in I_d} \left\|\frac{\partial v_i}{\partial x_j}\right\|_{0,\check{T}} = \|v_2\|_{0,\check{T}} + \left\|\frac{\partial v_2}{\partial x_1}\right\|_{0,\check{T}},$$

does not hold for $h \to 0$ when the maximum angle condition fails.

The example shows that the stability estimate does not hold without the maximum angle condition. This implies, that the type of anisotropic mesh refinement that was used in [Li18; LN18] to treat edge singularities, where the maximum angle condition is not satisfied, can in general not be used in connection with a method relying on Brezzi–Douglas–Marini interpolation. Later in our applications to incompressible flows we use meshes of tensor-product type instead, as described in Section 2.4.3.

4.2.3 Interpolation error estimates

In order to show the Brezzi–Douglas–Marini interpolation error results, we first show a Bramble–Hilbert type lemma for elements with regular vertex property. The following result can be found in [Ape99, Lemma 2.1] and is stated without proof.

Lemma 4.13. *Let $A \subset \mathbb{R}^d$ be a connected set which is star-shaped with respect to a ball $B \subset A$, let $\boldsymbol{\alpha}$ be a multi-index with $|\boldsymbol{\alpha}| \leq k$ and $v \in W^{m+1,p}(A)$, $m, k \in \mathbb{N}$, $0 \leq k \leq m+1$, $1 \leq p \leq \infty$. Then there is a polynomial $w \in P_m(A)$, so that*

$$\|D^{\boldsymbol{\alpha}}(v-w)\|_{m+1-k,p,A} \lesssim |D^{\boldsymbol{\alpha}} v|_{m+1-k,p,A} \tag{4.17}$$

holds, where the constant only depends on d, m, $\operatorname{diam} A$, $\operatorname{diam} B$ and the polynomial w only depends on m, v, B but not on $\boldsymbol{\alpha}$.

This lemma can be used on a reference element, where the dependencies of the constant are bounded. Using then the same transformations as before to get to the general element we get the final estimate. The next lemma is from [AADL11, Lemma 6.1], with an improved estimate for the divergence.

Lemma 4.14. *Let an element T satisfy the regular vertex property $RVP(\overline{c})$, with regular vertex $\boldsymbol{p}_{d+1}$ and vectors $\boldsymbol{l}_i$ and element size parameters h_i from Definition 2.11. Then for $\boldsymbol{v} \in \boldsymbol{W}^{m+1,p}(T)$, $m \geq 0$, $1 \leq p \leq \infty$, there is a polynomial $\boldsymbol{w} \in \boldsymbol{P}_m(T)$, so that the estimates*

$$\|\boldsymbol{v}-\boldsymbol{w}\|_{0,p,T} \lesssim \sum_{|\boldsymbol{\alpha}|=m+1} h^{\boldsymbol{\alpha}} \left\| \frac{\partial^{m+1}\boldsymbol{v}}{\partial \boldsymbol{l}^{\boldsymbol{\alpha}}} \right\|_{0,p,T},$$

$$\left\| \frac{\partial(\boldsymbol{v}-\boldsymbol{w})}{\partial \boldsymbol{l}_1} \right\|_{0,p,T} \lesssim \sum_{|\boldsymbol{\alpha}|=m} h^{\boldsymbol{\alpha}} \left\| \frac{\partial^{m+1}\boldsymbol{v}}{\partial \boldsymbol{l}_1^{\alpha_1+1} \partial \boldsymbol{l}_2^{\alpha_2} \cdots \partial \boldsymbol{l}_d^{\alpha_d}} \right\|_{0,p,T}$$

and analogous estimates for $\frac{\partial(\boldsymbol{v}-\boldsymbol{w})}{\partial \boldsymbol{l}_j}$, $j \in {}_1I_d$, hold. In addition, we have the estimate

$$\|\mathrm{div}\,(\boldsymbol{v}-\boldsymbol{w})\|_{0,p,T} \lesssim \sum_{|\boldsymbol{\alpha}|=m} h^{\boldsymbol{\alpha}} \|D_{\boldsymbol{l}}^{\boldsymbol{\alpha}} \mathrm{div}\,\boldsymbol{v}\|_{0,p,T},$$

where $D_{\boldsymbol{l}}^{\boldsymbol{\alpha}} = \frac{\partial^{|\boldsymbol{\alpha}|}}{\partial \boldsymbol{l}_1^{\alpha_1} \cdots \partial \boldsymbol{l}_d^{\alpha_d}}$.

Proof. We omit the proof of the second estimate, since it was detailed in the proof of [AADL11, Lemma 6.1]. The first estimate was proved in our publication as part of [AK20, Lemma 4.2], but we restate it here for completeness.

For a clearer notation we assume $\boldsymbol{p}_{d+1} = \boldsymbol{0}$. By Lemma 4.1 we know there is an element $\widetilde{T} \in \mathcal{R}_1$ and linear transformation with transformation matrix J_T, so that $T = J_T\widetilde{T}$ and $\|J_T\|_\infty, \left\|J_T^{-1}\right\|_\infty \leq C(\overline{c})$.

With $\boldsymbol{\alpha} = (0,0,0)$, $k = 0$ and (4.17) on the reference element $\widehat{T}$ we get

$$\|\widehat{v}_i - \widehat{w}_i\|_{0,p,\widehat{T}} \lesssim |\widehat{v}_i|_{m+1,p,\widehat{T}} \lesssim \sum_{|\boldsymbol{\alpha}|=m+1} \left\| \frac{\partial^{m+1}\widehat{v}_i}{\partial\widehat{x}_1^{\alpha_1}\cdots\partial\widehat{x}_d^{\alpha_d}} \right\|_{0,p,\widehat{T}} \tag{4.18}$$

for $i \in I_d$. Transforming onto the element $\widetilde{T} \in \mathcal{R}_1$ we get for $i,j \in I_d$ the functions

$$\widehat{v}_i = \det J_{\widetilde{T}} \frac{1}{h_i}\widetilde{v}_i, \qquad \widehat{w}_i = \det J_{\widetilde{T}} \frac{1}{h_i}\widetilde{w}_i, \qquad \frac{\partial\widehat{v}_i}{\partial\widehat{x}_j} = \det J_{\widetilde{T}} \frac{1}{h_i}\frac{\partial\widetilde{v}_i}{\partial\widetilde{x}_j}h_j,$$

which we can combine with (4.18) to get

$$\|\widetilde{v}_i - \widetilde{w}_i\|_{0,p,\widetilde{T}} \lesssim \sum_{|\boldsymbol{\alpha}|=m+1} h^{\boldsymbol{\alpha}} \left\| \frac{\partial^{m+1}\widetilde{v}_i}{\partial\widetilde{x}_1^{\alpha_1}\cdots\partial\widetilde{x}_d^{\alpha_d}} \right\|_{0,p,\widetilde{T}}.$$

From there we directly get

$$\|\widetilde{\boldsymbol{v}} - \widetilde{\boldsymbol{w}}\|_{0,p,\widetilde{T}} \lesssim \sum_{|\boldsymbol{\alpha}|=m+1} h^{\boldsymbol{\alpha}} \left\| \frac{\partial^{m+1}\widetilde{\boldsymbol{v}}}{\partial\widetilde{x}_1^{\alpha_1}\cdots\partial\widetilde{x}_d^{\alpha_d}} \right\|_{0,p,\widetilde{T}},$$

where $\widetilde{\boldsymbol{v}} \in \boldsymbol{W}^{m+1,p}(\widetilde{T})$, $\widetilde{\boldsymbol{w}} \in \boldsymbol{P}_m(\widetilde{T})$ are the Piola transforms of $\boldsymbol{v} \in \boldsymbol{W}^{m+1,p}(T)$, $\boldsymbol{w} \in \boldsymbol{P}_m(T)$ given by

$$\boldsymbol{v}(\boldsymbol{x}) = \frac{1}{\det J_T} J_T\widetilde{\boldsymbol{v}}(\widetilde{\boldsymbol{x}}), \qquad \boldsymbol{w}(\boldsymbol{x}) = \frac{1}{\det J_T} J_T\widetilde{\boldsymbol{w}}(\widetilde{\boldsymbol{x}}), \qquad \boldsymbol{x} = J_T\widetilde{\boldsymbol{x}}.$$

With these definitions we get the first estimate of the lemma.

For the proof of the estimate for the divergence we need the averaged Taylor polynomial of order m, which is defined for a function $f \in W^{m+1,p}(T)$ by

$$Q_m f = \frac{1}{|T|}\int_T \sum_{|\boldsymbol{\alpha}|\leq m} D^{\boldsymbol{\alpha}} f(\boldsymbol{y}) \frac{(\boldsymbol{x}-\boldsymbol{y})^{\boldsymbol{\alpha}}}{\boldsymbol{\alpha}!}\,\mathrm{d}\boldsymbol{y}.$$

For a vector function $\boldsymbol{f}$ let $\boldsymbol{Q}_m\boldsymbol{f}$ be the componentwise application of Q_m. Since by [BS08, Proposition 4.1.17] $\frac{\partial}{\partial x_i}Q_m f = Q_{m-1}\frac{\partial f}{\partial x_i}$, we get

$$\widehat{\operatorname{div}}\,\widehat{\boldsymbol{Q}}_m\widehat{\boldsymbol{v}} = \sum_{i=1}^d \frac{\partial}{\partial\widehat{x}_i}\widehat{Q}_m\widehat{v}_i = \widehat{Q}_{m-1}\sum_{i=1}^d \frac{\partial\widehat{v}_i}{\partial\widehat{x}_i} = \widehat{Q}_{m-1}\widehat{\operatorname{div}}\,\widehat{\boldsymbol{v}},$$

which used in combination with [AADL11, Equation (6.1)] on the reference element yields

$$\left\|\widehat{\mathrm{div}}\,(\widehat{\boldsymbol{v}}-\widehat{\boldsymbol{Q}}_m\widehat{\boldsymbol{v}})\right\|_{0,p,\widehat{T}}=\left\|\widehat{\mathrm{div}}\,\widehat{\boldsymbol{v}}-\widehat{Q}_{m-1}\widehat{\mathrm{div}}\,\widehat{\boldsymbol{v}}\right\|_{0,p,\widehat{T}}\lesssim\sum_{|\boldsymbol{\alpha}|=m}\left\|\frac{\partial^m(\widehat{\mathrm{div}}\,\widehat{\boldsymbol{v}})}{\partial\widehat{x}_1^{\alpha_1}\cdots\partial\widehat{x}_d^{\alpha_d}}\right\|_{0,p,\widehat{T}}.$$

Using $\widehat{\mathrm{div}}\,\widehat{\boldsymbol{v}}=\det J_{\widetilde{T}}\widetilde{\mathrm{div}}\,\widetilde{\boldsymbol{v}}$ and transforming to the element $\widetilde{T}$ we get

$$\left\|\widetilde{\mathrm{div}}\,(\widetilde{\boldsymbol{v}}-\widetilde{\boldsymbol{Q}}_m\widetilde{\boldsymbol{v}})\right\|_{0,p,\widetilde{T}}\lesssim\sum_{|\boldsymbol{\alpha}|=m}h^{\boldsymbol{\alpha}}\left\|\frac{\partial^m(\widetilde{\mathrm{div}}\,\widetilde{\boldsymbol{v}})}{\partial\widetilde{x}_1^{\alpha_1}\cdots\partial\widetilde{x}_d^{\alpha_d}}\right\|_{0,p,\widetilde{T}}.$$

Now with $\widetilde{\mathrm{div}}\,\widetilde{\boldsymbol{v}}=\det J_T\mathrm{div}\,\boldsymbol{v}$ and

$$\frac{\partial(\widetilde{\mathrm{div}}\,\widetilde{\boldsymbol{v}})}{\partial\widetilde{x}_j}=\det J_T\sum_{i\in I_d}\frac{\partial(\mathrm{div}\,\boldsymbol{v})}{\partial x_i}\frac{\partial x_i}{\partial\widetilde{x}_j}=\det J_T\frac{\partial(\mathrm{div}\,\boldsymbol{v})}{\partial\boldsymbol{l}_j}$$

we get

$$\|\mathrm{div}\,(\boldsymbol{v}-\boldsymbol{w})\|_{0,p,T}\lesssim\sum_{|\boldsymbol{\alpha}|=m}h^{\boldsymbol{\alpha}}\left\|\frac{\partial^m(\mathrm{div}\,\boldsymbol{v})}{\partial\boldsymbol{l}_1^{\alpha_1}\cdots\partial\boldsymbol{l}_d^{\alpha_d}}\right\|_{0,p,T}$$

where $\boldsymbol{w}\in\boldsymbol{P}_m(T)$. □

Now we are able to get to the interpolation error estimates. They were shown for the Hilbert-space case in [AK20, Theorems 4.3, 4.4].

Theorem 4.15. *Let an element T satisfy the regular vertex property RVP($\overline{c}$) with regular vertex $\boldsymbol{p}_{d+1}$, vectors $\boldsymbol{l}_i$ and element size parameters as in Definition 2.11. Then for $k\geq 1$, $0\leq m\leq k$ and $\boldsymbol{v}\in\boldsymbol{W}^{m+1,p}(T)$, $1\leq p\leq\infty$, the estimate*

$$\left\|\boldsymbol{v}-I_k^{\mathrm{BDM}}\boldsymbol{v}\right\|_{0,p,T}\lesssim\sum_{|\boldsymbol{\alpha}|=m+1}h^{\boldsymbol{\alpha}}\|D_{\boldsymbol{l}}^{\boldsymbol{\alpha}}\boldsymbol{v}\|_{0,p,T}+h_T\sum_{|\boldsymbol{\alpha}|=m}h^{\boldsymbol{\alpha}}\|D_{\boldsymbol{l}}^{\boldsymbol{\alpha}}\mathrm{div}\,\boldsymbol{v}\|_{0,p,T}\tag{4.19}$$

holds and the constant only depends on $\overline{c}$ and k.

Proof. Since the Brezzi–Douglas–Marini interpolation operator of order k is the identity operator for polynomials of order $m\leq k$ on an element T, we have

$$\boldsymbol{v}-I_k^{\mathrm{BDM}}\boldsymbol{v}=\boldsymbol{v}-\boldsymbol{w}-I_k^{\mathrm{BDM}}(\boldsymbol{v}-\boldsymbol{w})\tag{4.20}$$

for an arbitrary function $\boldsymbol{w}\in\boldsymbol{P}_m(T)$. With the triangle inequality, Theorem 4.10 and choosing the function $\boldsymbol{w}$ as in Lemma 4.14 we get

$$\begin{aligned}\left\|\boldsymbol{v}-I_k^{\mathrm{BDM}}\boldsymbol{v}\right\|_{0,p,T}&\leq\|\boldsymbol{v}-\boldsymbol{w}\|_{0,p,T}+\left\|I_k^{\mathrm{BDM}}(\boldsymbol{v}-\boldsymbol{w})\right\|_{0,p,T}\\&\lesssim\|\boldsymbol{v}-\boldsymbol{w}\|_{0,p,T}+\sum_{i,j\in I_d}h_j\left\|\frac{\partial(v_i-w_i)}{\partial\boldsymbol{l}_j}\right\|_{0,p,T}+h_T\|\mathrm{div}\,(\boldsymbol{v}-\boldsymbol{w})\|_{0,p,T}\\&\lesssim\sum_{|\boldsymbol{\alpha}|=m+1}h^{\boldsymbol{\alpha}}\|D_{\boldsymbol{l}}^{\boldsymbol{\alpha}}\boldsymbol{v}\|_{0,p,T}+h_T\sum_{|\boldsymbol{\alpha}|=m}h^{\boldsymbol{\alpha}}\|D_{\boldsymbol{l}}^{\boldsymbol{\alpha}}\mathrm{div}\,\boldsymbol{v}\|_{0,p,T}.\end{aligned}$$ □

Theorem 4.16. *Let an element T satisfy the maximum angle condition $MAC(\overline{\phi})$. Then for $k \geq 1$, $0 \leq m \leq k$ and $\boldsymbol{v} \in \boldsymbol{W}^{m+1,p}(T)$, $1 \leq p \leq \infty$, the estimate*

$$\left\|\boldsymbol{v} - I_k^{\mathrm{BDM}}\boldsymbol{v}\right\|_{0,p,T} \lesssim h_T^{m+1}\left\|D^{m+1}\boldsymbol{v}\right\|_{0,p,T} \tag{4.21}$$

holds and the constant only depends on $\overline{\phi}$ and k.

Proof. The proof is similar to that of Theorem 4.15 where we now use the stability estimate from Theorem 4.11. □

Example 4.17. The estimate (4.19) does not hold for elements which do not satisfy the regular vertex property. To see this, choose $p = 2$ and consider the function $\boldsymbol{v}(\boldsymbol{x}) = (-x_1x_2, 0, x_2x_3)^T$ on a tetrahedron $\widetilde{T}$ of the reference family $\mathcal{R}_2$, see Figure 4.2. The lowest order Brezzi–Douglas–Marini interpolation of $\boldsymbol{v}$ on such a tetrahedron is

$$(I_1^{\mathrm{BDM}}\boldsymbol{v})(\boldsymbol{x}) = h_2\begin{pmatrix} -\frac{3}{5}x_1 \\ -\frac{h_2}{10} + \frac{1}{5}x_2 \\ \frac{2}{5}x_3 \end{pmatrix},$$

which can easily be checked by inserting the two functions into (4.2a). Similarly, we can directly compute the norms and show

$$\begin{aligned}
&\left\|\boldsymbol{v} - I_1^{\mathrm{BDM}}\boldsymbol{v}\right\|_{0,\widetilde{T}} \lesssim \sum_{|\boldsymbol{\alpha}|=1} h^{\boldsymbol{\alpha}}\|D^{\boldsymbol{\alpha}}\boldsymbol{v}\|_{0,\widetilde{T}} + h_T\|\operatorname{div}\boldsymbol{v}\|_{0,\widetilde{T}} \\
\Leftrightarrow\quad &\left(\sum_{i=1}^{3}\left\|v_i - (I_1^{\mathrm{BDM}}\boldsymbol{v})_i\right\|_{0,\widetilde{T}}^2\right)^{1/2} \lesssim \sum_{i=1}^{3} h_i\left(\left\|\frac{\partial v_1}{\partial x_i}\right\|_{0,\widetilde{T}}^2 + \left\|\frac{\partial v_3}{\partial x_i}\right\|_{0,\widetilde{T}}^2\right)^{1/2} \\
\Leftrightarrow\quad &\left(\frac{38h_1^2 + 21h_2^2 + 38h_3^2}{3150}\right)^{1/2} \lesssim h_1 + h_3 + \left(\frac{h_1^2 + h_3^2}{3}\right)^{1/2} \\
\Leftrightarrow\quad &21h_2^2 \lesssim 4162(h_1^2 + h_3^2) + 6300\left(h_1h_3 + \left(\frac{h_1^4 + h_1^2h_3^2}{3}\right)^{1/2} + \left(\frac{h_1^2h_3^2 + h_3^4}{3}\right)^{1/2}\right).
\end{aligned}$$

This means that for a sufficiently stretched element with no regular vertex, i.e., $h_2 \gg h_1, h_3$, the interpolation error estimate does not hold.

4.3 Raviart–Thomas interpolation

The results for the Raviart–Thomas interpolation are largely analogous to those in Section 4.2 and were published in [AADL11], which was the main reference for our analysis of the Brezzi–Douglas–Marini interpolation in [AK20] and the previous section. Since the proofs are largely similar, we state most results in this section without proofs and only delve deeper if there are diverging points.

4.3.1 Interpolation operator

The Raviart–Thomas finite element was introduced in [RT77] for triangles, and generalized in [Néd80] to several three-dimensional geometries. The Raviart–Thomas functions of order k on an element are a subset of $\boldsymbol{P}_{k+1}(T)$, and as such a subset of the Brezzi–Douglas–Marini functions of order $k+1$, however the restriction of a Raviart–Thomas function of order k to the element facets is a polynomial of order k. Using the space $\mathrm{BDM}_{k+1}(\mathcal{T}_h)$, we can define the Raviart–Thomas function space of order k, $k \geq 0$, on a mesh.

Definition 4.18. The space defined by

$$\mathrm{RT}_k(\mathcal{T}_h) = \{\boldsymbol{v} \in \mathrm{BDM}_{k+1}(\mathcal{T}_h) : \boldsymbol{v}|_T \in \boldsymbol{P}_k(T) \oplus \boldsymbol{x}P_k(T)\ \forall T \in \mathcal{T}_h\}.$$

is called *Raviart–Thomas function space of order k* on the mesh $\mathcal{T}_h$.

By this definition, $\mathrm{RT}_k(\mathcal{T}_h)$ is $\boldsymbol{H}(\mathrm{div},\Omega)$-conforming and thus the functions have continuous normal components at element interfaces. Consequently, the facet degrees of freedom of the interpolation operator look similar to the Brezzi–Douglas–Marini variant, only with polynomials of one degree less. In detail, the Raviart–Thomas interpolation operator of order $k \geq 0$ is defined by, see also [BF91; Néd80],

$$\int_{e_i} (I_k^{\mathrm{RT}}\boldsymbol{v}) \cdot \boldsymbol{n}_{T,e_i} z \,\mathrm{d}\boldsymbol{s} = \int_{e_i} \boldsymbol{v} \cdot \boldsymbol{n}_{T,e_i} z \,\mathrm{d}\boldsymbol{s} \qquad \forall z \in P_{k-1}(e_i), \quad i \in I_{d+1}, \tag{4.22a}$$

$$\int_T (I_k^{\mathrm{RT}}\boldsymbol{v}) \cdot \boldsymbol{z} \,\mathrm{d}\boldsymbol{x} = \int_T \boldsymbol{v} \cdot \boldsymbol{z} \,\mathrm{d}\boldsymbol{x} \qquad \forall \boldsymbol{z} \in \boldsymbol{P}_{k-2}(T) \text{ if } k \geq 2. \tag{4.22b}$$

4.3.2 Interpolation error estimates

In order to keep this section brief and to the point, we skip the technical lemmas and stability estimates on the reference element and directly state the stability estimates on the general element, see [AADL11, Theorems 3.1, 4.1].

Theorem 4.19. *Let an element T satisfy the regular vertex property RVP($\overline{c}$) with regular vertex $\boldsymbol{p}_{d+1}$, vectors $\boldsymbol{l}_i$ and element size parameters as in Definition 2.11. Then for $\boldsymbol{v} \in \boldsymbol{W}^{1,p}(T)$, $1 \leq p \leq \infty$, the estimate*

$$\left\|I_k^{\mathrm{RT}}\boldsymbol{v}\right\|_{0,p,T} \lesssim \|\boldsymbol{v}\|_{0,p,T} + \sum_{j\in I_d} h_j \left\|\frac{\partial \boldsymbol{v}}{\partial \boldsymbol{l}_j}\right\|_{0,p,T} + h_T \|\mathrm{div}\,\boldsymbol{v}\|_{0,p,T}$$

is satisfied and the constant only depends on $\overline{c}$.

Theorem 4.20. *Let an element T satisfy the maximum angle condition MAC($\overline{\phi}$). Then for $\boldsymbol{v} \in \boldsymbol{W}^{1,p}(T)$, $1 \leq p \leq \infty$, the estimate*

$$\left\|I_k^{\mathrm{RT}}\boldsymbol{v}\right\|_{0,p,T} \lesssim \|\boldsymbol{v}\|_{0,p,T} + h_T \sum_{j\in I_d} \left\|\frac{\partial \boldsymbol{v}}{\partial x_j}\right\|_{0,p,T}$$

is satisfied and the constant only depends on $\overline{\phi}$.

The proofs for these theorems use the same steps as the proofs in the previous section for the Brezzi–Douglas–Marini elements. With these stability estimates and again using Lemma 4.14, we can show the following interpolation error results, see [AADL11, Theorems 6.2, 6.3].

Theorem 4.21. *Let an element T satisfy the regular vertex property RVP($\overline{c}$) with regular vertex $\boldsymbol{p}_{d+1}$, vectors $\boldsymbol{l}_i$ and element size parameters as in Definition 2.11. Then for $k \geq 0$, $0 \leq m \leq k$ and $\boldsymbol{v} \in \boldsymbol{W}^{m+1,p}(T)$, $1 \leq p \leq \infty$, the estimate*

$$\left\|\boldsymbol{v} - I_k^{\mathrm{RT}}\boldsymbol{v}\right\|_{0,p,T} \lesssim \sum_{|\boldsymbol{\alpha}|=m+1} h^{\boldsymbol{\alpha}} \|D_{\boldsymbol{l}}^{\boldsymbol{\alpha}}\boldsymbol{v}\|_{0,p,T} + h_T^{m+1}\|D^m \operatorname{div} \boldsymbol{v}\|_{0,p,T} \tag{4.23}$$

holds and the constant only depends on $\overline{c}$ and k.

Theorem 4.22. *Let an element T satisfy the maximum angle condition MAC($\overline{\phi}$). Then for $k \geq 0$, $0 \leq m \leq k$ and $\boldsymbol{v} \in \boldsymbol{W}^{m+1,p}(T)$, $1 \leq p \leq \infty$, the estimate*

$$\left\|\boldsymbol{v} - I_k^{\mathrm{RT}}\boldsymbol{v}\right\|_{0,p,T} \lesssim h_T^{m+1}\left\|D^{m+1}\boldsymbol{v}\right\|_{0,p,T} \tag{4.24}$$

holds and the constant only depends on $\overline{\phi}$ and k.

The error estimates are almost identical to those of the Brezzi–Douglas–Marini interpolation, with one significant difference that in essence stems from the worse interpolation property of the Raviart–Thomas interpolation operator. For a given value of k, the operators I_k^{BDM} and I_k^{RT} act as the identity on polynomials up to degree k, however the space $\mathrm{RT}_k(\mathcal{T}_h)$ contains some polynomials of degree $k+1$ and is thus larger than $\mathrm{BDM}_k(\mathcal{T}_h)$. This means that the Raviart–Thomas interpolation requires a larger function space to achieve the same approximation quality as the Brezzi–Douglas–Marini interpolation.

4.4 Alternative proof for lowest-order interpolation

Without using the technical Lemmas 4.3 and 4.5 for the proof as in the previous two sections, it is possible to show the error estimates for the lowest-order case, i.e. $k = 1$ for the Brezzi–Douglas–Marini and $k = 0$ for the Raviart–Thomas interpolation, by a more direct method. This less abstract proof uses mostly straightforward computations to show the stability estimates on the reference element and thus gives some insight in the structure of the lowest-order Raviart–Thomas and Brezzi–Douglas–Marini interpolation, which is the case we need for the construction of the pressure-robust methods later on. Since this proof differs from the previous one only in the way the stability estimates on the reference elements are derived, we only detail it up to this point.

In the lowest-order case, only the relations (4.2a), respectively (4.22a), matter for the interpolation operators I_1^{BDM}, respectively I_0^{RT}. By using the barycentric coordinates λ_i, $i \in I_{d+1}$, we can get the representations

$$I_1^{\mathrm{BDM}}\boldsymbol{v} = \sum_{i\in I_{d+1}} \begin{pmatrix} a_i\lambda_i(\boldsymbol{x}) \\ b_i\lambda_i(\boldsymbol{x}) \end{pmatrix} \qquad \text{and} \qquad I_1^{\mathrm{BDM}}\boldsymbol{v} = \sum_{i\in I_{d+1}} \begin{pmatrix} a_i\lambda_i(\boldsymbol{x}) \\ b_i\lambda_i(\boldsymbol{x}) \\ c_i\lambda_i(\boldsymbol{x}) \end{pmatrix} \tag{4.25}$$

for the Brezzi–Douglas–Marini interpolant in two and three dimensions, where $a_i, b_i, c_i \in \mathbb{R}$ are constants which are to be determined. The Raviart–Thomas interpolant takes the form

$$I_0^{\mathrm{RT}}\boldsymbol{v}(\boldsymbol{x}) = \boldsymbol{s} + t\boldsymbol{x}, \tag{4.26}$$

where $\boldsymbol{s} \in \mathbb{R}^d$ and $t \in \mathbb{R}$.

Denote by $\varphi_{i,j}$, $i \in I_{d+1}$, $j \in {}_iI_{d+1}$, the linear basis function of facet e_i with $\varphi_{i,j}(p_j) = 1$ and zero at the other vertices, and by $\psi_{i,j}$ the biorthogonal system, i.e., those linear functions on e_i, for which

$$\int_{e_i} \varphi_{i,j}\psi_{i,k}\,\mathrm{d}\boldsymbol{s} = \delta_{jk} \qquad \forall k \in {}_iI_{d+1}$$

holds, where δ_{jk} is the Kronecker delta. Then starting from (4.2a) we calculate on the reference element $\widehat{T}$

$$\begin{aligned}\int_{e_i} \widehat{\boldsymbol{v}} \cdot \boldsymbol{n}_{\widehat{T},e_i}\psi_{i,j}\,\mathrm{d}\boldsymbol{s} &= \int_{e_i} (\widehat{I}_1^{\mathrm{BDM}}\widehat{\boldsymbol{v}}) \cdot \boldsymbol{n}_{\widehat{T},e_i}\psi_{i,j}\,\mathrm{d}\boldsymbol{s} \\ &= \int_{e_i} \sum_{k\in {}_iI_{d+1}} \begin{pmatrix} a_k \\ b_k \end{pmatrix} \cdot \boldsymbol{n}_{\widehat{T},e_i}\varphi_{i,k}\psi_{i,j}\,\mathrm{d}\boldsymbol{s} = \begin{pmatrix} a_j \\ b_j \end{pmatrix} \cdot \boldsymbol{n}_{\widehat{T},e_i},\end{aligned}$$

since $\lambda_k|_{e_i} = \varphi_{i,k}$. In three dimensions this calculation is valid analogously, so we have the relations

$$\begin{pmatrix} a_j \\ b_j \end{pmatrix} \cdot \boldsymbol{n}_{\widehat{T},e_i} = \int_{e_i} \widehat{\boldsymbol{v}} \cdot \boldsymbol{n}_{\widehat{T},e_i}\psi_{i,j}\,\mathrm{d}\boldsymbol{s} \qquad \text{resp.} \qquad \begin{pmatrix} a_j \\ b_j \\ c_j \end{pmatrix} \cdot \boldsymbol{n}_{\widehat{T},e_i} = \int_{e_i} \widehat{\boldsymbol{v}} \cdot \boldsymbol{n}_{\widehat{T},e_i}\psi_{i,j}\,\mathrm{d}\boldsymbol{s}$$

for $i \in I_{d+1}$, $j \in {}_iI_{d+1}$, which are $d+1$ systems of d equations for the unknown coefficients. Solving them, we get the expressions

$$\begin{aligned} a_1 &= \int_{e_{d+1}} \sum_{i\in I_d} \widehat{v}_i\psi_{d+1,1}\,\mathrm{d}\boldsymbol{s} - \sum_{i\in {}_1I_d} \int_{e_i} \widehat{v}_i\psi_{i,1}\,\mathrm{d}\boldsymbol{s} \\ &= \int_{e_{d+1}} \widehat{v}_1\psi_{d+1,1}\,\mathrm{d}\boldsymbol{s} + \sum_{i\in {}_1I_d} \left(\int_{e_{d+1}} \widehat{v}_i\psi_{d+1,1}\,\mathrm{d}\boldsymbol{s} - \int_{e_i} \widehat{v}_i\psi_{i,1}\,\mathrm{d}\boldsymbol{s} \right), \qquad (4.27) \\ b_2 &= \int_{e_{d+1}} \sum_{i\in I_d} \widehat{v}_i\psi_{d+1,2}\,\mathrm{d}\boldsymbol{s} - \sum_{i\in {}_2I_d} \int_{e_i} \widehat{v}_i\psi_{i,2}\,\mathrm{d}\boldsymbol{s}, \\ c_3 &= \int_{e_{d+1}} \sum_{i\in I_d} \widehat{v}_i\psi_{d+1,3}\,\mathrm{d}\boldsymbol{s} - \sum_{i\in {}_3I_d} \int_{e_i} \widehat{v}_i\psi_{i,3}\,\mathrm{d}\boldsymbol{s}, \end{aligned}$$

and

$$\begin{aligned} a_i &= \int_{e_1} \widehat{v}_1 \psi_{1,i} \,\mathrm{d}\boldsymbol{s}, \quad i \in {}_1I_{d+1}, \\ b_i &= \int_{e_2} \widehat{v}_2 \psi_{2,i} \,\mathrm{d}\boldsymbol{s}, \quad i \in {}_2I_{d+1}, \\ c_i &= \int_{e_3} \widehat{v}_3 \psi_{3,i} \,\mathrm{d}\boldsymbol{s}, \quad i \in {}_3I_{d+1}. \end{aligned} \tag{4.28}$$

For the Raviart–Thomas interpolation we get by similar operations the relations

$$\int_{e_i} \widehat{\boldsymbol{v}} \cdot \boldsymbol{n}_{\widehat{T},e_i} \,\mathrm{d}\boldsymbol{s} = \boldsymbol{s} \cdot \boldsymbol{n}_{\widehat{T},e_i} |e_i| + t \sum_{j \in I_d} (\boldsymbol{n}_{\widehat{T},e_i})_j \int_{e_i} \widehat{x}_j \,\mathrm{d}\boldsymbol{s} \qquad \forall i \in I_{d+1},$$

and thus get the terms

$$s_i = 2 \int_{e_i} \widehat{v}_i \,\mathrm{d}\boldsymbol{s}, \qquad i \in I_d, \tag{4.29}$$

$$t = 2 \sum_{j \in I_d} \left(\int_{e_{d+1}} \widehat{v}_j \,\mathrm{d}\boldsymbol{s} - \sqrt{3} \int_{e_j} \widehat{v}_j \,\mathrm{d}\boldsymbol{s} \right), \tag{4.30}$$

for the constants in (4.26). Now we can prove the stability estimate for the reference element $\widehat{T}$ for the lowest-order case. Note that this case is of course included in Lemma 4.6 and the analogous lemma for the Raviart–Thomas interpolation.

Lemma 4.23. *Let $\widehat{\boldsymbol{v}} \in \boldsymbol{W}^{1,p}(\widehat{T})$, $1 \le p \le \infty$. Then for $i \in I_d$, the estimate*

$$\left\| (\widehat{I}_h^{\boldsymbol{H}(\mathrm{div})} \widehat{\boldsymbol{v}})_i \right\|_{0,p,\widehat{T}} \lesssim \|\widehat{v}_i\|_{1,p,\widehat{T}} + \left\| \widehat{\operatorname{div}}\, \widehat{\boldsymbol{v}} \right\|_{0,p,\widehat{T}} \tag{4.31}$$

holds, where $\widehat{I}_h^{\boldsymbol{H}(\mathrm{div})}$ is either $\widehat{I}_1^{\mathrm{BDM}}$ or $\widehat{I}_0^{\mathrm{RT}}$.

Proof. We detail the proof for $i = 1$ and $d = 3$, the other estimates follow analogously. From (4.25), (4.27), (4.28) we deduce

$$\begin{aligned} \left\| (\widehat{I}_1^{\mathrm{BDM}} \widehat{\boldsymbol{v}})_1 \right\|_{0,p,\widehat{T}}^p &\lesssim \left(\sum_{j \in I_{d+1}} \|a_j \lambda_j\|_{0,p,\widehat{T}} \right)^p \lesssim \sum_{j \in I_{d+1}} |a_j|^p \\ &\lesssim \left| \int_{e_{d+1}} \widehat{v}_1 \psi_{d+1,1} \,\mathrm{d}\boldsymbol{s} \right|^p + \sum_{j \in {}_1I_{d+1}} \left| \int_{e_1} \widehat{v}_1 \psi_{1,j} \,\mathrm{d}\boldsymbol{s} \right|^p \\ &\quad + \left| \sum_{j \in {}_1I_d} \left(\int_{e_{d+1}} \widehat{v}_j \psi_{d+1,1} \,\mathrm{d}\boldsymbol{s} - \int_{e_j} \widehat{v}_j \psi_{j,1} \,\mathrm{d}\boldsymbol{s} \right) \right|^p, \end{aligned} \tag{4.32}$$

and from (4.26), (4.29), (4.30) we get

$$\begin{aligned}\left\|(\widehat{I}_0^{\mathrm{RT}}\widehat{\boldsymbol{v}})_1\right\|_{0,p,\widehat{T}}^p &\lesssim |s_1|^p + |t|^p \\ &\lesssim \left|\int_{e_1}\widehat{v}_1\,\mathrm{d}\boldsymbol{s}\right|^p + \left|\int_{e_{d+1}}\widehat{v}_1\,\mathrm{d}\boldsymbol{s}\right|^p \\ &\quad + \left|\sum_{j\in{}_1I_d}\left(\int_{e_{d+1}}\widehat{v}_j\,\mathrm{d}\boldsymbol{s} - \sqrt{3}\int_{e_j}\widehat{v}_j\,\mathrm{d}\boldsymbol{s}\right)\right|^p. \end{aligned} \tag{4.33}$$

The first terms in both inequalities can be estimated using the Hölder inequality and a trace inequality, i.e.,

$$\left|\int_{e_{d+1}}\widehat{v}_1\psi_{d+1,1}\,\mathrm{d}\boldsymbol{s}\right|^p + \sum_{j\in{}_1I_{d+1}}\left|\int_{e_1}\widehat{v}_1\psi_{1,j}\,\mathrm{d}\boldsymbol{s}\right|^p \lesssim \|\widehat{v}_1\|_{0,p,\partial\widehat{T}}^p \lesssim \|\widehat{v}_1\|_{1,p,\widehat{T}}^p, \tag{4.34}$$

$$\left|\int_{e_1}\widehat{v}_1\,\mathrm{d}\boldsymbol{s}\right|^p + \left|\int_{e_{d+1}}\widehat{v}_1\,\mathrm{d}\boldsymbol{s}\right|^p \lesssim \|\widehat{v}_1\|_{0,p,\partial\widehat{T}}^p \lesssim \|\widehat{v}_1\|_{1,p,\widehat{T}}^p, \tag{4.35}$$

while for the other terms we need a closer look.

We start again with the Brezzi–Douglas–Marini interpolation. With the explicit terms

$$\begin{aligned}\psi_{4,1}(\widehat{x}_1, 1-\widehat{x_1}-\widehat{x}_3, \widehat{x}_3) &= \frac{24}{\sqrt{3}}\left(\widehat{x}_1 - \frac{1}{4}\right), \quad \psi_{2,1}(\widehat{x}_1, 0, \widehat{x}_3) = 24\left(\widehat{x}_1 - \frac{1}{4}\right), \\ \psi_{4,1}(\widehat{x}_1, \widehat{x}_2, 1-\widehat{x_1}-\widehat{x}_2) &= \frac{24}{\sqrt{3}}\left(\widehat{x}_1 - \frac{1}{4}\right), \quad \psi_{3,1}(\widehat{x}_1, \widehat{x}_2, 0) = 24\left(\widehat{x}_1 - \frac{1}{4}\right),\end{aligned}$$

of the dual basis functions $\psi_{i,j}$ in (4.32) and the Hölder inequality we calculate

$$\begin{aligned}&\left|\int_{e_4}\widehat{v}_2\psi_{4,1}\,\mathrm{d}\boldsymbol{s} - \int_{e_2}\widehat{v}_2\psi_{2,1}\,\mathrm{d}\boldsymbol{s} + \int_{e_4}\widehat{v}_3\psi_{4,1}\,\mathrm{d}\boldsymbol{s} - \int_{e_3}\widehat{v}_3\psi_{3,1}\,\mathrm{d}\boldsymbol{s}\right| \\ &\quad= \left|\int_0^1\int_0^{1-\widehat{x}_1}\widehat{v}_2(\widehat{x}_1, 1-\widehat{x_1}-\widehat{x}_3, \widehat{x}_3)\frac{24}{\sqrt{3}}\left(\widehat{x}_1 - \frac{1}{4}\right)\sqrt{3}\,\mathrm{d}\widehat{x}_3\,\mathrm{d}\widehat{x}_1\right. \\ &\qquad\qquad - \int_0^1\int_0^{1-\widehat{x}_1}\widehat{v}_2(\widehat{x}_1, 0, \widehat{x}_3)24\left(\widehat{x}_1 - \frac{1}{4}\right)\mathrm{d}\widehat{x}_3\,\mathrm{d}\widehat{x}_1 \\ &\qquad + \int_0^1\int_0^{1-\widehat{x}_1}\widehat{v}_3(\widehat{x}_1, \widehat{x}_2, 1-\widehat{x}_1-\widehat{x}_2)\frac{24}{\sqrt{3}}\left(\widehat{x}_1 - \frac{1}{4}\right)\sqrt{3}\,\mathrm{d}\widehat{x}_2\,\mathrm{d}\widehat{x}_1 \\ &\qquad\qquad\left. - \int_0^1\int_0^{1-\widehat{x}_1}\widehat{v}_3(\widehat{x}_1, \widehat{x}_2, 0)24\left(\widehat{x}_1 - \frac{1}{4}\right)\mathrm{d}\widehat{x}_2\,\mathrm{d}\widehat{x}_1\right| \\ &\quad= \left|24\int_0^1\int_0^{1-\widehat{x}_1}\int_0^{1-\widehat{x}_1-\widehat{x}_3}\frac{\partial\widehat{v}_2}{\partial\widehat{x}_2}\left(\widehat{x}_1 - \frac{1}{4}\right)\mathrm{d}\widehat{x}_2\,\mathrm{d}\widehat{x}_3\,\mathrm{d}\widehat{x}_1\right.\end{aligned}$$

$$
\begin{aligned}
&\quad +24\int_0^1\int_0^{1-\widehat{x}_1}\int_0^{1-\widehat{x}_1-\widehat{x}_2}\frac{\partial\widehat{v}_3}{\partial\widehat{x}_3}\left(\widehat{x}_1-\frac{1}{4}\right)\mathrm{d}\widehat{x}_3\,\mathrm{d}\widehat{x}_2\,\mathrm{d}\widehat{x}_1\Bigg| \\
&= \left|24\int_{\widehat{T}}\left(\frac{\partial\widehat{v}_2}{\partial\widehat{x}_2}+\frac{\partial\widehat{v}_3}{\partial\widehat{x}_3}\right)\left(\widehat{x}_1-\frac{1}{4}\right)\mathrm{d}\widehat{\boldsymbol{x}}\right| \\
&\lesssim \left\|\frac{\partial\widehat{v}_2}{\partial\widehat{x}_2}+\frac{\partial\widehat{v}_3}{\partial\widehat{x}_3}\right\|_{0,p,\widehat{T}}. \qquad (4.36)
\end{aligned}
$$

For the Raviart–Thomas interpolation a similar computation yields

$$
\begin{aligned}
&\left|\int_{e_4}\widehat{v}_2\,\mathrm{d}\boldsymbol{s}-\sqrt{3}\int_{e_2}\widehat{v}_2\,\mathrm{d}\boldsymbol{s}+\int_{e_4}\widehat{v}_3\,\mathrm{d}\boldsymbol{s}-\sqrt{3}\int_{e_3}\widehat{v}_3\,\mathrm{d}\boldsymbol{s}\right| \\
&= \Bigg|\int_0^1\int_0^{1-\widehat{x}_1}\widehat{v}_2(\widehat{x}_1,1-\widehat{x_1}-\widehat{x}_3,\widehat{x}_3)\sqrt{3}\,\mathrm{d}\widehat{x}_3\,\mathrm{d}\widehat{x}_1-\sqrt{3}\int_0^1\int_0^{1-\widehat{x}_1}\widehat{v}_2(\widehat{x}_1,0,\widehat{x}_3)\,\mathrm{d}\widehat{x}_3\,\mathrm{d}\widehat{x}_1 \\
&\quad +\int_0^1\int_0^{1-\widehat{x}_1}\widehat{v}_3(\widehat{x}_1,\widehat{x}_2,1-\widehat{x}_1-\widehat{x}_2)\sqrt{3}\,\mathrm{d}\widehat{x}_2\,\mathrm{d}\widehat{x}_1-\sqrt{3}\int_0^1\int_0^{1-\widehat{x}_1}\widehat{v}_3(\widehat{x}_1,\widehat{x}_2,0)\,\mathrm{d}\widehat{x}_2\,\mathrm{d}\widehat{x}_1\Bigg| \\
&= \left|\int_{\widehat{T}}\left(\frac{\partial\widehat{v}_2}{\partial\widehat{x}_2}+\frac{\partial\widehat{v}_3}{\partial\widehat{x}_3}\right)\mathrm{d}\widehat{\boldsymbol{x}}\right| \lesssim \left\|\frac{\partial\widehat{v}_2}{\partial\widehat{x}_2}+\frac{\partial\widehat{v}_3}{\partial\widehat{x}_3}\right\|_{0,p,\widehat{T}} \qquad (4.37)
\end{aligned}
$$

Now combining (4.32), (4.34), (4.36) and respectively (4.33), (4.35), (4.37) and using

$$
\left\|\frac{\partial\widehat{v}_2}{\partial\widehat{x}_2}+\frac{\partial\widehat{v}_3}{\partial\widehat{x}_3}\right\|_{0,p,\widehat{T}}\le\left\|\widehat{\operatorname{div}}\,\widehat{\boldsymbol{v}}\right\|_{0,p,\widehat{T}}+\left\|\frac{\partial\widehat{v}_1}{\partial\widehat{x}_1}\right\|_{0,p,\widehat{T}}
$$

gives the desired estimate for both operators. □

From here, the interpolation error estimates can be shown as before.

4.5 Brezzi–Douglas–Marini interpolation on triangular prisms

The proofs of anisotropic error estimates for the Brezzi–Douglas–Marini interpolation on simplices shown in Section 4.2 can be extended to triangular prisms with some minor modifications. The reference geometry of a prismatic element with the notation for the vertices is given in Figure 4.4. Concerning the facets of the prism element $\widehat{P}$, e_i denotes the facet opposite of the vertices $\boldsymbol{p}_i$ and $\boldsymbol{p}^i$, and the horizontal facet at $\widehat{x}_3=0$ is denoted by e_b, the one at $\widehat{x}_3=1$ by e_t. The facet normals of $\widehat{P}$ are given by

$$
\boldsymbol{n}_{\widehat{P},e_1}=\begin{pmatrix}-1\\0\\0\end{pmatrix},\quad \boldsymbol{n}_{\widehat{P},e_2}=\begin{pmatrix}0\\-1\\0\end{pmatrix},\quad \boldsymbol{n}_{\widehat{P},e_3}=\frac{1}{\sqrt{2}}\begin{pmatrix}1\\1\\0\end{pmatrix},
$$

$$
\boldsymbol{n}_{\widehat{P},e_b}=\begin{pmatrix}0\\0\\-1\end{pmatrix},\quad \boldsymbol{n}_{\widehat{P},e_t}=\begin{pmatrix}0\\0\\1\end{pmatrix}.
$$

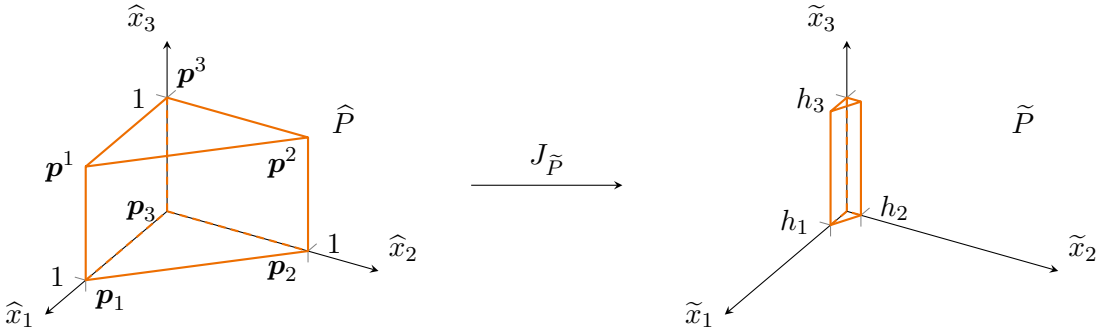

Figure 4.4: Reference prism $\widehat{P}$ with vertex numbering, and a transformed prism of the reference family $\mathcal{R}_P$.

The local Brezzi–Douglas–Marini interpolation operator I_k^{BDM} of order k on a prism P maps into the space $\boldsymbol{P}_{k,k}(P)$ of vector valued polynomials of total degree k in x_1 and x_2 and degree k in x_3. It is defined by the functionals, see [Néd86, p. 64],

$$\begin{aligned}
\int_{e_i} I_k^{\mathrm{BDM}}\boldsymbol{v}\cdot\boldsymbol{n}_{P,e_i} z \,\mathrm{d}\boldsymbol{s} &= \int_{e_i} \boldsymbol{v}\cdot\boldsymbol{n}_{P,e_i} z \,\mathrm{d}\boldsymbol{s} && \forall z \in P_k(e_i), \quad i \in \{b,t\},\\
\int_{e_i} I_k^{\mathrm{BDM}}\boldsymbol{v}\cdot\boldsymbol{n}_{P,e_i} z \,\mathrm{d}\boldsymbol{s} &= \int_{e_i} \boldsymbol{v}\cdot\boldsymbol{n}_{P,e_i} z \,\mathrm{d}\boldsymbol{s} && \forall z \in Q_k(e_i), \quad i \in I_3,\\
\int_P (I_k^{\mathrm{BDM}}\boldsymbol{v})_3 z_3 \,\mathrm{d}\boldsymbol{x} &= \int_P v_3 z_3 \,\mathrm{d}\boldsymbol{x} && \forall z_3 \in P_{k,k-2}(P),\\
\int_P (I_k^{\mathrm{BDM}}\boldsymbol{v})_1 z_1 + (I_k^{\mathrm{BDM}}\boldsymbol{v})_2 z_2 \,\mathrm{d}\boldsymbol{x} &= \int_P v_1 z_1 + v_2 z_2 \,\mathrm{d}\boldsymbol{x} && \forall (z_1,z_2) \in \mathcal{P}_{k-1,k}(P),
\end{aligned}$$

where $Q_k(e)$ is the space of polynomials with degree k in each of the dimensions of e, $P_{m,n}(P)$ is the space of polynomials with total degree m in x_1 and x_2, and degree n in x_3. The space $\mathcal{P}_{m,n}(P)$ consists of pairs of polynomials with degree n in x_3, which are for fixed x_3, i.e., on the triangle T_{x_3}, in the space $\boldsymbol{N}_m(T_{x_3})$ as defined in (4.3).

The general method to prove the interpolation error estimates on prisms is the same as on simplices, with a few changes in the proofs. We omit all parts of the proofs that work analogously to those in the previous sections. The first lemma is the analogous statement of Lemma 4.3 for the prism reference element.

Lemma 4.24. *Let $\widehat{P}$ be the reference element from Figure 4.4, $\widehat{f}_j \in L^p(e_j)$, $j \in \{1,2\}$, $\widehat{f}_3 \in L^p(e_b)$, $1 \le p \le \infty$, and*

$$\widehat{\boldsymbol{u}}(\widehat{\boldsymbol{x}}) = \begin{pmatrix} \widehat{f}_1(\widehat{x}_2,\widehat{x}_3)\\ 0\\ 0 \end{pmatrix}, \qquad \widehat{\boldsymbol{v}}(\widehat{\boldsymbol{x}}) = \begin{pmatrix} 0\\ \widehat{f}_2(\widehat{x}_1,\widehat{x}_3)\\ 0 \end{pmatrix}, \qquad \widehat{\boldsymbol{w}}(\widehat{\boldsymbol{x}}) = \begin{pmatrix} 0\\ 0\\ \widehat{f}_3(\widehat{x}_1,\widehat{x}_2) \end{pmatrix}.$$

Then there are functions $\widehat{q}_j \in P_k(e_j)$, $j \in \{1,2\}$, $\widehat{q}_3 \in P_k(e_b)$, so that

$$\widehat{I}_k^{\mathrm{BDM}}\widehat{\boldsymbol{u}} = \begin{pmatrix} \widehat{q}_1(\widehat{x}_2,\widehat{x}_3) \\ 0 \\ 0 \end{pmatrix}, \quad \widehat{I}_k^{\mathrm{BDM}}\widehat{\boldsymbol{v}} = \begin{pmatrix} 0 \\ \widehat{q}_2(\widehat{x}_1,\widehat{x}_3) \\ 0 \end{pmatrix}, \quad \widehat{I}_k^{\mathrm{BDM}}\widehat{\boldsymbol{w}} = \begin{pmatrix} 0 \\ 0 \\ \widehat{q}_3(\widehat{x}_1,\widehat{x}_2) \end{pmatrix}.$$

Proof. The proof follows the same steps as the proof of Lemma 4.3, checking that the interpolation functionals uniquely define the functions $\widehat{q}_i$. □

With the previous lemma, we get the stability estimate on the reference element.

Lemma 4.25. *Let $\widehat{\boldsymbol{u}} \in \boldsymbol{W}^{1,p}(\widehat{P})$, $1 \le p \le \infty$. Then the estimates*

$$\left\|(\widehat{I}_k^{\mathrm{BDM}}\widehat{\boldsymbol{u}})_i\right\|_{0,p,\widehat{P}} \lesssim \|\widehat{u}_i\|_{1,p,\widehat{P}} + \left\|\widehat{\operatorname{div}}\,\widehat{\boldsymbol{u}}\right\|_{0,p,\widehat{P}} + \left\|\frac{\partial\widehat{u}_3}{\partial\widehat{x}_3}\right\|_{0,p,\widehat{P}}, \qquad i \in I_2, \tag{4.39a}$$

$$\left\|(\widehat{I}_k^{\mathrm{BDM}}\widehat{\boldsymbol{u}})_3\right\|_{0,p,\widehat{P}} \lesssim \|\widehat{u}_3\|_{1,p,\widehat{P}} + \left\|\widehat{\operatorname{div}}\,\widehat{\boldsymbol{u}}\right\|_{0,p,\widehat{P}}, \tag{4.39b}$$

hold.

Proof. The proofs for $i \in I_2$ are analogous so we only show the details for $i \in \{1,3\}$, starting with $i = 1$. Let

$$\widehat{\boldsymbol{u}}_* = \begin{pmatrix} 0 \\ \widehat{u}_2(\widehat{x}_1,0,\widehat{x}_3) \\ \widehat{u}_3(\widehat{x}_1,\widehat{x}_2,0) \end{pmatrix}, \qquad \widehat{\boldsymbol{v}} = \widehat{\boldsymbol{u}} - \widehat{\boldsymbol{u}}_* = \begin{pmatrix} \widehat{u}_1 \\ \widehat{u}_2 - \widehat{u}_2(\widehat{x}_1,0,\widehat{x}_3) \\ \widehat{u}_3 - \widehat{u}_3(\widehat{x}_1,\widehat{x}_2,0) \end{pmatrix}.$$

The previous Lemma 4.24 thus yields $(\widehat{I}_k^{\mathrm{BDM}}\widehat{\boldsymbol{v}})_1 = (\widehat{I}_k^{\mathrm{BDM}}\widehat{\boldsymbol{u}})_1$, and it holds $\widehat{\operatorname{div}}\,\widehat{\boldsymbol{v}} = \widehat{\operatorname{div}}\,\widehat{\boldsymbol{u}} - \widehat{\operatorname{div}}\,\widehat{\boldsymbol{u}}_* = \widehat{\operatorname{div}}\,\widehat{\boldsymbol{u}}$. We define the two functions

$$\widehat{\boldsymbol{v}}_* = \begin{pmatrix} 0 \\ \widehat{x}_2\widehat{q}_2 \\ \widehat{x}_3\widehat{q}_3 \end{pmatrix}, \qquad \widehat{\boldsymbol{w}} = \widehat{\boldsymbol{v}} - \widehat{\boldsymbol{v}}_* = \begin{pmatrix} \widehat{v}_1 \\ \widehat{v}_2 - \widehat{x}_2\widehat{q}_2 \\ \widehat{v}_3 - \widehat{x}_3\widehat{q}_3 \end{pmatrix},$$

where $\widehat{q}_2 \in P_{k-1,k}(\widehat{P})$, $\widehat{q}_3 \in P_{k,k-1}(\widehat{P})$, so that

$$\int_{\widehat{P}} \widehat{w}_2 z \,\mathrm{d}\boldsymbol{x} = \int_{\widehat{P}} (\widehat{v}_2 - \widehat{x}_2\widehat{q}_2) z \,\mathrm{d}\boldsymbol{x} = 0 \qquad \forall z \in P_{k-1,k}(\widehat{P}), \tag{4.40}$$

$$\int_{\widehat{P}} \widehat{w}_3 z \,\mathrm{d}\boldsymbol{x} = \int_{\widehat{P}} (\widehat{v}_3 - \widehat{x}_3\widehat{q}_3) z \,\mathrm{d}\boldsymbol{x} = 0 \qquad \forall z \in P_{k,k-1}(\widehat{P}). \tag{4.41}$$

As before, this means that the functions $\widehat{q}_2$ and $\widehat{q}_3$ are well defined.

Since $\widehat{\boldsymbol{v}}_* \in \boldsymbol{P}_{k,k}(\widehat{P})$ it follows that $\widehat{I}_k^{\mathrm{BDM}}\widehat{\boldsymbol{v}}_* = \widehat{\boldsymbol{v}}_*$ and thus $(\widehat{I}_k^{\mathrm{BDM}}\widehat{\boldsymbol{w}})_1 = (\widehat{I}_k^{\mathrm{BDM}}\widehat{\boldsymbol{v}})_1 = (\widehat{I}_k^{\mathrm{BDM}}\widehat{\boldsymbol{u}})_1$. The interpolated function $\widehat{I}_k^{\mathrm{BDM}}\widehat{\boldsymbol{w}} = \widehat{\boldsymbol{t}} = (\widehat{t}_1,\widehat{t}_2,\widehat{t}_3)^T$ is then defined by the relations

$$\int_{e_b} \widehat{t}_3 z \,\mathrm{d}\boldsymbol{s} = \int_{e_b} \widehat{w}_3 z \,\mathrm{d}\boldsymbol{s} = 0 \qquad \forall z \in P_k(e_b),$$

$$
\begin{aligned}
\int_{e_t} \widehat{t}_3 z \,\mathrm{d}\boldsymbol{s} &= \int_{e_t} \widehat{w}_3 z \,\mathrm{d}\boldsymbol{s} \\
&= \int_{e_t} \widehat{w}_3 z \,\mathrm{d}\boldsymbol{s} - \int_{e_b} \widehat{w}_3 z \,\mathrm{d}\boldsymbol{s} = \int_{\widehat{P}} \frac{\partial \widehat{w}_3}{\partial \widehat{x}_3} z \,\mathrm{d}\boldsymbol{x} && \forall z \in P_k(e_t), \\
\int_{e_1} \widehat{t}_1 z \,\mathrm{d}\boldsymbol{s} &= \int_{e_1} \widehat{w}_1 z \,\mathrm{d}\boldsymbol{s} && \forall z \in Q_k(e_1), \\
\int_{e_2} \widehat{t}_2 z \,\mathrm{d}\boldsymbol{s} &= \int_{e_2} \widehat{w}_2 z \,\mathrm{d}\boldsymbol{s} = 0 && \forall z \in Q_k(e_2), \\
\int_{e_3} (\widehat{t}_1 + \widehat{t}_2) z \,\mathrm{d}\boldsymbol{s} &= \int_{e_3} (\widehat{w}_1 + \widehat{w}_2) z \,\mathrm{d}\boldsymbol{s} && \forall z \in Q_k(e_3), \\
\int_{\widehat{P}} \widehat{t}_3 z_3 \,\mathrm{d}\boldsymbol{x} &= \int_{\widehat{P}} \widehat{w}_3 z_3 \,\mathrm{d}\boldsymbol{x} = \int_{\widehat{P}} (\widehat{v}_3 - \widehat{x}_3 \widehat{q}_3) z_3 \,\mathrm{d}\boldsymbol{x} = 0 && \forall z_3 \in P_{k,k-2}(\widehat{P}), \\
\int_{\widehat{P}} \widehat{t}_1 z_1 + \widehat{t}_2 z_2 \,\mathrm{d}\boldsymbol{x} &= \int_{\widehat{P}} \widehat{w}_1 z_1 + \widehat{w}_2 z_2 \,\mathrm{d}\boldsymbol{x} = \int_{\widehat{P}} \widehat{w}_1 z_1 \,\mathrm{d}\boldsymbol{x} && \forall (z_1, z_2) \in \mathcal{P}_{k-1,k}(\widehat{P}),
\end{aligned}
$$

where the definitions of $\widehat{q}_2$, $\widehat{q}_3$, and that $\widehat{w}_2|_{e_2} \equiv 0$, $\widehat{w}_3|_{e_b} \equiv 0$ were used. Some computations are still required for the relation on e_3, which yield

$$
\begin{aligned}
\frac{1}{\sqrt{2}} \int_{e_3} (\widehat{t}_1 + \widehat{t}_2) z \,\mathrm{d}\boldsymbol{s} &= \frac{1}{\sqrt{2}} \int_{e_3} (\widehat{w}_1 + \widehat{w}_2) z \,\mathrm{d}\boldsymbol{s} = \int_{e_3} \widehat{\boldsymbol{w}} \cdot \boldsymbol{n}_{e_3} \,\mathrm{d}\boldsymbol{s} \\
&= \int_{\widehat{P}} \left(\frac{\partial \widehat{w}_1}{\partial \widehat{x}_1} + \frac{\partial \widehat{w}_2}{\partial \widehat{x}_2} \right) z \,\mathrm{d}\boldsymbol{x} + \int_{\widehat{P}} \widehat{w}_1 \frac{\partial z}{\partial \widehat{x}_1} \,\mathrm{d}\boldsymbol{x} - \int_{\partial \widehat{P} \setminus e_3} \widehat{\boldsymbol{w}} \cdot \boldsymbol{n}_{\partial \widehat{P}} z \,\mathrm{d}\boldsymbol{s} \\
&= \int_{\widehat{P}} \left(\widehat{\mathrm{div}}\, \widehat{\boldsymbol{w}} - 2 \frac{\partial \widehat{w}_3}{\partial \widehat{x}_3} \right) \mathrm{d}\boldsymbol{x} + \int_{\widehat{P}} \widehat{w}_1 \frac{\partial z}{\partial \widehat{x}_1} \,\mathrm{d}\boldsymbol{x} - \int_{e_1} \widehat{w}_1 z \,\mathrm{d}\boldsymbol{s}.
\end{aligned}
$$

Thus, the terms

$$
\begin{aligned}
\int_{e_1} \widehat{w}_1 z \,\mathrm{d}\boldsymbol{s} &= \int_{e_1} \widehat{u}_1 z \,\mathrm{d}\boldsymbol{s}, \\
\int_{\widehat{P}} \widehat{w}_1 z \,\mathrm{d}\boldsymbol{x} &= \int_{\widehat{P}} \widehat{u}_1 z \,\mathrm{d}\boldsymbol{x}, \\
\int_{\widehat{P}} \frac{\partial \widehat{w}_3}{\partial \widehat{x}_3} z \,\mathrm{d}\boldsymbol{x} &= \int_{\widehat{P}} \frac{\partial \widehat{u}_3 - \widehat{x}_3 \widehat{q}_3}{\partial \widehat{x}_3} z \,\mathrm{d}\boldsymbol{x}, \\
\int_{\widehat{P}} (\widehat{\mathrm{div}}\, \widehat{\boldsymbol{w}}) z \,\mathrm{d}\boldsymbol{x} &= \int_{\widehat{P}} \widehat{\mathrm{div}}\, (\widehat{\boldsymbol{u}} - \widehat{\boldsymbol{v}}_*) z \,\mathrm{d}\boldsymbol{x}
\end{aligned}
$$

define the interpolant, so that we get the desired estimate

$$
\left\| (\widehat{I}_k^{\mathrm{BDM}} \widehat{\boldsymbol{u}})_1 \right\|_{0,p,\widehat{P}} \lesssim \|\widehat{u}_1\|_{1,p,\widehat{P}} + \left\| \widehat{\mathrm{div}}\, \widehat{\boldsymbol{u}} \right\|_{0,p,\widehat{P}} + \left\| \frac{\partial \widehat{u}_3}{\partial \widehat{x}_3} \right\|_{0,p,\widehat{P}}
$$

by the same arguments as in the proofs of Lemmas 4.6 and 4.7. The proof for the second component works analogously.

For the third component we again start with the functions

$$\widehat{\boldsymbol{v}} = \widehat{\boldsymbol{u}} - \widehat{\boldsymbol{u}}_* = \begin{pmatrix} \widehat{u}_1 - \widehat{u}_1(0, \widehat{x}_2, \widehat{x}_3) \\ \widehat{u}_2 - \widehat{u}_2(\widehat{x}_1, 0, \widehat{x}_3) \\ \widehat{u}_3 \end{pmatrix}, \qquad \widehat{\boldsymbol{w}} = \begin{pmatrix} \widehat{v}_1 - \widehat{x}_1\widehat{q}_1 \\ \widehat{v}_2 - \widehat{x}_2\widehat{q}_2 \\ \widehat{v}_3 \end{pmatrix},$$

where the functions $\widehat{q}_1, \widehat{q}_2 \in P_{k-1,k}(\widehat{P})$ are defined by

$$\int_{\widehat{P}} \widehat{w}_1 z \,\mathrm{d}\boldsymbol{x} = \int_{\widehat{P}} (\widehat{v}_1 - \widehat{x}_1\widehat{q}_1) z \,\mathrm{d}\boldsymbol{x} = 0 \qquad \forall z \in P_{k-1,k}(\widehat{P}), \tag{4.43}$$

$$\int_{\widehat{P}} \widehat{w}_2 z \,\mathrm{d}\boldsymbol{x} = \int_{\widehat{P}} (\widehat{v}_2 - \widehat{x}_2\widehat{q}_2) z \,\mathrm{d}\boldsymbol{x} = 0 \qquad \forall z \in P_{k-1,k}(\widehat{P}). \tag{4.44}$$

This means that $(\widehat{I}_k^{\mathrm{BDM}}\widehat{\boldsymbol{w}})_3 = (\widehat{I}_k^{\mathrm{BDM}}\widehat{\boldsymbol{v}})_3 = (\widehat{I}_k^{\mathrm{BDM}}\widehat{\boldsymbol{u}})_3$, and $\widehat{\operatorname{div}}\,\widehat{\boldsymbol{v}} = \widehat{\operatorname{div}}\,\widehat{\boldsymbol{u}}$. Checking the interpolation relations for $\widehat{I}_k^{\mathrm{BDM}}\widehat{\boldsymbol{w}} = \widehat{\boldsymbol{t}} = (\widehat{t}_1, \widehat{t}_2, \widehat{t}_3)^T$ we get

$$\begin{aligned}
\int_{e_b} \widehat{t}_3 z \,\mathrm{d}\boldsymbol{s} &= \int_{e_b} \widehat{w}_3 z \,\mathrm{d}\boldsymbol{s} && \forall z \in P_k(e_b), \\
\int_{e_t} \widehat{t}_3 z \,\mathrm{d}\boldsymbol{s} &= \int_{e_t} \widehat{w}_3 z \,\mathrm{d}\boldsymbol{s} && \forall z \in P_k(e_t), \\
\int_{e_1} \widehat{t}_1 z \,\mathrm{d}\boldsymbol{s} &= \int_{e_1} \widehat{w}_1 z \,\mathrm{d}\boldsymbol{s} = 0 && \forall z \in Q_k(e_1), \\
\int_{e_2} \widehat{t}_2 z \,\mathrm{d}\boldsymbol{s} &= \int_{e_2} \widehat{w}_2 z \,\mathrm{d}\boldsymbol{s} = 0 && \forall z \in Q_k(e_2), \\
\int_{e_3} \widehat{\boldsymbol{t}} \cdot \boldsymbol{n}_{\widehat{P},e_3} z \,\mathrm{d}\boldsymbol{s} &= \int_{e_3} \widehat{\boldsymbol{w}} \cdot \boldsymbol{n}_{\widehat{P},e_3} z \,\mathrm{d}\boldsymbol{s} \\
&= \int_{\widehat{P}} \widehat{\operatorname{div}}\,\widehat{\boldsymbol{w}} z \,\mathrm{d}\boldsymbol{x} + \int_{\widehat{P}} \boldsymbol{w} \cdot \nabla z \,\mathrm{d}\boldsymbol{x} \\
&\quad - \int_{\partial\widehat{P}\setminus e_3} \widehat{\boldsymbol{w}} \cdot \boldsymbol{n}_{\partial\widehat{P}} z \,\mathrm{d}\boldsymbol{s} \\
&= \int_{\widehat{P}} \widehat{\operatorname{div}}\,\widehat{\boldsymbol{w}} z \,\mathrm{d}\boldsymbol{x} + \int_{\widehat{P}} \widehat{w}_3 \frac{\partial z}{\partial \widehat{x}_3} \,\mathrm{d}\boldsymbol{x} && \forall z \in Q_k(e_3), \\
\int_{\widehat{P}} \widehat{t}_3 z_3 \,\mathrm{d}\boldsymbol{x} &= \int_{\widehat{P}} \widehat{w}_3 z_3 \,\mathrm{d}\boldsymbol{x}, && \forall z_3 \in P_{k,k-2}(\widehat{P}), \\
\int_{\widehat{P}} \widehat{t}_1 z_1 + \widehat{t}_2 z_2 \,\mathrm{d}\boldsymbol{x} &= \int_{\widehat{P}} \widehat{w}_1 z_1 + \widehat{w}_2 z_2 \,\mathrm{d}\boldsymbol{x} = 0, && \forall (z_1, z_2) \in \mathcal{P}_{k-1,k}(\widehat{P}),
\end{aligned}$$

where the last relation holds due to the definition of the functions $\widehat{q}_1$, $\widehat{q}_2$, and since $\mathcal{P}_{k-1,k}(\widehat{P}) \subset (P_{k-1,k}(\widehat{P}))^2$. The rest of the proof can be done analogously to the proof for the first component and leads to the estimate in the lemma. □

Just as for the simplicial elements, we now transform the stability estimate from the reference element to an element $\widetilde{P}$ of the reference family $\mathcal{R}_P$, see Figure 4.4. The affine

map to get this result is the same as for the transformation to the reference families in the simplex case, i.e.,

$$\widetilde{\boldsymbol{x}} = J_{\widetilde{P}}\widehat{\boldsymbol{x}}, \qquad J_{\widetilde{P}} = \begin{pmatrix} h_1 & 0 & 0 \\ 0 & h_2 & 0 \\ 0 & 0 & h_3 \end{pmatrix}.$$

Lemma 4.26. *Let $\widetilde{P} = J_{\widetilde{P}}\widehat{P} + \boldsymbol{x}_0$, $\boldsymbol{x}_0 \in \mathbb{R}^3$, and $\widetilde{\boldsymbol{v}} \in \boldsymbol{W}^{1,p}(\widetilde{P})$, $1 \le p \le \infty$. Then on the prism $\widetilde{P}$ the estimate*

$$\left\|I_k^{\mathrm{BDM}}\widetilde{\boldsymbol{v}}\right\|_{0,p,\widetilde{P}} \lesssim \sum_{|\boldsymbol{\alpha}|\le 1} h^{\boldsymbol{\alpha}} \|D^{\boldsymbol{\alpha}}\widetilde{\boldsymbol{v}}\|_{0,p,\widetilde{P}} + h_{\widetilde{P}} \|\mathrm{div}\,\widetilde{\boldsymbol{v}}\|_{0,p,\widetilde{P}} + (h_1+h_2)\left\|\frac{\partial \widetilde{v}_3}{\partial \widetilde{x}_3}\right\|_{0,p,\widetilde{P}} \tag{4.45}$$

holds, where $h_{\widetilde{P}} = \max\{h_1, h_2, h_3\}$.

Proof. Using (4.13), (4.14) and Lemma 4.25 we can compute

$$\begin{aligned}
\left\|I_k^{\mathrm{BDM}}\widetilde{\boldsymbol{v}}\right\|_{0,p,\widetilde{P}} &\le (\det J_{\widetilde{P}})^{1/p} \sum_{i\in I_3} {}_i h^{-1} \left\|(\widehat{I}_k^{\mathrm{BDM}}\widehat{\boldsymbol{v}})_i\right\|_{0,p,\widehat{P}} \\
&\lesssim (\det J_{\widetilde{P}})^{1/p} \left[\sum_{i\in I_3} {}_i h^{-1} \left(\|\widehat{v}_i\|_{1,p,\widehat{P}} + \left\|\widehat{\mathrm{div}}\,\widehat{\boldsymbol{v}}\right\|_{0,p,\widehat{P}}\right) + \frac{h_1+h_2}{h_1h_2h_3}\left\|\frac{\partial \widehat{v}_3}{\partial \widehat{x}_3}\right\|_{0,p,\widehat{P}}\right] \\
&= \sum_{i\in I_3}\left(\sum_{|\boldsymbol{\alpha}|\le 1} h^{\boldsymbol{\alpha}}\|D^{\boldsymbol{\alpha}}\widetilde{v}_i\|_{0,p,\widetilde{P}} + h_i\left\|\widetilde{\mathrm{div}}\,\widetilde{\boldsymbol{v}}\right\|_{0,p,\widetilde{P}}\right) + (h_1+h_2)\left\|\frac{\partial \widetilde{v}_3}{\partial \widetilde{x}_3}\right\|_{0,p,\widetilde{P}} \\
&\lesssim \sum_{|\boldsymbol{\alpha}|\le 1} h^{\boldsymbol{\alpha}}\|D^{\boldsymbol{\alpha}}\widetilde{\boldsymbol{v}}\|_{0,p,\widetilde{P}} + h_{\widetilde{P}}\left\|\widetilde{\mathrm{div}}\,\widetilde{\boldsymbol{v}}\right\|_{0,p,\widetilde{P}} + (h_1+h_2)\left\|\frac{\partial \widetilde{v}_3}{\partial \widetilde{x}_3}\right\|_{0,p,\widetilde{P}}.
\end{aligned}$$

□

This stability estimate can easily be written as an estimate for the general prism with the analogous proof as for Theorem 4.10.

Theorem 4.27. *Let P be a prism element that emerges by an affine transformation of the element $\widetilde{P} \in \mathcal{R}_P$ so that the top and bottom facets are parallel and satisfy a maximal angle condition $MAC(\overline{\phi})$. Then for $\boldsymbol{v} \in \boldsymbol{W}^{1,p}(P)$, $1 \le p \le \infty$, the estimate*

$$\left\|I_k^{\mathrm{BDM}}\boldsymbol{v}\right\|_{0,p,P} \lesssim \|\boldsymbol{v}\|_{0,p,P} + \sum_{j\in I_3} h_j \left\|\frac{\partial \boldsymbol{v}}{\partial \boldsymbol{l}_j}\right\|_{0,p,P} + h_P\|\mathrm{div}\,\boldsymbol{v}\|_{0,p,P} + (h_1+h_2)\left\|\frac{\partial v_3}{\partial \boldsymbol{l}_3}\right\|_{0,p,P} \tag{4.46}$$

is satisfied and the constant only depends on $\overline{\phi}$. The vector $\boldsymbol{l}_3$ is the outward normal on the top facet.

Proof. For a prism, where the top and bottom facets satisfy a maximum angle condition, there is at least one vertex on the bottom and the top, so that the adjacent edges satisfy the requirement for the regular vertex property, see Definition 2.11. With one of these vertices taken as the regular vertex of the prism, the rest of the proof is entirely analogous to the proof of Theorem 4.10. □

As in the previous sections, the proof of the interpolation error estimate is now straightforward.

Theorem 4.28. *Let a prism P satisfy the same condition as in Theorem 4.27. Then for $k \geq 1$, $0 \leq m \leq k$ and $\boldsymbol{v} \in \boldsymbol{W}^{m+1,p}(P)$, $1 \leq p \leq \infty$, the estimate*

$$\begin{aligned}\left\|\boldsymbol{v} - I_k^{\mathrm{BDM}}\boldsymbol{v}\right\|_{0,p,P} \lesssim \sum_{|\boldsymbol{\alpha}|=m+1} h^{\boldsymbol{\alpha}} \|D_{\boldsymbol{l}}^{\boldsymbol{\alpha}}\boldsymbol{v}\|_{0,p,P} + h_P \sum_{|\boldsymbol{\alpha}|=m} h^{\boldsymbol{\alpha}} \|D_{\boldsymbol{l}}^{\boldsymbol{\alpha}} \operatorname{div} \boldsymbol{v}\|_{0,p,P} \\ + (h_1 + h_2) \sum_{|\boldsymbol{\alpha}|=m} h^{\boldsymbol{\alpha}} \left\| \frac{\partial^{m+1} v_3}{\partial \boldsymbol{l}_1^{\alpha_1} \partial \boldsymbol{l}_2^{\alpha_2} \partial \boldsymbol{l}_3^{\alpha_3+1}} \right\|_{0,p,P}\end{aligned}$$

holds and the constant only depends on $\overline{\phi}$ and k.

Proof. The computations are the same as in the proof of Theorem 4.15. □

CHAPTER 5

A-priori error analysis of pressure-robust methods on anisotropic meshes

The reconstruction approach that was already briefly introduced in Section 3.3.2 is a straightforward method to attain pressure-robustness for classical inf-sup stable mixed methods. The cost it brings is an additional consistency error due to the non-standard discretization of the right hand side linear form, which has to be estimated in the error analysis.

In Section 5.1 we show pressure-robust error estimates for reconstructed methods on anisotropic meshes in a general setting under certain assumptions on the used method. To make this analysis useful, we introduce in Sections 5.2 and 5.3 two methods which use the interpolation operators from Chapter 4 as reconstruction operators and show that they fit in the general framework of Section 5.1.

5.1 General error analysis

The basic approach is to set several assumptions, prove the error estimates under these assumptions and later show for the actual methods, that the assumptions are satisfied. This gives a certain flexibility for the development of other methods, since only the assumptions from this section have to be checked.

Before introducing the necessary assumptions we state a lemma that relates the solution of the Stokes problem (2.10) with the solution of a slightly modified problem, see also [AK21, Lemma 2].

Lemma 5.1. *The functions $(\boldsymbol{u}, p)$ are the solutions of (2.9) with right hand side data function $\boldsymbol{f} = \mathbb{P}\boldsymbol{f} + \nabla\phi$ if and only if the functions $(\boldsymbol{u}, \nu^{-1}(p-\phi))$ are the solutions of the Stokes equations with unit viscosity and data function $\nu^{-1}\mathbb{P}\boldsymbol{f}$.*

Proof. Starting with the Stokes momentum balance the proof is a straightforward calcu-

lation:

$$\begin{aligned} & -\nu\Delta\boldsymbol{u} + \nabla p = \boldsymbol{f} \\ \Leftrightarrow \quad & -\nu\Delta\boldsymbol{u} + \nabla(p-\phi) = \mathbb{P}\boldsymbol{f} \\ \Leftrightarrow \quad & -\Delta\boldsymbol{u} + \nabla(\frac{p-\phi}{\nu}) = \nu^{-1}\mathbb{P}\boldsymbol{f}. \end{aligned}$$

The claim for the divergence constraint is trivial. □

The first assumption is necessary to ensure that $\|\cdot\|_{1,h}$ is a norm on the space $\boldsymbol{X} \oplus \boldsymbol{X}_h$, see [LMT16, Assumption A2, Remark 2.2] and [CR73, Lemma 2]. The assumption always holds for conforming velocity spaces, see [CR73, Remark 2].

Assumption 1. There is an $r \in \mathbb{N}$, with $r \geq k-1$ where k is the polynomial order of $\boldsymbol{X}_h$, so that on every facet $F \in \mathcal{F}(\mathcal{T}_h)$ and every $i \in I_d$

$$(q, (\llbracket \boldsymbol{v}_h \rrbracket)_i)_{0,F} = 0 \qquad \forall q \in P_r(F)$$

holds for all $\boldsymbol{v}_h \in \boldsymbol{X}_h$, where $(\cdot)_i$ is the i-th component of a vector function.

Next is an assumption that defines the required properties of the reconstruction operator. Recall that for our approach towards pressure-robustness we use the modified linear form $l_h(\boldsymbol{v}_h) = (\boldsymbol{f}, I_h\boldsymbol{v}_h)$ from (3.6) on the right hand side of the Stokes discretization.

Assumption 2. The reconstruction operator $I_h : \boldsymbol{X}_h \to \boldsymbol{Y}_h \subset \boldsymbol{H}_0(\mathrm{div}, \Omega)$ satisfies

$$\nabla \cdot (I_h\boldsymbol{v}_h) = \nabla_h \cdot \boldsymbol{v}_h \qquad \forall \boldsymbol{v}_h \in \boldsymbol{X}_h^0, \tag{5.1a}$$

$$\|\boldsymbol{v}_h - I_h\boldsymbol{v}_h\|_0 \lesssim h\|\boldsymbol{v}_h\|_{1,h} \qquad \forall \boldsymbol{v}_h \in \boldsymbol{X}_h, \tag{5.1b}$$

where the constant in the interpolation error estimate is independent of the aspect ratio of the triangulation and the mesh size parameter h.

The following assumptions are concerned with the finite element pair of the mixed method.

Assumption 3. There is an operator $I_h^F : \boldsymbol{X} \to \boldsymbol{X}_h$ that for all $\boldsymbol{v} \in \boldsymbol{X}$ satisfies the properties

$$\begin{aligned} & b_h(\boldsymbol{v}, q_h) = b_h(I_h^F\boldsymbol{v}, q_h) \qquad \forall q_h \in Q_h, \\ & \left\|I_h^F\boldsymbol{v}\right\|_{1,h} \leq C_F\|\boldsymbol{v}\|_{1,h}, \end{aligned}$$

with a stability constant C_F that is independent of the aspect ratio of the mesh and the mesh size parameter h.

An operator that satisfies Assumption 3 is called Fortin operator. It is a standard result that the existence of a Fortin operator with a stability constant C_F that is independent of the mesh size parameter h is equivalent to the discrete inf-sup stability of a finite element pair, see, e.g., [EG04, Lemma 4.19]. In the following lemma we only show the direction that Assumption 3 implies the inf-sup condition.

Lemma 5.2. *Let Assumption 3 hold and let $\boldsymbol{X}_h \subset \boldsymbol{X}$, $Q_h \subset Q$. Then there is a constant $\widetilde{\beta} > 0$ so that*

$$\inf_{0 \neq q_h \in Q_h} \sup_{\mathbf{0} \neq \boldsymbol{v}_h \in \boldsymbol{X}_h} \frac{b_h(\boldsymbol{v}_h, q_h)}{\|\boldsymbol{v}_h\|_{1,h} \|q_h\|_0} \geq \widetilde{\beta} \tag{5.2}$$

holds, where $\widetilde{\beta}$ is independent of the mesh size parameter h.

Proof. Let $q_h \in Q_h$. Then we have

$$\sup_{\mathbf{0} \neq \boldsymbol{v}_h \in \boldsymbol{X}_h} \frac{b_h(\boldsymbol{v}_h, q_h)}{\|\boldsymbol{v}_h\|_{1,h}} \geq \sup_{\mathbf{0} \neq \boldsymbol{v} \in \boldsymbol{X}} \frac{b_h(I_h^F \boldsymbol{v}, q_h)}{\|I_h^F \boldsymbol{v}\|_{1,h}} = \sup_{\mathbf{0} \neq \boldsymbol{v} \in \boldsymbol{X}} \frac{b_h(\boldsymbol{v}, q_h)}{\|I_h^F \boldsymbol{v}\|_{1,h}} \geq \sup_{\mathbf{0} \neq \boldsymbol{v} \in \boldsymbol{X}} \frac{b_h(\boldsymbol{v}, q_h)}{C_F \|\boldsymbol{v}\|_{1,h}},$$

which, since q_h is arbitrarily chosen and we have the continuous inf-sup stability condition (2.11), concludes the proof and we get $\widetilde{\beta} = \frac{\beta}{C_F}$, where β is the continuous inf-sup constant. □

The stated result assumes a conforming discretization, but the proof can be applied to the non-conforming Crouzeix–Raviart element, see, e.g., [Joh16, Theorem 3.151, Remark 3.152].

Assumption 4. Let $(\boldsymbol{u}, p)$ be the solution of the Stokes problem with unit viscosity. The consistency error estimates

$$|a_h(\boldsymbol{u}, \boldsymbol{v}_h) + b_h(\boldsymbol{v}_h, p) - (\boldsymbol{f}, \boldsymbol{v}_h)| \lesssim h \|\boldsymbol{v}_h\|_{1,h} \|\boldsymbol{f}\|_0 \qquad \forall \boldsymbol{v}_h \in \boldsymbol{X}_h, \tag{5.3a}$$

$$|a_h(\boldsymbol{u}, \boldsymbol{v}_h) - (\boldsymbol{f}, \boldsymbol{v}_h)| \lesssim h \|\boldsymbol{v}_h\|_{1,h} \|\boldsymbol{f}\|_0 \qquad \forall \boldsymbol{v}_h \in \boldsymbol{X}_h^0 \tag{5.3b}$$

hold, where the constants are independent of the aspect ratio of the mesh and the mesh size parameter h.

The first estimate in Assumption 4 is always satisfied for standard conforming velocity approximations $\boldsymbol{X}_h \subset \boldsymbol{X}$. On the other hand, the second estimate follows from the first only if $\boldsymbol{X}_h^0 \subset \boldsymbol{X}^0$ which is in general not the case. However, we can show a property, see also [Lin14, p. 787] and [AK21, Lemma 3], that is useful for checking (5.3b) in certain cases, e.g., for the Crouzeix–Raviart method.

Lemma 5.3. *Let $\boldsymbol{X}_h$, Q_h be a finite element pair for the Stokes equations, for which $\nabla_h \cdot \boldsymbol{v}_h \in Q_h$ for all $\boldsymbol{v}_h \in \boldsymbol{X}_h$. Then* (5.3a) *implies* (5.3b).

Proof. For $\boldsymbol{v}_h \in \boldsymbol{X}_h^0$ it holds $\nabla_h \cdot \boldsymbol{v}_h = 0$, since we can test with $q_h = \nabla_h \cdot \boldsymbol{v}_h$ in the definition of $\boldsymbol{X}_h^0$ which yields

$$\boldsymbol{X}_h^0 \subseteq \left\{ \boldsymbol{v}_h \in \boldsymbol{X}_h : b_h(\boldsymbol{v}_h, \nabla_h \cdot \boldsymbol{v}_h) = \int_\Omega (\nabla_h \cdot \boldsymbol{v}_h)^2 \, \mathrm{d}\boldsymbol{x} = 0 \right\}.$$

Thus we get $b_h(\boldsymbol{v}_h, p) = 0$ for $\boldsymbol{v}_h \in \boldsymbol{X}_h^0$. □

Assumption 5. Let $(\boldsymbol{u}, p)$ be the solution of the Stokes problem (2.10). The approximation properties

$$\inf_{\boldsymbol{v}_h \in \boldsymbol{X}_h^0} \|\boldsymbol{u} - \boldsymbol{v}_h\|_{1,h} \lesssim h \|\mathbb{P}(\Delta \boldsymbol{u})\|_0,$$
$$\inf_{q_h \in Q_h} \|p - q_h\|_0 \lesssim h \|\boldsymbol{f}\|_0$$

hold, where the constants are independent of the aspect ratio of the mesh and the mesh size parameter h.

Using these assumptions, we can prove the general pressure-robust error estimate on anisotropic triangulations.

Theorem 5.4. *Let Assumptions 1 to 4 hold and let $(\boldsymbol{u}, p)$ and $(\boldsymbol{u}_h, p_h)$ be the solutions of (2.10) and (3.1), respectively. Then we have the estimate*

$$\|\boldsymbol{u} - \boldsymbol{u}_h\|_{1,h} \lesssim \inf_{\boldsymbol{v}_h \in \boldsymbol{X}_h^0} \|\boldsymbol{u} - \boldsymbol{v}_h\|_{1,h} + h \|\mathbb{P}(\Delta \boldsymbol{u})\|_0. \tag{5.4}$$

Proof. Let $\boldsymbol{v}_h \in \boldsymbol{X}_h^0$ be the best-approximation of $\boldsymbol{u}$ with respect to $\|\cdot\|_{1,h}$ and set $\boldsymbol{w}_h = \boldsymbol{u}_h - \boldsymbol{v}_h \in \boldsymbol{X}_h^0$. Then due to the Pythagoras theorem we have

$$\|\boldsymbol{u} - \boldsymbol{u}_h\|_{1,h}^2 = \|\boldsymbol{u} - \boldsymbol{v}_h\|_{1,h}^2 + \|\boldsymbol{w}_h\|_{1,h}^2. \tag{5.5}$$

Using (3.2) and $a_h(\boldsymbol{u} - \boldsymbol{v}_h, \boldsymbol{w}_h) = 0$ we can estimate

$$\begin{aligned}
\|\boldsymbol{w}_h\|_{1,h}^2 &= a_h(\boldsymbol{w}_h, \boldsymbol{w}_h) = a_h(\boldsymbol{u}_h - \boldsymbol{v}_h, \boldsymbol{w}_h) \\
&= a_h(\boldsymbol{u} - \boldsymbol{v}_h, \boldsymbol{w}_h) - a_h(\boldsymbol{u}, \boldsymbol{w}_h) + a_h(\boldsymbol{u}_h, \boldsymbol{w}_h) \\
&\leq \left| a_h(\boldsymbol{u}, \boldsymbol{w}_h) - \nu^{-1}(\boldsymbol{f}, I_h \boldsymbol{w}_h) \right|.
\end{aligned}$$

Dividing by $\|\boldsymbol{w}_h\|_{1,h}$ and combining this inequality with (5.5) yields

$$\|\boldsymbol{u} - \boldsymbol{u}_h\|_{1,h} \leq \|\boldsymbol{u} - \boldsymbol{v}_h\|_{1,h} + \frac{\left| a_h(\boldsymbol{u}, \boldsymbol{w}_h) - \nu^{-1}(\boldsymbol{f}, I_h \boldsymbol{w}_h) \right|}{\|\boldsymbol{w}_h\|_{1,h}}. \tag{5.6}$$

Recall the Helmholtz–Hodge decomposition of the data $\boldsymbol{f} = \mathbb{P}\boldsymbol{f} + \nabla \phi$ and note that $\nabla \cdot I_h \boldsymbol{w}_h = 0$ due to Assumption 2 and $\boldsymbol{w}_h \in \boldsymbol{X}_h^0$. With $(\nabla \phi, I_h \boldsymbol{w}_h) = 0$ we get

$$\begin{aligned}
\left| a_h(\boldsymbol{u}, \boldsymbol{w}_h) - \frac{1}{\nu}(\boldsymbol{f}, I_h \boldsymbol{w}_h) \right| &= \left| a_h(\boldsymbol{u}, \boldsymbol{w}_h) - \nu^{-1}(\mathbb{P}\boldsymbol{f}, I_h \boldsymbol{w}_h) \right| \\
&= \left| a_h(\boldsymbol{u}, \boldsymbol{w}_h) - \nu^{-1}(\mathbb{P}\boldsymbol{f}, \boldsymbol{w}_h) + \nu^{-1}(\mathbb{P}\boldsymbol{f}, \boldsymbol{w}_h - I_h \boldsymbol{w}_h) \right| \\
&\leq \left| a_h(\boldsymbol{u}, \boldsymbol{w}_h) - \nu^{-1}(\mathbb{P}\boldsymbol{f}, \boldsymbol{w}_h) \right| + \left| \nu^{-1}(\mathbb{P}\boldsymbol{f}, \boldsymbol{w}_h - I_h \boldsymbol{w}_h) \right|.
\end{aligned} \tag{5.7}$$

By Lemma 5.1, $\boldsymbol{u}$ is also the velocity solution of the Stokes problem with unit viscosity and right hand side $\nu^{-1}\mathbb{P}\boldsymbol{f}$, which means that we can apply the consistency estimate of Assumption 4, which yields

$$\left| a_h(\boldsymbol{u}, \boldsymbol{w}_h) - \nu^{-1}(\mathbb{P}\boldsymbol{f}, \boldsymbol{w}_h) \right| \lesssim \nu^{-1} h \|\boldsymbol{w}_h\|_{1,h} \|\mathbb{P}\boldsymbol{f}\|_0. \tag{5.8}$$

The second term in (5.7) can be estimated using the Cauchy–Schwarz inequality and the interpolation error estimate for the reconstruction operator I_h from Assumption 2, which gets us

$$\left|\nu^{-1}(\mathbb{P}\boldsymbol{f}, \boldsymbol{w}_h - I_h\boldsymbol{w}_h)\right| \leq \nu^{-1}\|\mathbb{P}\boldsymbol{f}\|_0\|\boldsymbol{w}_h - I_h\boldsymbol{w}_h\|_0 \lesssim \nu^{-1}h\|\mathbb{P}\boldsymbol{f}\|_0\|\boldsymbol{w}_h\|_{1,h}. \tag{5.9}$$

We can now combine the individual estimates (5.8), (5.9) with (5.7) and insert the result in (5.6). Since $\boldsymbol{v}_h$ was chosen as the best-approximation of $\boldsymbol{u}$ in $\boldsymbol{X}_h^0$, we now have the final estimate

$$\|\boldsymbol{u} - \boldsymbol{u}_h\|_{1,h} \lesssim \inf_{\boldsymbol{v}_h \in \boldsymbol{X}_h^0} \|\boldsymbol{u} - \boldsymbol{v}_h\|_{1,h} + h\|\mathbb{P}(\Delta\boldsymbol{u})\|_0,$$

where we also used the identity (2.13). □

If we additionally use Assumption 5, we can bound the best-approximation error and get an overall estimate.

Corollary 5.5. *Under the assumptions from Theorem 5.4 and Assumption 5 the estimate*

$$\|\boldsymbol{u} - \boldsymbol{u}_h\|_{1,h} \lesssim h\|\mathbb{P}(\Delta\boldsymbol{u})\|_0$$

holds.

Proof. The proof is a direct application of Assumption 5 to (5.4). □

Remark 5.6. Looking at Theorem 5.4 and Corollary 5.5, we see that the estimates are presented in terms of the norm of the divergence-free part of the Laplacian of the velocity solution $\|\mathbb{P}(\Delta\boldsymbol{u})\|_0$. The estimate does not include the viscosity parameter at all. However, if we use the identity (2.13), the term $\nu^{-1}\|\mathbb{P}\boldsymbol{f}\|_0$ appears. Of course both forms of the estimate are pressure-robust, but in one of them the factor ν^{-1} is present.

This is of interest, when we look at how typical numerical examples for pressure-robust methods are constructed. In some cases, a fixed solution $(\boldsymbol{u}, p)$ is chosen, and the data is computed using the Stokes momentum balance equation (2.9a), where different values for ν are chosen to show that the discrete solution of the pressure-robust method does not depend on ν. This approach is represented in the given form of the estimates in the theorem and corollary.

On the other hand, in a setting where the data function $\boldsymbol{f}$ is fixed and ν is varied, the velocity solution scales with ν^{-1} and so does the discrete solution and thus the error of pressure-robust methods. In such a numerical experiment, the pressure-robustness of a method can instead be shown by adding an additional gradient field to the data, which does not influence the continuous velocity solution, and thus does not influence the discrete velocity solution of the pressure-robust method.

Similar observations are stated in [LMN20, Remark 3.2] and [AK21, Remark 3].

For the pressure error we can get the following estimate.

Proposition 5.7. *Under the assumptions from Theorem 5.4 and with Q_h being the space of piecewise constants, the estimate*

$$\|p - p_h\|_0 \lesssim \inf_{q_h \in Q_h} \|p - q_h\|_0 + \frac{\nu}{\widetilde{\beta}} \inf_{\boldsymbol{v}_h \in \boldsymbol{X}_h^0} \|\boldsymbol{u} - \boldsymbol{v}_h\|_{1,h} + \frac{h}{\widetilde{\beta}} \|\boldsymbol{f}\|_0 \tag{5.10}$$

is satisfied, where $\widetilde{\beta}$ is the discrete inf-sup constant.

Proof. Using the Pythagoras theorem, we can estimate

$$\|p - p_h\|_0^2 = \|p - \pi_h p\|_0^2 + \|\pi_h p - p_h\|_0^2,$$

where $\pi_h : L_0^2(\Omega) \to Q_h$ is the L^2-projection into the discrete pressure space. For the first term it holds $\|p - \pi_h p\|_0^2 = \inf_{q_h \in Q_h} \|p - q_h\|_0^2$, and since $\pi_h p - p_h \in Q_h$ we can use the discrete inf-sup condition (5.2) to estimate

$$\begin{aligned} \|\pi_h p - p_h\|_0 &\leq \frac{1}{\widetilde{\beta}} \sup_{\boldsymbol{v}_h \in \boldsymbol{X}_h} \frac{b_h(\boldsymbol{v}_h, \pi_h p - p_h)}{\|\boldsymbol{v}_h\|_{1,h}} \\ &= \frac{1}{\widetilde{\beta}} \sup_{\boldsymbol{v}_h \in \boldsymbol{X}_h} \frac{b_h(\boldsymbol{v}_h, \pi_h p - p) + b_h(\boldsymbol{v}_h, p - p_h)}{\|\boldsymbol{v}_h\|_{1,h}}. \end{aligned} \tag{5.11}$$

We estimate the first term in the numerator using the Cauchy–Schwarz inequality, the error estimate for the L^2-projection into piecewise constant functions from [EG04, Theorem 1.103] and Proposition 2.6, which yields

$$|b_h(\boldsymbol{v}_h, \pi_h p - p)| \leq \|\nabla_h \cdot \boldsymbol{v}_h\|_0 \|\pi_h p - p\|_0 \lesssim \|\boldsymbol{v}_h\|_{1,h} \|\pi_h p - p\|_0 \lesssim h \|\boldsymbol{v}_h\|_{1,h} \|\boldsymbol{f}\|_0. \tag{5.12}$$

The function p_h is the solution of the discrete problem, so we get for the second term

$$\begin{aligned} |b_h(\boldsymbol{v}_h, p - p_h)| &= |b_h(\boldsymbol{v}_h, p) + \nu a_h(\boldsymbol{u}_h, \boldsymbol{v}_h) - (\boldsymbol{f}, I_h \boldsymbol{v}_h)| \\ &= |\nu a_h(\boldsymbol{u}, \boldsymbol{v}_h) + b_h(\boldsymbol{v}_h, p) - (\boldsymbol{f}, \boldsymbol{v}_h) + \nu a_h(\boldsymbol{u}_h - \boldsymbol{u}, \boldsymbol{v}_h) + (\boldsymbol{f}, \boldsymbol{v}_h - I_h \boldsymbol{v}_h)| \\ &\lesssim \nu \|\boldsymbol{u} - \boldsymbol{u}_h\|_{1,h} \|\boldsymbol{v}_h\|_{1,h} + h \|\boldsymbol{f}\|_0 \|\boldsymbol{v}_h\|_{1,h}, \end{aligned} \tag{5.13}$$

where in the last step the consistency error estimate from Assumption 4, the Cauchy–Schwarz inequality and the interpolation error estimate from Assumption 2 was used. Now putting (5.12) and (5.13) into (5.11) and using Theorem 5.4 yields the claimed pressure estimate. □

Similarly to the velocity estimate, we can easily get an additional result for the pressure error in terms of the data.

Corollary 5.8. *Under the assumptions from Proposition 5.7 and Assumption 5 the estimate*

$$\|p - p_h\|_0 \lesssim h \widetilde{\beta}^{-1} \|\boldsymbol{f}\|_0$$

holds.

Proof. Starting from (5.10), we can use Assumption 5 for the first and second terms and arrive at the claimed estimate. □

After the general error analysis in this section, we now show two examples of finite element discretizations that fit into the framework. Starting in Section 5.2 with a conforming discretization, we verify the assumptions from this section and thus see that the method yields a pressure-robust discretization on anisotropic meshes. Unfortunately this method is only applicable in certain two-dimensional anisotropic settings as explained below. In Section 5.3 we use the same approach for a non-conforming classical method, which can be used for arbitrary two- and three-dimensional meshes satisfying the maximum angle condition.

5.2 Modified Bernardi–Raugel method

The Bernardi–Raugel finite element method from [BR85] is a lowest-order conforming method for the Stokes equations that is inf-sup stable without stabilization, which is shown for shape-regular meshes in, e.g., [GR86, Lemma II.2.2].

On a simplicial element T with $d \in \{2, 3\}$, the polynomial function space of this method for the velocity approximation is given by

$$\mathrm{BR}(T) = \boldsymbol{P}_1(T) \oplus \operatorname{span}\{\boldsymbol{t}_{e_1}, \dots, \boldsymbol{t}_{e_{d+1}}\},$$

where, denoting by λ_j, $j = 1, \dots, d+1$, the barycentric coordinates of T,

$$\boldsymbol{t}_{e_i} = \boldsymbol{n}_{e_i} \prod_{j \in_i I_{d+1}} \lambda_j. \tag{5.14}$$

Recall that $\boldsymbol{n}_{e_i}$ denotes the outward pointing unit normal vector to the facet e_i. The functions $\boldsymbol{t}_i$ are called *facet bubbles*. Pressure approximation is done using the space of piecewise constant functions

$$Q_h = \{q_h \in L^2_0(\Omega) : q_h|_T \in P_0(T) \quad \forall T \in \mathcal{T}_h\}. \tag{5.15}$$

The global approximation space on a mesh $\mathcal{T}_h$ is then defined by, see also [GR86, Section II.2.1],

$$\mathrm{BR}(\mathcal{T}_h) = \{\boldsymbol{v}_h \in \boldsymbol{C}(\overline{\Omega}) : \boldsymbol{v}_h|_T \in \mathrm{BR}(T)\ \forall T \in \mathcal{T}_h\} \cap \boldsymbol{X}. \tag{5.16}$$

Avoiding some technicalities we define the Bernardi–Raugel interpolation operator I_h^{BR} for functions $\boldsymbol{v} \in \boldsymbol{H}^2(\Omega)$ by the relations

$$\begin{aligned} I_h^{\mathrm{BR}}\boldsymbol{v}(\boldsymbol{p}) &= \boldsymbol{v}(\boldsymbol{p}) && \forall \boldsymbol{p} \in \mathcal{V}(\mathcal{T}_h), \\ \int_e I_h^{\mathrm{BR}}\boldsymbol{v} \cdot \boldsymbol{n}_e \,\mathrm{d}\boldsymbol{s} &= \int_e \boldsymbol{v} \cdot \boldsymbol{n}_e \,\mathrm{d}\boldsymbol{s} && \forall e \in \mathcal{F}(\mathcal{T}_h). \end{aligned}$$

Our aim now is to show the validity of Assumptions 1 to 5 for this method, so that the general error estimates from Section 5.1 are valid for this method. As mentioned

in [LM16, Section 4] for shape-regular meshes, the lowest-order Raviart–Thomas and Brezzi–Douglas–Marini interpolation operators, see Sections 4.2.1 and 4.3.1, can be used as reconstruction operators for the Bernardi–Raugel element.

Theorem 5.9. *Let $\boldsymbol{X}_h$ and Q_h be the Bernardi–Raugel finite element pair as introduced in* (5.15) *and* (5.16)*, and let the domain $\Omega \subset \mathbb{R}^2$ be a convex polygon. Further let the reconstruction operator I_h be defined by either $(I_h \boldsymbol{v}_h)|_T = I_1^{\mathrm{BDM}} \boldsymbol{v}_h|_T$ or $(I_h \boldsymbol{v}_h)|_T = I_0^{\mathrm{RT}} \boldsymbol{v}_h|_T$ for all $\boldsymbol{v}_h \in \boldsymbol{X}_h$ and $T \in \mathcal{T}_h$. Then Assumptions 1 to 5 hold for the wide class of two-dimensional meshes described in [AN04, Section 2].*

Proof. We go through the proof of every assumption individually:

1. Since $\boldsymbol{X}_h \subset \boldsymbol{X}$, it holds for every $\boldsymbol{v}_h \in \boldsymbol{X}_h$ on every $F \in \mathcal{F}(\mathcal{T}_h)$ that $[\![\boldsymbol{v}_h]\!]_F = \boldsymbol{0}$. Thus Assumption 1 is satisfied with $r = 0$ and $k = 1$.

2. We immediately see that since $\mathrm{BR}(\mathcal{T}_h) \subset \boldsymbol{C}(\overline{\Omega}) \cap \boldsymbol{X}$ the operator I_h maps to a subspace of $\boldsymbol{H}_0(\mathrm{div}, \Omega)$. The interpolation error estimate (5.1b) can be verified by setting $h = \max_{T \in \mathcal{T}_h} h_T$ and summing the elementwise error estimates (4.21) or (4.24), respectively.

   To show (5.1a) we need to prove that the reconstruction operator preserves the discrete divergence of the functions from $\mathrm{BR}(\mathcal{T}_h)$, i.e.,

   $$\int_T \nabla \cdot I_h \boldsymbol{v}_h q_h \,\mathrm{d}\boldsymbol{x} = \int_T \nabla \cdot \boldsymbol{v}_h q_h \,\mathrm{d}\boldsymbol{x} \qquad \forall q_h \in Q_h$$

   holds for all $\boldsymbol{v}_h \in \boldsymbol{X}_h$ and all $T \in \mathcal{T}_h$, see also [BBF13, Proposition 2.5.2] and [Joh16, Lemma 4.134]. Integrating by parts we get

   $$\int_T \nabla \cdot (I_h \boldsymbol{v}_h - \boldsymbol{v}_h) q_h \,\mathrm{d}\boldsymbol{x} = \int_T (\boldsymbol{v}_h - I_h \boldsymbol{v}_h) \cdot \nabla q_h \,\mathrm{d}\boldsymbol{x} + \sum_{F \in \mathcal{F}(T)} \int_F (I_h \boldsymbol{v}_h - \boldsymbol{v}_h) \cdot \boldsymbol{n}_F q_h \,\mathrm{d}\boldsymbol{s}.$$

   Since q_h is piecewise constant it holds $\nabla q_h = \boldsymbol{0}$ and by using the definition of the operators I_1^{BDM}, I_0^{RT}, we see that the right hand side vanishes. Thus Assumption 2 holds.

3. The proof for Assumption 3 is the proof for [AN04, Theorem 1]. In particular the meshes described in Section 2.4.2 are included in the results from the reference.

4. The first estimate in Assumption 4 is satisfied since for the Bernardi–Raugel method $\mathrm{BR}(\mathcal{T}_h) \subset \boldsymbol{X}$ holds, which implies $|a_h(\boldsymbol{u}, \boldsymbol{v}_h) + b_h(\boldsymbol{v}_h, p) - (\boldsymbol{f}, \boldsymbol{v}_h)| = 0$ for all $\boldsymbol{v}_h \in \mathrm{BR}(\mathcal{T}_h)$.

   For the second estimate with $\boldsymbol{v}_h \in \boldsymbol{X}_h^0$ we write

   $$|a_h(\boldsymbol{u}, \boldsymbol{v}_h) - (\boldsymbol{f}, \boldsymbol{v}_h)| \leq |a_h(\boldsymbol{u}, \boldsymbol{v}_h) + b_h(\boldsymbol{v}_h, p) - (\boldsymbol{f}, \boldsymbol{v}_h)| + |b_h(\boldsymbol{v}_h, p)|,$$

where the first term vanishes since $\boldsymbol{X}_h^0 \subset \boldsymbol{X}_h$. Estimating the second term, using the L^2-projection operator π_h onto Q_h, we get

$$\begin{aligned}|a_h(\boldsymbol{u}, \boldsymbol{v}_h) - (\boldsymbol{f}, \boldsymbol{v}_h)| &\leq |b_h(\boldsymbol{v}_h, p)| \\ &= |b_h(\boldsymbol{v}_h, \pi_h p) + b_h(\boldsymbol{v}_h, p - \pi_h p)| \\ &= |b_h(\boldsymbol{v}_h, p - \pi_h p)| \\ &\leq \|\nabla_h \cdot \boldsymbol{v}_h\|_0 \|p - \pi_h p\|_0 \\ &\leq \|\boldsymbol{v}_h\|_{1,h} \|p - \pi_h p\|_0.\end{aligned}$$

The error of the L^2-projection onto the piecewise constant functions can be estimated using [EG04, Theorem 1.103] which, using Proposition 2.6 and the comment in the subsequent paragraph, leads to the final estimate

$$|a_h(\boldsymbol{u}, \boldsymbol{v}_h) - (\boldsymbol{f}, \boldsymbol{v}_h)| \lesssim h \|\boldsymbol{v}_h\|_{1,h} \|p\|_1 \lesssim h \|\boldsymbol{v}_h\|_{1,h} \|\boldsymbol{f}\|_0.$$

5. To prove the approximation estimates required for Assumption 5, we need the stability estimate for the Bernardi–Raugel interpolation operator from [AN04, Section 5.2], where it was shown that for $\boldsymbol{v} \in \boldsymbol{H}^2(\Omega)$ the estimate

$$\left\| I_h^{\mathrm{BR}} \boldsymbol{v} \right\|_{1,h} \lesssim \|\boldsymbol{v}\|_{1,h} + h|\boldsymbol{v}|_2 \tag{5.17}$$

holds on the types of meshes we use. Employing the technique seen in the proof of [GR86, II.(1.16)], we get

$$\inf_{\boldsymbol{v}_h \in \boldsymbol{X}_h^0} \|\boldsymbol{u} - \boldsymbol{v}_h\|_{1,h} \lesssim \inf_{\boldsymbol{v}_h \in \boldsymbol{X}_h} \|\boldsymbol{u} - \boldsymbol{v}_h\|_{1,h} \lesssim \left\| \boldsymbol{u} - I_h^{\mathrm{BR}} \boldsymbol{u} \right\|_{1,h},$$

which leaves estimating the error of the Bernardi–Raugel interpolation. This can be done by seeing that the operator I_h^{BR} preserves linear polynomials and then using the stability estimate (5.17) and a Bramble–Hilbert type argument as seen in the proofs for the Brezzi–Douglas–Marini interpolation error estimate in Section 4.2.3, which in the end leads to the estimate

$$\inf_{\boldsymbol{v}_h \in \boldsymbol{X}_h^0} \|\boldsymbol{u} - \boldsymbol{v}_h\|_{1,h} \lesssim h|\boldsymbol{u}|_2.$$

As $\boldsymbol{u} \in \boldsymbol{H}^2(\Omega)$ is the Stokes velocity solution for data $\boldsymbol{f}$, we know from Lemma 5.1 that it also solves a Stokes system with data $\nu^{-1}\mathbb{P}\boldsymbol{f}$. Thus we can use Proposition 2.6 to estimate

$$|\boldsymbol{u}|_2 \lesssim \nu^{-1} \|\mathbb{P}\boldsymbol{f}\|_0.$$

With (2.13) we now get the desired estimate

$$\inf_{\boldsymbol{v}_h \in \boldsymbol{X}_h^0} \|\boldsymbol{u} - \boldsymbol{v}_h\|_{1,h} \lesssim h \|\mathbb{P}(\Delta \boldsymbol{u})\|_0.$$

The estimate for the pressure can be acquired by again using the error estimate for the L^2-projection into piecewise constants π_h from [EG04, Theorem 1.103], with which we can compute

$$\inf_{q_h \in Q_h} \|p - q_h\|_0 = \|p - \pi_h p\|_0 \lesssim h\|p\|_1 \lesssim h\|\boldsymbol{f}\|_0,$$

where in the last step Proposition 2.6 was used. □

Unfortunately, in contrast to the Crouzeix–Raviart method in the next section, we are unable to show the existence of a Fortin operator for the Bernardi–Raugel finite element pair on arbitrary meshes, but the method is stable on a large class of two-dimensional meshes, as mentioned above.

An interesting result regarding practical applications for the reconstructed Bernardi–Raugel method is that the Raviart–Thomas and Brezzi–Douglas–Marini interpolation operators yield the same function when acting on the normal-weighted facet bubbles.

Proposition 5.10. *Let $\boldsymbol{t}_{e_i}$ be a Bernardi–Raugel normal-weighted facet bubble function from* (5.14)*. Then it holds*

$$I_1^{\mathrm{BDM}} \boldsymbol{t}_{e_i} = I_0^{\mathrm{RT}} \boldsymbol{t}_{e_i}.$$

Proof. Let $I_1^{\mathrm{BDM}} \boldsymbol{t}_{e_i} = \sum_{k=1}^{d} a_k \phi_{ik}$ and $I_0^{\mathrm{RT}} \boldsymbol{t}_{e_i} = b\psi_i$, where ϕ_{ik} and ψ_i are the Brezzi–Douglas–Marini and Raviart–Thomas basis functions associated with facet e_i, as defined in [BBF13, Section 2.6] for which it holds $\psi_i = \sum_{k=1}^{d} \phi_{ik}$.

The rest of the proof is a lengthy direct computation of the coefficients

$$a_k = \int_{e_i} \boldsymbol{t}_{e_i} \cdot \boldsymbol{n}_i \phi_{ik}^* \,\mathrm{d}\boldsymbol{s}, \quad k \in \{1, \dots, d\},$$
$$b = |e_i|^{-1} \int_{e_i} \boldsymbol{t}_{e_i} \cdot \boldsymbol{n}_i \,\mathrm{d}\boldsymbol{s},$$

which yields $a_k = b$ for all $k \in \{1, \dots, d\}$. Here ϕ_{ik}^* are the $P_1(e_i)$ basis functions dual to ϕ_{ik} with respect to the functionals defining the Brezzi–Douglas–Marini interpolation. This computation was done using the symbolic computation library SymPy. □

This result and the fact that the lowest-order Brezzi–Douglas–Marini interpolation operator preserves the linear basis functions from $\mathrm{BR}(\mathcal{T}_h)$ means that for practical applications of the method we only need to reconstruct the facet bubbles using Raviart–Thomas interpolation, which has a simpler interpolation operator. This aspect is also discussed in [LM16, Remark 4.2].

Numerical examples of the performance of the method are given in Chapter 6. To conclude this section we show the reconstruction of a facet bubble in detail.

Example 5.11. To give an impression of how the reconstruction acts on the Bernardi–Raugel facet bubble functions, we look at a reference configuration of two triangular elements $T_1 = \boldsymbol{p}_1\boldsymbol{p}_3\boldsymbol{p}_4$ and $T_2 = \boldsymbol{p}_1\boldsymbol{p}_2\boldsymbol{p}_3$, where the vertices are set to $\boldsymbol{p}_1 = (0,0)^T, \boldsymbol{p}_2 = (1,0)^T, \boldsymbol{p}_3 = (0,1)^T, \boldsymbol{p}_4 = (-1,0)^T$. This is sufficient, since we only need to consider

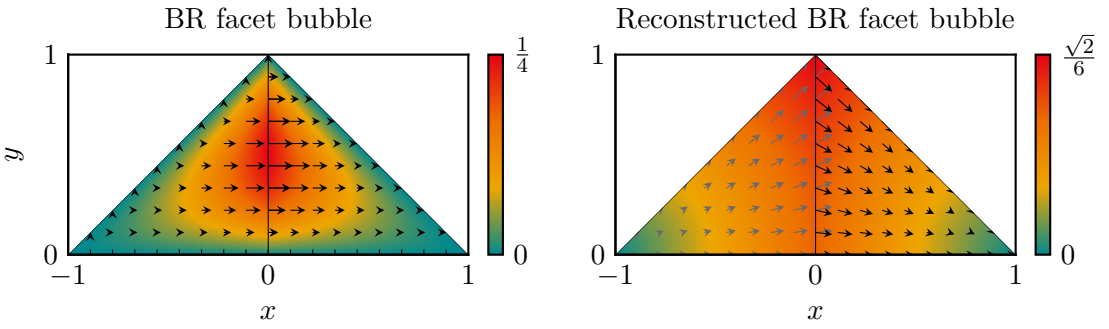

Figure 5.1: Comparison of Bernardi–Raugel facet bubble before and after reconstruction using Brezzi–Douglas–Marini interpolation. Color visualizes function magnitude $|\boldsymbol{t}_F(x,y)|$ resp. $\left|I_1^{\mathrm{BDM}}\boldsymbol{t}_F(x,y)\right|$.

the Brezzi–Douglas–Marini interpolation of the facet bubble functions which, as well as the interpolated function, have support only on two triangles. The facet bubble $\boldsymbol{t}_F = \boldsymbol{n}_F\lambda_1\lambda_3$ associated with the facet $F = \boldsymbol{p}_1\boldsymbol{p}_3$ is now of interest, and fixing the normal as $\boldsymbol{n}_F = (1,0)^T$ it is defined by

$$\boldsymbol{t}_F(x,y) = \begin{pmatrix}(1 \pm x - y)y\\ 0\end{pmatrix}, \quad \text{on } T_{1/2}.$$

With the definition of the lowest-order Brezzi–Douglas–Marini basis functions on triangles from [BBF13, Section 2.6.1] and the definition of the associated interpolation operator, see (4.2), we can compute the reconstructed basis function as

$$I_1^{\mathrm{BDM}}\boldsymbol{t}_F(x,y) = \frac{1}{6}\begin{pmatrix}1 \pm x\\ \pm y\end{pmatrix}, \quad \text{on } T_{1/2}.$$

Both functions are plotted in Figure 5.1. As expected, the tangential component of the function is no longer continuous after the reconstruction.

5.3 Modified Crouzeix–Raviart method

The reconstruction approach was first applied to the Crouzeix–Raviart method, see [Lin14], which is also exceptionally well suited for meshes containing anisotropic elements. Having already introduced the method in Section 3.1, we briefly recall the approximation spaces

$$\mathrm{CR}(\mathcal{T}_h) = \{\boldsymbol{v}_h \in \boldsymbol{L}^2(\Omega) : \boldsymbol{v}_h|_T \in \boldsymbol{P}_1(T)\ \forall T \in \mathcal{T}_h, [\![\boldsymbol{v}_h]\!](\boldsymbol{x}_F) = \boldsymbol{0}\ \forall F \in \mathcal{F}(\mathcal{T}_h)\},$$

for the velocity and

$$Q_h = \{q_h \in Q : q_h|_T \in P_0(T)\ \forall T \in \mathcal{T}_h\}$$

for the pressure. While the method is not $\boldsymbol{H}_0^1(\Omega)$-conforming, the velocity functions are weakly continuous at the element interfaces, meaning that the mean values of the

function on both sides of a facet are equal. Consequently, for $\boldsymbol{v} \in \boldsymbol{X}$ the Crouzeix–Raviart interpolation operator I_h^{CR} is defined by

$$\int_F I_h^{\mathrm{CR}} \boldsymbol{v} \,\mathrm{d}\boldsymbol{s} = \int_F \boldsymbol{v} \,\mathrm{d}\boldsymbol{s} \qquad \forall F \in \mathcal{F}(\mathcal{T}_h). \tag{5.18}$$

Possible reconstruction operators are the lowest-order Raviart–Thomas interpolation operator from Section 4.3.1, for which we use the equivalent definition

$$\boldsymbol{n}_F \cdot I_0^{\mathrm{RT}} \boldsymbol{v}(\boldsymbol{x}_F) = \frac{1}{|F|} \int_F \boldsymbol{v} \cdot \boldsymbol{n}_F \,\mathrm{d}\boldsymbol{s} \qquad \forall F \in \mathcal{F}(\mathcal{T}_h),$$

and a slightly modified version of the lowest-order Brezzi–Douglas–Marini interpolation operator, see Section 4.2.1, where averaging on the facets is used to have a well-defined interpolant for Crouzeix–Raviart functions. This operator I_h^{BDM} is thus defined by

$$\int_F (I_h^{\mathrm{BDM}} \boldsymbol{v}) \cdot \boldsymbol{n}_F z \,\mathrm{d}\boldsymbol{s} = \begin{cases} \int_F \{\!\!\{ \boldsymbol{v} \cdot \boldsymbol{n}_F \}\!\!\} z \,\mathrm{d}\boldsymbol{s} & \text{if } F \in \mathcal{F}^i(\mathcal{T}_h), \\ \int_F (I_0^{\mathrm{RT}} \boldsymbol{v}) \cdot \boldsymbol{n}_F z \,\mathrm{d}\boldsymbol{s} & \text{if } F \in \mathcal{F}^b(\mathcal{T}_h), \end{cases} \qquad \forall z \in P_1(F).$$

Additionally, another slightly adjusted Brezzi–Douglas–Marini interpolation operator is required for meshes where neighboring elements have a large size difference, which for example occurs in the Shishkin-type meshes from Section 2.4.2. This operator is defined by

$$\int_F (I_h^{\mathrm{BDM}'} \boldsymbol{v}) \cdot \boldsymbol{n}_F z \,\mathrm{d}\boldsymbol{s} = \begin{cases} \int_F \langle\!\langle \boldsymbol{v} \cdot \boldsymbol{n}_F \rangle\!\rangle z \,\mathrm{d}\boldsymbol{s} & \text{if } F \in \mathcal{F}^i(\mathcal{T}_h), \\ \int_F (I_0^{\mathrm{RT}} \boldsymbol{v}) \cdot \boldsymbol{n}_F z \,\mathrm{d}\boldsymbol{s} & \text{if } F \in \mathcal{F}^b(\mathcal{T}_h), \end{cases} \qquad \forall z \in P_1(F),$$

where instead of averaging on interior facets we use the values of the function on that side of the facet where the element has larger volume. This is expressed in the notation

$$\langle\!\langle \boldsymbol{v} \cdot \boldsymbol{n}_F \rangle\!\rangle = \begin{cases} \boldsymbol{v} \cdot \boldsymbol{n}_F|_{T_{F,1}} & \text{if } |T_{F,1}| \geq |T_{F,2}|, \\ \boldsymbol{v} \cdot \boldsymbol{n}_F|_{T_{F,2}} & \text{if } |T_{F,2}| > |T_{F,1}|, \end{cases} \tag{5.19}$$

where $\overline{T_{F,1}} \cap \overline{T_{F,2}} = F$.

As this method was investigated in detail in several recent publications, there is a considerable amount of results available. We provide an overview in Table 5.1.

To bring the method into the framework of Section 5.1, we need to check Assumptions 1 to 5.

Theorem 5.12. *Let $\boldsymbol{X}_h$ and Q_h be the Crouzeix–Raviart finite element pair. Further let the reconstruction operator I_h for all $\boldsymbol{v}_h \in \boldsymbol{X}_h$ and $T \in \mathcal{T}_h$ be defined by either $(I_h \boldsymbol{v}_h)|_T = I_0^{\mathrm{RT}} \boldsymbol{v}_h|_T$, or by $I_h \boldsymbol{v}_h = I_h^{\mathrm{BDM}} \boldsymbol{v}_h$ resp. $I_h \boldsymbol{v}_h = I_h^{\mathrm{BDM}'} \boldsymbol{v}_h$ depending on whether neighboring mesh elements are of similar size or not. Then Assumptions 1 to 3 hold for meshes satisfying the maximum angle condition and Assumptions 4 and 5 hold*

i) in two or three dimensions for meshes satisfying the maximum angle condition if the Stokes solution satisfies $(\boldsymbol{u}, p) \in \boldsymbol{H}^2(\Omega) \times H^1(\Omega)$,

Table 5.1: References and results concerning the modified Crouzeix–Raviart method

	Assumptions			
Reference	$(\boldsymbol{u}, p) \in$	Mesh	I_h	Relevant new results
[Lin14]	$\boldsymbol{H}^2 \times H^1$	shape reg.	I_0^{RT}	introduction of method, pressure-rob. gradient estimate for velocity
[BLMS15]	$\boldsymbol{H}^2 \times H^1$	shape reg.	I_h^{BDM}	pressure-rob. gradient and $\boldsymbol{L}^2$ estimate
[LMW17]	$\boldsymbol{H}^2 \times H^1$	shape reg.	I_0^{RT}	pressure-rob. $\boldsymbol{L}^2$ estimate
[LMN20]	$\boldsymbol{H}^{1+s} \times H^s$, $s \in (0, 1]$	shape reg.	$I_0^{\mathrm{RT}}, I_h^{\mathrm{BDM}}$	pressure-rob. gradient estimate with reduced regularity assumptions
[AKLM21]	$\boldsymbol{H}^2 \times H^1$	anisotropic, $MAC(\overline{\phi})$	$I_0^{\mathrm{RT}}, I_h^{\mathrm{BDM}}$	pressure-rob. gradient estimate on anisotropic meshes
[AK21]	see Lemma 2.7	anisotropic, $MAC(\overline{\phi})$	$I_0^{\mathrm{RT}}, I_h^{\mathrm{BDM}}$	optimal convergence rates on graded meshes for singular solutions due to re-entrant edges

ii) in three dimensions for the type of domains and graded meshes described in Section 2.4.3, if the grading parameter μ satisfies $\mu < \lambda$, where λ is the singularity exponent determined by (2.12).

Proof. We again provide proofs for all assumptions individually.

1. Since $\boldsymbol{X}_h$ contains piecewise linear functions, it suffices to show that for $i \in I_d$

$$(q, (\llbracket \boldsymbol{v}_h \rrbracket)_i)_{0,F} = 0 \qquad \forall q \in P_0(F)$$

holds for all $\boldsymbol{v}_h \in \boldsymbol{X}_h$ on every $F \in \mathcal{F}(\mathcal{T}_h)$. Since the jump is a linear function on every facet we have due to the definition of $\mathrm{CR}(\mathcal{T}_h)$ and the midpoint rule

$$(q, (\llbracket \boldsymbol{v}_h \rrbracket)_i)_{0,F} = q \int_F (\llbracket \boldsymbol{v}_h \rrbracket)_i \, \mathrm{d}\boldsymbol{s} = 0.$$

Thus Assumption 1 holds.

2. We observe that (5.1a) holds due to the divergence theorem, see, e.g., [Lin14, Lemma 1] and [LMNN18, Lemma 3.3].

Concerning the interpolation error estimate (5.1b) we can directly apply Theorem 4.22 in the case $I_h = I_0^{\mathrm{RT}}$. For the other possible choices I_h^{BDM} or $I_h^{\mathrm{BDM}'}$ as reconstruction operator we need an additional argument, since it is not simply the elementwise application of I_1^{BDM}. Proofs have been given for the shape regular case in [LMNN18, Lemma 3.3] and [BLMS15, Remark 2.2], which we adapt in the following to the anisotropic setting using some refined arguments.

We start with the proof for I_h^{BDM}. Let $\boldsymbol{v}_h \in \boldsymbol{X}_h$ and look at an individual element T. Then using the triangle inequality we get

$$\left\|\boldsymbol{v}_h - I_h^{\mathrm{BDM}}\boldsymbol{v}_h\right\|_{0,T} \leq \underbrace{\left\|\boldsymbol{v}_h - I_1^{\mathrm{BDM}}\boldsymbol{v}_h\right\|_{0,T}}_{\lesssim h_T\|\nabla \boldsymbol{v}_h\|_{0,T}} + \left\|I_1^{\mathrm{BDM}}\boldsymbol{v}_h - I_h^{\mathrm{BDM}}\boldsymbol{v}_h\right\|_{0,T}, \tag{5.20}$$

where the bound for the first term on the right hand side comes from Theorem 4.16. Now observe that $I_1^{\mathrm{BDM}}\boldsymbol{v}_h - I_h^{\mathrm{BDM}}\boldsymbol{v}_h \in \boldsymbol{P}_1(T)$ and that elements from $\boldsymbol{P}_1(T)$ are uniquely determined by the values of their normal traces on ∂T. Using this on the reference element and transforming to the general element we get

$$\frac{1}{|T|}\left\|I_1^{\mathrm{BDM}}\boldsymbol{v}_h - I_h^{\mathrm{BDM}}\boldsymbol{v}_h\right\|_{0,T}^2 \lesssim \sum_{F\in\mathcal{F}(T)} \frac{1}{|F|}\left\|(I_1^{\mathrm{BDM}}\boldsymbol{v}_h - I_h^{\mathrm{BDM}}\boldsymbol{v}_h)\cdot\boldsymbol{n}_F\right\|_{0,F}^2. \tag{5.21}$$

Since $\left|(I_1^{\mathrm{BDM}}\boldsymbol{v}_h - I_h^{\mathrm{BDM}}\boldsymbol{v}_h)\cdot\boldsymbol{n}_F\right| = \frac{1}{2}|[\![\boldsymbol{v}_h]\!]\cdot\boldsymbol{n}_F|$ on each $F \in \mathcal{F}(T)$, we get

$$|T|^{-1}\left\|I_1^{\mathrm{BDM}}\boldsymbol{v}_h - I_h^{\mathrm{BDM}}\boldsymbol{v}_h\right\|_{0,T}^2 \lesssim \sum_{F\in\mathcal{F}(T)} |F|^{-1}\|[\![\boldsymbol{v}_h]\!]\cdot\boldsymbol{n}_F\|_{0,F}^2. \tag{5.22}$$

Using a Poincaré inequality on the facet F and the trace inequality

$$\|\nabla \boldsymbol{w}_h\cdot\boldsymbol{n}_F\|_{0,F} \lesssim \frac{|F|^{1/2}}{|T|^{1/2}}\|\nabla\boldsymbol{w}_h\|_{0,T},$$

for functions $\boldsymbol{w}_h \in \boldsymbol{P}_k(T)$, see, e.g., [WH03] and [Riv08, p. 23], yields

$$\begin{aligned}\|[\![\boldsymbol{v}_h]\!]\cdot\boldsymbol{n}_F\|_{0,F} &\lesssim h_F\|\nabla[\![\boldsymbol{v}_h]\!]\cdot\boldsymbol{n}_F\|_{0,F} = h_F\|\nabla(\boldsymbol{v}_h|_T - \boldsymbol{v}_h|_{T'})\cdot\boldsymbol{n}_F\|_{0,F}\\ &\lesssim h_F\left(\frac{|F|^{1/2}}{|T|^{1/2}}\|\nabla\boldsymbol{v}_h\|_{0,T} + \frac{|F|^{1/2}}{|T'|^{1/2}}\|\nabla\boldsymbol{v}_h\|_{0,T'}\right),\end{aligned} \tag{5.23}$$

where $\overline{T}\cap\overline{T'} = F$. Combining the estimates (5.22) and (5.23) and using $h_F \leq h_T$ we get

$$\left\|I_1^{\mathrm{BDM}}\boldsymbol{v}_h - I_h^{\mathrm{BDM}}\boldsymbol{v}_h\right\|_{0,T}^2 \lesssim h_T^2 \sum_{F\in\mathcal{F}(T)}\left(\|\nabla\boldsymbol{v}_h\|_{0,T} + \frac{|T|^{1/2}}{|T'|^{1/2}}\|\nabla\boldsymbol{v}_h\|_{0,T'}\right)^2. \tag{5.24}$$

Now combining (5.24) with (5.20) and summing over all elements yields the estimate (5.1b) for meshes where the elements do not rapidly change size, i.e., where for all neighboring elements T and T'

$$\frac{|T|}{|T'|} \leq C, \quad C \in \mathbb{R}, \tag{5.25}$$

holds.

For meshes where (5.25) is not valid, e.g., meshes of Shishkin-type, we can instead use the operator $I_h^{\mathrm{BDM}'}$. The proof in this case is analogous until (5.21), where we now see with the definition of $I_h^{\mathrm{BDM}'}$ that those summands vanish from the sum, where the element T is the larger of the two elements adjacent to the facet F. We collect those facets F for which the summands do not vanish in the possibly empty set $\mathcal{F}^r(T)$, and can proceed in the same way as above since $\left|(I_1^{\mathrm{BDM}}\boldsymbol{v}_h - I_h^{\mathrm{BDM}'}\boldsymbol{v}_h)\cdot\boldsymbol{n}_F\right| = |[\![\boldsymbol{v}_h]\!]\cdot\boldsymbol{n}_F|$ for the remaining summands. This leads to an estimate analogous to (5.24), where the sum is taken over $\mathcal{F}^r(T)$ instead of $\mathcal{F}(T)$ and we have

$$\frac{|T|}{|T'|} \leq 1,$$

since for all remaining facets in the set $\mathcal{F}^r(T)$ the element T' has larger volume than T.

Thus Assumption 2 holds.

3. Let $\boldsymbol{v} \in \boldsymbol{X}$. Using integration by parts, the fact that $q_h \in Q_h$ is piecewise constant and the interpolation property from (5.18), we compute

$$\begin{aligned}
b_h(\boldsymbol{v} - I_h^{\mathrm{CR}}\boldsymbol{v}, q_h) &= -\int_\Omega \nabla_h \cdot (\boldsymbol{v} - I_h^{\mathrm{CR}}\boldsymbol{v}) q_h \,\mathrm{d}\boldsymbol{x} \\
&= \sum_{T\in\mathcal{T}_h} -\int_T \nabla\cdot(\boldsymbol{v} - I_h^{\mathrm{CR}}\boldsymbol{v})\cdot q_h \,\mathrm{d}\boldsymbol{x} \\
&= \sum_{T\in\mathcal{T}_h} \left(\int_T (\boldsymbol{v} - I_h^{\mathrm{CR}}\boldsymbol{v})\cdot\nabla q_h \,\mathrm{d}\boldsymbol{x} + \int_{\partial T} (I_h^{\mathrm{CR}}\boldsymbol{v} - \boldsymbol{v})\cdot\boldsymbol{n}_{\partial T} q_h \,\mathrm{d}\boldsymbol{s}\right) \\
&= \sum_{T\in\mathcal{T}_h} q_h|_T \sum_{F\in\mathcal{F}(T)} \int_F (I_h^{\mathrm{CR}}\boldsymbol{v} - \boldsymbol{v})\cdot\boldsymbol{n}_{T,F} \,\mathrm{d}\boldsymbol{s} \\
&= \sum_{T\in\mathcal{T}_h} q_h|_T \sum_{F\in\mathcal{F}(T)} \left(\int_F (I_h^{\mathrm{CR}}\boldsymbol{v} - \boldsymbol{v}) \,\mathrm{d}\boldsymbol{s}\right)\cdot\boldsymbol{n}_{T,F} = 0,
\end{aligned}$$

where the integral of a vector function is to be understood componentwise. For the proof of the elementwise estimate $\left\|I_h^{\mathrm{CR}}\boldsymbol{v}\right\|_{1,T} \leq \|\boldsymbol{v}\|_{1,T}$ see [ANS01b, Lemma 2] in combination with the comment after [ANS01b, Corollary 1]. Summing over all elements gives a global stability estimate. Thus Assumption 3 holds.

For Assumptions 4 and 5 we give separate proofs for the cases we defined in the theorem.

4. i) The first consistency error estimate (5.3a) for meshes satisfying a maximum angle condition and the Crouzeix–Raviart discretization was shown in [AD99, Lemma 3.1], using the error estimate for the lowest-order Raviart–Thomas interpolation, which we provided in Chapter 4. Estimate (5.3b) follows immediately due to Lemma 5.3.

ii) Inequality (5.3a) for this case is the statement of [ANS01a, Lemma 3.3], estimate (5.3b) follows again due to Lemma 5.3.

5. i) First recall the approximation result

$$\inf_{\boldsymbol{v}_h \in \boldsymbol{X}_h^0} \|\boldsymbol{u} - \boldsymbol{v}_h\|_{1,h} \lesssim \inf_{\boldsymbol{v}_h \in \boldsymbol{X}_h} \|\boldsymbol{u} - \boldsymbol{v}_h\|_{1,h}$$

from, e.g., [AKLM21, Lemma 3.5] and the elementwise Crouzeix–Raviart interpolation error estimates from [AD99, Lemma 2.3] which for $\boldsymbol{v} \in \boldsymbol{X} \cap \boldsymbol{H}^2(\Omega)$ give the global estimate

$$\left\|\boldsymbol{v} - I_h^{\mathrm{CR}} \boldsymbol{v}\right\|_{1,h} \lesssim h|\boldsymbol{v}|_2,$$

see also [AKLM21, Lemma 3.4]. Combining these two estimates and using Lemma 5.1 as well as (2.13) we get the estimate

$$\inf_{\boldsymbol{v}_h \in \boldsymbol{X}_h^0} \|\boldsymbol{u} - \boldsymbol{v}_h\|_{1,h} \lesssim h|\boldsymbol{u}|_2 \lesssim h\nu^{-1}\|\mathbb{P}\boldsymbol{f}\|_0 = h\|\mathbb{P}(\Delta \boldsymbol{u})\|_0,$$

which we need for Assumption 5. The approximation result for the pressure space of piecewise constants was already shown in Item 5 of the proof of Theorem 5.9. Thus the assumption is satisfied for this case.

ii) For this case we get from [ANS01a, Lemma 3.2] and by using Lemma 5.1 in combination with (2.13) the estimate

$$\inf_{\boldsymbol{v}_h \in \boldsymbol{X}_h} \|\boldsymbol{u} - \boldsymbol{v}_h\|_{1,h} \lesssim h\|\mathbb{P}(\Delta \boldsymbol{u})\|_0,$$

which in conjunction with [AKLM21, Lemma 3.5] gives the first estimate of Assumption 5. The second inequality of the assumption is directly contained in [ANS01a, Lemma 3.2]. □

Example 5.13. Just as before with the Bernardi–Raugel method we want to look at the effect of the reconstruction on the Crouzeix–Raviart basis functions. We again look at the reference configuration of two triangles $T_1 = \boldsymbol{p}_1\boldsymbol{p}_3\boldsymbol{p}_4$ and $T_2 = \boldsymbol{p}_1\boldsymbol{p}_2\boldsymbol{p}_3$, with the same vertices as in Example 5.11. We now use the Raviart–Thomas reconstruction on one of the basis functions associated with the facet $F = \boldsymbol{p}_1\boldsymbol{p}_3$, which is defined by

$$\boldsymbol{t}_{F,1}(x,y) = \begin{pmatrix} 1 \pm 2x \\ 0 \end{pmatrix}, \quad \text{on } T_{1/2},$$

which yields the reconstructed basis function

$$I_0^{\mathrm{RT}} \boldsymbol{t}_{F,1}(x,y) = \begin{pmatrix} 1 \pm x \\ \pm y \end{pmatrix}, \quad \text{on } T_{1/2}.$$

Both functions are visualized in Figure 5.2.

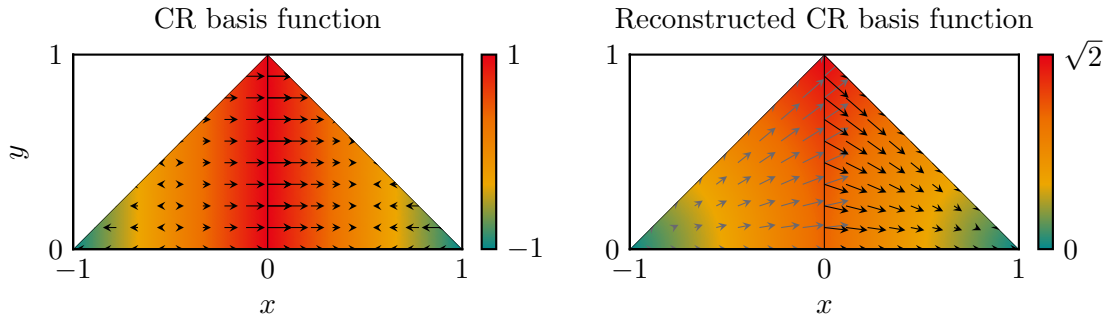

Figure 5.2: Comparison of Crouzeix–Raviart basis function before and after reconstruction using Raviart–Thomas interpolation. Color visualizes function magnitude $|\boldsymbol{t}_{F,1}(x,y)|$ resp. $\left|I_0^{\mathrm{RT}}\boldsymbol{t}_{F,1}(x,y)\right|$.

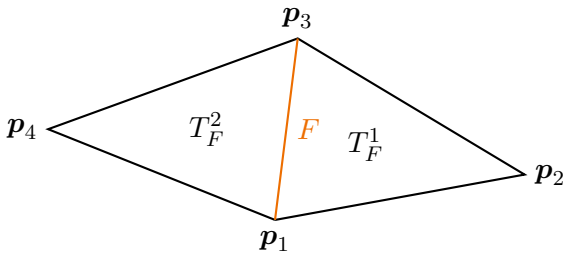

Figure 5.3: Geometric setting for Remark 5.14

Remark 5.14. The reconstructed Bernardi–Raugel facet bubble from Example 5.11, which is due to Proposition 5.10 the same for the two types of reconstruction, and the reconstructed Crouzeix–Raviart basis function from Example 5.13 are, except for scaling, the same function.

This is not just a result of the used reference geometry, but a general connection. Consider the general setting of two triangles, as illustrated in Figure 5.3. Then the Bernardi–Raugel bubble function $\boldsymbol{t}_F^{\mathrm{BR}}$ and Crouzeix–Raviart basis function $\boldsymbol{t}_{F,1}^{\mathrm{CR}}$ from the two examples have the form

$$\boldsymbol{t}_F^{\mathrm{BR}} = \phi_1\phi_3\boldsymbol{n}_F, \qquad \boldsymbol{t}_{F,1}^{\mathrm{CR}} = \begin{pmatrix} \phi_1 + \phi_3 - \phi_2 - \phi_4 \\ 0 \end{pmatrix},$$

with the standard hat functions ϕ_i associated to the mesh vertices $\boldsymbol{p}_i$.

We now want to compare $I_0^{\mathrm{RT}}\boldsymbol{t}_F^{\mathrm{BR}}$ to $I_0^{\mathrm{RT}}\boldsymbol{t}_{F,1}^{\mathrm{CR}}$. The fastest way to do this is to compute the interpolation coefficients for the representations

$$I_0^{\mathrm{RT}}\boldsymbol{t}_F^{\mathrm{BR}} = \sum_E a_E^{\mathrm{BR}}\boldsymbol{\phi}_E^{\mathrm{RT}}, \qquad I_0^{\mathrm{RT}}\boldsymbol{t}_{F,1}^{\mathrm{CR}} = \sum_E a_E^{\mathrm{CR}}\boldsymbol{\phi}_E^{\mathrm{RT}},$$

where $\boldsymbol{\phi}_E^{\mathrm{RT}}$ is the Raviart–Thomas basis function associated with the facet E, and

according to (4.22a)

$$a_E^{\mathrm{BR}} = \int_E \boldsymbol{t}_F^{\mathrm{BR}} \cdot \boldsymbol{n}_E \,\mathrm{d}\boldsymbol{s}, \qquad a_E^{\mathrm{CR}} = \int_E \boldsymbol{t}_{F,1}^{\mathrm{CR}} \cdot \boldsymbol{n}_E \,\mathrm{d}\boldsymbol{s}.$$

Since for $E \neq F$ it holds $\boldsymbol{t}_F^{\mathrm{BR}} \equiv 0$ and $\int_E \boldsymbol{t}_{F,1}^{\mathrm{CR}} \cdot \boldsymbol{n}_E \,\mathrm{d}\boldsymbol{s} = 0$, the interpolation problem is reduced to finding a_F^{BR} and a_F^{CR}, which we can directly compute as

$$\begin{aligned} a_F^{\mathrm{BR}} &= \int_F \boldsymbol{t}_F^{\mathrm{BR}} \cdot \boldsymbol{n}_F \,\mathrm{d}\boldsymbol{s} = \int_F \phi_1\phi_3 \boldsymbol{n}_F \cdot \boldsymbol{n}_F \,\mathrm{d}\boldsymbol{s} = \int_0^{|F|} \frac{x}{|F|}\left(1 - \frac{x}{|F|}\right) \mathrm{d}x = \frac{|F|}{6}, \\ a_F^{\mathrm{CR}} &= \int_F \boldsymbol{t}_{F,1}^{\mathrm{CR}} \cdot \boldsymbol{n}_F \,\mathrm{d}\boldsymbol{s} = (\boldsymbol{n}_F)_1 \int_F \mathrm{d}\boldsymbol{s} = (\boldsymbol{n}_F)_1 |F|. \end{aligned}$$

Thus we identified the scaling factor and have

$$I_0^{\mathrm{RT}} \boldsymbol{t}_{F,1}^{\mathrm{CR}} = 6(\boldsymbol{n}_F)_1 I_0^{\mathrm{RT}} \boldsymbol{t}_F^{\mathrm{BR}},$$

which agrees with the functions from Examples 5.11 and 5.13 for the fixed geometry.

CHAPTER 6

Numerical examples

The following sections contain applications of the methods from Sections 5.2 and 5.3, where with each example a specific aspect of the methods is highlighted. We start in Section 6.1 with an example that uses a manufactured solution that prescribes a boundary layer in the velocity and pressure. This example shows the general applicability and performance of the pressure-robust methods in combination with anisotropic meshes. Continuing in Section 6.2 with the stagnation point flow, see, e.g., [SG06, Section 5.1.3], we show that the methods perform well in more realistic applications, and also work with the nonlinear term present in the discretization of the stationary Navier–Stokes equations. In Section 6.3 we numerically investigate edge singularities of the Stokes flow with pressure-robust methods and anisotropically graded meshes from Section 2.4.3.

In the following examples we use the abbreviations CR and BR for the Crouzeix–Raviart and Bernardi–Raugel methods and add a suffix -RT or -BDM for the pressure robust variants from Sections 5.2 and 5.3.

6.1 Boundary layer

Problem setting The purpose of this first example is to examine the performance of the pressure-robust methods in combination with anisotropic meshes. The example employs a manufactured solution of the Stokes equations on the unit square $\Omega = (0,1)^2$ described by the velocity and pressure functions

$$\boldsymbol{u}(\boldsymbol{x}) = \begin{pmatrix} \tanh\left(\frac{y}{\sqrt{\varepsilon}}\right) \\ 0 \end{pmatrix}, \qquad p(\boldsymbol{x}) = \tanh\left(\frac{y}{\sqrt{\varepsilon}}\right) - C(\varepsilon),$$

with a positive parameter ε. Both functions exhibit a boundary layer near $y = 0$, as can be seen in the visualization in Figure 6.1. The functions can be viewed as a fluid flow

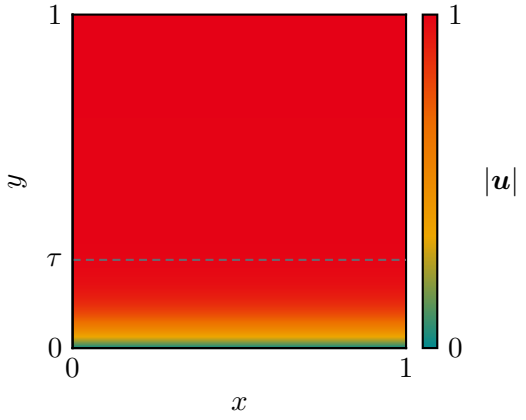

Figure 6.1: Magnitude of velocity solution for $\varepsilon = 10^{-2}$. The transition parameter τ is chosen so that the boundary layer is contained in the graded part of the mesh, see the dashed line in the figure.

along a wall with no-slip boundary condition. The parameter ε can be used to adjust the width of the boundary layer. Defining the boundary layer width as the distance from the wall where 99% of the free flow velocity is reached, we compute

$$\begin{aligned} |\boldsymbol{u}(\cdot,\tau)| &= \tanh\left(\frac{\tau}{\sqrt{\varepsilon}}\right) = 0.99 \\ \Leftrightarrow \qquad \tau &= 0.5\sqrt{\varepsilon}\ln(199) \approx 2.65\sqrt{\varepsilon} \end{aligned}$$

for the transition point parameter τ of the Shishkin-type meshes we want to use, see Section 2.4.2 and Figure 2.5, and additionally choose the mesh parameter $q = 0.5$, meaning that half of the total mesh elements are to be used in the layer. The constant $C(\varepsilon)$ is needed to set the mean pressure to zero and can be computed by

$$C(\varepsilon) = \int_\Omega \tanh\left(\frac{y}{\sqrt{\varepsilon}}\right) \mathrm{d}\boldsymbol{x} = \sqrt{\varepsilon}\ln\Big(\cosh\Big(\varepsilon^{-1/2}\Big)\Big).$$

Numerical results Computations were performed with the CR, CR-RT, CR-BDM as well as the BR and BR-BDM methods for parameter choices $\varepsilon \in \{10^{-4}, 10^{-5}\}$ and $\nu \in \{10^{-3}, 10^{-5}\}$ on uniform and Shishkin-type meshes. For the presentation of the numerical results in this and the next sections we use the relative errors

$$\|\boldsymbol{u} - \boldsymbol{u}_h\|_{1,h,\mathrm{rel}} = \frac{\|\boldsymbol{u} - \boldsymbol{u}_h\|_{1,h}}{\|\boldsymbol{u}\|_{1,h}}, \qquad \|p - p_h\|_{0,\mathrm{rel}} = \frac{\|p - p_h\|_0}{\|p\|_0}.$$

Figure 6.2 shows the convergence results of the CR, CR-RT and CR-BDM methods for viscosity $\nu = 10^{-3}$. The plots show on the one hand the clear advantage of the pressure-robust methods, where the velocity errors are significantly smaller than for the standard method. On the other hand, the effect of the anisotropic mesh grading is

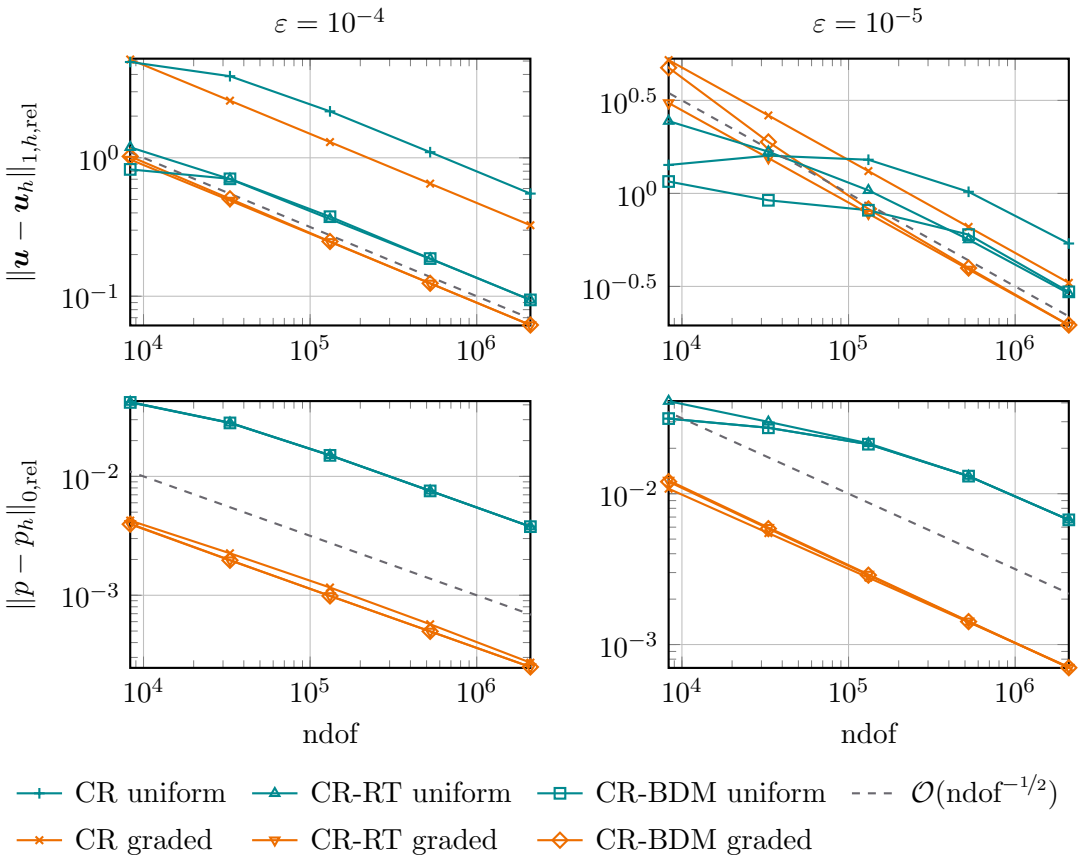

Figure 6.2: Convergence plots for the boundary layer example for $\varepsilon \in \{10^{-4}, 10^{-5}\}$, $\nu = 10^{-3}$, with CR, CR-RT and CR-BDM methods.

obvious in the velocity errors as well as the pressure errors. In this example and for these methods the positive effect of using a pressure-robust method seems to be larger than the positive effect of the mesh grading.

To better observe the effect of the pressure-robustness of the methods, Table 6.1 compares the errors of the CR, CR-RT and CR-BDM methods for two viscosity values on graded meshes. The typical viscosity locking effect of the classical method can be seen by the scaling with ν^{-1} of the velocity errors for the standard method, while the pressure-robust modifications yield exactly the same results for each of the viscosity values.

Computations were also carried out for the BR and BR-BDM methods with parameters $\nu = 10^{-4}$, $\varepsilon \in \{10^{-4}, 10^{-5}\}$ and the results are shown in Figure 6.3. Here the general picture looks similar, the use of both a pressure-robust method and anisotropic mesh grading results in a significant reduction of the error.

Table 6.1: Comparison of $\|\boldsymbol{u} - \boldsymbol{u}_h\|_{1,h}$ for parameters $\varepsilon = 10^{-4}$, $\nu \in \{10^{-3}, 10^{-5}\}$, computed with CR, CR-RT and CR-BDM methods on Shishkin-type meshes.

	CR		CR-RT		CR-BDM	
ndof	$\nu = 10^{-3}$	$\nu = 10^{-5}$	$\nu = 10^{-3}$	$\nu = 10^{-5}$	$\nu = 10^{-3}$	$\nu = 10^{-5}$
8 320	5.1285e+0	5.1381e+2	9.7122e−1	9.7122e−1	1.0228e+0	1.0228e+0
33 024	2.5865e+0	2.5913e+2	4.9162e−1	4.9162e−1	5.0568e−1	5.0568e−1
131 584	1.2989e+0	1.3013e+2	2.4719e−1	2.4719e−1	2.4863e−1	2.4863e−1
525 312	6.5090e−1	6.5214e+1	1.2387e−1	1.2387e−1	1.2400e−1	1.2400e−1
2 099 200	3.2578e−1	3.2641e+1	6.1977e−2	6.1977e−2	6.1973e−2	6.1973e−2

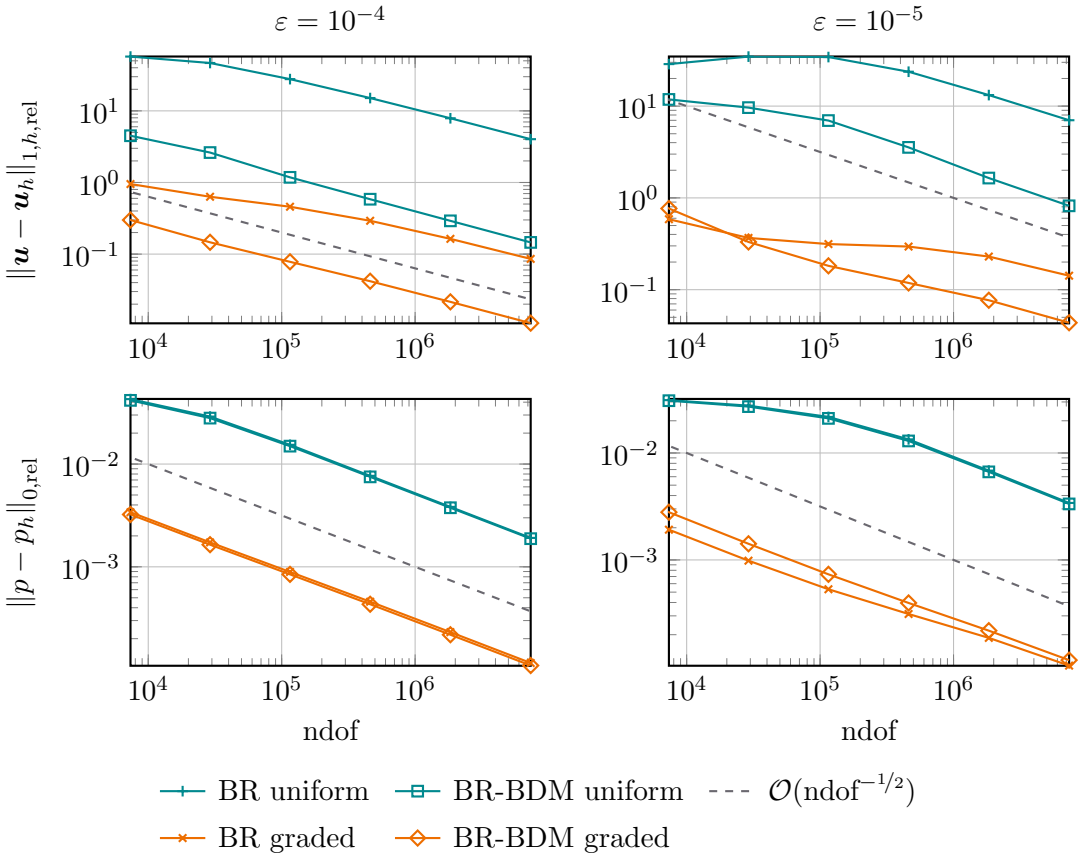

Figure 6.3: Convergence plots for the boundary layer example for $\varepsilon \in \{10^{-4}, 10^{-5}\}$, $\nu = 10^{-4}$, with BR and BR-BDM methods.

6.2 Stagnation point flow

For this example we can compute the exact solution to numerical accuracy for the case of homogeneous stationary Navier–Stokes equations, which we use in the first subsection to generate a data function $\boldsymbol{f} = -(\boldsymbol{u} \cdot \nabla)\boldsymbol{u}$ for our Stokes model. In the second subsection we test the methods with the included nonlinear term and zero right hand side data.

6.2.1 Stokes model

Problem setting The stagnation point flow example describes the stationary laminar flow of a fluid against a flat wall. In this setting the Navier–Stokes equations reduce to a boundary value problem with an ordinary differential equation. The example has originally been investigated in [Hie11], and is described in detail in [SG06, Section 5.1.3] and [DR06, Section 2.3]. We already showed some numerical results in [Kem21].

Assuming the wall is situated at the $y = 0$ boundary and a potential flow

$$\begin{aligned} \boldsymbol{U} &= \begin{pmatrix} U_1 \\ U_2 \end{pmatrix} = \begin{pmatrix} ax \\ -ay \end{pmatrix}, & a &\in \mathbb{R}_+, \\ P &= P_0 - \frac{1}{2}(U_1^2 + U_2^2) = P_0 - \frac{a^2}{2}(x^2 + y^2), & P_0 &\in \mathbb{R}, \end{aligned}$$

is present far from the wall, where $P_0 \in \mathbb{R}$ is the pressure in the stagnation point $(0, 0)^T$, the viscosity effects in the boundary layer near the wall can be included by using the ansatz

$$\boldsymbol{u} = \begin{pmatrix} u_1 \\ u_2 \end{pmatrix} = \begin{pmatrix} axf'(\eta) \\ -\sqrt{a\nu} f(\eta) \end{pmatrix}, \tag{6.1a}$$

$$p = P_0 - \frac{a^2}{2}\left(x^2 + \frac{2\nu}{a} F(\eta)\right), \tag{6.1b}$$

where $\eta = \sqrt{\frac{a}{\nu}} y$ is a transformed coordinate and f satisfies an ordinary differential equation, which we get by inserting (6.1) into the homogeneous Navier–Stokes momentum equation for the x-component, which yields

$$-\nu\Delta u_1 + u_1\partial_x u_1 + u_2\partial_y u_1 + \partial_x p = -a^2 x(f''' + ff'' + 1 - f'^2) = 0,$$

i.e., f needs to satisfy

$$f''' + ff'' + 1 - f'^2 = 0. \tag{6.2}$$

Using the analogous approach with the y-component of the momentum equation, we get

$$-\nu\Delta u_2 + u_1\partial_x u_2 + u_2\partial_y u_2 + \partial_y p = a\sqrt{a\nu}(f'' + ff' - F') = 0,$$

which after integration leads to $F = f' + \frac{1}{2}f^2$.

From the no-slip condition at the wall and the assumption that far from the wall the original potential flow is present, we can derive the boundary conditions $f(0) = f'(0) = 0$

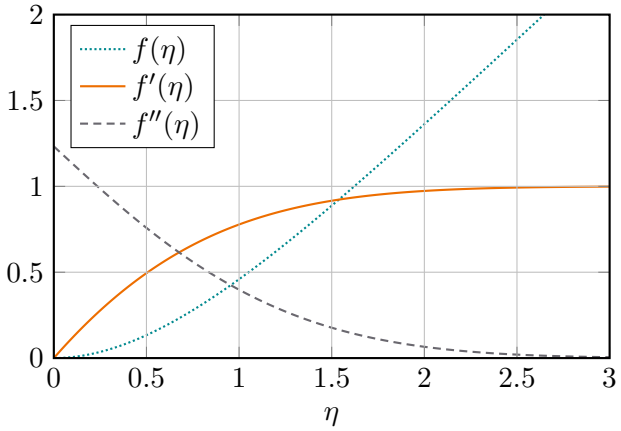

Figure 6.4: Plot of the solution of (6.2) and its derivatives.

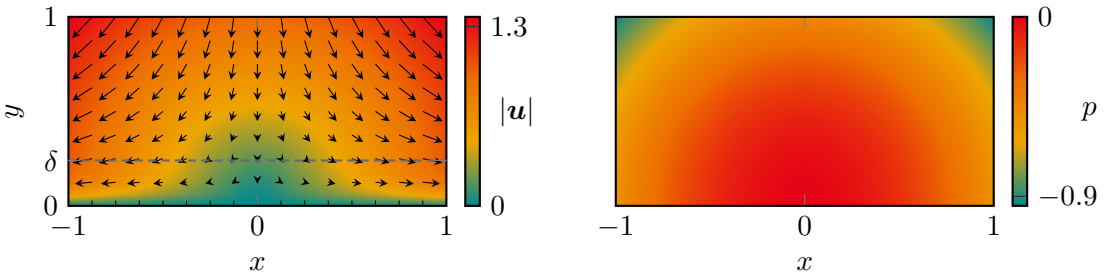

Figure 6.5: Visualization of the velocity (left) and pressure (right) solution $\boldsymbol{u}$ and p for $\nu = 0.01$, $a = 1$, $P_0 = 0$. Color indicates the magnitude of the velocity and the pressure value, respectively. Arrows show the flow direction and strength. The boundary layer width is indicated at $\delta = 0.24$.

and $\lim_{\eta\to\infty} f'(\eta) = 1$ for (6.2), which then can be solved numerically to high precision, e.g., using a shooting method. Figure 6.4 shows a plot of f and its derivatives. At $\eta_\delta \approx 2.4$ we have $f'(\eta_\delta) \approx 0.99$, and since $f' = \frac{u_1}{U_1}$ is the ratio of the viscous flow velocity and the potential flow velocity in x-direction, we define $\delta = \eta_\delta \sqrt{\frac{\nu}{a}}$ as the boundary layer width. Plugging the numerical solution for f back into (6.1), we get the exact solution $(\boldsymbol{u}, p)$ for the stagnation point flow, which is shown in Figure 6.5 in the domain $\Omega = (-1, 1) \times (0, 1)$ for $\nu = 10^{-2}$, $a = 1$ and $P_0 = 0$. The boundary layer structure is only present in the velocity profile, the pressure does not show a similar behavior.

With this setup, since $\boldsymbol{u}$ is the solution of the homogeneous stationary Navier–Stokes equations, we can test our numerical methods for the Stokes equations by using the expression $\boldsymbol{f} = -(\boldsymbol{u} \cdot \nabla)\boldsymbol{u}$ as right hand side data function where $\boldsymbol{u}$ is the exact solution from (6.1a) and by taking $\boldsymbol{u}$ also as boundary condition on $\partial\Omega$.

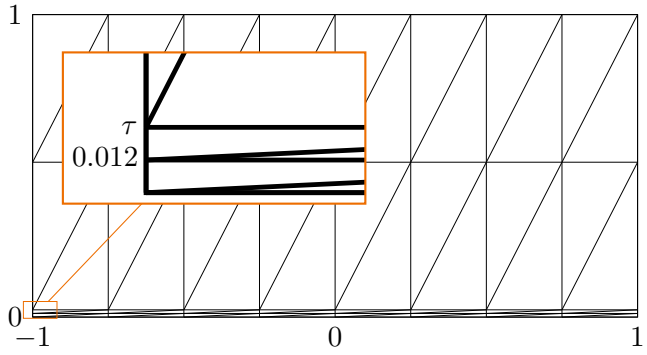

Figure 6.6: Shishkin type mesh used in the calculations. Grading for $\nu = 10^{-4}$, resulting in an aspect ratio of $\sigma \approx 21.4$.

Numerical results For the computations we use the domain $\Omega = (-1, 1) \times (0, 1)$ and set $a = 1$, $P_0 = 0$ and $\nu = 10^{-4}$, which results in a rather sharp boundary layer with width $\delta = 0.024$. The purpose of this numerical experiment is to show a benefit from using anisotropic elements, so we compare the errors on quasi-uniform meshes to those on graded meshes. We also want to see the effect of the pressure-robust methods, so we compare the CR, CR-RT and CR-BDM, as well as the BR and BR-BDM methods.

We choose a simple type of mesh grading and use Shishkin-type meshes, as pictured in Figure 6.6, where the transition point τ is set to δ. For both uniform and graded meshes we divide the domain in $4N \times 2N$ quadrilaterals which we then subdivide in two triangles each. This results in rectangular isosceles triangles for the uniform meshes, and in rectangular triangles satisfying the maximum angle condition for the Shishkin-type meshes.

Figure 6.7 shows the calculated errors and convergence rates. We can clearly see a large improvement of the error when switching from the standard method to the pressure-robust variant, and another reduction when we use graded meshes in addition to the reconstruction.

Looking at the results from the standard method on graded meshes however, we find that the error is larger than on the uniform meshes which seems wrong, considering the boundary layer structure of the velocity solution. To explain this behavior, we examine the elementwise gradient error $\|\nabla(\boldsymbol{u} - \boldsymbol{u}_h)\|^2_{0,T}$ of the discrete velocity solution for both methods, see Figure 6.8.

From these visualizations of the error it is easy to see why the grading works for the modified but not for the unmodified method: Due to the pollution of the discrete velocity solution by the pressure in the standard method, the error is not only significantly larger, but also distributed throughout the domain, while for the pressure-robust version of the method it is concentrated near the boundary layer as would be expected. Thus, for the standard method, the mesh grading is not adapted to the actual error which then results in a worse approximation.

The same aspect can be looked at from a less experimental viewpoint by directly

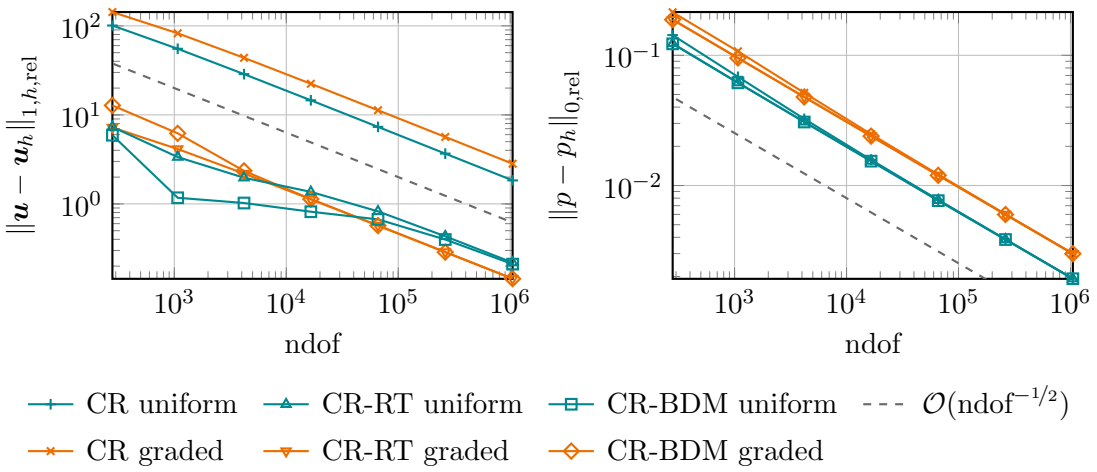

Figure 6.7: Convergence plots for the stagnation point example, $\nu = 10^{-4}$.

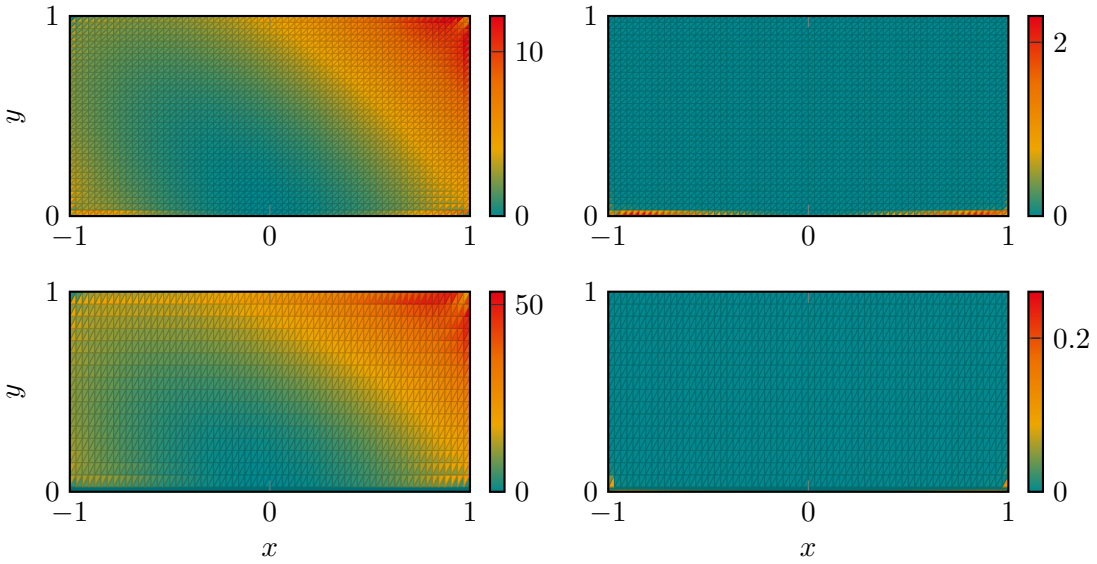

Figure 6.8: Squared elementwise gradient error $\|\nabla(\boldsymbol{u} - \boldsymbol{u}_h)\|_{0,T}^2$ of the velocity solution for the standard (left) and modified (right) method on uniform (top) and graded (bottom) meshes.

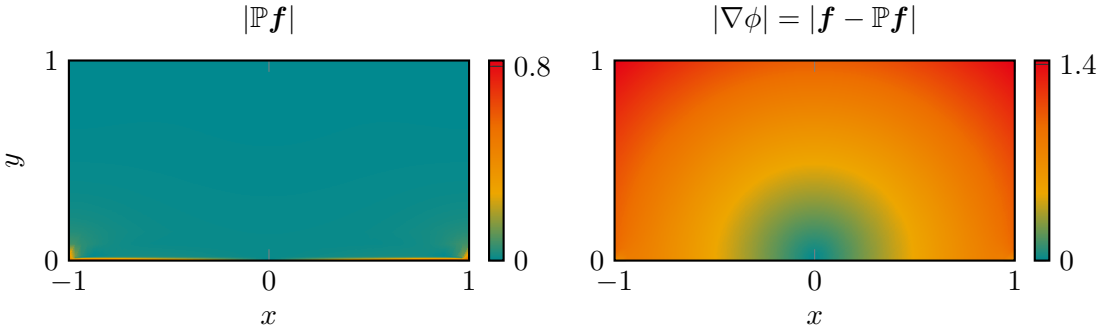

Figure 6.9: Helmholtz–Hodge decomposition of the data function $\boldsymbol{f} = -(\boldsymbol{u} \cdot \nabla)\boldsymbol{u}$ into divergence-free part $\mathbb{P}\boldsymbol{f}$ and irrotational part $\nabla\phi$.

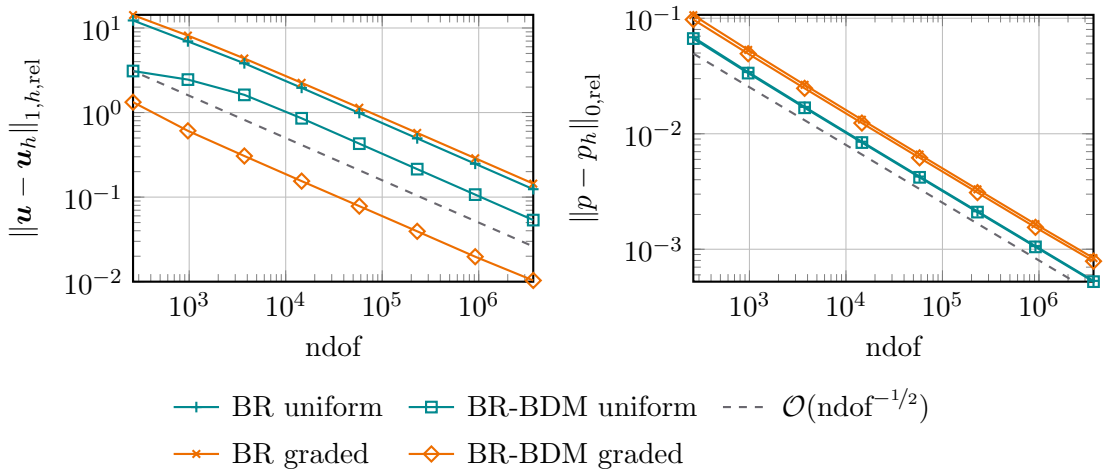

Figure 6.10: Convergence plots for the stagnation point example, comparison of BR and BR-BDM methods, $\nu = 10^{-3}$.

computing the Helmholtz–Hodge decomposition of the data function $\boldsymbol{f} = -(\boldsymbol{u} \cdot \nabla)\boldsymbol{u}$ by solving problem (2.3). The visualization in Figure 6.9 shows that the divergence-free part $\mathbb{P}\boldsymbol{f}$ of the data is only relevant in the boundary layer, while the irrotational part $\nabla\phi$ takes nonzero values throughout the domain. Contrary to pressure-robust methods that only see the divergence-free part, non-pressure-robust methods use the whole data function, so the structure of the data presents another explanation why the graded meshes fail for the standard method.

Finally we also considered this example with the standard and modified Bernardi–Raugel discretizations for $\nu = 10^{-3}$. Figure 6.10 shows the results of these computations. We observe the same behavior of the errors for which the same explanation holds as already described for the standard and pressure-robust Crouzeix–Raviart methods.

6.2.2 Stationary Navier–Stokes model

Problem setting The stagnation point flow is in fact an exact solution to the stationary Navier–Stokes problem, i.e., problem (2.5) where $\partial_t \boldsymbol{u} \equiv 0$. Thus the computations from the previous subsection using a Stokes model, where the convection term of the Navier–Stokes equation with the exact velocity solution was taken as the right hand side data function $\boldsymbol{f} = -(\boldsymbol{u} \cdot \nabla)\boldsymbol{u}$, are only a test with reduced complexity to show the performance of the methods we analyzed analytically. We now want to show that the methods also perform well when we use an implementation of the stationary Navier–Stokes equations.

To this effect, we use a Picard-iteration type scheme and linearize the nonlinear convection term in the equations. Using the function $\boldsymbol{u}_h^{(0)} \equiv \boldsymbol{0}$ to start the iteration, we use the linearized scheme

$$\begin{aligned} a_h(\boldsymbol{u}_h^{(m+1)}, \boldsymbol{v}_h) + c_h(\boldsymbol{u}_h^{(m)}, \boldsymbol{u}_h^{(m+1)}, \boldsymbol{v}_h) + b_h(\boldsymbol{v}_h, p_h^{(m+1)}) &= (\boldsymbol{f}, I_h \boldsymbol{v}_h), \\ b_h(\boldsymbol{u}_h^{(m+1)}, q_h) &= 0, \end{aligned}$$

to solve for the solution $\boldsymbol{u}_h^{(m+1)}$, $m \in \mathbb{N}_0$, which should converge to the solution of the nonlinear problem, see, e.g., [Joh16, Remark 6.41]. The trilinear form $c : \boldsymbol{X}_h^3 \to \mathbb{R}$ is defined by

$$c_h(\boldsymbol{u}_h, \boldsymbol{w}_h, \boldsymbol{v}_h) = ((I_h \boldsymbol{u}_h \cdot \nabla)\boldsymbol{w}_h, I_h \boldsymbol{v}_h),$$

where again I_h is the reconstruction operator. The operator is needed in the definition of the trilinear form since the irrotational part of the Helmholtz–Hodge decomposition of the nonlinear term $(\boldsymbol{u} \cdot \nabla)\boldsymbol{u}$ can also be large, as we already saw for the stagnation point example in Figure 6.9, see also [BLMS15, Remark 2.3].

Numerical results Results for this setting were computed for the CR and CR-RT method on uniform and Shishkin-type meshes for viscosity values $\nu \in \{10^{-2}, 10^{-3}, 10^{-3.5}\}$. Table 6.2 shows an overview of the number of iterations that were necessary to reach convergence of the nonlinear system and the corresponding observed convergence rate of the discrete velocity solution in the $\|\cdot\|_{1,h}$-norm.

The nonlinear iterations were stopped if the distance in the L^2-norm of two consecutive discrete velocity solutions was less than 10^{-8} or if the iteration count reached 50, in which case the table has the entry *dnc*.

From the results it is clear that as the viscosity decreases, the problem gets harder to solve, so that for lower viscosity values convergence is reached only on the finest meshes. We also see that the anisotropically graded meshes do not help with respect to the convergence of the nonlinear solver. The pressure-robust CR-RT method seems require slightly less iterations in the pre-asymptotic area.

In Table 6.3 the corresponding errors for the data from Table 6.2 is shown. The behavior of the methods on uniform and anisotropic meshes with the nonlinear term is similar to that in the Stokes case. We see that the modified method yields lower errors than the standard method, and that the mesh grading only improves the result for the pressure-robust method.

Table 6.2: Iterations until convergence and convergence orders for gradient error of velocity, different viscosities on uniform and graded meshes. Comparison of CR and CR-RT methods. The entry *dnc* means the Picard-iteration did not converge to the required precision within 50 iterations.

	$\nu = 10^{-2}$				$\nu = 10^{-3}$				$\nu = 10^{-3.5}$			
	CR		CR-RT		CR		CR-RT		CR		CR-RT	
ndof	It.	eoc	It.	eoc	It.	eoc	It.	eoc	It.	eoc	It.	eoc
Uniform meshes												
4 192	14	0.95	13	1.25	dnc	–	dnc	–	dnc	–	dnc	–
16 576	13	0.97	12	1.07	dnc	–	dnc	–	dnc	–	dnc	–
65 920	12	0.99	12	1.00	20	–	19	–	dnc	–	dnc	–
262 912	12	1.00	12	1.00	19	1.01	17	1.38	27	–	31	–
1 050 112	12	1.00	12	1.00	17	1.00	17	1.07	22	1.03	19	1.57
Shishkin-type meshes												
4 192	15	–	14	1.31	dnc	–	dnc	–	dnc	–	dnc	–
16 576	14	1.05	12	1.05	dnc	–	dnc	–	dnc	–	dnc	–
65 920	13	1.00	12	1.00	21	–	19	–	dnc	–	dnc	–
262 912	12	1.00	12	1.00	20	1.11	17	1.30	dnc	–	23	–
1 050 112	12	1.00	12	1.00	18	1.04	17	1.04	23	–	19	1.55

Table 6.3: Velocity gradient error $\|\boldsymbol{u} - \boldsymbol{u}_h\|_{1,h,rel}$ for numerical results corresponding to data from Table 6.2.

	$\nu = 10^{-2}$		$\nu = 10^{-3}$		$\nu = 10^{-3.5}$	
ndof	CR	CR-RT	CR	CR-RT	CR	CR-RT
Uniform meshes						
4 192	7.0704e−1	2.8876e−1	dnc	dnc	dnc	dnc
16 576	3.6190e−1	1.3832e−1	dnc	dnc	dnc	dnc
65 920	1.8278e−1	6.9438e−2	1.2145e+0	3.5425e−1	dnc	dnc
262 912	9.1771e−2	3.4887e−2	6.0384e−1	1.3610e−1	1.5378e+0	3.9340e−1
1 050 112	4.5946e−2	1.7476e−2	3.0113e−1	6.4976e−2	7.5250e−1	1.3255e−1
Shishkin-type meshes						
4 192	8.9324e−1	2.1411e−1	dnc	dnc	dnc	dnc
16 576	4.3390e−1	1.0389e−1	dnc	dnc	dnc	dnc
65 920	2.1697e−1	5.2106e−2	1.9280e+0	2.1808e−1	dnc	dnc
262 912	1.0884e−1	2.6133e−2	8.9713e−1	8.8953e−2	dnc	2.4797e−1
1 050 112	5.4493e−2	1.3081e−2	4.3631e−1	4.3246e−2	1.1691e+0	8.4660e−2

6.3 Edge singularity

This example was presented in similar forms in [AKLM21] and [AK21]. It demonstrates the optimal convergence characteristics and the pressure-robustness of the modified Crouzeix–Raviart method on anisotropically graded meshes for domains with a re-entrant edge as introduced in Section 2.4.3.

With the observations of Remark 5.6 in mind, we present two variations of this example. The first one has a fixed exact solution, so that the data function changes when the viscosity is altered, the second one uses a modification of the irrotational part of the data function to see the pressure-robustness of the modified methods.

6.3.1 Fixed exact solution

Problem setting We consider a domain

$$\Omega = \{(r\cos\phi, r\sin\phi, z) \in \mathbb{R}^3 : 0 < r < 1,\ 0 < \phi < \omega,\ 0 < z < 1\}, \tag{6.3}$$

which describes a cylindrical body that has a cut-out so that a non-convex edge with interior angle ω coincides with part of the z-axis, as indicated in the left plot of Figure 6.11. In all computations we use an interior angle of $\omega = \frac{3}{2}\pi$, which by (2.12) results in a singularity exponent of $\lambda \approx 0.54448$.

We use the manufactured velocity and pressure solutions

$$\boldsymbol{u} = \begin{pmatrix} zr^{\lambda}u_1(\phi) \\ zr^{\lambda}u_2(\phi) \\ r^{2/3}\sin\left(\frac{2}{3}\phi\right) \end{pmatrix}, \qquad p = zr^{\lambda-1}\Phi(\phi), \tag{6.4}$$

for the Stokes equations, where

$$\begin{aligned} u_1(\phi) &= -\sin(\lambda\phi)\cos(\omega) - \lambda\sin(\phi)\cos(\lambda\omega - (\lambda-1)\phi) + \lambda\sin(\omega-\phi)\cos((\lambda-1)\phi) \\ &\quad + \sin(\lambda(\omega-\phi)), \\ u_2(\phi) &= -\sin(\lambda\phi)\sin(\omega) - \lambda\sin(\phi)\sin(\lambda\omega - (\lambda-1)\phi) - \lambda\sin(\omega-\phi)\sin((\lambda-1)\phi), \\ \Phi(\phi) &= 2\lambda[\sin(\omega + (\lambda-1)\phi) - \sin(\lambda\omega - (\lambda-1)\phi)]. \end{aligned} \tag{6.5}$$

An illustration of these functions is shown in Figure 6.11. The velocity field describes an upward flow through the domain, with a component in the angular direction of the cylindrical coordinate system around the re-entrant edge that gets stronger with increasing z-coordinate. At the flat faces on the x-z- and y-z-planes the flow velocity vanishes, indicating a no-slip boundary, whereas there is a flow through the rest of the boundary. As in the stagnation point example, the change from the theoretical setting with homogeneous boundary conditions to inhomogeneous Dirichlet boundary conditions for parts of the boundary does not impact the performance of the methods. The low regularity of the solution is most visible in the pressure plot on the right hand side of Figure 6.11, where the effect of the singular factor $r^{\lambda-1}$ can be seen directly.

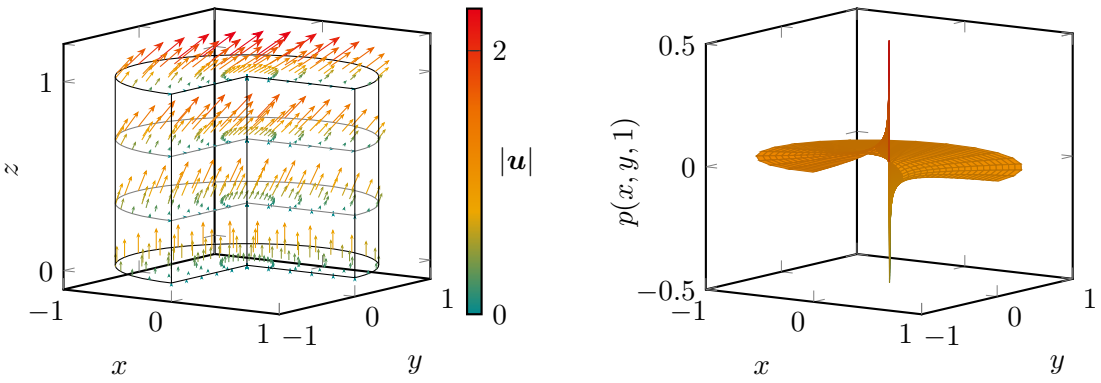

Figure 6.11: Illustration of domain (6.3) for $\omega = \frac{3}{2}\pi$, velocity solution (left) and pressure solution at $z = 1$.

By inserting these functions in the momentum equation we get the function

$$\boldsymbol{f} = \begin{pmatrix} 2\lambda(\lambda-1)(\nu-1)zr^{\lambda-2}[\sin(\lambda\omega-(\lambda-2)\phi)-\sin(\omega+(\lambda-2)\phi)] \\ 2\lambda(\lambda-1)(1-\nu)zr^{\lambda-2}[\cos(\lambda\omega-(\lambda-2)\phi)+\cos(\omega+(\lambda-2)\phi)] \\ r^{\lambda-1}\Phi(\phi) \end{pmatrix} \tag{6.6}$$

for the right hand side of the problem. Note that for $\nu = 1$ the first two components of the data function vanish, while for $\nu \neq 1$ the singular factors $r^{\lambda-2}$ are present on the right hand side. This leads to severe computational difficulties, as the function is not in $\boldsymbol{L}^2(\Omega)$ in this case. The problems arise during the numerical integration on the right hand side, and require extra care during the calculations, especially in the case of the Brezzi–Douglas–Marini reconstruction. We go into more detail later in this section.

Numerical results We compare the CR, CR-RT and CR-BDM methods on quasi-uniform meshes and anisotropically graded meshes. The anisotropic meshes were generated by the procedure described in Section 2.4.3 with a grading parameter $\mu = 0.4$, which results in an aspect ratio of $\sigma \approx 939.3$ for the finest mesh with 1376733 degrees of freedom.

Setting $\nu = 1$ and $\nu = 10^{-2}$, the methods yield the results shown in Figure 6.12. For $\nu = 1$ the plots on the left hand side clearly show the improved convergence rate of the velocity and the pressure solution for all methods on anisotropically graded meshes compared to the quasi-uniform meshes. However, the advantage of the pressure-robust methods over the standard method is barely noticeable.

This changes when the viscosity is decreased to $\nu = 10^{-2}$: The CR method exhibits the locking effect as before and the velocity error is scaled by roughly two orders of magnitude, while at the same time the errors of the CR-RT and CR-BDM methods remain unchanged. Additionally, the CR method seems to fail on the anisotropic meshes, and the error even increases in the last step.

In order to get a better idea of the effect of the anisotropic grading, Figure 6.13 visualizes the location of the computational error throughout the domain. The visualization uses

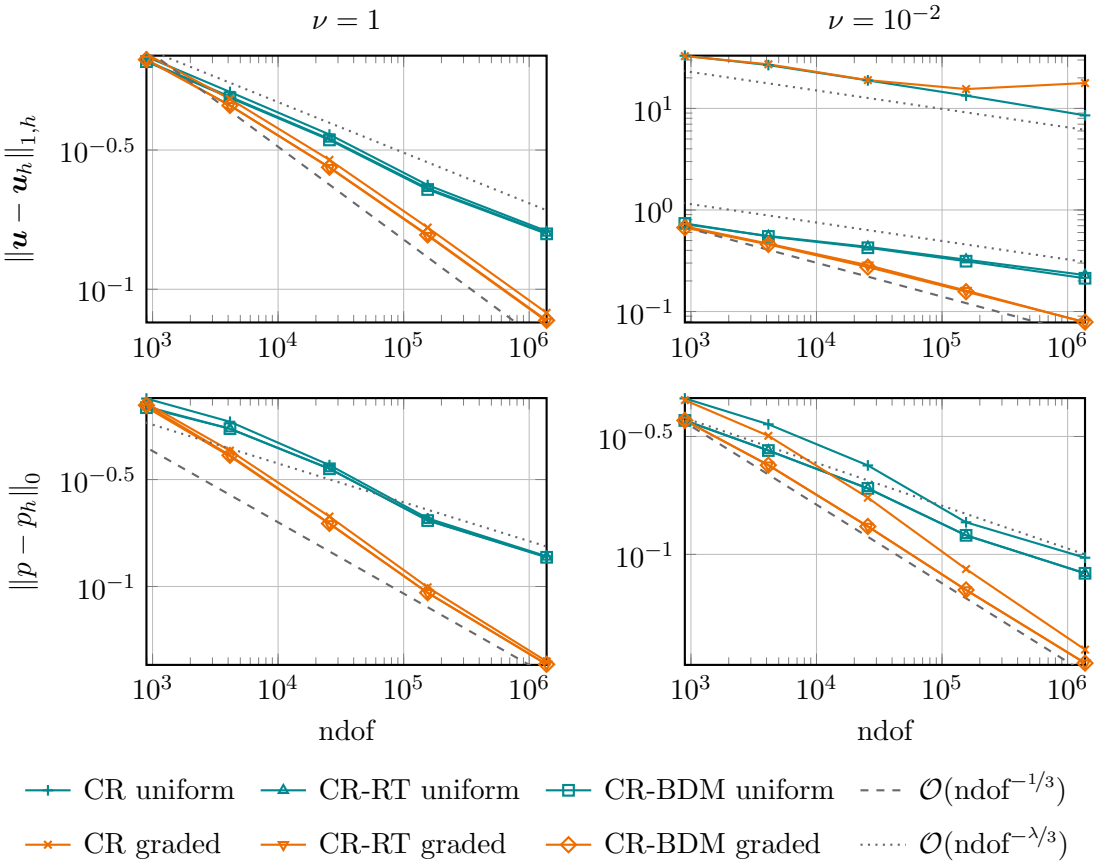

Figure 6.12: Convergence plots for the singular edge example for $\nu \in \{1, 10^{-2}\}$.

the layer structure of the meshes, by first calculating the elementwise error of every triangular prism, see the mesh generation process in Section 2.4.3, and afterwards adding the values of stacked prisms from all layers. Then the bottom mesh is used to show the aggregated error of the mesh volume above each triangle.

The left hand side shows the error distribution for the quasi-uniform meshes, where the overwhelming part of the error is concentrated in the elements touching the singular edge. In the plot for the graded mesh on the right hand side of the figure a slight concentration of the error around the re-entrant edge is still noticeable, but the error is more spread out through the whole domain. Observing the scaling of the color bars shows that the graded meshes offer a much better discrete solution for the same computational effort.

Remark 6.1. As mentioned, the right hand side function $\boldsymbol{f}$ contains the factor $r^{\lambda-2}$ in its first two components if $\nu \neq 1$, which is a challenge for the numerical integration of the linear form. The smaller ν gets, the larger the quadrature errors get. Thus $\nu = 10^{-2}$ is the lowest we get here, and even for this value the quadrature had to be extremely precise.

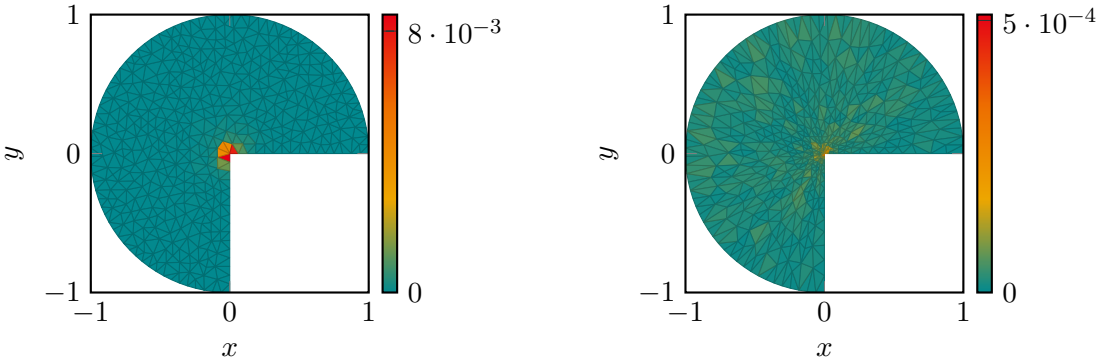

Figure 6.13: Cellwise error $\|\nabla \boldsymbol{u} - \nabla \boldsymbol{u}_h\|_{1,T}^2$ aggregated on bottom mesh for quasi-uniform (left) and anisotropically graded (right) meshes.

The implementation uses the FEniCS framework, which provides support for arbitrary quadrature degree, limited of course by the capabilities of the machine. Increasing this degree helped, but additional local mesh refinement for the quadrature procedure near the singular edge provided a better result.

To put the difficulties into perspective, for the computations with $\nu = 1$ it sufficed to set the quadrature degree to 12 with no additional mesh refinement. For the most challenging computation, which was the CR-BDM method for $\nu = 10^{-2}$, we additionally uniformly refined the elements adjacent to the singular edge iteratively 14 times, to get the results from Figure 6.12.

6.3.2 Fixed data function

Problem setting To circumvent the difficulties mentioned in Remark 6.1 but still show the pressure-robustness of the method, we modify the data function in another way. As the velocity solution of a pressure-robust discretization is unaffected by changes in the irrotational part of the data function, see Section 2.3, we compare the solutions for the two right hand sides

$$\boldsymbol{f}_i = \boldsymbol{f}_0 + \nabla \Psi_i, \qquad i \in \{1, 2\},$$

where we set

$$\boldsymbol{f}_0 = \begin{pmatrix} 0 \\ 0 \\ r^{\lambda-1}\Phi(\phi) \end{pmatrix}, \qquad \Psi_1 = 0, \qquad \Psi_2 = 10 r^{\lambda} \Phi(\phi),$$

with $\Phi(\phi)$ from (6.5). Since $\boldsymbol{f}_0$ is the function from (6.6) for $\nu = 1$, which is in $\boldsymbol{L}^2(\Omega)$, this construction guarantees that $\boldsymbol{f}_i \in \boldsymbol{L}^2(\Omega)$. Additionally, since $\boldsymbol{f}_0 \cong \boldsymbol{f}_1 \cong \boldsymbol{f}_2$, see Definition 2.9, and due to Lemma 5.1 and the discussion in Remark 5.6 we can deduce that the analytical solutions for these data functions are $(\nu^{-1}\boldsymbol{u}, p + \Psi_i)$, with $\boldsymbol{u}$ and p from (6.4). Knowing the solutions, we can use them for the convergence analysis.

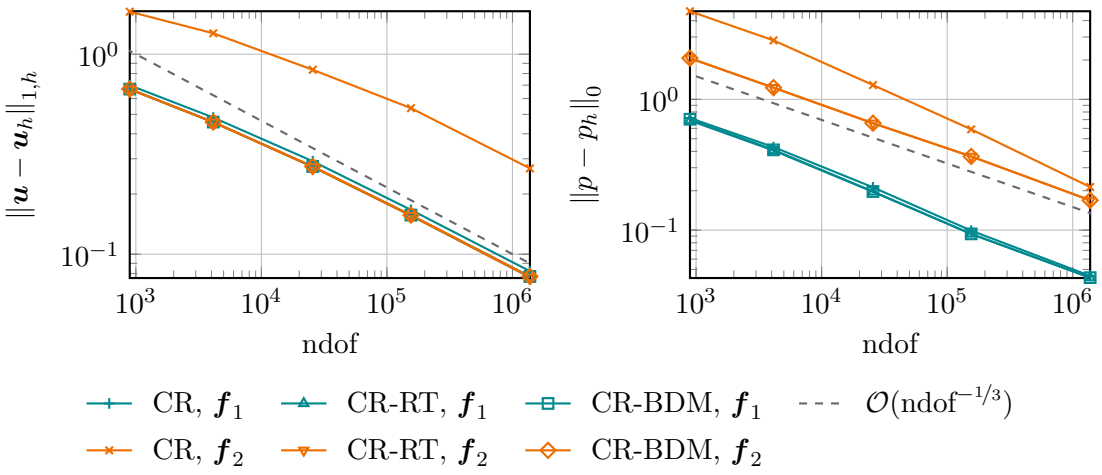

Figure 6.14: Convergence plots for the singular edge example with fixed data on graded meshes for $\nu = 10^{-3}$.

Numerical results The results are illustrated in Figure 6.14 only for the graded meshes, since the difference to the quasi-uniform meshes was already highlighted in the previous subsection. We see that all methods reach the predicted convergence rates. However, the velocity solution of the standard method is severely worsened by the additional irrotational part $\nabla\Psi_2$. In contrast, the velocity solutions of the reconstructed methods are not influenced at all, the lines in the plot for the CR-RT and CR-BDM methods for data $\boldsymbol{f}_1$ and $\boldsymbol{f}_2$ are exactly on top of each other. For the pressure solutions we see the expected increase of the error for all methods when switching from $\boldsymbol{f}_1$ to $\boldsymbol{f}_2$.

CHAPTER 7

Conclusion and outlook

The main results of this thesis include new error estimates for the Brezzi–Douglas–Marini interpolation on anisotropic triangles, tetrahedra and triangular prisms, a generalized error estimation for pressure-robust discretizations of the Stokes equations using the reconstruction approach on anisotropic meshes and the application of this procedure to the modified Bernardi–Raugel and Crouzeix–Raviart methods.

For the interpolation error estimates in Theorems 4.15 and 4.16 we extended our previous results from [AK20], where the estimates were shown for functions from the spaces $\boldsymbol{H}^m(\Omega)$, $m \in \mathbb{N}$, to functions from the more general spaces $\boldsymbol{W}^{m,p}(\Omega)$, $m \in \mathbb{N}$, $1 \leq p \leq \infty$.

Pressure-robust methods for incompressible flows were already investigated in our publications [AK21; AKLM21], where the modified Crouzeix–Raviart method was considered for special settings. In Section 5.1 we formulated the error estimation of discretizations using the reconstruction approach on anisotropic triangulations in a more abstract setting, by proving error estimates using our Assumptions 1 to 5 on the used finite element pair and the reconstruction operator. This framework is supposed to facilitate the construction of new pressure-robust methods that are useful on anisotropic meshes, since only these assumptions need to be checked for a specific method. We showed this process for the modified Crouzeix–Raviart methods in Section 5.3, where we reformulated the results from [AK21; AKLM21] to fit the assumptions for the general analysis. Additionally we could implement this approach for certain settings and the modified Bernardi–Raugel method in Section 5.2 to obtain the new results from Theorem 5.9.

All results are supported by the numerical experiments in Chapter 6, which cover a variety of different settings in which pressure-robust methods and anisotropically graded meshes lead to more accurate discrete solutions.

Further research in this area could be focused on developing pressure-robust higher-

order methods that work on anisotropic meshes. For now, the two methods we investigated in detail, the modified Bernardi–Raugel and Crouzeix–Raviart finite element pairs, are lowest-order methods that, due to the facet bubbles of the former and the non-conformity of the latter method, contain the full space of first order polynomials in the velocity approximation space but not the space $\boldsymbol{P}_2(\mathcal{T}_h)$. A promising direction concerning higher-order methods could be the $\boldsymbol{H}(\mathrm{div}, \Omega)$-conforming discontinuous Galerkin method we briefly described in Section 3.2.2. In that subsection we showed numerically that the discrete inf-sup constant on certain anisotropic meshes seems bounded from below, and the approach from [KT21] to show coercivity of the bilinear form seems extendable to the vector-valued case.

All of the more closely inspected element pairs in this thesis rely on discontinuous pressure approximations, while many of the classical pairs that are in use have continuous pressure approximation spaces. The well known Taylor–Hood pair was recently shown to be inf-sup stable in its lowest-order variant on certain two-dimensional anisotropic meshes, see [BW19], and reconstruction operators for continuous pressure methods have been proposed and analyzed for isotropic meshes, see [LLMS17]. As a research option in this direction, it would be interesting to see whether the mentioned reconstruction operator is stable on anisotropic meshes or if one that is can be found.

In the example in Section 6.2.2 we could numerically show that the pressure-robust methods work well on anisotropic meshes with the nonlinear term present in the equations. Thus, another interesting direction could be an extension of the theoretical results to the nonlinear case.

References

[AADL11] G. Acosta, T. Apel, R. G. Durán, and A. L. Lombardi. "Error estimates for Raviart–Thomas interpolation of any order on anisotropic tetrahedra". *Math. Comp.* 80.273 (2011), 141–163. DOI: 10.1090/S0025-5718-2010-02406-8 (cit. on pp. 19, 39, 40, 50–59).

[AD99] G. Acosta and R. G. Durán. "The maximum angle condition for mixed and nonconforming elements: application to the Stokes equations". *SIAM J. Numer. Anal.* 37.1 (1999), 18–36. DOI: 10.1137/S0036142997331293 (cit. on pp. 19, 85, 86).

[AF03] R. A. Adams and J. J. F. Fournier. *Sobolev spaces*. 2nd ed. Amsterdam: Academic Press, 2003. URL: http://www.sciencedirect.com/science/book/9780120441433 (cit. on pp. 7–9).

[ADN64] S. Agmon, A. Douglis, and L. Nirenberg. "Estimates near the boundary for solutions of elliptic partial differential equations satisfying general boundary conditions II". *Comm. Pure Appl. Math.* 17.1 (1964), 35–92. DOI: 10.1002/cpa.3160170104 (cit. on p. 23).

[AP21a] M. Ainsworth and C. Parker. "Mass Conserving Mixed *hp*-FEM Approximations to Stokes Flow. Part I: Uniform Stability". *SIAM J. Numer. Anal.* 59.3 (2021), 1218–1244. DOI: 10.1137/20M1359109 (cit. on pp. 27–29).

[AP21b] M. Ainsworth and C. Parker. "Mass Conserving Mixed *hp*-FEM Approximations to Stokes Flow. Part II: Optimal Convergence". *SIAM J. Numer. Anal.* 59.3 (2021), 1245–1272. DOI: 10.1137/20M1359110 (cit. on pp. 27, 29).

[Ape99] T. Apel. *Anisotropic finite elements: local estimates and applications*. Advances in Numerical Mathematics. Stuttgart: B. G. Teubner, 1999. URL: https://athene-forschung.unibw.de/111589 (cit. on pp. 19, 20, 22, 23, 53, 54).

[AD92] T. Apel and M. Dobrowolski. "Anisotropic interpolation with applications to the finite element method". *Computing* 47 (1992), 277–293. DOI: 10.1007/BF02320197 (cit. on p. 23).

[AD03] T. Apel and N. Düvelmeyer. "Transformation of hexahedral finite element meshes into tetrahedral meshes according to quality criteria". *Computing* 71.4 (2003), 293–304. DOI: 10.1007/s00607-003-0031-5 (cit. on p. 21).

[AEHK21] T. Apel, L. Eckardt, C. Haubner, and V. Kempf. "The maximal angle condition on finite elements: useful or not?" *PAMM. Proc. Appl. Math. Mech.* 20.1 (2021), e202000116. DOI: 10.1002/pamm.202000116 (cit. on p. 18).

[AK20] T. Apel and V. Kempf. "Brezzi–Douglas–Marini interpolation of any order on anisotropic triangles and tetrahedra". *SIAM J. Numer. Anal.* 58.3 (2020), 1696–1718. DOI: 10.1137/19M1302910 (cit. on pp. 3, 20, 30, 33, 39, 41, 42, 44, 50–53, 55–57, 105).

[AK21] T. Apel and V. Kempf. "Pressure-robust error estimate of optimal order for the Stokes equations: domains with re-entrant edges and anisotropic mesh grading". *Calcolo* 58.2 (2021), Art. No. 15. DOI: 10.1007/s10092-021-00402-z (cit. on pp. 1, 2, 9, 23, 71, 73, 75, 83, 100, 105).

[AKLM21] T. Apel, V. Kempf, A. Linke, and C. Merdon. "A nonconforming pressure-robust finite element method for the Stokes equations on anisotropic meshes". *IMA J. Numer. Anal.* 42.1 (2021), 392–416. DOI: 10.1093/imanum/draa097 (cit. on pp. 1, 2, 83, 86, 100, 105).

[AN04] T. Apel and S. Nicaise. "The inf-sup condition for low order elements on anisotropic meshes". *Calcolo* 41.2 (2004), 89–113. DOI: 10.1007/s10092-004-0086-5 (cit. on pp. 78, 79).

[ANS01a] T. Apel, S. Nicaise, and J. Schöberl. "A non-conforming finite element method with anisotropic mesh grading for the Stokes problem in domains with edges". *IMA J. Numer. Anal.* 21.4 (2001), 843–856. DOI: 10.1093/imanum/21.4.843 (cit. on pp. 2, 14, 20, 23, 86).

[ANS01b] T. Apel, S. Nicaise, and J. Schöberl. "Crouzeix–Raviart Type Finite Elements on Anisotropic Meshes". *Numer. Math.* 89.2 (2001), 193–223. DOI: 10.1007/PL00005466 (cit. on pp. 2, 85).

[AS02] T. Apel and J. Schöberl. "Multigrid methods for anisotropic edge refinement". *SIAM J. Numer. Anal.* 40.5 (2002), 1993–2006. DOI: 10.1137/S0036142900375414 (cit. on p. 23).

[AFS68] J. H. Argyris, I. Fried, and D. W. Scharpf. "The TUBA family of plate elements for the matrix displacement method". *The Aeronautical Journal* 72.692 (1968), 701–709. DOI: 10.1017/S000192400008489X (cit. on p. 29).

[BS92] I. Babuška and M. Suri. "On locking and robustness in the finite element method". *SIAM J. Numer. Anal.* 29.5 (1992), 1261–1293. DOI: 10.1137/0729075 (cit. on p. 1).

[Bak69] N. S. Bakhvalov. “The optimization of methods of solving boundary value problems with a boundary layer”. *USSR Computational Mathematics and Mathematical Physics* 9 (1969), 139–166. DOI: 10.1016/0041-5553(69)90038-X (cit. on p. 22).

[BW19] G. R. Barrenechea and A. Wachtel. “The inf-sup stability of the lowest order Taylor–Hood pair on affine anisotropic meshes”. *IMA J. Numer. Anal.* 40.4 (2019), 2377–2398. DOI: 10.1093/imanum/drz028 (cit. on p. 106).

[BR85] C. Bernardi and G. Raugel. “Analysis of some finite elements for the Stokes problem”. *Math. Comput.* 44.169 (1985), 71–79. DOI: 10.2307/2007793 (cit. on p. 77).

[BNPB13] H. Bhatia, G. Norgard, V. Pascucci, and P.-T. Bremer. “The Helmholtz-Hodge decomposition—A survey”. *IEEE Trans. Vis. Comput. Graphics* 19.8 (2013), 1386–1404. DOI: 10.1109/TVCG.2012.316 (cit. on p. 9).

[BBF13] D. Boffi, F. Brezzi, and M. Fortin. *Mixed Finite Element Methods and Applications*. Berlin: Springer, 2013. DOI: 10.1007/978-3-642-36519-5 (cit. on pp. 33, 42, 78, 80, 81).

[BLMS15] C. Brennecke, A. Linke, C. Merdon, and J. Schöberl. “Optimal and pressure-independent L^2 velocity error estimates for a modified Crouzeix–Raviart Stokes element with BDM reconstructions”. *J. Comput. Math.* 33.2 (2015), 191–208. DOI: 10.4208/jcm.1411-m4499 (cit. on pp. 1, 83, 98).

[BS08] S. C. Brenner and L. R. Scott. *The Mathematical Theory of Finite Element Methods*. 3rd ed. New York: Springer, 2008. DOI: 10.1007/978-0-387-75934-0 (cit. on pp. 8, 15, 46, 55).

[BDM85] F. Brezzi, J. Douglas, and L. D. Marini. “Two families of mixed finite elements for second order elliptic problems”. *Numer. Math.* 47.2 (1985), 217–235. DOI: 10.1007/BF01389710 (cit. on pp. 1, 29, 41).

[BF91] F. Brezzi and M. Fortin. *Mixed and Hybrid Finite Element Methods*. New York: Springer, 1991. DOI: 10.1007/978-1-4612-3172-1 (cit. on pp. 29, 41, 58).

[BFS11] A. Buffa, C. de Falco, and G. Sangalli. “IsoGeometric Analysis: stable elements for the 2D Stokes equation”. *Int. J. Numer. Methods Fluids* 65.11-12 (2011), 1407–1422. DOI: 10.1002/fld.2337 (cit. on p. 27).

[Cat61] L. Cattabriga. “Su un problema al contorno relativo al sistema di equazioni di Stokes”. *Rendiconti del Seminario Matematico della Università di Padova* 31 (1961), 308–340. URL: http://www.numdam.org/item?id=RSMUP_1961__31__308_0 (cit. on p. 13).

[CL14] T. Chacón Rebollo and R. Lewandowski. *Mathematical and numerical foundations of turbulence models and applications*. New York: Birkhäuser, 2014. DOI: 10.1007/978-1-4939-0455-6 (cit. on p. 11).

[CM90] A. J. Chorin and J. E. Marsden. *A mathematical introduction to fluid mechanics*. 2nd ed. New York: Springer, 1990. DOI: 10.1007/978-1-4684-0364-0 (cit. on p. 10).

[CKS07] B. Cockburn, G. Kanschat, and D. Schötzau. "A note on discontinuous Galerkin divergence-free solutions of the Navier-Stokes equations". *J. Sci. Comput.* 31.1-2 (2007), 61–73. DOI: 10.1007/s10915-006-9107-7 (cit. on pp. 1, 33).

[CR73] M. Crouzeix and P.-A. Raviart. "Conforming and nonconforming finite element methods for solving the stationary Stokes equations. I". *R.A.I.R.O.* 7 (1973), 33–75. DOI: 10.1051/m2an/197307R300331 (cit. on pp. 26, 72).

[Dau89] M. Dauge. "Stationary Stokes and Navier–Stokes systems on two- or three-dimensional domains with corners. I. Linearized equations". *SIAM J. Math. Anal.* 20.1 (1989), 74–97. DOI: 10.1137/0520006 (cit. on pp. 14, 23).

[DE12] D. A. Di Pietro and A. Ern. *Mathematical Aspects of Discontinuous Galerkin Methods*. Berlin: Springer, 2012. DOI: 10.1007/978-3-642-22980-0 (cit. on pp. 25, 26, 29, 30).

[DR06] P. G. Drazin and N. Riley. *The Navier–Stokes equations*. Cambridge: Cambridge University Press, 2006. DOI: 10.1017/cbo9780511526459 (cit. on p. 93).

[DL08] R. G. Durán and A. L. Lombardi. "Error estimates for the Raviart–Thomas interpolation under the maximum angle condition". *SIAM J. Numer. Anal.* 46.3 (2008), 1442–1453. DOI: 10.1137/060665312 (cit. on p. 19).

[EG04] A. Ern and J.-L. Guermond. *Theory and Practice of Finite Elements*. New York: Springer, 2004. DOI: 10.1007/978-1-4757-4355-5 (cit. on pp. 72, 76, 79, 80).

[EH13a] J. A. Evans and T. J. R. Hughes. "Isogeometric divergence-conforming B-splines for the steady Navier-Stokes equations". *Math. Models Method Appl. Sci.* 23.8 (2013), 1421–1478. DOI: 10.1142/S0218202513500139 (cit. on p. 27).

[EH13b] J. A. Evans and T. J. R. Hughes. "Isogeometric divergence-conforming B-splines for the unsteady Navier-Stokes equations". *J. Comput. Phys.* 241 (2013), 141–167. DOI: 10.1016/j.jcp.2013.01.006 (cit. on p. 27).

[FNP01] M. Farhloul, S. Nicaise, and L. Paquet. "Some mixed finite element methods on anisotropic meshes". *ESAIM Math. Model. Numer. Anal.* 35.5 (2001), 907–920. DOI: 10.1051/m2an:2001142 (cit. on p. 23).

[Fra21] S. Franz. "Anisotropic H_{div}-norm error estimates for rectangular H_{div}-elements". *Appl. Math. Lett.* 121 (2021). 107453. DOI: 10.1016/j.aml.2021.107453 (cit. on p. 41).

[FM20] D. Frerichs and C. Merdon. "Divergence-preserving reconstructions on polygons and a really pressure-robust virtual element method for the Stokes problem". *IMA J. Numer. Anal.* (2020). DOI: 10.1093/imanum/draa073 (cit. on p. 34).

[GSS94] G. P. Galdi, C. G. Simader, and H. Sohr. "On the Stokes problem in Lipschitz domains". *Ann. Mat. Pura Appl.* 167 (1994), 147–163. DOI: 10.1007/BF01760332 (cit. on p. 13).

[GJ05] S. Ganesan and V. John. "Pressure separation—a technique for improving the velocity error in finite element discretisations of the Navier-Stokes equations". *Appl. Math. Comput.* 165.2 (2005), 275–290. DOI: 10.1016/j.amc.2004.04.071 (cit. on p. 15).

[GLS19] N. R. Gauger, A. Linke, and P. W. Schroeder. "On high-order pressure-robust space discretisations, their advantages for incompressible high Reynolds number generalised Beltrami flows and beyond". *SMAI J. Comput. Math.* 5 (2019), 89–129. DOI: 10.5802/smai-jcm.44 (cit. on pp. 15, 16).

[GLB97] J.-F. Gerbeau, C. Le Bris, and M. Bercovier. "Spurious velocities in the steady flow of an incompressible fluid subjected to external forces". *Internat. J. Numer. Methods Fluids* 25.6 (1997), 679–695. DOI: 10.1002/(SICI)1097-0363(19970930)25:6<679::AID-FLD582>3.0.CO;2-Q (cit. on p. 15).

[GR86] V. Girault and P.-A. Raviart. *Finite Element Methods for Navier-Stokes Equations*. Berlin: Springer, 1986. DOI: 10.1007/978-3-642-61623-5 (cit. on pp. 10, 13, 15, 77, 79).

[Gri11] P. Grisvard. *Elliptic Problems in Nonsmooth Domains*. Philadelphia, PA: Society for Industrial and Applied Mathematics, 2011. DOI: 10.1137/1.9781611972030 (cit. on p. 23).

[GN14a] J. Guzmán and M. Neilan. "Conforming and divergence-free Stokes elements in three dimensions". *IMA J. Numer. Anal.* 34.4 (2014), 1489–1508. DOI: 10.1093/imanum/drt053 (cit. on pp. 3, 28).

[GN14b] J. Guzmán and M. Neilan. "Conforming and divergence-free Stokes elements on general triangular meshes". *Math. Comput.* 83.285 (2014), 15–36. DOI: 10.1090/S0025-5718-2013-02753-6 (cit. on pp. 3, 28).

[Hac17] W. Hackbusch. *Theorie und Numerik elliptischer Differentialgleichungen*. 4th ed. Wiesbaden: Springer, 2017. DOI: 10.1007/978-3-658-15358-8 (cit. on p. 23).

[Hie11] K. Hiemenz. "Die Grenzschicht an einem in den gleichförmigen Flüssigkeitsstrom eingetauchten geraden Kreiszylinder". *Dingl. polytechn. J.* 326 (1911), 321–324, 344–348, 357–362, 372–376, 391–393, 407–410. URL: http://dingler.culture.hu-berlin.de/article/pj326/ar326095 (cit. on p. 93).

[Joh16] V. John. *Finite Element Methods for Incompressible Flow Problems*. Cham: Springer, 2016. DOI: 10.1007/978-3-319-45750-5 (cit. on pp. 10–13, 73, 78, 98).

[JKN18] V. John, P. Knobloch, and J. Novo. "Finite elements for scalar convection-dominated equations and incompressible flow problems: a never ending story?" *Comput. Vis. Sci.* 19.5-6 (2018), 47–63. DOI: 10.1007/s00791-018-0290-5 (cit. on p. 11).

[Joh+17] V. John, A. Linke, C. Merdon, M. Neilan, and L. G. Rebholz. "On the divergence constraint in mixed finite element methods for incompressible flows". *SIAM Rev.* 59.3 (2017), 492–544. DOI: 10.1137/15M1047696 (cit. on pp. 1, 15, 16, 25, 27–29, 37).

[KT21] T. Kashiwabara and T. Tsuchiya. "A robust discontinuous Galerkin scheme on anisotropic meshes". *Jpn. J. Ind. Appl. Math.* (2021). DOI: 10.1007/s13160-021-00474-y (cit. on pp. 30, 33, 106).

[KNS21] K. Kean, M. Neilan, and M. Schneier. *The Scott–Vogelius Method for Stokes Problem on Anisotropic Meshes*. 2021. arXiv: 2109.14780 [math.NA] (cit. on p. 27).

[KO76] R. B. Kellogg and J. E. Osborn. "A regularity result for the Stokes problem in a convex polygon". *J. Funct. Anal.* 21.4 (1976), 397–431. DOI: 10.1016/0022-1236(76)90035-5 (cit. on pp. 14, 23).

[Kem21] V. Kempf. "Pressure-robustness for the Stokes equations on anisotropic meshes". *PAMM. Proc. Appl. Math. Mech.* (2021), e202100112. DOI: 10.1002/pamm.202100112 (cit. on p. 93).

[KR19] K. L. A. Kirk and S. Rhebergen. "Analysis of a pressure-robust hybridized discontinuous Galerkin method for the stationary Navier-Stokes equations". *J. Sci. Comput.* 81.2 (2019), 881–897. DOI: 10.1007/s10915-019-01040-y (cit. on pp. 27, 29).

[KVZ21] C. Kreuzer, R. Verfürth, and P. Zanotti. "Quasi-optimal and pressure robust discretizations of the Stokes equations by moment- and divergence-preserving operators". *Comput. Methods Appl. Math.* 21.2 (2021), 423–443. DOI: 10.1515/cmam-2020-0023 (cit. on p. 34).

[KZ20] C. Kreuzer and P. Zanotti. "Quasi-optimal and pressure-robust discretizations of the Stokes equations by new augmented Lagrangian formulations". *IMA J. Numer. Anal.* 40.4 (2020), 2553–2583. DOI: 10.1093/imanum/drz044 (cit. on p. 34).

[Kří92] M. Křížek. "On the maximum angle condition for linear tetrahedral elements". *SIAM J. Numer. Anal.* 29.2 (1992), 513–520. DOI: 10.1137/0729031 (cit. on p. 18).

[LLMS17] P. L. Lederer, A. Linke, C. Merdon, and J. Schöberl. "Divergence-free reconstruction operators for pressure-robust Stokes discretizations with continuous pressure finite elements". *SIAM J. Numer. Anal.* 55.3 (2017), 1291–1314. DOI: 10.1137/16M1089964 (cit. on pp. 1, 2, 34, 37, 106).

[LR20] P. L. Lederer and S. Rhebergen. "A pressure-robust embedded discontinuous Galerkin method for the Stokes problem by reconstruction operators". *SIAM J. Numer. Anal.* 58.5 (2020), 2915–2933. DOI: 10.1137/20M1318389 (cit. on p. 29).

[LS18] P. L. Lederer and J. Schöberl. "Polynomial robust stability analysis for $H(\mathrm{div})$-conforming finite elements for the Stokes equations". *IMA J. Numer. Anal.* 38.4 (2018), 1832–1860. DOI: 10.1093/imanum/drx051 (cit. on pp. 1, 29, 33).

[LS16] C. Lehrenfeld and J. Schöberl. "High order exactly divergence-free hybrid discontinuous Galerkin methods for unsteady incompressible flows". *Comput. Methods Appl. Mech. Engrg.* 307 (2016), 339–361. DOI: 10.1016/j.cma.2016.04.025 (cit. on pp. 1, 3, 30).

[Li18] H. Li. "An anisotropic finite element method on polyhedral domains: interpolation error analysis". *Math. Comp.* 87.312 (2018), 1567–1600. DOI: 10.1090/mcom/3290 (cit. on pp. 23, 54).

[LN18] H. Li and S. Nicaise. "Regularity and a priori error analysis on anisotropic meshes of a Dirichlet problem in polyhedral domains". *Numer. Math.* 139.1 (2018), 47–92. DOI: 10.1007/s00211-017-0936-0 (cit. on pp. 23, 54).

[Lin09] A. Linke. "Collision in a cross-shaped domain—a steady 2d Navier-Stokes example demonstrating the importance of mass conservation in CFD". *Comput. Methods Appl. Mech. Engrg.* 198.41-44 (2009), 3278–3286. DOI: 10.1016/j.cma.2009.06.016 (cit. on pp. 1, 15).

[Lin14] A. Linke. "On the role of the Helmholtz decomposition in mixed methods for incompressible flows and a new variational crime". *Comput. Methods Appl. Mech. Engrg.* 268 (2014), 782–800. DOI: 10.1016/j.cma.2013.10.011 (cit. on pp. 1–3, 15, 16, 25, 34, 37, 73, 81, 83).

[LMT16] A. Linke, G. Matthies, and L. Tobiska. "Robust arbitrary order mixed finite element methods for the incompressible Stokes equations with pressure independent velocity errors". *ESAIM Math. Model. Numer. Anal.* 50.1 (2016), 289–309. DOI: 10.1051/m2an/2015044 (cit. on pp. 16, 34, 37, 38, 72).

[LM16] A. Linke and C. Merdon. "Pressure-robustness and discrete Helmholtz projectors in mixed finite element methods for the incompressible Navier–Stokes equations". *Comput. Methods Appl. Mech. Engrg.* 311 (2016), 304–326. DOI: 10.1016/j.cma.2016.08.018 (cit. on pp. 2, 78, 80).

[LMN20] A. Linke, C. Merdon, and M. Neilan. "Pressure-robustness in quasi-optimal a priori estimates for the Stokes problem". *Electron. Trans. Numer. Anal.* 52 (2020), 281–294. DOI: 10.1553/etna_vol52s281 (cit. on pp. 9, 14, 75, 83).

[LMNN18] A. Linke, C. Merdon, M. Neilan, and F. Neumann. "Quasi-optimality of a pressure-robust nonconforming finite element method for the Stokes-problem". *Math. Comp.* 87.312 (2018), 1543–1566. DOI: 10.1090/mcom/3344 (cit. on p. 83).

[LMW17] A. Linke, C. Merdon, and W. Wollner. "Optimal L^2 velocity error estimate for a modified pressure-robust Crouzeix–Raviart Stokes element". *IMA J. Numer. Anal.* 37.1 (2017), 354–374. DOI: 10.1093/imanum/drw019 (cit. on p. 83).

[Lin99] T. Linß. "An upwind difference scheme on a novel Shishkin-type mesh for a linear convection-diffusion problem". *J. Comput. Appl. Math.* 110.1 (1999), 93–104. DOI: 10.1016/S0377-0427(99)00198-3 (cit. on p. 22).

[Lin00] T. Linß. "Analysis of a Galerkin finite element method on a Bakhvalov-Shishkin mesh for a linear convection-diffusion problem". *IMA J. Numer. Anal.* 20.4 (2000), 621–632. DOI: 10.1093/imanum/20.4.621 (cit. on p. 22).

[Lin10] T. Linß. *Layer-Adapted Meshes for Reaction-Convection-Diffusion Problems.* Berlin: Springer, 2010. DOI: 10.1007/978-3-642-05134-0 (cit. on pp. 21, 22).

[Mal81] D. S. Malkus. "Eigenproblems associated with the discrete LBB condition for incompressible finite elements". *Int. J. Eng. Sci.* 19.10 (1981), 1299–1310. DOI: 10.1016/0020-7225(81)90013-6 (cit. on p. 32).

[Mon06] S. Monniaux. "Navier–Stokes equations in arbitrary domains: the Fujita–Kato scheme". *Math. Res. Lett.* 13.3 (2006), 455–461. DOI: 10.4310/MRL.2006.v13.n3.a9 (cit. on p. 10).

[MS75] J. Morgan and R. Scott. "A nodal basis for C^1 piecewise polynomials of degree $n \geq 5$". *Math. Comput.* 29.131 (1975), 736–740. DOI: 10.1090/S0025-5718-1975-0375740-7 (cit. on p. 29).

[MYZ21] L. Mu, X. Ye, and S. Zhang. "A Stabilizer-Free, Pressure-Robust, and Superconvergence Weak Galerkin Finite Element Method for the Stokes Equations on Polytopal Mesh". *SIAM J. Sci. Comput.* 43.4 (2021), A2614–A2637. DOI: 10.1137/20M1380405 (cit. on pp. 27, 34).

[Néd80] J.-C. Nédélec. "Mixed finite elements in $\mathbb{R}^3$". *Numer. Math.* 35.3 (1980), 315–341. DOI: 10.1007/BF01396415 (cit. on pp. 1, 29, 58).

[Néd86] J.-C. Nédélec. "A new family of mixed finite elements in $\mathbb{R}^3$". *Numer. Math.* 50.1 (1986), 57–81. DOI: 10.1007/BF01389668 (cit. on pp. 1, 29, 41, 42, 64).

[OR04] M. A. Olshanskii and A. Reusken. "Grad-div stabilization for Stokes equations". *Math. Comp.* 73.248 (2004), 1699–1718. DOI: 10.1090/S0025-5718-03-01629-6 (cit. on p. 15).

[Pan13] R. L. Panton. *Incompressible Flow*. 4th ed. Hoboken, NJ: John Wiley & Sons, 2013. DOI: 10.1002/9781118713075 (cit. on p. 10).

[Pra05] L. Prandtl. "Über Flüssigkeitsbewegung bei sehr kleiner Reibung". In: *Verh. d. 3. intern. Math.-Kongr. Heidelb.* 1905. DOI: 10.1007/978-3-662-11836-8_43 (cit. on p. 21).

[Qin94] J. Qin. "On the convergence of some low order mixed finite elements for incompressible fluids". PhD thesis. Pennsylvania State University, 1994. URL: https://www-users.math.umn.edu/~arnold//papers/QinThesis.pdf (cit. on p. 27).

[RT77] P.-A. Raviart and J. M. Thomas. "A mixed finite element method for 2nd order elliptic problems". In: *Mathematical aspects of finite element methods*. 1977, 292–315. DOI: 10.1007/BFb0064470 (cit. on pp. 1, 29, 58).

[RW17] S. Rhebergen and G. N. Wells. "Analysis of a hybridized/interface stabilized finite element method for the Stokes equations". *SIAM J. Numer. Anal.* 55.4 (2017), 1982–2003. DOI: 10.1137/16M1083839 (cit. on p. 29).

[RW18] S. Rhebergen and G. N. Wells. "A hybridizable discontinuous Galerkin method for the Navier-Stokes equations with pointwise divergence-free velocity field". *J. Sci. Comput.* 76.3 (2018), 1484–1501. DOI: 10.1007/s10915-018-0671-4 (cit. on pp. 27, 29).

[RW20] S. Rhebergen and G. N. Wells. "An embedded-hybridized discontinuous Galerkin finite element method for the Stokes equations". *Comput. Methods Appl. Mech. Engrg.* 358 (2020), 112619. DOI: 10.1016/j.cma.2019.112619 (cit. on pp. 27, 29).

[Riv08] B. Rivière. *Discontinuous Galerkin methods for solving elliptic and parabolic equations*. Philadelphia, PA: Society for Industrial and Applied Mathematics, 2008. DOI: 10.1137/1.9780898717440 (cit. on p. 84).

[SG06] H. Schlichting and K. Gersten. *Grenzschicht-Theorie*. 10th ed. Berlin: Springer, 2006. DOI: 10.1007/3-540-32985-4 (cit. on pp. 21, 89, 93).

[SL13] J. Schöberl and C. Lehrenfeld. "Domain decomposition preconditioning for high order hybrid discontinuous Galerkin methods on tetrahedral meshes". In: *Advanced finite element methods and applications*. Vol. 66. Lect. Notes Appl. Comput. Mech. Heidelberg: Springer, 2013, 27–56. DOI: 10.1007/978-3-642-30316-6_2 (cit. on p. 30).

[Sch19] P. W. Schroeder. "Robustness of High-Order Divergence-Free Finite Element Methods for Incompressible Computational Fluid Dynamics". Doctoral Thesis. Georg-August-Universität Göttingen, 2019. DOI: 10.53846/goediss-7330 (cit. on pp. 3, 29).

[SLLL18] P. W. Schroeder, C. Lehrenfeld, A. Linke, and G. Lube. "Towards computable flows and robust estimates for inf-sup stable FEM applied to the time-dependent incompressible Navier–Stokes equations". *SeMA J.* 75.4 (2018), 629–653. DOI: 10.1007/s40324-018-0157-1 (cit. on pp. 15, 29).

[SL18] P. W. Schroeder and G. Lube. "Divergence-free $H(\mathrm{d}iv)$-FEM for time-dependent incompressible flows with applications to high Reynolds number vortex dynamics". *J. Sci. Comput.* 75.2 (2018), 830–858. DOI: 10.1007/s10915-017-0561-1 (cit. on p. 29).

[Sch98] C. Schwab. *p- and hp-finite element methods*. New York: Oxford University Press, 1998. URL: https://lccn.loc.gov/98023129 (cit. on pp. 9, 13).

[SV85] L. R. Scott and M. Vogelius. "Norm estimates for a maximal right inverse of the divergence operator in spaces of piecewise polynomials". *ESAIM Math. Model. Numer. Anal.* 19.1 (1985), 111–143. DOI: 10.1051/m2an/1985190101111 (cit. on pp. 1, 27).

[Sco18] L. R. Scott. *Introduction to Automated Modeling with FEniCS*. Chicago: Computational Modeling Initiative, 2018. URL: https://lccn.loc.gov/2018905482 (cit. on p. 28).

[Syn57] J. L. Synge. *The hypercircle in mathematical physics: a method for the approximate solution of boundary value problems*. Cambridge: Cambridge University Press, 1957. URL: https://www.cambridge.org/9781107666559 (cit. on p. 18).

[TH73] C. Taylor and P. Hood. "A numerical solution of the Navier–Stokes equations using the finite element technique". *Internat. J. Comput. & Fluids* 1.1 (1973), 73–100. DOI: 10.1016/0045-7930(73)90027-3 (cit. on p. 16).

[VZ19] R. Verfürth and P. Zanotti. "A quasi-optimal Crouzeix–Raviart discretization of the Stokes equations". *SIAM J. Numer. Anal.* 57.3 (2019), 1082–1099. DOI: 10.1137/18M1177688 (cit. on pp. 34–36).

[Vul83] R. Vulanović. "On a numerical solution of a type of singularly perturbed boundary value problem by using a special discretization mesh". *Novi Sad J. Math.* 13 (1983), 187–201. URL: https://sites.dmi.uns.ac.rs/nsjom/Papers/13/NSJOM_13_187_201.pdf (cit. on p. 22).

[Vul01] R. Vulanović. "A priori meshes for singularly perturbed quasilinear two-point boundary value problems". *IMA J. Numer. Anal.* 21.1 (2001), 349–366. DOI: 10.1093/imanum/21.1.349 (cit. on p. 22).

[WH03] T. Warburton and J. S. Hesthaven. "On the constants in *hp*-finite element trace inverse inequalities". *Comput. Methods Appl. Mech. Engrg.* 192.25 (2003), 2765–2773. DOI: 10.1016/S0045-7825(03)00294-9 (cit. on p. 84).

[Zha05] S. Zhang. "A new family of stable mixed finite elements for the 3D Stokes equations". *Math. Comp.* 74.250 (2005), 543–554. DOI: 10.1090/S0025-5718-04-01711-9 (cit. on p. 28).

[Zha11] S. Zhang. "Divergence-free finite elements on tetrahedral grids for $k \geq 6$". *Math. Comp.* 80.274 (2011), 669–695. DOI: 10.1090/S0025-5718-2010-02412-3 (cit. on p. 28).